Large Eddy Simulation of Three-dimensional Mixed Convection on a Vertical Plate

Large Eddy Simulation von dreidimensionaler Mischkonvektion an einer vertikalen Platte

Von der Fakultät für Maschinenwesen der
Rheinisch-Westfälischen Technischen Hochschule Aachen
zur Erlangung des akademischen Grades eines
Doktors der Ingenieurwissenschaften
genehmigte Dissertation

vorgelegt von
Oliver Garbrecht

Berichter:
Univ.-Prof. Dr.-Ing. Reinhold Kneer
Univ.-Prof. Dr.-Ing. Stephan Kabelac

Tag der mündlichen Prüfung:
23.08.2017

Diese Dissertation ist auf den Internetseiten
der Universitätsbibliothek online verfügbar.

Abstract

Convective heat losses on solar central receivers arise from a combination of buoyancy-driven natural and forced convection. This mixed convection is characterized by two factors: First, the direction of gravity. Gravity aligned with the imposed flow results in a two-dimensional flow case. Three-dimensional mixed convection occurs when gravity acts perpendicular to the free stream. The second factor is the relative influence of buoyancy, as described by $\mathrm{Gr}/\mathrm{Re}^2$. In this work, three regimes are distinguished: Buoyancy-dominated, interia-dominated, and mixed convection with equipollent mechanisms.

This thesis seeks to investigate the thermo-fluid interaction of turbulent three-dimensional mixed convection by using computational fluid dynamics. For that purpose, a large-eddy simulation model has been developed and qualitatively validated. In a series of simulations, a flat, hot, vertical plate was exposed to a horizontal fluid flow. Interpretation of the simulation results proved that buoyancy-induced instabilities are a key factor in the onset of turbulence. Reducing the plate temperature led to a significant reduction in turbulence. It was also found that an increase in free-stream velocity suppresses instabilities, delaying the laminar-turbulent transition. These findings are of high relevance for the heat transfer, as an evaluation of the heat transport mechanisms revealed that most of the transfer is linked to turbulence. Depending on flow conditions, a higher velocity can thus reduce the average heat transfer rate off the plate.

In order to understand the underlying mechanisms, boundary layer profiles were evaluated. A three-dimensional mixed convection boundary layer flow can be described by a local flow angle and a local velocity magnitude. In wall proximity, a high-angle region was found, exhibiting a significant vertical updraft. After transition, the turbulent transport of horizontal momentum from the free stream into this region is reflected in a reduction of the angle. Consequently, the highest angles were found in the transition zone. When buoyancy had a high influence, a distinct velocity peak emerged in the velocity magnitude.

The turbulent coherent structures showed a characteristic pattern: In the laminar flow, elongated streaks form prior to transition. These streaks soon exhibit secondary instabilities and eventually break up into structures like wall-attached hairpin vortices. Here, the buoyancy-fueled updraft has an impact by partially distorting these vortices.

While the simulation results are successful in providing insights into the physics, they also point out challenges in finding physically meaningful modeling approaches. This is true i.e. for heat transfer correlations and numerical wall models.

Zusammenfassung

Konvektive Wärmeverluste an solaren Strahlungsempfängern sind eine Überlagerung von natürlicher und erzwungener Konvektion. Diese sogenannte gemischte Konvektion wird von zwei Faktoren beeinflusst: Erstens, von der Richtung der Gravitation. Ist diese parallel zur aufgeprägten Strömung, stellt sich ein zweidimensionaler Strömungsfall ein. Steht die Gravitation senkrecht zum Freistrom, ergibt sich dreidimensionale gemischte Konvektion. Zweitens, vom relativen Einfluss des Auftriebs, beschrieben durch die Richardson-Zahl ($\mathrm{Gr}/\mathrm{Re}^2$). In der vorliegenden Arbeit werden hierfür drei Regime unterschieden: auftriebsdominierte, trägheitsdominierte und gemischte Konvektion mit gleichstarken Mechanismen.

Das Ziel der Arbeit ist die Untersuchung der Thermo-Fluid-Interaktion bei dreidimensionaler gemischter Konvektion mittels numerischer Stömungsmechanik. Ein Grobstruktursimulationsmodell wurde entwickelt und qualitativ validiert. Mehrere Simulationen eines horizontalen Fluidstromes entlang einer vertikalen, flachen, heißen Platte wurden durchgeführt. Die Ergebnisse zeigen, dass Instabilitäten durch Auftrieb der entscheidende Faktor für den laminar-turbulenten Umschlag sind. Eine geringere Oberflächentemperatur führt so zu einer erheblichen Verringerung der Turbulenz. Weiterhin wurde gezeigt, dass eine höhere Freistromgeschwindigkeit die Instabilitäten unterdrückt und somit die Transition verzögert. Diese Ergebnisse sind für den Wärmeübergang von Relevanz, da dieser von den turbulenten Transportmechanismen dominiert wird. In Abhängigkeit der Strömungsbedingungen kann eine höhere Strömungsgeschwindigkeit somit den mittleren Wärmeübergang verringern.

Um die hierfür zugrunde liegenden Mechanismen zu untersuchen wurden Grenzschichtprofile ausgewertet. Hierbei kann die Grenzschichtströmung bei dreidimensionaler, gemischter Konvektion durch einen lokalen Strömungswinkel und den Betrag des Geschwindigkeitsvektors beschrieben werden. In Wandnähe wurde so eine Region mit hohen Winkeln gefunden, in welcher der Auftrieb eine wichtige Rolle spielt. Nach dem laminar-turbulenten Umschlag spiegelt sich hier der turbulente Transport von horizontalem Impuls aus dem Freistrom heraus in einer Verringerung des Strömungswinkel wider. Deshalb traten die höchsten Winkel grundsätzlich in der Transitionszone auf. In den Simulationsfällen, in denen Auftrieb eine große Rolle spielt, entwickelte sich ein ausgeprägtes Geschwindigkeitsmaximum.

In den turbulenten kohärenten Strukturen zeigte sich ein charakteristisches Muster: In der laminaren Strömung entwickeln sich langgezogene Wirbelfäden, die aufgrund von sekundären Instabilitäten in verschiedene kohärente Strukturen

zerfallen (z.B. in Haarnadel-Wirbel). Diese Wirbel werden von der Auftriebsströmung verzerrt.
Die Strömungsergebnisse erlauben weitreichende Einblicke in die Physik der gemischten Konvektion. Jedoch wurden so auch die Herausforderungen für zukünftige Modellierungsansätze aufgezeigt. Dies betrifft insbesondere die Entwicklung von Wärmeübergangskorrelationen und numerischen Wandmodellen.

Acknowledgments

I would like to thank all colleagues at the Institute for Heat and Mass Transfer for their support throughout the development of this thesis and for making my time at the institute very enjoyable. Especially, I wish to thank my friend Philipp Pischke for proof-reading and for the numerous discussions, both inside and outside the office. This work would not have been possible without the HPC-support of Kurt Nährich and the IT-support of Bernhard Thalheim and Fabian Heusinger. I would further like to thank Manuel Rietz, Leif Schumacher, and Claas Ehrenpreis for conducting the flow visualization experiments.

I would like to thank my supervisor Prof. Reinhold Kneer for providing an excellent scientific environment and the freedom to try out new research fields. I also wish to thank the committee members, especially Prof. Stephan Kabelac for his review of this thesis.

Most of all, I wish to thank my wife Eva for her support and patience.

The simulations of this work were performed with computing resources granted by JARA-HPC from RWTH Aachen University under the project number 0147.

Contents

1 Motivation **1**

2 Mixed convection **5**
2.1 Fundamentals of fluid dynamics 7
2.1.1 Governing equations of fluid flow and heat transfer 7
2.1.2 Numerical solution method 9
2.1.3 Turbulence and its modeling 10
2.1.4 Boundary layer 22
2.2 Introduction to convective heat transfer 29
2.2.1 Experimental investigation methods 36
2.2.2 Numerical simulation methods 39
2.3 Review of literature on mixed convection 42
2.3.1 Two-dimensional flow cases 42
2.3.2 Three-dimensional flow cases 47
2.4 Chapter summary 49

3 Computational methodology **53**
3.1 Modeling approach 53
3.1.1 Large eddy simulation 53
3.1.2 Thermophysical properties 55
3.2 Solution algorithm 58
3.3 Computational mesh and boundary conditions 61
3.4 Numerical schemes 68
3.5 Initialization 73
3.6 Qualitative validation and evaluation methods 76
3.6.1 Aiding flow 80
3.6.2 Opposing flow 109
3.7 Chapter summary 113

4 Physical description of the investigation **115**
4.1 Buoyancy-dominated mixed convection . . . 119
4.2 Inertia-dominated mixed convection . . . 119
4.3 Mixed convection with equipollent mechanisms . . . 119
4.4 Chapter summary . . . 120

5 Simulation results **121**
5.1 Reference case . . . 122
5.1.1 Flow fields . . . 122
5.1.2 Boundary layers . . . 126
5.1.3 Heat transfer . . . 137
5.1.4 Turbulence . . . 141
5.2 Influence of the free stream . . . 148
5.2.1 Flow fields . . . 148
5.2.2 Boundary layers . . . 152
5.2.3 Heat transfer . . . 161
5.2.4 Turbulence . . . 164
5.3 Influence of buoyancy . . . 168
5.3.1 Flow fields . . . 168
5.3.2 Boundary layers . . . 172
5.3.3 Heat transfer . . . 180
5.3.4 Turbulence . . . 181
5.4 Chapter summary . . . 186

6 Discussion **189**

Bibliography **193**

A Solution algorithm and linear solvers **201**

B Numerical solution parameters **209**

C Heat transfer mechanisms **211**

D OpenFOAM dictionary files **215**

E Modified source code **231**

Glossary **236**

Nomenclature

Latin Symbols

a	Coefficient scalar
$\boldsymbol{A}$	Coefficient matrix
c	Heat capacity
c	Coefficient
C_{k}	Universal Kolmogorov constant
C	Model constant
$\boldsymbol{C}$	Cross-term stress tensor
d	Distance
e	Energy
E	Spectral energy
$\boldsymbol{F}$	Force
$\boldsymbol{g}$	Gravity
G	Filter function
h	Heat transfer coefficient
h	Enthalpy
H	Plate height
I	Turbulence intensity
$\boldsymbol{I}$	Identity matrix
k	Molecular thermal conductivity
k	Turbulent kinetic energy (TKE)
K	Independent sources
$\boldsymbol{K}$	Independent source vector
$\boldsymbol{L}$	Leonard stress tensor
N	Number of cells
l	Length scale
l^+	Dimensionless length scale
L	Plate length
lh	Adapted length scale
LH	Length scale
$\boldsymbol{n}$	Normal vector
p	Pressure
Q	Second invariant of the velocity gradient tensor
r	Flux-limiting factor
$\boldsymbol{R}$	Reynolds stress tensor
S	Surface

S	Source and sink terms
$\boldsymbol{S}$	Strain-rate tensor
$\boldsymbol{S}_f$	Face area vector
t	Time
T	Temperature
v	Kolmogorov velocity scale
u^+	Dimensionless velocity
u_τ	Friction velocity
$\boldsymbol{u}$	Velocity
V	Volume
w	Weighting factor
$\boldsymbol{W}$	Rotation-rate tensor
x	Horizontal coordinate
x	Space
y	Vertical coordinate
z	Wall-normal coordinate
z^+	Dimensionless wall distance

Greek Symbols

α	Thermal diffusivity
α	Under-relaxation factor
β	Volumetric coefficient of thermal expansion
β_m	Cut-off factor
γ	Blending factor
γ	Flow angle
Γ	Diffusion coefficient
δ_1	Displacement thickness
δ_2	Momentum thickness
δ_3	Energy thickness
δ_{99}	Velocity boundary layer thickness
δ_T	Temperature boundary layer thickness
Δ	Mesh spacing
Δ	Filter width
ϵ	Turbulent dissipation rate
η	Kolmogorov length scale
κ	Wavenumber
κ	Kármán's constant
λ	Eigenvalue
μ	Dynamic viscosity
ν	Kinematic viscosity

ν_t	Turbulent viscosity
ρ	Density
σ	Model constant
τ	Kolmogorov time scale
ϕ	General scalar property
φ	Flux
$\boldsymbol{\phi}$	General vector or matrix
$\boldsymbol{\tau}$	Stress tensor
ψ	Flux limiter
$\boldsymbol{\omega}$	Vorticity

Dimensionless Numbers

Ar	Archimedes number
Co	Courant number
Gr	Grashof number
Nu	Nusselt number
Pr	Prandtl number
Re	Reynolds number
Ri	Richardson number

Mathematical operators and nomenclature

ϕ	Scalar
$\boldsymbol{\phi}$	Vector or tensor
$\boldsymbol{\phi}^T$	Transposed vector
Δ	Difference
$\mathrm{tr}(\boldsymbol{\phi})$	Trace of $\boldsymbol{\phi}$
$k\boldsymbol{\phi}$	$(k\phi_1, k\phi_2, k\phi_3)$
$\nabla(\boldsymbol{\phi})$	Gradient of a vector
$\nabla \cdot (\boldsymbol{\phi})$	Divergence of a vector
$\boldsymbol{\phi} \cdot \boldsymbol{\phi}$	Inner product $\phi_1\phi_1 + \phi_2\phi_2 + \phi_3\phi_3$
$\boldsymbol{\phi}\boldsymbol{\phi}$	Outer product $\boldsymbol{\phi_{ij}}$
$\boldsymbol{\tau} \cdot \cdot \nabla\boldsymbol{\phi}$	Outer product $\tau_{11}\partial\phi_1/\partial x_1 + \tau_{21}\partial\phi_1/\partial x_2 + \tau_{31}\partial\phi_1/\partial x_3 + ...$ $+\tau_{12}\partial\phi_2/\partial x_1 + ...$
$\boldsymbol{\phi_1} \times \boldsymbol{\phi_2}$	Cross product of $\boldsymbol{\phi_1}$ and $\boldsymbol{\phi_2}$
$\boldsymbol{\tau} : \nabla\boldsymbol{\phi}$	Double dot product $\tau_{11}\partial\phi_1/\partial x_1 + \tau_{12}\partial\phi_1/\partial x_2 + ... + \tau_{21}\partial\phi_2/\partial x_1 +$ $+\tau_{22}\partial\phi_2/\partial x_2 + ... + \tau_{31}\partial\phi_3/\partial x_1 + \tau_{32}\partial\phi_3/\partial x_2 + ...$
$G * \phi$	Convolution integral

Filtering and Averaging Operators

$\overline{\phi}$	Time-averaged mean
ϕ'	Turbulent fluctuation
$\tilde{\phi}$	Favre-averaged mean
ϕ''	Turbulent Favre fluctuation
$\overline{\phi}$	Filtered part in LES
ϕ'	Subgrid-scale part

Indices

a	Ambient
avg	Average
b	Buoyant
c	Cell
cd	Central differencing
e	Energy
eff	Effective
f	Face
f	Forced
∞	Free stream
max	Maximum
min	Minimum
N	Neighbor cell
nat	Natural
p	Parcel
P	Present cell
t	Turbulent
sgs	Subgrid scale
up	Updraft
ud	Upwind differencing
W	Wall

Chapter 1.

Motivation

The present work on the computation of three-dimensional mixed convection is motivated by the aim to quantify the thermal performance of a solar receiver. This component is central in solar power towers. Here, a large number of heliostats biaxially track the sun to reflect its radiation onto the top of the tower, where the receiver is mounted. As its surface is considerably smaller than the heliostats' surfaces, the impinging solar radiation is highly concentrated. The receiver's function is to absorb this radiation and transfer it as heat into a fluid. The most significant thermal losses are by reflection of incoming radiation and by thermal emissions. In addition, heat is lost to the ambiance as consequence of wind (forced convection) and buoyancy (natural convection). These last two mechanisms are combined into mixed convection.

The concept of a solar tower power plant is illustrated in Figure 1.1, where the Spanish Gemasolar plant is shown. This commercial facility features a 140 m high tower and a central receiver capable of absorbing 120 $\mathrm{MW_{th}}$ of solar radiation (Burgaleta et al., 2012). For the use of molten salt as the heat transfer fluid, two general receiver concepts are state of the art: In *Open receivers*, tubes arranged around the top of the tower contain the salt flow. Radiation from a surrounding heliostat field impinges the tube's outer surface. This surface, however, is in direct contact with the ambiance, and thermal losses are therefore comparably high, i.e. any reflection has to be considered a loss. Furthermore, due to the large receiver height (10 m), the large temperature difference between the surrounding air and the surface (580 K), and the exposed location, convection losses by mixed convection are significant. For Gemasolar, Lata et al. (2008) have broken down the respective mechanisms and quantified convection to represent approximately 15% of the entire thermal losses.
The second design are *Cavity receivers* where concentrated radiation enters an enclosure through an opening. The tubes are arranged at the inner walls of the cavity. This concept dramatically reduces convection and radiation losses, as only a small fraction of the heat can leave the cavity. The gain in efficiency, however, comes at the price of not being able to collect solar radiation from a surrounding heliostat field.
When the author – back in 2010 – started to develop the *Novel receiver* shown in Figure 1.1, he focused on reducing the radiation losses. This resulted in a surface texture formed by many hexagonal pyramids arranged in a honeycomb-like struc-

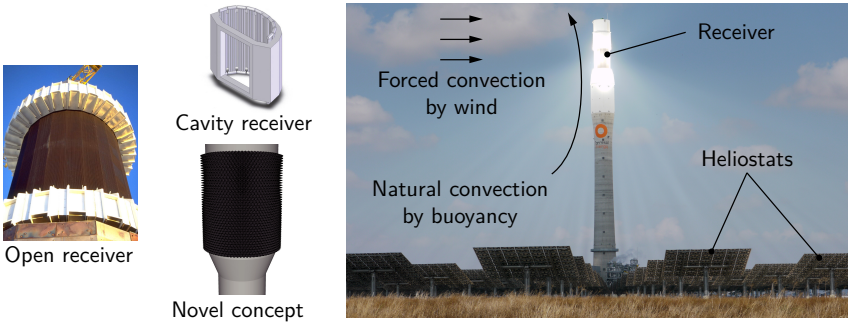
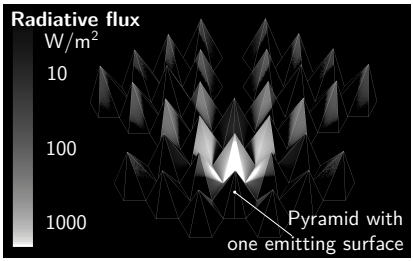


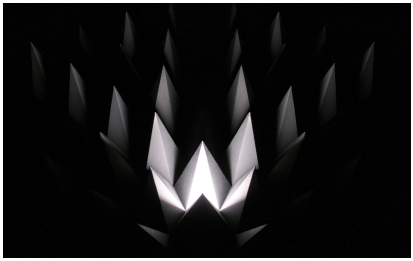
Figure 1.1.: Overview of the Gemasolar solar power plant with the two convection loss mechanisms indicated. On the left is a comparison of different receiver concepts: Open receiver (Image courtesy of Sandia National Laboratories), cavity receiver (Li et al., 2010) and the novel radiation trap concept.

ture reminding of a waffle-iron. The apex of each pyramid points toward the heliostat field, the concentrated radiation can thus enter the system through an aperture spanned by the pyramid apices. Subsequently, it impinges the pyramid side faces, where the lion's share is absorbed. Reflection occurring at this point is very likely to impinge on the side face of another pyramid. Effectively, the system acts as a radiation trap. Thermal emissions are reduced by cooling the element through a molten salt flow in a way that the apex is the coldest spot of the pyramid. Due to the geometry, this is the very point where view factors to the ambiance reach their maximum. The opposite is true for the region with highest temperature at the pyramid base. The theoretical concept is discussed in Garbrecht et al. (2013), and its implementation into a commercial-scale receiver is subject to a patent (Garbrecht, 2014). With the radiation trap reducing losses, at the same time allowing for a surrounding heliostat field, the novel receiver combines the main advantages of open receivers and cavity receivers.

The approach for the investigation of the novel receiver's thermal performance was to couple different simulations: One simulation covered the reflections and one the thermal emissions, both using a raytracing model. In order to evaluate the performance of the radiation model (i.e. ensuring a sufficient number of rays for the raytracing), the visual experiment shown in Figure 1.2 was conducted: One side face of a pyramid at the center of a physical receiver model homogeneously emitted light. The distribution within the receiver system was captured and compared to the results of a corresponding numerical simulation. The figure shows both results in excellent agreement with each other, with respect to shadow structures and the distribution of radiation intensity.



(a) Simulation

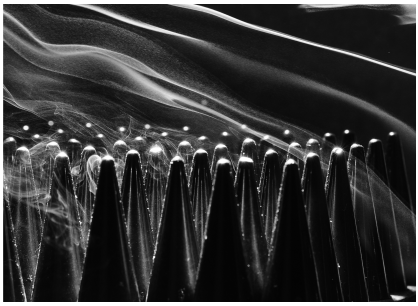


(b) Experiment

Figure 1.2.: Comparison of the numerical simulation results and the visual experiment (Garbrecht et al., 2013). The setup is identical for both cases: One pyramid side face homogeneously emits radiation. Both distribution patterns are in excellent agreement.



(a) Experimental setup



(b) Flow interaction with geometry



(c) Flows within the receiver



(d) Increasing complexity

Figure 1.3.: Flow channel visualization experiments reveal the vast degree of complexity exhibited by the flow around the receiver elements. It becomes evident that – even when neglecting buoyancy effects – a reasonable estimation of the convective heat transfer using simple models is virtually impossible.

A finite volume simulation was used for the heat conduction through the receiver shell. The molten salt flow on the inside, including the convective heat transfer, was investigated using computational fluid dynamics (CFD). At this point, the author encountered the problem of lacking methods that would reliably describe mixed convection heat losses. A simple Nusselt-correlation blending forced (Bergan, 1986) and natural convection (Siebers and Kraabel, 1984) was used. This correlation, however, is no more than a "best guess". A conclusive assessment of the receiver's thermal performance is therefore still pending.
The general question arose whether a rather simple correlation can capture even the most prominent effects of mixed convection. Therefore, a second experiment was conducted: A large number of small pyramids were arranged in a flow channel. By vaporizing Glycerol, the flow around the pyramids was visualized. Figure 1.3 shows the general setup of the experiment (a) and three different aspects of the flow: First, the strong interaction between the imposed flow and the geometry is illustrated (b). Second, flow structures are formed in the wake of the first pyramids (c) and increase in complexity as the flow passes more elements (d). From this visualization, it becomes evident that simple models will not succeed in predicting the convective heat transfer in this particular case. This becomes even more true as buoyancy has been neglected in the experiment.

Therefore, the motivation of this work is to investigate the mechanisms of mixed convection and to provide a solid basis for the development of further modeling. Apart from the motivating application for solar receivers, mixed convection plays an important role in several other relevant technical applications. This includes the performance of photovoltaic cells which is very sensitive to the cell's temperature. As only approximately 15% of incoming solar radiation is converted into electrical energy (most of the remaining 85% dissipate into heat), convection as a cooling mechanism is of high interest (see e.g. Lau et al., 2012). Further applications are safety curtains for fire protection or the cooling of electronic components on circuit boards (see e.g. Raghavan and Rahman, 1997). When modeling climate change impacts, understanding convection is a key issue (see Keitzl et al., 2016, on the melting of polar ice).

The present work is divided into four main sections: Chapter 2 will give an introduction to mixed convection, which includes fundamentals in fluid dynamics, challenges in its investigation, the current state of research, and a formulation of open research questions. Please note, that the nomenclature has been adapted to match the one used in the present work (i.e. x denoting the horizontal, y denoting the vertical and z denoting the wall-normal direction). The Chapters 3 and 4 and will address the methods used, including the physical boundaries of the study and the numerical models. The results are presented in Chapter 5 and discussed at the end of this work in Chapter 6.

Chapter 2.

Mixed convection

Convection – sometimes also referred to as advection – is the transport of heat by fluid motion. Displaced fluid molecules carry their inner energy from one place to another. This mechanism is by far the dominant heat transport mechanism in moving fluids. The driving force of fluid motion can be a pressure gradient, surface tension, or differences in density in combination with gravity (buoyancy). In general, there are two types of convective flows: First, forced convection is an imposed flow (usually pressure-driven) and second, natural or free convection is a flow driven by buoyancy. When heat is transferred into a fluid, the local temperature will change. In real and non-ideal fluids, this change in temperature results in a change in density (in relation to the surrounding fluid), causing a volumetric buoyant force that locally accelerates the fluid. This fluid motion is referred to as natural (free) convection.

In an environment with gravity $\boldsymbol{g}$ in y-direction, an infinitely small fluid parcel with lower density within its volume $\mathrm{d}V^*$ experiences an updraft caused by the pressure difference between its top and bottom face. Assuming that the density around the fluid parcel ρ_a is constant, the pressure gradient $\nabla p = \boldsymbol{g}\rho_\mathrm{a}$ gives the Archimedes' principle

$$\mathrm{d}\boldsymbol{F}_\mathrm{b} = -\boldsymbol{g}\rho_\mathrm{a}\mathrm{d}V^* \tag{2.1}$$

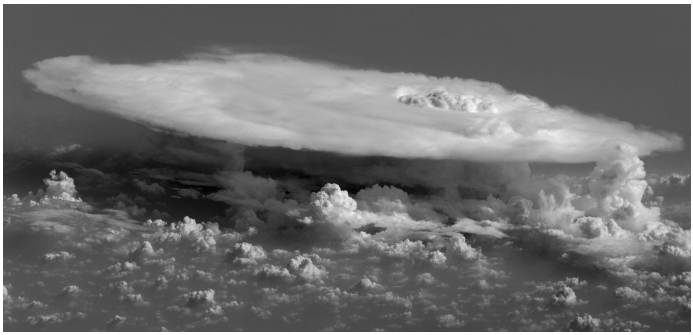
With the parcel's weight of

$$\mathrm{d}\boldsymbol{F}_\mathrm{p} = \boldsymbol{g}\rho_\mathrm{p}\mathrm{d}V^* \tag{2.2}$$

the updraft is

$$\mathrm{d}\boldsymbol{F}_\mathrm{up} = \mathrm{d}\boldsymbol{F}_\mathrm{b} + \mathrm{d}\boldsymbol{F}_\mathrm{p} \tag{2.3}$$

The combination of an imposed flow (forced convection) and a buoyancy-driven flow (natural convection) is referred to as mixed convection. In Chapter 1, convection as a heat loss mechanism on central receivers has been introduced as key motivation for this work. These flows are a textbook example of mixed convection in technical applications. In nature, large-scale convection flows can be observed in the formation of Cumulonimbus clouds. A schematic of the formation process is shown in Figure 2.1: Close to the surface, heat originating from solar radiation is transferred from the ground into the air by forced



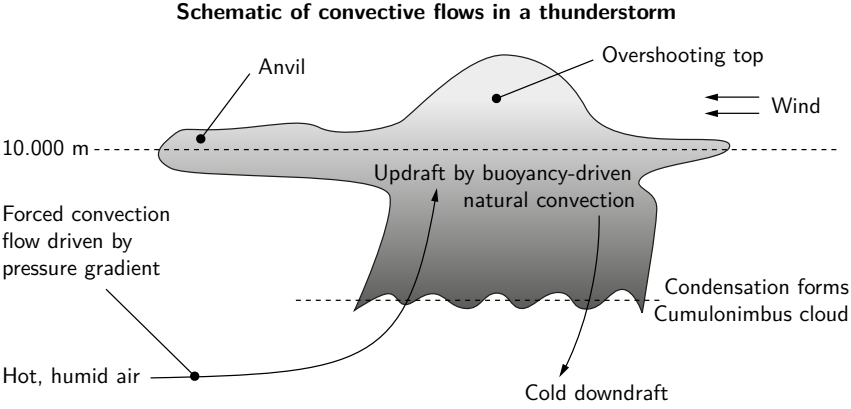


Figure 2.1.: Photograph of a typical Cumulonimbus cloud taken from the International Space Station over Africa (Image courtesy of the Earth Science and Remote Sensing Unit, NASA Johnson Space Center) and schematic of a thunderstorm in mature stage. Highlighted are forced and natural convection in a meteorological context.

convection. The consequent change in air density causes an updraft, rising the hot and humid air to higher altitudes where water droplets will condense. This phase change releases the enthalpy of vaporization which continues to heat the air and causes further convection. The photograph in Figure 2.1 shows the resulting impressive cloud "tower", which can rise up to 20 km in the tropics where extremely humid air is present. While rising, the air masses expand and cool due to the decrease in atmospheric pressure. When reaching the so-called

tropopause – the boundary beyond which air no longer reduces its temperature with increasing altitude – the updraft comes to a stop. Potentially, the rising air masses overshoot, as can be observed in the photograph. The reason for the stop is a stable temperature inversion in the atmospheric layer above the tropopause. The strong wind in this altitude spreads the cloud, giving it the characteristic anvil-like shape.

Convective flows and the occurring heat transfer can be described by the fundamental equations of fluid- and thermodynamics and by a set of dimensionless numbers. The following Chapter 2.1 will give a brief overview of the governing equations, numerical models and solution methods. The aim of Chapter 2.2 is to give an introduction to convective heat transfer as well as the methods and challenges of its investigation, allowing a better understanding of the literature review in Chapter 2.3.1 and 2.3.2.

2.1. Fundamentals of fluid dynamics

The flow of a fluid is mathematically described by a set of differential equations (the Navier-Stokes equations), which were independently derived by the French scientist Claude-Louis Navier and the Irish scientist George Gabriel Stokes in the 19th century. To date, the existence of a generally valid analytic solution has not been proven. Exact solutions only exist for simplified flows like Poiseuille or Couette flows.

2.1.1. Governing equations of fluid flow and heat transfer

The mathematical description of a fluid flow by the Navier-Stokes-equations follows the principles of conservation. All equations balance the temporal change of a conservative scalar or vector with the sum of fluxes, sources, and sinks. A detailed derivation can be found in literature, e.g. Versteeg and Malalasekera (2007), Patankar (1980), Moukalled et al. (2015) in the context of numerical simulations, and in Lesieur (2008), Pope (2000) in the context of turbulent flows.

The conservation of mass in a fluid is expressed by the continuity equation

$$\underbrace{\frac{\partial \rho}{\partial t}}_{\text{(i)}} + \underbrace{\nabla \cdot (\rho \boldsymbol{u})}_{\text{(ii)}} = 0 \tag{2.4}$$

where the temporal change in density (i) is set in relation to the divergence of the advective mass flows (ii). Even though the fluid in this work is considered incompressible – as the flow is sub-sonic by far – the density has a nonzero temporal derivative (i). While in compressible fluids like ideal gases, a change

in density is commonly the result of a change in pressure, the density is here expressed as a function of temperature $\rho(T)$. As temperature varies in time and space, the resulting variation in density is taken into account in all conservation equations.

The change in momentum must equal the forces applied to the fluid, which is also known as second law of motion. In the Navier-Stokes equations, this principle is ensured by one momentum equation per dimension. The general equation for conservation of momentum is

$$\underbrace{\frac{\partial(\rho \boldsymbol{u})}{\partial t}}_{\text{(i)}} + \underbrace{\nabla \cdot (\rho \boldsymbol{u}\boldsymbol{u})}_{\text{(ii)}} = \underbrace{-\nabla p}_{\text{(iii)}} + \underbrace{\nabla \cdot (\mu \boldsymbol{\tau})}_{\text{(iv)}} + \underbrace{\rho \boldsymbol{g}}_{\text{(v)}} \tag{2.5}$$

where (i) denotes the acceleration (with respect to time) and (ii) the convective acceleration (with respect to space). The gradient of static pressure p is (iii), part (iv) of the equation represents the introduction of momentum by viscous stress. The stress tensor $\boldsymbol{\tau}$ is expressed by:

$$\boldsymbol{\tau} = \left[\nabla \boldsymbol{u} + (\nabla \boldsymbol{u})^T - \frac{2}{3}\boldsymbol{I}(\nabla \cdot \boldsymbol{u})\right] \tag{2.6}$$

with the identity matrix $\boldsymbol{I}$. The first part of $\boldsymbol{\tau}$ is the strain-rate tensor, which will also be relevant in the discussion of different turbulence models later on. In order to maintain consistency with literature, it is multiplied by $\frac{1}{2}$

$$\boldsymbol{S} = \frac{1}{2}\left(\nabla \boldsymbol{u} + (\nabla \boldsymbol{u})^T\right) \tag{2.7}$$

Buoyancy and acceleration by gravity as a source of momentum is taken into account as a body force (v). It only applies in y-direction, as the gravity vector only has one entry in y-direction:

$$\boldsymbol{g} = (0 \; g \; 0)^T \tag{2.8}$$

In words, the momentum equation can be understood as: The increase of momentum in a fluid element (i), the flow of momentum in and out of the element (ii), the net flux by diffusion included in (iv) and general source terms (iii), (iv) and (v).

The same form also applies to the energy equation, which strongly influences the momentum equation through the temperature-dependent thermophysical properties and thus also through buoyancy.

$$\underbrace{\frac{\partial(\rho e)}{\partial t}}_{\text{(i)}} + \underbrace{\nabla\cdot(\rho e\boldsymbol{u})}_{\text{(ii)}} = \underbrace{-\nabla\cdot(p\boldsymbol{u})}_{\text{(iii)}} + \underbrace{\nabla\cdot(k\nabla T)}_{\text{(iv)}} + \underbrace{S_e}_{\text{(v)}} \tag{2.9}$$

In this equation, the term (i) denotes the change in energy with respect to time. Term (ii) is the advective or enthalpy transport. The pressure work is introduced by term (iii). Term (iv) is the molecular diffusion of heat (conduction) with the conductivity k and the temperature field T. Term (v) is a general expression for sources and sinks.[1] In this form of the energy equation, work from mechanical sources like viscous heating $\nabla\cdot(\mu\boldsymbol{\tau}\boldsymbol{u})$ and the work done by body forces are neglected.

The Navier-Stokes equations do not provide an explicit equation for pressure. However, the pressure field can be obtained from an iterative procedure ensuring that the continuity equation is satisfied for the resulting velocity and pressure fields. In CFD codes, this procedure is referred to as pressure-velocity coupling.

When considering a buoyancy-influenced flow with only small temperature differences, the Navier-Stokes equations can be simplified by using the Boussinesq-approximation. Its general idea is that the variation in density is small enough to be neglected everywhere except for the buoyancy term in the momentum equation. The density is expressed as

$$\rho = \rho_\mathrm{a}\left(1-\beta\Delta T\right) \tag{2.10}$$

where the index a denotes the bulk and β a general volumetric thermal expansion coefficient. The buoyant force thus writes as

$$\mathrm{d}\boldsymbol{F}_\mathrm{up} = \boldsymbol{g}\rho_\mathrm{a}\beta\left(T-T_\mathrm{a}\right)\mathrm{d}V^* \tag{2.11}$$

For further reference, please see Gebhart et al. (1988). It should be noted that the temperature and density changes in this work are considered to be significant and the Boussinesq-approximation can thus not be applied.

2.1.2. Numerical solution method

In practice, problems that are described by the laws of conservation (e.g. in fluid dynamics: mass, momentum and energy, see Eqns. 2.4, 2.5, 2.9), are commonly solved numerically by using the finite volume method (FVM). The differential form of the conservation laws, which has been derived for an infinitesimal small volume, is then adapted to finite volumes. The flow problem is thus spatially

[1] The terms *source* and *sink* are used in a modeling sense rather than in a thermodynamic sense.

discretized, the volumes are defined in a computational grid. As noted in the previous section, all laws of conservation have a common form:

$$\underbrace{\frac{\partial(\rho\phi)}{\partial t}}_{\text{(i)}} + \underbrace{\nabla\cdot(\rho\phi\boldsymbol{u})}_{\text{(ii)}} = \underbrace{\nabla\cdot(\Gamma\nabla\phi)}_{\text{(iv)}} + \underbrace{S_\phi}_{\text{(v)}} \tag{2.12}$$

with the rate of increase (i), net rate of advective transport (ii), net rate of diffusive transport (iv) where Γ is a diffusion coefficient, and the net rate of change due to sources (v). The integral form of the conservation law is obtained by integrating over the finite volume V^*:

$$\int_{\mathrm{V}^*}\frac{\partial(\rho\phi)}{\partial t}\mathrm{d}V + \int_{\mathrm{V}^*}\nabla\cdot(\rho\phi\boldsymbol{u})\,\mathrm{d}V = \int_{\mathrm{V}^*}\nabla\cdot(\Gamma\nabla\phi)\,\mathrm{d}V + \int_{\mathrm{V}^*}S_\phi\mathrm{d}V \tag{2.13}$$

Applying Gauss's theorem, the advective and diffusive fluxes over the faces of the finite volume are balanced with the sources and the temporal change rate:

$$\int_{\mathrm{V}^*}\frac{\partial(\rho\phi)}{\partial t}\mathrm{d}V + \oint_{\mathrm{V}^*}\boldsymbol{n}\cdot\rho\phi\boldsymbol{u}\mathrm{d}S = \oint_{\mathrm{V}^*}\boldsymbol{n}\cdot\Gamma\nabla\phi\mathrm{d}S + \int_{\mathrm{V}^*}S_\phi\mathrm{d}V \tag{2.14}$$

The integrals can be expressed as sums with the face value of ϕ being interpolated. Temporal integration is possible with a small timestep Δt (temporal discretisation). Assuming a non-adaptive computational grid, the equation can be rewritten as follows.

$$\begin{aligned}\int_{\Delta t}\mathrm{V}^*\frac{\partial}{\partial t}(\rho\phi)\,\mathrm{d}t + \int_{\Delta t}\left(\sum_{\mathrm{V}^*}\boldsymbol{n}\cdot\rho\phi_f\boldsymbol{u}S_f\right)\mathrm{d}t = \\ \int_{\Delta t}\left(\sum_{\mathrm{V}^*}\boldsymbol{n}\cdot\Gamma\nabla\phi_f S_f\right)\mathrm{d}t + \int_{\Delta t}(\mathrm{V}^*S_\phi)\,\mathrm{d}t\end{aligned} \tag{2.15}$$

Using further discretisation for the gradients of ϕ, a system of linear equations is formed. Supposing that a sufficient number of boundary conditions is available, this system can be solved numerically.

2.1.3. Turbulence and its modeling

Fluid motion with a small flow velocity is characterized by a stable, laminar flow. With increasing velocities, however, the viscous stresses (responsible for the diffusion of momentum) are overcome by the flow inertia (causing the advection of momentum), making the flow unstable. This transition from a stable to an



Figure 2.2.: Example of a buoyancy-driven flow with transition from a laminar to a turbulent fluid motion (image credit: Brigitte Werner, Creative Commons License).

unstable condition is considered the transition from a laminar to a turbulent flow. In the latter, the flow is fully three-dimensional and unsteady in time. Figure 2.2 shows an example of a turbulent, buoyancy-driven flow. The essential question of when and how a flow turns turbulent has already been the subject of Osborne Reynolds' research in the late 19th century. Groundbreaking and still impressive considering today's standards were his experiments on the fluid dynamic in pipes, published in Reynolds (1883). Ever since, turbulence has been an ambitious field of research, and even today, precisely predicting the onset and the influence of turbulence is challenging. Modern turbulence research like Avila et al. (2011) uses very complex numerical simulations to find the flow condition where decaying and spreading turbulence are in balance. However, even those sophisticated methods only succeed in rather simple setups such as a pipe flow.

Generally, turbulence can be understood as fluctuations around an average value on a wide range of spacial and temporal scales. In order to assess these fluctuations, the turbulent kinetic energy (TKE)

$$k = \frac{3}{2} u'^2 \tag{2.16}$$

is introduced as a theoretical measure of how much kinetic energy is carried by the turbulent velocity fluctuations

$$u' = \sqrt{\frac{1}{3}\left(u'^2_x + u'^2_y + u'^2_z\right)} \tag{2.17}$$

For the description of production, dissipation and transport of turbulent kinetic energy, a new transport equation (Schlichting and Gersten, 2006) is introduced, similar to the transport of mass, momentum or energy:

$$\begin{aligned} \underbrace{\frac{\partial(\rho k)}{\partial t}}_{\text{(i)}} + \underbrace{\nabla\cdot(\rho\bar{\boldsymbol{u}}k)}_{\text{(ii)}} = \underbrace{\nabla\cdot(\mu\nabla k) + \nabla\cdot\left(\mu\nabla\cdot\left(\overline{\boldsymbol{u'u'}}\right)\right)}_{\text{(iii)}} \\ \underbrace{-\nabla\cdot\left(\overline{\boldsymbol{u'}p' + \frac{1}{2}\rho\boldsymbol{u'}\left((\boldsymbol{u'u'})\cdot\boldsymbol{I}\right)}\right)}_{\text{(iv)}} \underbrace{-\rho\left(\overline{\boldsymbol{u'u'}}:\nabla\overline{\boldsymbol{u}}\right)}_{\text{(v)}} \\ \underbrace{-\mu\left(\overline{\nabla\boldsymbol{u'}:\nabla\boldsymbol{u'} + \nabla\boldsymbol{u'}\cdot\cdot\nabla\boldsymbol{u'}}\right)}_{\text{(vi)}} \underbrace{+\boldsymbol{g}\cdot\overline{\rho'\boldsymbol{u'}}}_{\text{(vii)}} \end{aligned} \tag{2.18}$$

This equation uses Reynolds-averaging where the velocity is decomposed into a time-averaged part $\bar{\boldsymbol{u}}$ and a fluctuating part $\boldsymbol{u'}$. The terms (i) and (ii) denote the temporal change and the advective transport of k. The third term (iii) is the viscous transport (viscous diffusion), (iv) the turbulent kinetic energy transported through velocity fluctuations (turbulent diffusion) and through pressure fluctuations (pressure diffusion). The fifth term (v) is the production of turbulent kinetic energy by the mean strain rate and (vi) its dissipation into heat. In flows influenced by buoyancy, turbulent kinetic energy can be lost or gained through buoyancy effects. A gain occurs in an unstable flow, e.g with a fluid heated from below or by a hot vertical wall. As the present work investigates a vertical wall configuration, the term (vii), representing buoyancy, is considered to be positive. Note that the density fluctuations are neglected throughout the equation, but are included in (vii).

Equation 2.18 allows to balance the turbulent kinetic energy and to investigate the contribution of each mechanism. However, no information on the respective scales of turbulence is included, as it balances integral values of k. For the spectral distribution, it is of interest to Fourier-transform k into an energy spectral density E:

$$k = \int_0^\infty E(\kappa)\,\mathrm{d}\kappa \tag{2.19}$$

where κ is the wavenumber. Larger eddies are represented by smaller wavenumbers and vice versa. Figure 2.3 illustrates the spectral distribution of turbulent

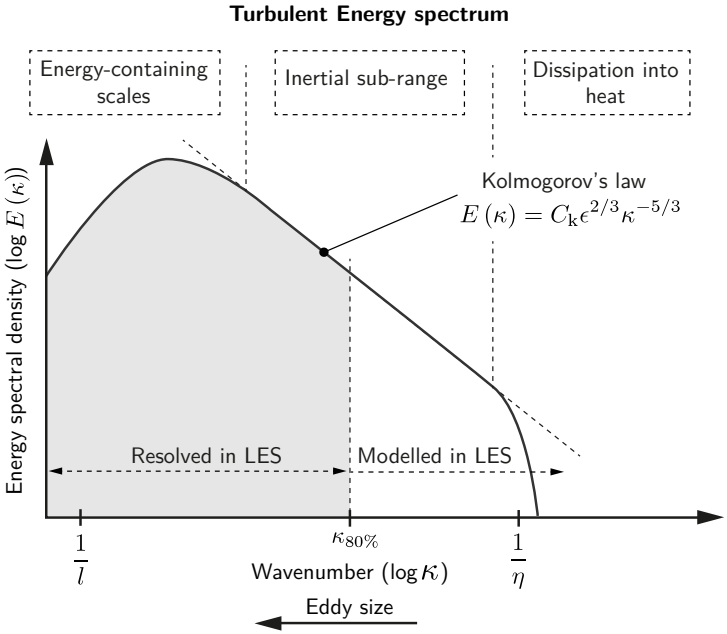


Figure 2.3.: The spectral distribution of turbulent energy (Fröhlich, 2006; Wilcox, 2006), showing three distinct scales: 1. The energy-containing scales where the turbulent energy is injected. 2. The inertial sub-range, where energy is transported from larger to smaller eddies. The spectral energy within these scales is described by Kolmogorov's law. 3. Dissipative range, where viscous effects strongly dampen the turbulence. All turbulent energy is thus dissipated into heat. The wavenumber up to which all turbulent scales are usually resolved in an LES is marked by $\kappa_{80\%}$.

kinetic energy: Most of the energy is carried by the large-scale eddies (scale l), which usually is the scale at which it is introduced into the flow. These energy-containing scales are mainly responsible for the enhanced transfer of mass, energy and momentum, referred to as turbulent diffusion (Wilcox, 2006). One major feature of turbulence is the so-called energy cascade where turbulent energy is transferred from larger to smaller scales by the collapse of larger structures. As shown in the spectrum above, this mechanism transports energy through the inertial subrange where the spectral density is described by the Kolmogorov law

$$E(\kappa) = C_k \epsilon^{2/3} \kappa^{-5/3} \tag{2.20}$$

Kolmogorov (1941) concluded, that – within this range – the spectral distribution solely depends on the the wavenumber κ and the rate of dissipation:

$$\epsilon = -\frac{\mathrm{d}k}{\mathrm{d}t} \sim \frac{k^{3/2}}{l} \tag{2.21}$$

The rate as stated by Taylor (1935) (for high Re numbers) basically is the rate, at which energy is supplied by the larger eddies. The Kolmogorov constant C_k is universal.
On the far side of the spectrum in Figure 2.3, the kinetic energy sharply drops to zero at a certain length scale η. As this scale was predicted by Kolmogorov (1941) through dimensional analysis, it is named the Kolmogorov scale

$$\eta = \left(\frac{\nu^3}{\epsilon}\right)^{1/4} \tag{2.22}$$

Below the Kolmogorov scale, viscous effects strongly dampen the turbulence. The turbulent kinetic energy available at these scales is consequently dissipated into heat. It should be noted that – even though Kolmogorov's work was of theoretical nature – his predictions have been proven correct for many different flows, even in the atmosphere (Boer and Shepherd, 1982).

For the numerical simulation of turbulence, the important question arising from these considerations is: Which scales need to be resolved and which scales can be modeled? The challenge in simulating turbulent flows is to find a balance between losing too much information by applying extensive modeling on one hand, and over-resolving the problem on the other hand. It is, for example, of little use to fully resolve all scales in a simulation that is only supposed to give a rough estimation. On the other hand, under-resolving or modeling the turbulence in a scientific experiment might mean that significant effects are not seen. Unfortunately, no universal solution for the treatment of turbulence in CFD simulations exists, which is the main reason that – even with the significant increase in computational power over the last decades – turbulence remains the key problem in the numerical simulation of fluid flows. To date, three major approaches are commonly used:

Reynolds-Averaged Navier-Stokes (RANS) The concept of RANS takes advantage of the statistical nature of turbulence. The instantaneous value of a scalar ϕ or a vector $\boldsymbol{\phi}$ is decomposed into an time-averaged (mean) and a fluctuating value:

$$\phi = \bar{\phi} + \phi' \tag{2.23}$$

Using the decomposition for the velocity and the pressure and taking into account that the mean of all fluctuations is $\overline{\phi'} = 0$, but $\overline{\phi'\phi'} \neq 0$, the Reynolds-averaged form of the momentum equation (Eqn. 2.5) is:

$$\frac{\partial\left(\rho\bar{\boldsymbol{u}}\right)}{\partial t}+\nabla\cdot\left(\rho\left(\bar{\boldsymbol{u}}\bar{\boldsymbol{u}}+\overline{\boldsymbol{u}'\boldsymbol{u}'}\right)\right)=-\nabla\bar{p}+\nabla\cdot\left(\mu\bar{\boldsymbol{\tau}}\right)+\rho\boldsymbol{g} \tag{2.24}$$

or in the more common form

$$\frac{\partial\left(\rho\bar{\boldsymbol{u}}\right)}{\partial t}+\nabla\cdot\left(\rho\bar{\boldsymbol{u}}\bar{\boldsymbol{u}}\right)=-\nabla\bar{p}+\nabla\cdot\left(\mu\bar{\boldsymbol{\tau}}-\rho\overline{\boldsymbol{u}'\boldsymbol{u}'}\right)+\rho\boldsymbol{g} \tag{2.25}$$

The Reynolds-stress tensor $-\overline{\boldsymbol{u}'\boldsymbol{u}'}$ is a description of the mean rate of momentum transport caused by turbulence. As the Navier-Stokes equations do not provide sufficient information for a direct solution, modeling of the Reynolds-stress tensor is required. In literature, this problem is referred to as the *Closure problem.*

For flows with a variable fluid density, Reynolds-averaging has to be applied to the density as well. This adds additional terms to Eqn. 2.25 because of the correlation between velocity and density fluctuations. In order to reduce the number of separate terms, density-averaged values are used in the Favre averaging approach

$$\phi=\tilde{\phi}+\phi''=\frac{\overline{\rho\phi}}{\bar{\rho}}+\phi'' \tag{2.26}$$

where $\tilde{\phi}$ is the mean and ϕ'' the fluctuations. Applying this method to the velocity significantly simplifies the averaged momentum equation and yields a form that is identical with Eqn. 2.25, except for using $\tilde{u}$ instead of $\bar{u}$, $\bar{\rho}$ instead of ρ, and u'' instead of u' (see e.g. Wilcox (2006), Versteeg and Malalasekera (2007) for further reading).

To date, the majority of turbulent CFD simulations in industrial applications is based on RANS-modeling of turbulence, i.e. by using two-equation models like the popular k-ϵ-model originally introduced by Launder and Spalding (1974). In this class of models, the closure is obtained by using the Boussinesq eddy viscosity assumption:

$$-\overline{\boldsymbol{u}'\boldsymbol{u}'}=2\nu_{\mathrm{t}}\bar{\boldsymbol{S}}-\frac{2}{3}k\boldsymbol{I} \tag{2.27}$$

where $\bar{\boldsymbol{S}}$ is the mean stress tensor defined in Eqn. 2.7. The turbulent viscosity (or eddy viscosity) is defined as

$$\nu_{\mathrm{t}}=C_{\mu}\frac{k^2}{\epsilon} \tag{2.28}$$

In order to model the transport of turbulent kinetic energy k (see Eqn. 2.18) and its dissipation rate ϵ, two additional, simplified transport equations are introduced, giving the k-ϵ-model its name:

$$\frac{\partial(\rho k)}{\partial t} + \nabla\cdot(\rho\bar{\boldsymbol{u}}k) = \nabla\cdot\left(\rho\left(\nu + \frac{\nu_\mathrm{t}}{\sigma_\mathrm{k}}\right)\nabla k\right) - \rho\overline{\boldsymbol{u}'\boldsymbol{u}'} : \nabla\bar{\boldsymbol{u}} - \rho\epsilon \tag{2.29}$$

and

$$\frac{\partial(\rho\epsilon)}{\partial t} + \nabla\cdot(\rho\bar{\boldsymbol{u}}\epsilon) = \nabla\cdot\left(\rho\left(\nu + \frac{\nu_\mathrm{t}}{\sigma_\epsilon}\right)\nabla\epsilon\right) - C_{\epsilon1}\frac{\epsilon}{k}\left(\rho\overline{\boldsymbol{u}'\boldsymbol{u}'} : \nabla\bar{\boldsymbol{u}}\right) - C_{\epsilon2}\rho\frac{\epsilon^2}{k} \tag{2.30}$$

Similar to the transport equations introduced before, these two equations can be read as follows: the local change in k or ϵ with respect to time plus the advective transport is equal to the diffusive transport plus the production minus the destruction of k or ϵ. A number of model constants (C_μ, $C_{\epsilon1}$, $C_{\epsilon2}$, σ_k, σ_ϵ) is used, see Wilcox (2006). With a new, effective viscosity

$$\mu_\mathrm{eff} = \mu + \rho\nu_\mathrm{t} \tag{2.31}$$

and the interpretation of ρk as a pressure

$$p_\mathrm{eff} = \bar{p} + \frac{2}{3}\rho k \tag{2.32}$$

the Reynolds-averaged momentum equation (Eqn. 2.25) can finally be rearranged in a more convenient form by using the closure in Eqn. 2.27:

$$\frac{\partial(\rho\bar{\boldsymbol{u}})}{\partial t} + \nabla\cdot(\rho\bar{\boldsymbol{u}}\bar{\boldsymbol{u}}) = -\nabla(p_\mathrm{eff}) + \nabla\cdot(\mu_\mathrm{eff}\bar{\boldsymbol{\tau}}) + \rho\boldsymbol{g} \tag{2.33}$$

By using the Reynolds-decomposition (Eqn. 2.23) for the temperature field, the enhancement in heat transport by turbulence can easily be assessed. In the energy equation (Eqn. 2.9), the terms for advective and molecular diffusive heat transport are evaluated using the Reynolds-averaged velocity $\overline{\boldsymbol{u}}$ and temperature $\overline{T}$. Consequently, a term $\nabla\cdot\left(\overline{\boldsymbol{u}'T'}\right)$ describing the turbulent transport needs to be added (see e.g. Schlichting and Gersten, 2006). As the laminar viscous heating was already neglected in Eqn. 2.9, the same applies to the turbulent viscous heating as well.

Direct numerical simulation (DNS) Here, even the smallest turbulent scales (η and τ) are completely resolved instead of being modeled. This approach implies very small timesteps and poses tremendous requirements on the mesh resolution – with the number of cells $N_\mathrm{DNS} \sim \mathrm{Re}^{9/3}$ even in a non-uniformly spaced grid (Wilcox, 2006). With today's computational power,

only simple flow cases can be simulated using DNS. However, this kind of simulation can be understood as a well-controlled physical experiment with no modeling of turbulence involved. As all scales are resolved, all properties are accessible.

Large eddy simulation (LES) The main idea behind LES is to reduce the extensive computational cost of DNS by resolving only the relevant scales and modeling the rest in a subgrid-scale model. As shown in Figure 2.3, the concept of LES seeks to resolve approximately 80% of the turbulent kinetic energy spectrum. This approach benefits from the fact that only the large scales are flow and problem-specific, while the smallest scales are universal (Eqn. 2.22). The turbulent diffusion caused by the energy-containing large-scale eddies is thus resolved, while the influence of small-scale turbulence is modeled. Instead of time-averaging, as it is the case when performing a simulation using RANS, a large eddy simulation separates the scales though spatial filtering

$$\phi' = \phi - \bar{\phi} \tag{2.34}$$

where ϕ denotes the original, unfiltered scalar, $\bar{\phi}$ the resolvable-scale (large) filtered part of ϕ and ϕ' the subgrid-scale (small) part (sgs). Note that – contrary to the nomenclature of RANS – the overline does not denote a time-averaged value. The filtering operation can be implicit (ILES) or explicit (ELES). For the first, the computational grid serves as a low-pass filter and no filter operator is required. In ELES, a filter function $G(\boldsymbol{x}, \boldsymbol{x}', \Delta)$ is applied. This function can be defined as a convolution integral (Leonard, 1974):

$$\bar{\phi}\left(\boldsymbol{x},t\right) = G * \phi = \int_{-\infty}^{\infty}\int_{-\infty}^{\infty}\int_{-\infty}^{\infty} G(\boldsymbol{x}, \boldsymbol{x}', \Delta)\phi\left(\boldsymbol{x}',t\right) \mathrm{d}x_1'\mathrm{d}x_2'\mathrm{d}x_3' \tag{2.35}$$

The filter cutoff width Δ is proportional to the wavenumber κ of the smallest resolved scale (see Figure 2.3). Figure 2.4 illustrates the filter concept at a given point in time: An unfiltered scalar ϕ is a function of the space x. By applying the filter with the width Δ at the point x_0, the resolvable scale $\bar{\phi}$ is separated. However, all information on the smaller scales is destroyed. The filter function G depends on the point in space x_0 and is a function of the distance from this point x' and the filter width. Three different filters are commonly used in LES: The Gaussian filter, the Fourier cutoff filter, and the simple box (top-hat) filter, (see Wilcox (2006) or Versteeg and Malalasekera (2007) for further review and Fröhlich (2006) or Piomelli (1999) for the performance of the different filters). In order to prevent the introduction of a scaling factor when performing the filtering,

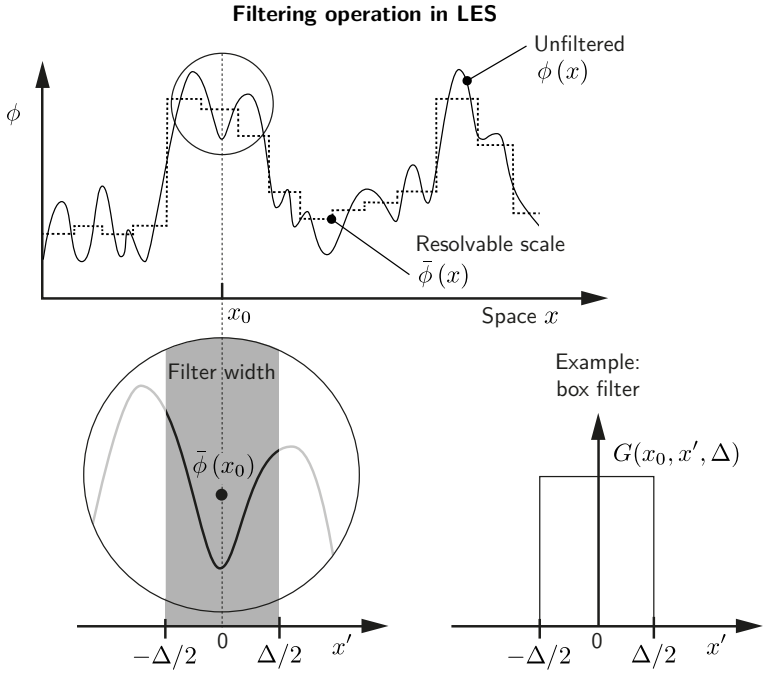


Figure 2.4.: Example of a one dimensional filtering operation of ϕ (de Villiers, 2006; Fröhlich, 2006). The top graph shows the unfiltered, original function and the resolvable-scale filtered part in the x-coordinate system. As the filter width Δ is the grid cell size, the figure exhibits steps for $\bar{\phi}$. The bottom shows the filter operation in the x' system (left) and an exemplary filter function G.

G is normalized (i.e. the integral of G over all x' is 1). While in ELES, the grid resolution has to be smaller than the filter width, ILES can be understood as the use of the box filter with the respective cell size being the filter width Δ.

Filtering the momentum equation with a constant density ρ yields

$$\frac{\partial\,(\rho\bar{\boldsymbol{u}})}{\partial t} + \nabla\cdot(\rho\overline{\boldsymbol{u}\boldsymbol{u}}) = -\nabla\bar{p} + \nabla\cdot(\mu\bar{\boldsymbol{\tau}}) + \rho\boldsymbol{g} \tag{2.36}$$

which is very similar to the Reynolds-averaged Eqn. 2.25. The convective flux is given by

$$\rho\overline{\boldsymbol{u}\boldsymbol{u}} = \rho\bar{\boldsymbol{u}}\bar{\boldsymbol{u}} + \underbrace{\rho\left(\overline{\bar{\boldsymbol{u}}\bar{\boldsymbol{u}}} - \bar{\boldsymbol{u}}\bar{\boldsymbol{u}}\right)}_{\boldsymbol{L}} + \underbrace{\rho\left(\overline{\bar{\boldsymbol{u}}\boldsymbol{u}'} + \overline{\boldsymbol{u}'\bar{\boldsymbol{u}}}\right)}_{\boldsymbol{C}} + \underbrace{\rho\left(\overline{\boldsymbol{u}'\boldsymbol{u}'}\right)}_{\boldsymbol{R}} \tag{2.37}$$

The tensor $\boldsymbol{L}$ is the Leonard stress that represents the production of subgrid-scale (sgs) turbulence by the interaction between resolved scales. $\boldsymbol{C}$ is the cross-term stress that describes the transfer of energy from resolved and to subgrid scales. The subgrid-scale Reynolds stress $\boldsymbol{R}$ is the interaction of eddies on the subgrid scale. The three sgs stresses are summarized as

$$\boldsymbol{\tau}_{\text{sgs}} = \boldsymbol{L} + \boldsymbol{C} + \boldsymbol{R} \tag{2.38}$$

which yields the common form for the filtered momentum equation

$$\frac{\partial\left(\rho\bar{\boldsymbol{u}}\right)}{\partial t} + \nabla\cdot\left(\rho\bar{\boldsymbol{u}}\bar{\boldsymbol{u}}\right) = -\nabla\bar{p} + \nabla\cdot\left(\mu\bar{\boldsymbol{\tau}} - \boldsymbol{\tau}_{\text{sgs}}\right) + \rho\boldsymbol{g} \tag{2.39}$$

At this point – like in RANS – an appropriate model for $\boldsymbol{\tau}_{\text{sgs}}$ is needed. Before describing the most commonly used models, a brief look at the filtering of compressible (variable density) flow equations is useful in the context of the present work.

As in the compressible RANS equations, the concept of Favre averaging (see Eqn. 2.26) – or in LES: Favre filtering – is used. $\tilde{\phi}$ denotes the resolved part and ϕ'' the modeled part which includes the small-scale fluctuations in density. Instead of Reynolds averaging, the overline in Eqn. 2.26 now is the filtering operation as described above. Using this Favre filtering e.g. for the momentum equation yields:

$$\frac{\partial\left(\bar{\rho}\tilde{\boldsymbol{u}}\right)}{\partial t} + \nabla\cdot\left(\bar{\rho}\tilde{\boldsymbol{u}}\tilde{\boldsymbol{u}}\right) = -\nabla\bar{p} + \nabla\cdot\left(\mu\left(\bar{\boldsymbol{\tau}} - \tilde{\boldsymbol{\tau}}\right) + \mu\tilde{\boldsymbol{\tau}} - \tilde{\boldsymbol{\tau}}_{\text{sgs}}\right) + \bar{\rho}\boldsymbol{g} \tag{2.40}$$

Note that the filtered pressure is not density weighted. The stress tensor $\tilde{\boldsymbol{\tau}}$ is evaluated as defined in Eqn. 2.6 but using the Favre-filtered velocity vector $\tilde{\boldsymbol{u}}$. The term $\nabla\cdot\left(\bar{\boldsymbol{\tau}} - \tilde{\boldsymbol{\tau}}\right)$ is a consequence of generally determining the viscosity μ using the Favre-filtered temperature $\tilde{T}$. In practice, it is safe to neglect its influence (Vreman et al., 1995). The three components of the subgrid-scale stress tensor $\tilde{\boldsymbol{\tau}}_{\text{sgs}} = \tilde{\boldsymbol{L}} + \tilde{\boldsymbol{C}} + \tilde{\boldsymbol{R}}$ in a compressible LES are (Garnier et al., 2009):

$$\tilde{\boldsymbol{L}} = \bar{\rho}\left(\widetilde{\tilde{\boldsymbol{u}}\tilde{\boldsymbol{u}}} - \tilde{\boldsymbol{u}}\tilde{\boldsymbol{u}}\right) \tag{2.41}$$

$$\tilde{\boldsymbol{C}} = \bar{\rho}\left(\widetilde{\tilde{\boldsymbol{u}}\boldsymbol{u}''} + \widetilde{\boldsymbol{u}''\tilde{\boldsymbol{u}}}\right) \tag{2.42}$$

$$\tilde{\boldsymbol{R}} = \bar{\rho}\left(\widetilde{\boldsymbol{u}''\boldsymbol{u}''}\right) \tag{2.43}$$

For the modeling of the subgrid-scale stress tensor $\boldsymbol{\tau}_{\mathrm{sgs}}$, three different approaches have gained relevance: Algebraic models, dynamic models and one-equation models. The models are briefly explained in the following, for detailed review and further secondary literature, see Wilcox (2006).

The algebraic model proposed by Smagorinsky (1963) assumes that the production and dissipation of turbulence at subgrid scales is balanced, thus no transport of subgrid-scale turbulent kinetic energy k_{sgs} can occur. Like in RANS turbulence models, closure is achieved by using the Boussinesq eddy viscosity hypothesis

$$\boldsymbol{\tau}_{\mathrm{sgs}} = -2\rho\nu_{sgs}\bar{\boldsymbol{S}} + \frac{1}{3}\mathrm{tr}\left(\boldsymbol{\tau}_{\mathrm{sgs}}\right)\boldsymbol{I} \tag{2.44}$$

with the filtered strain-rate tensor $\bar{\boldsymbol{S}}$ as introduced in Eqn. 2.7. The sgs viscosity is defined as

$$\nu_{\mathrm{sgs}} = \left(C_{\mathrm{S}}\Delta\right)^2 \sqrt{2\bar{\boldsymbol{S}} : \bar{\boldsymbol{S}}} \tag{2.45}$$

Consequently, for both ILES and ELES, the filter width Δ does not only define the resolution (and thus the error introduced by spatial discretization) but is also part of the subgrid-scale model. The Smagorinsky coefficient C_{S} is a constant adapted to the flow problem. Besides its inability to model a non-equilibrium of subgrid-scale turbulence production and dissipation, a major drawback in this method is the need of damping for ν_{sgs} in the near-wall region (e.g. the van Driest damping function).

Based on the Smagorinsky model, Germano et al. (1991) proposed a dynamic sgs model. In this LES method, the constant C_{S} is determined locally by using two different filters: The filter for the separation of scales and an additional larger test filter. The subgrid-scale stresses are evaluated on both filters. Subsequently, using a least squares approach suggested by Lilly (1992), the local value of C_{S} that matches best on both scales, is found and used.

One-equation sgs models introduce an additional transport equation for the subgrid-scale turbulence energy. The implementation in the model proposed by Yoshizawa and Horiuti (1985) reads as follows:

$$\begin{aligned}\frac{\partial\left(\rho k_{\mathrm{sgs}}\right)}{\partial t} + \nabla\cdot\left(\rho\bar{\boldsymbol{u}}k_{\mathrm{sgs}}\right) = \\ \nabla\cdot\left(\left(\mu+\rho\nu_{\mathrm{sgs}}\right)\nabla k_{sgs}\right) - \rho\frac{C_\epsilon k_{\mathrm{sgs}}^{\frac{3}{2}}}{\Delta} - \boldsymbol{\tau}_{\mathrm{sgs}} : \bar{\boldsymbol{S}}\end{aligned} \tag{2.46}$$

which, in its structure, is identical to its RANS counterpart with temporal change, advective transport, diffusive transport, dissipation and production

of subgrid-scale turbulent kinetic energy (which is the decay of turbulence from the resolved scales). The subgrid-scale turbulent viscosity is defined as

$$\nu_{\mathrm{sgs}} = C_{\mathrm{k}} \Delta \sqrt{k_{\mathrm{sgs}}} \tag{2.47}$$

The two constants C_ϵ and C_{k} are model constants (Yoshizawa and Horiuti, 1985) or determined dynamically (Kim and Menon, 1995). Again, closure is achieved through the eddy viscosity hypothesis

$$\boldsymbol{\tau}_{\mathrm{sgs}} = -2\rho\nu_{sgs}\bar{\boldsymbol{S}} + \frac{2}{3}\rho k_{\mathrm{sgs}}\boldsymbol{I} \tag{2.48}$$

where – in comparison to Eqn. 2.44 – the trace of $\boldsymbol{\tau}_{\mathrm{sgs}}$ has been replaced by the subgrid-scale turbulent kinetic energy, whose field is available because of the transport equation incorporated.

One drawback in all models based on the closure through the eddy viscosity is the assumption of isotropy in the subgrid scales. At the price of higher computational cost, the subgrid stress can also be modeled by introducing a transport equation for $\boldsymbol{\tau}_{\mathrm{sgs}}$ as proposed by Fureby et al. (1997c). An extensive review on the performance of different subgrid-scale models in LES is given by Fureby et al. (1997a,b) and Menon and Yeung (1996).

When filtering the energy equation (Eqn. 2.9), a subgrid enthalpy flux is introduced. The total flux can then be expressed as a function of the temperature gradient by replacing the (molecular) conductivity k with an effective conductivity, or – if the diffusive transport in the energy equation is evaluated using the gradient of the enthalpy – by an effective thermal diffusivity:

$$\alpha_{\mathrm{eff}} = \alpha + \alpha_{\mathrm{sgs}} \tag{2.49}$$

The subgrid-scale turbulent thermal diffusivity α_{sgs} describes the subgrid enthalpy flux. The ratio of viscous to thermal diffusion is described by the Prandtl number, or in the scale of subgrid turbulence by the turbulent Prandtl number

$$\mathrm{Pr}_{\mathrm{t}} = \frac{\mu_{\mathrm{sgs}}}{\alpha_{\mathrm{sgs}}} \tag{2.50}$$

Using e.g. the simple Reynolds analogy, it is set to $\mathrm{Pr}_{\mathrm{t}} = 1$.

The approach chosen in the present work is an ILES using the one-equation model described above. The details of the implementation and the chosen subgrid-scale model will be described in Section 3.1.1.

2.1.4. Boundary layer

For the present work with buoyancy-affected flows, the convective heat transfer from a surface into a fluid is of high relevance. As this mechanism occurs within the boundary layer, this particular region is in the focus of this study. Furthermore, the resolution requirements of the boundary layer flow define the size of the computational grid.

Generally, placing a surface in a flow has two consequences: Fluid transport in the normal direction through the surface is disabled, and the flow close to the surface is slowed down by shear stress. The region where the fluid flow is affected by a surface is referred to as the boundary layer. Within the velocity boundary layer, viscous effects influence the flow, causing a high velocity gradient in wall-normal direction. Consequently, the local flow is characterized by high rates of shear stress, even for fluids with low viscosity. By comparing the order of magnitude of the respective terms, the dimensionless Navier-Stokes equations can be simplified, yielding Prandtl's boundary layer equations (Prandtl, 1904). Even though the dimensionless form is required for correct derivation, the resulting boundary layer equations for momentum are given with dimensions, see Schlichting and Gersten (2006):

$$\rho\left(u_x\frac{\partial u_x}{\partial x}+u_y\frac{\partial u_x}{\partial y}+u_z\frac{\partial u_x}{\partial z}\right)=-\frac{\partial p}{\partial x}+\frac{\partial}{\partial z}\left(\mu\frac{\partial u_x}{\partial z}\right) \tag{2.51}$$

$$\rho\left(u_x\frac{\partial u_y}{\partial x}+u_y\frac{\partial u_y}{\partial y}+u_z\frac{\partial u_y}{\partial z}\right)=-\frac{\partial p}{\partial y}+\frac{\partial}{\partial z}\left(\mu\frac{\partial u_y}{\partial z}\right)+\rho g \tag{2.52}$$

where x is the streamwise, y the spanwise, and z the wall-normal direction. Shear is only considered in wall-parallel direction. A similar solution has been derived by Blasius (1907). When comparing these equations to the momentum equation (Eqn. 2.5), the following simplifications stand out: First, no pressure gradient in wall-normal direction. The pressure is thus imposed to the boundary layer by the free flow. Second, no gradient of the wall-normal velocity u_z in z-direction. Those two assumptions eliminate the momentum equation in wall-normal direction. For reasons of simplicity, a steady-state solution is assumed. Note that the equations above are derived for a laminar boundary layer flow. The description of turbulent boundary layers is more complicated due to the time-dependent fluctuations. For turbulent boundary layers with coupled momentum and energy (i.e. through buoyancy), mass-weighted Favre-averaging of the velocity and the consideration of turbulent transport is required (see Chapter 2.1.3).

The thickness of a boundary layer is commonly defined as the wall distance δ_{99}, at which the flow velocity has reached 99% of the ambient velocity. This definition, however, is arbitrary. A physically meaningful measure is the boundary

layer displacement thickness δ_1, which is evaluated through integration of the difference between the velocity u_∞ outside of the boundary layer and the local boundary layer velocity u (Schlichting and Gersten, 2006):

$$\delta_1\,(x,y) = \int_{z=0}^{\infty} \left(1 - \frac{u(x,y,z)}{u_\infty}\right) \mathrm{d}z = 0.34\ \delta_{99} \tag{2.53}$$

In words, δ_1 describes, how far the streamlines of the free flow are moved outward by the formation of the boundary layer. Accordingly, the displacement thickness is a measure for the overall reduction of mass flow by the boundary layer. For a flat plate, δ_1 is approximately 1/3 of the value of δ_{99}. Similar considerations lead to the evaluation of a momentum thickness

$$\delta_2\,(x,y) = \int_{z=0}^{\infty} \frac{u(x,y,z)}{u_\infty} \left(1 - \frac{u(x,y,z)}{u_\infty}\right) \mathrm{d}z = 0.13\ \delta_{99} \tag{2.54}$$

describing the thickness of a flow at u_∞ that would compensate for the reduction in momentum flow through friction in the boundary layer. Correspondingly, the loss of kinetic energy can be described by the energy thickness

$$\delta_3\,(x,y) = \int_{z=0}^{\infty} \frac{u(x,y,z)}{u_\infty} \left(1 - \frac{u^2(x,y,z)}{u_\infty^2}\right) \mathrm{d}z = 0.2\ \delta_{99} \tag{2.55}$$

These three measures are for the boundary layer at a flat plate with the highest velocity occurring in the free stream (u_∞). As it will be discussed in Section 2.2, this condition is not necessarily true for mixed convection, where the highest velocity can occur in an updraft within the boundary layer. Hence, Abedin et al. (2012a) have redefined the displacement thickness (Eqn. 2.53) by referencing the velocity difference ($u_\infty - u$) to the local difference of $u_{\max}$ and $u_{\min}$:

$$\delta_1\,(x,y) = \int_{z=0}^{\infty} \left(\frac{|u_\infty - u(x,y,z)|}{u_{\max}(x,y) - u_{\min}(x,y)}\right) \mathrm{d}z \tag{2.56}$$

The maximum velocity can occur either in the updraft or in the free stream, depending on the influence of buoyancy. The minimum velocity is most likely $u_{\min} = 0$ at the wall, unless a flow is imposed in the direction of gravity (a case later referred to as two-dimensional opposing flow), where $u_{\min} = -u_\infty$.

It should be noted that for compressible fluids, the local density has to be taken into account when evaluating the boundary layer thickness by multiplying the integrand with $\rho\,(x,y,z)\,/\rho_\infty$ (see Schlichting and Gersten, 2006). This is true especially for the momentum thickness δ_2. The present work studies mixed convection in an incompressible fluid with temperature-dependent and thus varying density. However, in literature (i.e. Abedin et al., 2012a), taking into

account the local density is not common. In order to be consistent with literature, the definition given in Eqn. 2.56 will be used instead.

One of the major challenges in the numerical investigation of boundary layer flows is the vast resolution requirement. Consequently, describing and modeling the physical wall effects has for long been subject to research. The derivation given by Wilcox (2006) will be cited in short in the following. A general observation in measurements is that the streamwise velocity of a turbulent flow varies logarithmically with the wall distance in the near-wall region, which is known as the law of the wall. As this law is a self similar solution, velocity and wall distance have to be expressed in a dimensionless manner. By replacing the local shear stress with the wall shear stress and comparing the dimensions (length/time), the reference velocity (friction velocity) is derived as

$$u_\tau = \sqrt{\frac{\tau_\mathrm{W}}{\rho}} \tag{2.57}$$

The dimensionless velocity is thus defined as

$$u^+ = \frac{u}{u_\tau} \tag{2.58}$$

Using ν/u_τ as characteristic length scale, the dimensionless wall distance is

$$z^+ = \frac{u_\tau z}{\nu} \tag{2.59}$$

Note that this value is referred to as y^+ in literature, but has been changed to z^+ in order to match the nomenclature of the present work. The dimensionless law of the wall is given by

$$u^+ = \frac{1}{\kappa} \ln z^+ + C \tag{2.60}$$

where κ is the so-called Kármán's constant and C an experimentally determined constant. The typical velocity profile in a turbulent boundary layer is shown in Figure 2.5. Beyond a wall distance of $z^+ \approx 50$, the dimensionless velocity is accurately represented by the law of the wall. This boundary layer region is called the log layer and merges, at approximately $z^+ \approx 10^3$ into the deflect layer. The viscous (laminar) sublayer in direct vicinity of the wall ($z^+ < 7$) is the region where viscous effects dominate the flow. Here, the velocity is

$$u^+ = z^+ \tag{2.61}$$

The transition from the viscous sublayer into the log layer, between $z^+ \approx 7$ and $z^+ \approx 50$ is commonly referred to as buffer layer.

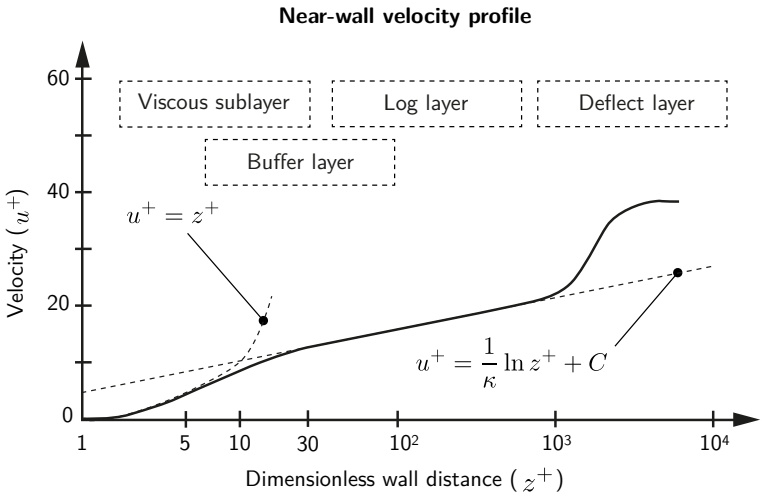


Figure 2.5.: The profile of the dimensionless velocity u^+ as a function of the dimensionless wall distance z^+ shows the distinct regions of the near-wall boundary layer (Fröhlich, 2006; Wilcox, 2006): The viscous sublayer, the buffer layer, and the log layer.

A common strategy to reduce the computational cost of CFD simulations is the use of modeling for near-wall effects. The region between the wall itself and the log layer is thus not resolved but described by so-called wall functions. While this approach is reasonable for flows without buoyancy in the boundary layer, mixed and natural convection flows require very specific wall treatment (e.g. Gerasimov, 2003). Furthermore, for these cases, a modeling of the temperature profile in the near-wall region is required (e.g. Balaji et al., 2008). As this model defines the wall temperature gradient, it has a high influence on the heat transferred into the fluid. Due to the coupling of momentum and energy, the simulation of buoyancy-influenced flows is very sensitive to the choice of wall modeling. It should therefore be noted at this point, that the present work does not use wall functions. Furthermore, all considerations on the law of the wall above do not incorporate buoyancy effects.

One characteristic feature of turbulent wall-bounded flows is the presence of coherent structures. The wide range of different structures is shown in Figure 2.6 with two distinct features highlighted: Coherent vortices (in blue) and so-called low speed streaks in streamwise direction (in red). The latter are areas of low flow velocity (and accordingly of low momentum) in the viscous sublayer and in the buffer layer. It is striking that these two features occur in conjunction, suggesting

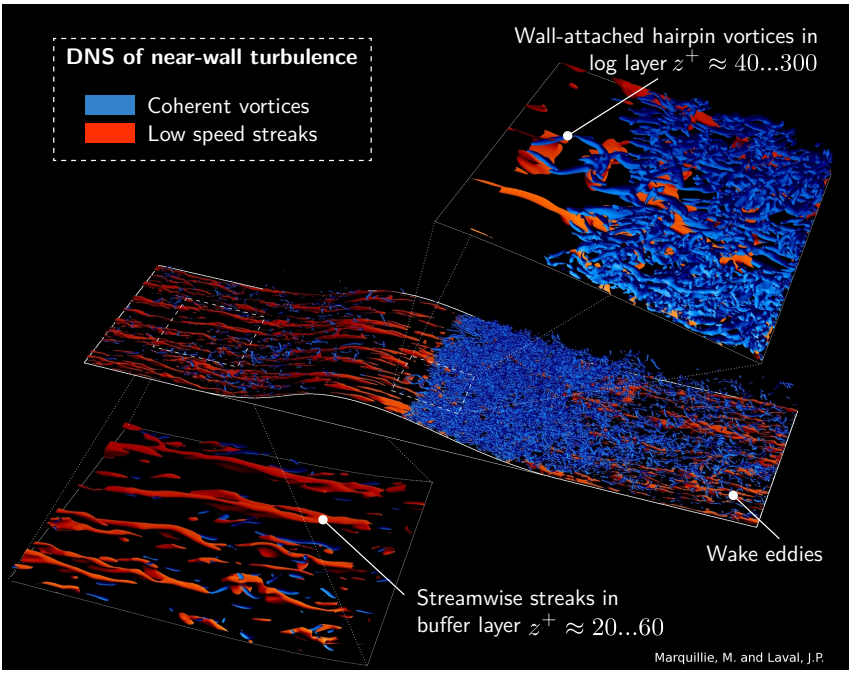


Figure 2.6.: Visualization of DNS results for a converging-diverging channel flow (Laval et al., 2012; Marquillie et al., 2011) using the Q-criterion. Low speed streaks in the buffer layer are represented by red color and intense turbulent coherent structures in blue color. The figure is adapted from the work of M. Marquillie and J.P Laval.

a mutual influence. A review of historical and present-day theories is given in the review paper by Alfonsi (2006). Generally accepted is that the low speed streaks are the result of fluid being lifted from the direct wall proximity (low flow velocity, low momentum) into the buffer layer. In this region, the streaks are characterized by instability with respect to perturbations parallel to the surface. The instability then induces – amongst others – slightly overlapping vortices in streamwise direction, which in turn lift more slow fluid into the buffer layer. This cycle of streak generation, streak instability and vortex generation, referred to as streak instability cycle, is located in the buffer layer between $z^+ \approx 20$ and 60. It is self-sustaining and mostly independent from the flow outside of the boundary layer. The characteristic elongated form of the streaks – visible in Figure 2.6 – is caused by the fact that the streamwise vortices are farther away from the wall than the streaks. Consequently, the vortices are transported significantly faster and the streak structure grows in length.

While most of the generated streamwise vortices desintegrate when drifting away from the wall, some form the hairpin-shaped vortices in the outer boundary layer. The top of the hairpin extends far into the outer region of the boundary layer (z^+ of up to 300) while the legs appear to be attached to the wall. These vortices are responsible for the lion's share in turbulent energy and momentum transfer. A more detailed discussion on hairpin vortices and their interaction with streaks can be found in Adrian et al. (2000), Adrian (2007), Boiko et al. (2011), and more recently in Eitel-Amor et al. (2015). The eddies in the wake region (Fig. 2.6) are very likely to be the "leftovers" of hairpin vortices detached from the wall (de Villiers, 2006). In summary, concerning coherent structures in the boundary layer, the inner region is dominated by streaks while the outer region is dominated by the motion of vortices.
The four most common methods of detecting vortex structures in numerical simulation results or in measurements of the velocity field are summarized by de Villiers (2006):

Magnitude of the vorticity The vorticity magnitude is a measure commonly used to describe the local tendency of a fluid to rotate. It is defined as the curl of the velocity (Pope, 2000):

$$\boldsymbol{\omega} = \nabla \times \boldsymbol{u} \tag{2.62}$$

While this method is applicable in free shear flows, it cannot be used in boundary layers. The premise of successfully detecting a vortex using the vorticity method is a local difference in shear. Close to the wall, however, the shear rate surrounding a vortex is approximately in the same order of magnitude as within of the vortex. This is especially true in direct wall proximity, where the magnitude of the vorticity $|\boldsymbol{\omega}|$ reaches its highest value.

Q-criterion This method involves the invariants of the tensor $\nabla \boldsymbol{u}$ (rate-of-deformation tensor), which includes the gradients of all three velocity components in all three spacial directions. The eigenvalues of this tensor are defined as (Alfonsi, 2006):

$$\det\left(\nabla \boldsymbol{u} - \boldsymbol{\lambda I}\right) = 0 \tag{2.63}$$

leading to the characteristic polynomial

$$\lambda^3 + P\lambda^2 + Q\lambda + R = 0 \tag{2.64}$$

with the three invariants of the velocity gradient tensor P, Q, and R. The second invariant can also be expressed as :

$$Q = \frac{1}{2}\left(\boldsymbol{W} : \boldsymbol{W} - \boldsymbol{S} : \boldsymbol{S}\right) \tag{2.65}$$

with the strain-rate tensor $\boldsymbol{S}$ (representing irrotational motion) as defined in Eqn. 2.7 and the rotation-rate tensor $\boldsymbol{W}$ (representing rotational shear)

$$\boldsymbol{W} = \frac{1}{2}\left(\nabla \boldsymbol{u} - (\nabla \boldsymbol{u})^T\right) \tag{2.66}$$

For a large and positive Q, $\boldsymbol{W}$ exceeds $\boldsymbol{S}$ and thus, rotation dominates the flow. The Q-criterion makes use of this conclusion by defining a vortex as the region where $Q > 0$.

Complex eigenvalues This method evaluates the complex eigenvalues of the velocity gradient tensor defined in Eqn. 2.64. The discriminant of the problem is defined as:

$$D = \left(\frac{R}{2}\right)^2 + \left(\frac{Q}{3}\right)^3 \tag{2.67}$$

For $D > 0$, two conjugate complex solutions exist and the flow will feature a rotational part around one point. The third invariant R characterizes the direction of the motion: $R > 0$ describes an out-bound flow around the point and $R < 0$ the opposite.

$\boldsymbol{\lambda_2}$-criterion For this technique, the eigenvalues of $(\boldsymbol{W} \cdot \boldsymbol{W} + \boldsymbol{S} \cdot \boldsymbol{S})$ are evaluated. The method has been derived by Jeong and Hussain (1995) and takes advantage of the assumption that any vortex is accompanied by a local pressure minimum. In order to determine such a minimum, the tensor $(\boldsymbol{W} \cdot \boldsymbol{W} + \boldsymbol{S} \cdot \boldsymbol{S})$ is used as an indication. A vortex region is present if two of its eigenvalues are negative. As $\lambda_1 \leq \lambda_2 \leq \lambda_3$ (due to the symmetric nature of the tensor), the criterion is that the second largest eigenvalue of $(\boldsymbol{W} \cdot \boldsymbol{W} + \boldsymbol{S} \cdot \boldsymbol{S})$ is $\lambda_2 < 0$. For the detailed derivation, please see e.g. Alfonsi (2006) or the original paper.

The four definitions of a vortex structure (ω, Q, D and λ_2) have been applied to DNS results by Jeong and Hussain (1995) in order to compare their respective suitability. The clear conclusion is that the positive second variant (Q) and the second largest eigenvalue (λ_2) methods are more suitable than the vorticity and the D-criterion. In most of the test cases, the Q-criterion and the λ_2-criterion give similar results.

Up to this point, all discussions of boundary layer effects were related to the velocity boundary layer. However, when looking at a flow along a heated surface, the temperature boundary layer at the surface defines the amount of heat that is transferred into the fluid. With the no-slip condition ($u = 0$) at the wall, the heat transfer at the surface solely depends on heat conduction. Therefore, the

temperature gradient at the wall is of particular interest. The temperature and the velocity boundary layer are very similar, as the transport mechanisms for energy and momentum are alike with different transport coefficients. Consequently, for the ideal case of a laminar, forced convection boundary layer, the ratio of the boundary layer thicknesses can be expressed as the ratio of the respective transport coefficients (ν for momentum and the diffusivity $k/\rho c$ for thermal energy), which is defined as the Prandtl number (see Eqn. 2.72). This however, does not account for transport by turbulence or for acceleration by buoyancy. For buoyancy-influenced flows, the temperature boundary layer defines where an updraft can occur. The outer edge of this region can be identified by the same method as for the velocity boundary layer thickness: simply the point where the local temperature is to 99% identical with T_∞. Yet, a more reasonable definition can be obtained by balancing the energy content of the boundary layer (Schlichting and Gersten, 2006), similar to the energy thickness defined above. However, the energy thickness δ_3 considered the reduced flow of kinetic energy in the boundary layer. The same consideration applied to the thermal energy gives:

$$\delta_T\,(x,y) = \int_{z=0}^{\infty} \left(\frac{u(x,y,z)}{u_\infty} \frac{T(x,y,z) - T_\infty}{T_{\text{wall}}\,(x,y) - T_\infty} \right) dz \tag{2.68}$$

Keeping in mind that in the present work, the fluid's specific heat c will be set constant so that the enthalpy is $h = c\,(T - T_{\text{ref}})$, the evaluation of the enthalpy thickness δ_h will result in the same expression. When investigating boundary layers with a coupling of energy and momentum through buoyancy, there is limited sense in using different boundary layer thicknesses for scaling, e.g. y/δ_T for the temperature and y/δ_1 for the velocity. Consequently, all dimensionless locations within the boundary layer will be in reference to δ_1 in the following.

2.2. Introduction to convective heat transfer

While the *transport* of heat from one place to another by fluid motion is referred to as convection, the *transfer* of heat from a surface into a fluid is called convective heat transfer. The mechanism takes place at the fluid-solid boundary, where the fluid has formed a boundary layer. Convective heat transfer involves advection of heat (which is most of the transport within the boundary layer) and thermal conduction (which – due to the no-slip condition and the resulting zero velocity at the wall – is the only transport of heat into this boundary layer). The combination of those two mechanisms results in a specific temperature profile. As heat conduction is governed by the temperature gradient, the profile-changing transport by advection has a significant influence on the heat transfer rate. Therefore, when looking at the heat transfer in forced convection, the heat transfer is severely influenced by the imposed flow. On the other hand, the

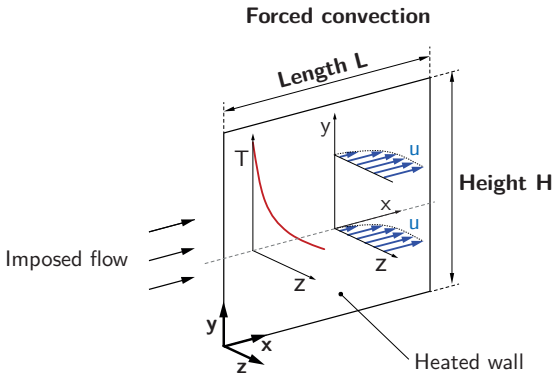


Figure 2.7.: Schematic of temperature and velocity profiles for pure forced convection on a vertical plate.

flow is considered independent from the introduced heat. In natural and mixed convection, however, heat transfer and fluid flow are characterized by a mutual influence. Heat transfer cases of this kind are considered thermo-fluid interaction problems.

The velocity and temperature boundary layer profiles for forced convection heat transfer are shown in Figure 2.7. The hot surface is a vertical flat plate of height H and length L. The imposed flow $\boldsymbol{u} = (u_\infty\ 0\ 0)$ approaches the plate from the left side. Directly at the wall, the no-slip condition applies, as the tendency of the fluid to adhere to the wall (adhesion) is higher than the molecules' tendency to "stick" together (cohesion). Consequently, the fluid at the wall has zero velocity. In wall-normal z-direction, the velocity steadily increases. Outside of the boundary layer, the fluid in the free stream continues with the imposed velocity. The highest fluid temperature occurs directly at the wall, where – due to the no-slip condition – conduction is the only heat transport mechanism. As the velocity increases in z-direction, more heat is transported by advection. This results in the temperature profile shown in the figure, with decreasing temperature gradient, which is typical of convective heat transfer. The size of both boundary layers may change in streamwise x-direction. However, no change in the profiles applies in the vertical y-direction.

In order to describe the nature of the flow problem and allow the comparison of similar cases e.g. with different dimensions, the imposed flow is characterized by the dimensionless Reynolds number:

$$\mathrm{Re_L} = \frac{u_\infty L}{\nu} \tag{2.69}$$

Here, L is the length of the plate in flow direction and the characteristic velocity u_∞ is the bulk velocity. Re relates fluid interia to the viscous forces. If the number is above a critical value (for plates, $\mathrm{Re_{crit}} \approx 5 \cdot 10^5$, Schlichting and Gersten, 2006), the flow transitions into turbulent flow conditions.
The convective heat transfer of a given flow case is described either by the convective heat transfer coefficient h or – in a dimensionless manner – by the Nusselt number of the problem.

$$\mathrm{Nu_L} = \frac{hL}{k} \tag{2.70}$$

The Nusselt number expresses the ratio of the convective heat transfer and a fictive conductive heat transport through the boundary layer. In technical applications, the Nusselt number is usually evaluated in form of a correlation, where the dimensionless Reynolds number $\mathrm{Re_L}$ characterizes the flow and the Prandtl number describes the influence of the fluid's thermophysical properties:

$$\mathrm{Nu_L} = f\left(\mathrm{Re_L}, \mathrm{Pr}\right) \tag{2.71}$$

with the Prandtl-number

$$\mathrm{Pr} = \frac{\nu \rho c}{k} \tag{2.72}$$

For two (simple) flow cases with identical Re and Pr, the law of similitude can be applied, stating that the Nusselt number is the same for both cases.

The buoyancy-induced nature of the flow in natural convection strongly couples fluid flow and heat transfer. The flow is driven by a change in density, which, in turn, is the result of the heat transfer. As advection influences the heat transfer rate, the flow itself has an impact on the heat transfer. Consequently, contrary to forced convection, the temperature cannot be considered a passive scalar anymore. On the same plate as above, the qualitative profiles of velocity and temperature for pure natural convection are shown in Figure 2.8. The temperature profile in the boundary layer has a similar shape as in the forced convection case with the highest temperature at the heated wall and a resulting heat flow in wall-normal z-direction. In order to allow an intuitive approach to the problem, gravity is imposed in negative y-direction. This results in a fluid flow in positive y-direction. Far away from the wall, the flow velocity is zero. Directly at the wall, the no-slip condition also causes a zero velocity. However, as the temperature is higher close to the wall, the buoyant forces are highest in this region. Originating from the wall, the velocity increases in z-direction and soon reaches a maximum. Further away from the wall, the decreasing fluid temperature results in lower

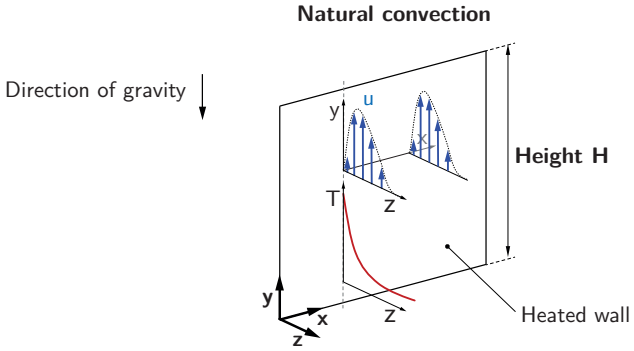


Figure 2.8.: Schematic of temperature and velocity profiles for pure natural convection on a vertical plate.

buoyant forces. At the same time, the viscous forces from the fluid outside of the boundary add additional drag, reducing the velocity. For different positions in x-direction, the idealized temperature and velocity profiles are identical.

As no velocity is imposed to the problem, the Reynolds number cannot characterize the flow. Instead, the Grashof number is used:

$$\mathrm{Gr_H} = \frac{|g|\beta\Delta T H^3}{\nu^2} \tag{2.73}$$

Here, g is the acceleration by gravity and H the characteristic length in the direction of gravity. The volumetric coefficient of thermal expansion

$$\beta = -\frac{1}{\rho}\left(\frac{\partial\rho}{\partial T}\right) \tag{2.74}$$

is evaluated for a constant pressure at ambient or free-stream temperature. The second fluid property relevant to natural convection is the kinematic viscosity ν. The temperature difference ΔT is the thermal potential. Gr is highly influenced by the characteristic length (usually the height) which is introduced in the third power H^3. Its physical interpretation – similar to Re – is the ratio of buoyant to viscous forces. As the number describes the natural convection flow, it defines the criteria for the transition to turbulence. For vertical plates, $\mathrm{Gr_{crit}}$ is considered to be in the range of 10^9 to 10^{10} (Incropera et al., 2007).
The Nusselt number is consequently evaluated with the characteristic length H and is a function of Gr and Pr:

$$\mathrm{Nu_H} = f\left(\mathrm{Gr_H}, \mathrm{Pr}\right) \tag{2.75}$$

In many real-life applications (e.g. the heat losses at receivers and the cooling of photovoltaic panels mentioned before), both mechanisms occur at the same time. Therefore, heat transfer by mixed convection is the result of a superposition of buoyancy-driven natural and forced convection. The Archimedes number

$$\mathrm{Ar} = \frac{g L^3 \Delta\rho}{\nu^2 \rho_\mathrm{a}} \tag{2.76}$$

is the ratio of buoyant forces to viscous forces and thus expresses the influence of natural convection. With the Grashof number describing the contribution of the natural convection flow (buoyant force), and the Reynolds number describing the imposed flow (inertia), the relative effect of buoyancy on mixed convection can also be expressed though the Richardson number (Gebhart et al., 1988):

$$\mathrm{Ri} = \frac{\mathrm{Gr_H}}{(\mathrm{Re_L})^2} \tag{2.77}$$

For varying length scales, i.e. a horizontal L and a vertical H, the Richardson number is more suitable to characterize mixed convection. The extrema $\mathrm{Ri} \to 0$ and $\mathrm{Ri} \to \infty$ represent pure forced and pure natural convection, respectively. Transition between the flow regimes occurs at $\mathrm{Ri} \approx 0.3$ (from forced to mixed convection) and $\mathrm{Ri} \approx 16$ (from mixed to pure natural convection) (Sparrow et al., 1959). Heat transfer by mixed convection depends on both flow types and the thermophysical properties of the fluid:

$$\mathrm{Nu_{LH}} = f\left(\mathrm{Gr_H}, \mathrm{Re_L}, \mathrm{Pr}\right) \tag{2.78}$$

While the Reynolds number bases on the length in direction of the imposed flow L, the Grashof number is based on the height H. As the forced flow is not necessarily imposed in the same direction as the gravity ($H \neq L$), a new reference length LH has to be found for the Nusselt number. This length must reflect the actual flow regime as expressed by the Richardson number (see Siebers et al., 1983).

Like for natural convection, the flow resulting from mixed convection is highly dependent on heat transfer, as a change in fluid temperature drives the buoyancy-effects within the boundary layer. The heat transfer into the fluid on the other hand is highly influenced by the flow. This mutual dependency is one of the main challenges when investigating mixed convection. Compounding the problem, the buoyancy-driven boundary layer has a different, sometimes higher, velocity and – in certain cases – even a different flow direction than the imposed free flow. Furthermore, mixed convection typically occurs when the temperature difference ΔT between the surface and the fluid is high (e.g. in fire protection applications) or at large technical parts (e.g. a solar receiver). The resulting high $\mathrm{Gr} \sim \Delta T, H^3$ quickly forces a transition to turbulent flow conditions.

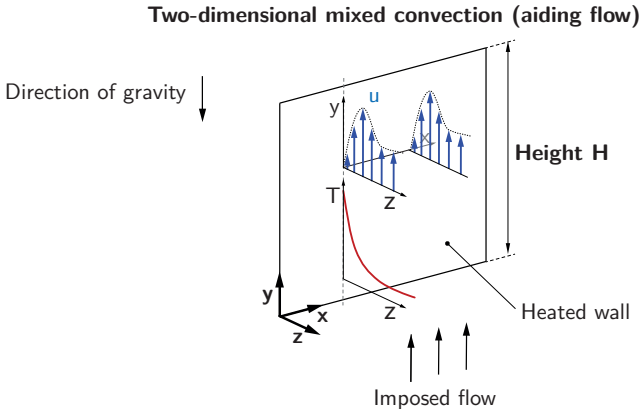


Figure 2.9.: Schematic of temperature and velocity profiles for two-dimensional mixed convection with an aiding flow on a vertical plate.

When looking at mixed convection on vertical walls, two general cases can be distinguished: a *two-dimensional* (aiding or opposing) flow field results from buoyancy forces being aligned in parallel to the imposed flow. Even though the flow itself can be three-dimensional, i.e. because of turbulence, the flow case is considered two-dimensional as any change occurs in the direction of the flow. If buoyancy acts perpendicular to the direction of the flow, a more complex, *three-dimensional* flow field develops. In this case, both the velocity and the flow direction vary in wall-normal, horizontal, and in vertical direction.

Figure 2.9 illustrates the boundary layer profiles of velocity and temperature for a two-dimensional aiding flow. Here, buoyancy acts in the direction of the flow, further accelerating the boundary layer. The velocity profile resembles the one for pure natural convection shown in Figure 2.8 with a velocity maximum within the boundary layer. However, instead of being zero, the free-stream velocity is u_∞. The illustration shows, that – unlike for forced convection – an increase in imposed velocity does not necessarily increase the velocity difference between the boundary layer flow and the free stream. A smaller difference in the velocity reduces the shear stress and thus leads to less mixing within the boundary layer. By increasing the imposed flow velocity, the heat transfer could thus be constrained instead of being enhanced, as intuition would tell.

Compared to the aiding flow case, the opposing case is by far more complex. Here, the imposed flow and buoyant updraft are in opposing directions. Depending on the Richardson number, buoyancy slows the boundary layer down

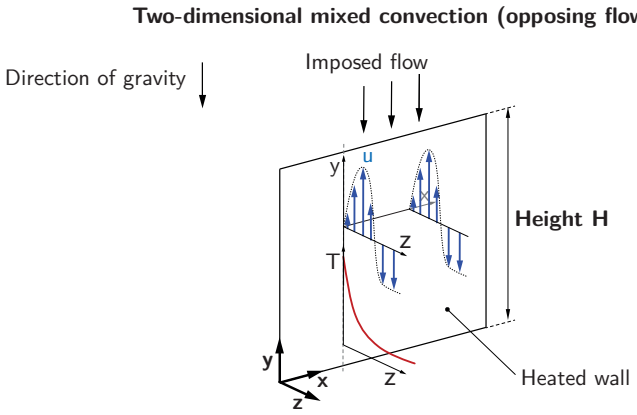


Figure 2.10.: Schematic of temperature and velocity profiles in two-dimensional mixed convection with an opposing flow on a vertical plate.

(for smaller Ri numbers) or even accelerates it in the opposite direction (for higher Ri numbers). The temperature and velocity boundary layer profiles for the latter are shown in Figure 2.10. While the imposed flow forces fluid from the top to the bottom, the buoyant force is strong enough to drive the boundary layer from the bottom to the top. However, buoyancy only affects fluid whose temperature is higher than the free flow – a condition that limits the updraft to the temperature boundary layer (illustrated by the red line). At the wall, the no-slip condition applies. These boundary conditions result in a profile characterized by a distinct velocity maximum (in positive y-direction). The resulting velocity gradient is very steep, which creates a strong shear stress zone where vortices and the production of turbulence will enhance mixing. Also, the entrainment of cold fluid from outside the temperature boundary layer further enhances the heat transfer from the plate into the flow.

Figure 2.11 is an illustration of three-dimensional mixed convection on a vertical plate, the case on which this work is focused. The imposed flow is horizontal, in positive x-direction from the left to the right, while gravity is in negative y-direction. The resulting velocity boundary layer profile is shown for a central position at the plate. While the flow far away from the surface is undisturbed, the buoyancy effects induced by the increased temperature in the boundary layer cause a local updraft. Like in the two-dimensional cases, a distinct maximum in flow velocity can be observed, this, however being subject to the case setup (i.e. the Richardson number). The flow direction depends on the impact of the buoyant force, which adds a vertical component to the flow. The resulting flow

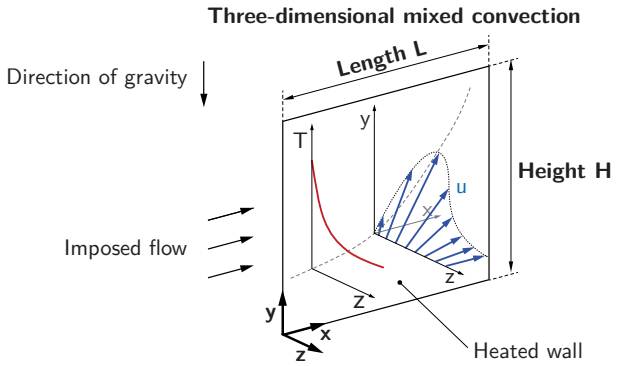


Figure 2.11.: Schematic of temperature and velocity profiles for three-dimensional mixed convection on a vertical plate.

angle is thus a superposition of the imposed horizontal flow, the decrease in velocity caused by drag from the wall, and the buoyancy-induced updraft. The higher the influence of buoyancy, the steeper the flow angle becomes. For the two-dimensional cases, only the height of the plate was relevant, as the flow did not change in crosswise direction. For the present three-dimensional case, both flow velocity and direction are a function of the position in x, y and z-direction, making the flow field fully three-dimensional without any symmetry. A flow streamline is illustrated as a dashed line in the Figure 2.11. Note that a new line would have to be drawn for different z positions and for different staring points at the plate's edge, respectively.

Besides these general flow cases, further differentiation is possible based on the flow condition (present work: turbulent), the type of fluid (present work: incompressible), the temperature level influencing the thermophysical properties, and the Grashof number (present work: $\mathrm{Gr} \lesssim 10^{11}$). Mixed convection on horizontal plates is a different research topic on its own, and not subject of the present work. In literature, mixed convection flow and heat transfer have been investigated in experiments and in numerical simulations. Both approaches have different advantages and particular challenges. Before reviewing the state of the art of science and technology in Chapter 2.3.1 and 2.3.2, a brief overview of the different methods will be given in the following two sections.

2.2.1. Experimental investigation methods

Designing an experiment for the investigation of mixed convection is challenging, as for most applications, the effect occurs on rather large scales and when the

temperature differences are high. Conducting an experiment e.g. at an existing central receiver of a solar tower is not realistic because of the unfavorable conditions (i.e. high radiative heat fluxes and logistic problems caused by the height). Furthermore, the influence of the ambiance could be eliminated. Fluctuations in the wind velocity would have a significant impact on the experiment. A scaled experiment under controlled laboratory conditions therefore seems favorable for the investigation of mixed convection. When scaling according to the similitude theory, the dimensionless numbers have to correspond to the ones of the real application. For the present flow, this applies to the Reynolds and the Grashof number. The scaling for Re is straightforward, as a decrease in dimension can be balanced by a linear increase in velocity or the choice of a fluid with an adapted viscosity ν. However, scaling Gr is challenging. The characteristic length has a very strong impact ($\mathrm{Gr} \sim H^3$). Reducing the size of the problem to an experiment-friendly scale has to be compensated either through a significantly higher temperature difference ΔT – which does not seem practical for most laboratories – or through the use of a fluid with a low viscosity ν^2 or through high volumetric coefficient of expansion β. It is obvious that a change in gravity would be difficult to implement. Additionally, as the heat transfer in form of the dimensionless Nusselt number is of interest, the Prandtl number has to correspond to the application as well, which further complicates the choice of a fluid.

However, if a chillingly high degree of complexity in the experimental setup is not considered problematic, the use of pressurized sulfur hexafluoride (SF_6) as proposed by Thess and Wagner (2008) is an option. Körner (2014) has developed a corresponding facility where the actual flow experiment is conducted in a cylindrical vessel flooded with SF_6 at up to 10 bar relative pressure. Achievable Grashof numbers are in the order of $\mathrm{Gr} \approx 10^{12}$, while maximum Reynolds numbers are in the order of $\mathrm{Re} \approx 10^6$. As the Prantl number of pressurized SF_6 is in the same range as for air, the facility was used for the investigation of indoor turbulent mixed convection airflows. Little less effort has been undertaken by Flesch et al. (2015), who experimentally investigated the influence of wind on the convection losses of a cavity receiver. Their measurements were performed in a cryogenic wind tunnel at an ambient temperature as low as 100 K. At these conditions, the low air viscosity and the viable wall-fluid temperature difference allows to achieve Grashof numbers of almost $4 \cdot 10^{10}$.

A different approach is pursued by Bünger and Herwig (2009) and Jin and Herwig (2010) who have presented an extended similitude theory. Besides taking temperature-dependent variations in the thermophysical properties into account, their method is applicable even for small deviations in the characteristic numbers. The method was successfully applied on a benchmark-case (a lid-driven heated cavity), however, there is a limitation of the obtainable heat transfer rates.

Yeh et al. (2005) have taken advantage of the fact, that the governing transport mechanisms for heat and for mass transfer are similar to each other. Using this analogy, a buoyancy-driven flow was generated by the diffusion of fresh water into salt water. Their investigation of a natural convection flow in a scaled solar cavity receiver produced flow visualizations for different Grashof numbers, yet without being able to provide detailed information on the heat transfer.

When investigating the heat transfer, a precise measurement of the boundary layer profiles for temperature and velocity is of interest. Different measurement techniques have been used, each with its own advantages and disadvantages.
For the most comprehensive experiment on turbulent mixed convection on a vertical flat plate in air, conducted by Siebers et al. (1983), the velocity was measured with a pitot probe. This instrument uses the measurement of pressure to determine the local flow velocity. In the study, measurements of the boundary layer mean velocity and the flow angle were taken. Additionally, thermocouples were used to record the temperature. The entire probe construction was mounted on a traverse mechanism, allowing to conduct measurements at almost any position within the boundary layer. The main problem in this measurement strategy is that the technique is not non-invasive. As this is not considered a problem when measuring temperature, thermocouples mounted on probes have been used in a number of other studies as well (e.g. Li et al., 2004; Tsuji and Nagano, 1989; Wang et al., 2004). However, when measuring the velocity in the near-wall region, the flow is strongly disturbed by the probe.
Therefore, Abu-Mulaweh et al. (1992) used Laser Doppler anemometry (LDA) as a non-invasive method to determine the velocity distribution. In their experiments, they investigated a laminar airflow along a heated vertical plate. While LDA allows time-resolved measurements, two problems arise in the context of boundary layer flows in large-scale flow problems: First, the measurement only gives information on the velocity in one spot, and second, tracer particles that follow the boundary layer flow have to be seeded.
A commonly used time-resolved velocity measurement method is the particle image velocimetry (PIV). The velocity of seeded particles can be determined in a plane or in a volume, depending on the complexity of the setup. A comprehensive overview of PIV is given in Adrian and Westerweel (2011). Recently, combined measurements of three-dimensional velocity and temperature fields have been conducted using a light-field PIV camera and temperature-sensitive liquid crystals as tracer particles (Rietz et al., 2014). In the context of mixed convection, PIV has been used by Hattori et al. (2001) for two-dimensional mixed convection, in addition to hot and cold wires. The hot wire technique measures the velocity magnitude at one spot by taking advantage of the effect that the cooling of a wire by a flow changes its electric resistance. By calibrating, a correlation between resistance and flow velocity can be obtained. Through the same principle, cold

wires can be used to measure temperature fluctuations in the fluid. Furthermore, for natural convection along a vertical flat plate in water, Tsuji and Kajitani (2006) used PIV to determine the turbulent characteristics in the boundary layer.

As mentioned above, for the convective heat transfer – described either in form of the convective heat transfer coefficient h, the dimensionless Nu number, or the actual heat flux – the temperature profile within the boundary layer is of special interest. The temperature gradient in wall-normal direction in direct wall proximity is directly related to the heat transfer, as heat conduction is the only heat transport mechanism. However, obtaining the temperature gradient in this region is challenging. Therefore, other methods have been used or are under development: In the work by Siebers et al. (1983) (mentioned above), the convective heat flux was determined by a local energy balance around the plate. Thermal losses could only occur at the back of the setup, after the heat was conducted through an insulation. This heat flux could thus be derived by measuring two temperatures in wall-normal direction within the plate and applying Fourier's law. The main disadvantage is the huge amount of thermocouples required (Siebers et al. (1983) have installed a total of 341 thermocouples).
A promising new method, the temperature oscillation IR-thermography (TOIRT), has successfully been tested by Freund (2008) on forced convection. TOIRT allows the non-invasive measurement of convective heat transfer coefficients by imposing a small oscillating heat flux on the surface (e.g. by radiation). With an infrared camera, the reaction of the surface temperature is recorded and compared to the oscillation. Using inverse methods, the coefficient can be reconstructed from the phase shift between imposed signal and temperature response. To date, further methods like the use of analogies from mass transfer or painting heated surfaces with temperature-sensitive liquid crystals have not gained relevance for the investigation of mixed convection.

2.2.2. Numerical simulation methods

As described above, the experimental investigation of mixed convection is challenging. Besides the difficulty of scaling the flow problem, measuring the flow and the temperature requires sophisticated techniques. With the steady increase in computational power, numerical simulations have become a promising approach for the investigation of mixed convection heat transfer and flow phenomena. A major advantage is that in numerical simulations, properties that cannot be measured in an experiment can be determined. This applies for example to the production and dissipation rates of turbulent kinetic energy and its influence on the transport mechanisms. However, the simulation of a large-scale mixed convection problem is fraught with a significant amount of challenges:

Dimension: The length scale of mixed convection problems imposes a challenging size on the computational domain. In some two-dimensional cases, the use of periodic boundary conditions allows the reduction of the computational domain to a minimum flow cell. However, this particular approach is not possible for three-dimensional mixed convection as it fails to describe the fully three-dimensional nature of the problem. Therefore, the entire flow domain needs to be considered, which results in large simulation cases.

Boundary layer resolution: For well-known problems like pure forced convection, the velocity and temperature profiles in the boundary layer can be modeled by a wall function, as they display a self-similarity. For mixed convection (i.e. three-dimensional mixed convection), it is yet unclear, whether the profiles can be described by this approach. As the heat transfer is defined by the temperature gradient in wall proximity, it is necessary to resolve most of the boundary layer by very small cells. This requirement – in combination with the large dimensions of the simulation cases – results in an extremely high computational cost.

Time scales: Aside from the large variety of spatial scales, the mixed convection flow exhibits a broad range of temporal scales as well. Due to the large domain, a long time period is required to reach the quasi-steady state solution in all domain regions. On the other hand, the simulation timestep needs to be comparably small in order to resolve the transient fluctuations in the boundary layer.

Numerical stability: Convergence and numerical stability is an issue in most CFD simulations. For mixed convection, convergence becomes even more of an issue, as momentum and energy equation are strongly coupled (i.e. the buoyancy-driven flow is the result of a heat transfer).

Turbulence: When the Reynolds and Grashof numbers of the flow case exceed their respective critical values, turbulence has to be considered in the simulation. The dimension of the case makes the use of direct numerical simulations (DNS) unrealistic for the next decade or so. Therefore, the influence of turbulence has to be modeled to a certain degree. Most of the modeling approaches presented in Section 2.1.3 have been applied to mixed convection problems. However, the choice of a turbulence model always has a big impact on the simulation. It is therefore advantageous to limit the degree of modeling to the inevitable.

As early as 1977, RANS was used by Plumb and Kennedy (1977) for natural convection on a vertical plate, where the original $k - \epsilon$ turbulence-model proposed by Launder and Spalding (1974) was modified to incorporate buoyancy effects. In a two-dimensional study, Patel et al. (1996) described turbulence

by a low-Reynolds number $k-\epsilon$ model. Using experimental data as boundary condition, Evans et al. (2005) compared the performance of two different RANS models (standard $k-\epsilon$ and $\overline{v^2}-f$) with the experiment. For this purpose, the simulated and the measured heat transfer for turbulent mixed convection on a vertical plate was compared. Even though the measured surface temperatures were imposed – the simulation thus pushed towards the expected solution – the convective heat transfer coefficients deviated between 5% and 35% from the experiment. In this study, the results obtained by using the $\overline{v^2}-f$ model were better than the ones obtained with the $k-\epsilon$ model. Recently, Oosthuizen (2010) performed a RANS simulation of two-dimensional mixed convection in the aiding flow configuration. The implementation of the $k-\epsilon$ model in the commercial CFD-software *Fluent* was used to describe turbulence effects. Only the area-weighted average heat transfer was evaluated and standard wall functions were used, which significantly simplified the configuration and thus did not provide any information on local effects. However, it is worth noting that the integral results succeed in representing general trends such as transition from a laminar to a turbulent flow case. All studies described here used the Boussinesq approximation to address the issue of numerical instability. When gravity is considered in y-direction, the x and y-momentum equations are therefore to the greatest possible extent decoupled from the energy equation.
One major drawback when using RANS is that all eddy sizes are described by one single formulation. However, as large-scale turbulence contains most of the energy, its influence on the turbulent transport of momentum and energy is significantly higher (Versteeg and Malalasekera, 2007). Because of the relatively low level of detail in the solution (i.e. the loss of transient fluctuations), RANS fails to provide insights into the mixed convection heat transfer mechanisms. For the use of wall-functions, which are often used in RANS simulations, it is yet unclear whether the formulation represents the actual conditions in the near-wall region for mixed convection.

Contrary to an extensive degree of modeling, the increase in computational performance in the last decades allows fully resolved simulations (DNS) for some flow cases. However, the computational cost brings up the issue of the required domain size. DNS of large flow domains will not be an option in the near future. Therefore, studies like Abedin et al. (2010, 2012a,b) investigated two-dimensional mixed convection flow cases, which allowed the use of periodic boundary conditions. Kis (2011) numerically investigated mixed convection in a flow channel through DNS. The domain size was not problematic for his work, as the flow cases studied were characterized by rather small Grashof numbers in the range of $\mathrm{Gr} < 6 \cdot 10^6$ (which is five orders of magnitude lower than in the present work). Like for RANS, numerical stability has been increased in all DNS studies by the use of the Boussinesq approximation.

Located in between the two extremes – RANS and DNS – scale-resolving simulations like LES are a promising option for the investigation of convection (Ojofeitimi (2013), de Villiers (2006) and recently Nakao et al. (2016)). The issue of turbulence is addressed by introducing a certain amount of modeling on the small scales. Nonetheless, performing an LES still results in large computational grids (dimension problem) and long simulation times (time scale problem). Barhaghi and Davidson (2009) have investigated two-dimensional mixed convection in a vertical channel in combination with radiation by using the Boussinesq approximation in an LES. Concerning their simulation method, they concluded that the use of this simplification – when applied to high temperature differences – leads to considerable inaccuracies in the solution. The concept of using wall functions as a possibility to reduce the boundary layer resolution requirements has been pursued by Yan and Nilsson (2005). They simulated pure natural convection on a vertical plane in the context of fire protection applications. In the near-wall region, two different wall functions were applied. When discussing their results, the authors concluded that the choice of the respective wall functions has a major impact on the result accuracy. This finding underlines the challenge of describing the boundary layer in an appropriate way. In this context, the unconditional use of wall functions is not an option when conducting a baseline investigation of the related heat transfer.

2.3. Review of literature on mixed convection

After discussing different methods for the scientific investigation of mixed convection in the preceding section, an overview of research findings will be given here. Before focusing on the three-dimensional mixed convection, the state of the art in two-dimensional mixed convection will be discussed. Later on, data from literature covering the two-dimensional flow will be used to validate the simulation model of the present work.

2.3.1. Two-dimensional flow cases

An early experimental investigation of two-dimensional mixed convection was conducted by Hall and Price (1970). They introduced a 1.35 m high vertical aluminum plate in a wind channel airflow of up to 1 m/s. Through heating strips, Grashof numbers in the range of $10^9 < \mathrm{Gr} < 10^{10}$ were reached. The main focus was the investigation of the convective heat transfer. Compared to pure natural convection, the heat transfer rate decreased when imposing a weak *aiding flow*. The authors suggested that this behavior is caused by a reduction of the turbulence level in the outer boundary layer region (laminarization). This explanation is consistent with the finding, that the lowest heat transfer was measured when the imposed free-flow velocity was in the same order of magnitude as the peak velocity in the boundary layer. Accordingly, when increasing

the free-flow velocity beyond this point, the heat transfer coefficient started to increase again.
The observation that aiding mixed convection stabilizes the boundary layer was later confirmed in high-pressure experiments in air (Krishnamurthy and Gebhart, 1989). Large-scale experiments supporting these findings were conducted i.e. by Abu-Mulaweh et al. (2000) and Hattori et al. (2000, 2001) using air or Kitamura and Inagaki (1987) using liquid water. In these experiments, the respective height of the heated plates was in the range of 4 m. The boundary conditions varied: In Hattori's setup, temperature differences between 20 K and 80 K allowed the investigation of a flow characterized by $10^8 \leq \mathrm{Gr} \leq 10^{11}$ and $10^3 \leq \mathrm{Re} \leq 10^6$. In Abu-Mulaweh et al. (2000), the imposed flow velocity was up to 0.44 m/s at a wall-fluid temperature difference of 30 K, which corresponds to a Grashof number of $\mathrm{Gr} = 6{,}5 \cdot 10^{10}$. Kitamura and Inagaki (1987) worked on a water flow of up to 0.11 m/s ($\mathrm{Re} = 5.7 \cdot 10^5$) and a maximum temperature difference of 20 K ($\mathrm{Gr} = 3.5 \cdot 10^{12}$). Hattori et al. (2000) investigated the turbulent characteristics of a the mixed-convection flow and were able to evaluate the waveforms of the velocity and the temperature fluctuations. For pure natural convection, large-scale, low-frequency (0.8 Hz) fluid motion was dominant. When increasing the Reynolds number, higher-frequency waveforms started to appear, finally resulting in an almost single high-frequency (10 Hz) oscillation. This observation was confirmed by evaluating the respective spectra.

Numerical investigations on this subject were started by Oosthuizen (1974). He used a simple turbulence model which was based on Prandtl's mixing length model. The boundary conditions were those of the experiments by Hall and Price (1970), however, the entire calculation was two-dimensional. Compared to the experimental data, Oosthuizen was able to qualitatively reproduce the general flow features. However, the author noted, that an empirical constant was needed to be chosen correctly, which limits the result's general validity. Similar studies have been published by Chen et al. (1987) and Cebeci et al. (1990). By using the k-ϵ turbulence model, Patel et al. (1996) numerically derived correlations for different two-dimensional mixed convection flow regimes on a vertical plate. The same approach was recently pursued by Oosthuizen (2010). However, as discussed before, only average values for the convective heat transfer were successfully evaluated.

By eliminating modeling (i.e. for turbulence as well as for temperature and velocity profiles in the boundary layer), recent DNS have succeeded in providing extensive insights into two-dimensional mixed convection. Direct numerical simulations have successfully been conducted by Abedin et al. (2010, 2012b). For the aiding flow cases with air (Prandtl number of 0.71), they were able to reproduce the effect of laminarization discussed above. In addition, the authors

have investigated cases with an *opposing flow*. For these cases, the authors observed a slight increase in heat transfer rate with increasing free-stream velocity. By comparing results of the two different setups under varying flow conditions, they investigated the transition from laminar to turbulent flow conditions. When increasing the aiding flow velocity, transition was delayed to higher Grashof numbers and occurred approximately in the range of $\mathrm{Gr} \approx 10^{10}$ for a Reynolds number of $\mathrm{Re} \approx 10^4$. For opposing flows, transition occurred faster for increasing free-stream velocities. For the same Reynolds number as in the aiding case, transition was already observed around $\mathrm{Gr} \approx 10^9$, which is lower by one order of magnitude.

By comparing mean velocity and temperature profiles in the near-wall boundary layer region with experimental data (Hattori et al., 2000), Abedin et al. (2010) demonstrated the suitability of numerical simulations for the investigation of mixed convection. Unlike experimental investigations, fluctuations i.e. in the velocity could be evaluated in transient numerical simulations. The computed fluctuation fields showed long-drawn regular patterns in spanwise direction for the aiding flow. When increasing the free-flow velocity, the laminarization became noticeable through lower fluctuations at smaller scales and in a thinner shape. For the opposing flow, the scales of these structures were generally much larger and grew even further when increasing the free-flow velocity. Unsurprisingly, this indicates a significantly higher amount of turbulence in the opposing flow boundary layer. The availability of detailed flow data allowed to evaluate the turbulence characteristics within the boundary layer, i.e. by budgeting the turbulent kinetic energy (Abedin et al., 2012b). Using a simplified form of the conservation equation (Eqn. 2.18), production, transport, and dissipation of k were associated to the respective provoking mechanisms:

Aiding flows exhibit two peaks in k production in the near-wall region, both the result of a gradient in mean velocity (see term (vi) in Eqn. 2.18). The first peak occurs at $z/\delta \approx 0.05$, where δ is the integral boundary layer thickness. This position corresponds to the location of the maximum velocity gradient between the wall and the updraft. The second peak is caused by the velocity gradient between updraft and free stream. It consequently occurs in the outer region of the boundary layer ($z/\delta \approx 1$) and is less distinct. Throughout most of the boundary layer, buoyancy production attributes only slightly to the gain of turbulent kinetic energy. The produced energy from the first peak locally dissipates or is transported by viscous diffusion toward the wall, where it is then dissipated. The second peak in production is balanced with the sum of dissipation and the sum of transports (by pressure diffusion, viscous diffusion and turbulent diffusion).

For opposing flows, most turbulent kinetic energy is produced in the outer region of the boundary layer, where the buoyancy-influenced flow is adjacent to the opposing free flow. The turbulent energy produced in this region is transported

towards the wall by turbulent diffusion. The dissipation rate is low in the region of maximum updraft velocity, which results in the energy-cumulating large-scale flow structures described above. As the velocity difference between wall and updraft is smaller in the opposing cases, the resulting production of k in the near-wall region is at a moderate level. However, buoyancy production becomes more significant. Similar to the aiding flow cases, turbulent kinetic energy is transported to the wall by viscous diffusion and is then dissipated.

While the studies discussed above are for air, almost identical results have been obtained for water with a Prandtl number of 6.0 (Abedin et al., 2012a). Figure 2.12 shows the dimensionless heat transfer rate (Nusselt number) of two-dimensional mixed convection in water with aiding and opposing flows in the coordinates Gr_y. Here, the Nusselt number exhibits a steep increase when the flow starts to transition. The effect of laminarization is clearly visible in the aiding flow cases, where the heat transfer rate actually decreases for increasing velocities. This rather counterintuitive behavior is the result of suppressed mixing in the boundary layer. In comparison to the natural convection case, it is worth noting that any aiding flow delays transition. As the opposing flow features a higher shear between boundary layer flow and free stream, the opposite is true and transition occurs faster for higher velocities. The figures also show that the actual increase in Nusselt number by turbulence depends on the flow velocity.

The physical findings discussed above are in very good agreement with the DNS results of Kasagi and Nishimura (1997), who simulated mixed convection in air for lower Grashof and Reynolds numbers in a vertical channel with a heated and a cooled side (opposing and aiding flow in one domain).

Using LES with a dynamic Smagorinsky subgrid-scale model, Ojofeitimi (2013) simulated the mixed convection experiment by Hattori et al. (2000). By resolving the boundary layer (wall-resolved LES), the author was able to produce very good agreement with the experimental results for both the flow characteristics and the turbulence statistics. As in the experiments, when increasing the free-stream velocity, a reduction in boundary layer thickness in combination with a decreasing heat transfer rate was observed. The transition to full turbulence was delayed for higher flow velocities. The fluctuation waveform frequency spectra agree very well with Hattori et al. (2000).
In addition, the use of a blending concept for temperature and velocity wall functions, as proposed by Balaji et al. (2008), was tested in two different near-wall grid resolution configurations. This approach allowed the reduction of cell numbers across the boundary layer from 130 to 23 and 11. For the flow field, modeling the inner layer of the turbulent boundary layer still yielded good agreement with DNS data available in literature. However, as most of the near-wall

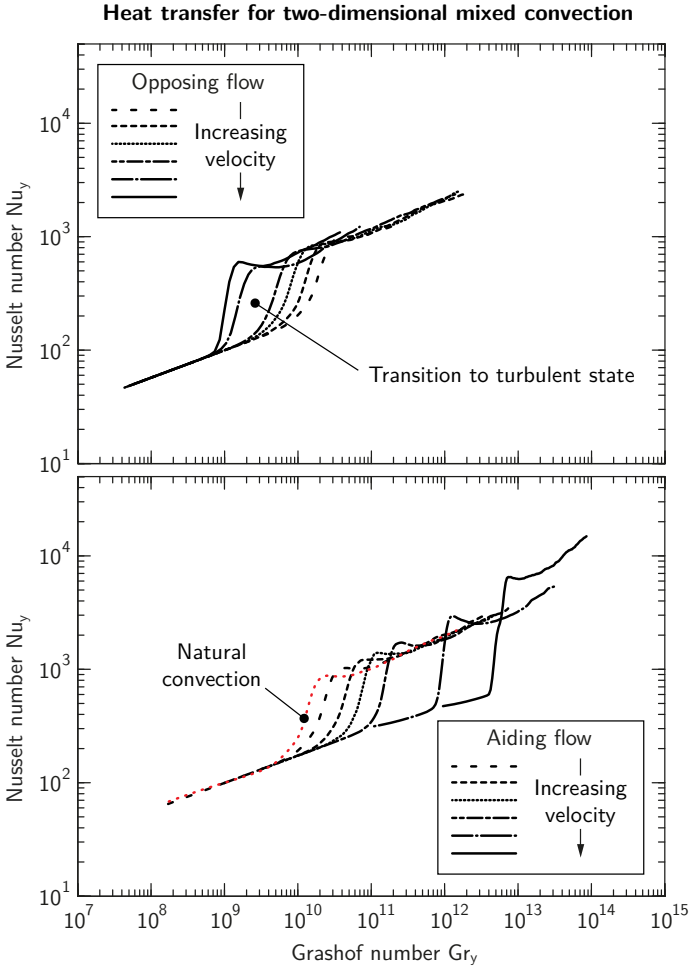


Figure 2.12.: Heat transfer (Nusselt number) as a function of height (Grashof number) for the two-dimensional mixed convection DNS simulation cases run by Abedin et al. (2012a). The upper figure shows imposed opposing flows, where a higher flow velocity results in a faster transition towards turbulence. The lower figure with imposed aiding flows shows that transition is delayed when the aiding velocity increases. The diagram also shows that the actual increase in heat transfer by turbulence depends on the flow velocity.

physics remained unresolved, deviations occurred for the turbulent properties, i.e. a significant over-estimation of velocity fluctuations and a slight over-estimation of temperature fluctuations. As a result, the computed turbulent heat flux was highly over-predicted as well. Furthermore, the author noted differences in the computed wall heat flux between the wall-resolved and the wall-modeled cases. He thus concludes that literature lacks wall models applicable to turbulent mixed convection flows.

Recently, Lance (2015) performed PIV measurements in different mixed convection flows with the objective of providing validation data for CFD applications. However, his setup exhibits rather low Richardson numbers and is thus subject to a low influence of buoyancy.

2.3.2. Three-dimensional flow cases

While two-dimensional mixed convection has been the subject of research for decades and thus is well-documented in literature, three-dimensional flow cases are rarely investigated. This lack of research is mainly the result of an extremely high degree of complexity and the large size of the required setups. Like the present work, most of the research on this topic is motivated by the lack of predictability in the convective heat losses of solar thermal central receivers.

The most extensive experimental investigation of three-dimensional mixed convection on a vertical plate was performed by Siebers (1983) in the context of Sandia National Laboratory's solar thermal program. Accordingly, the main focus of his work was the measurement of the convective heat transfer under controlled boundary conditions. His large-scale experiment featured a heated plate of 2.95 m width and 3 m height capable of reaching a maximum wall temperature of 861 K. Uniform heating was achieved by using thin electrical heating strips and an insulation at the back of the plate. The plate was mounted in a wind tunnel which could produce an airflow of up to 6.2 m/s. The author specifies[2] the maximum Grashof number as $\mathrm{Gr_H} = 2 \cdot 10^{12}$ and the maximum Reynolds number as $\mathrm{Re_L} = 2 \cdot 10^{6}$. The resulting configuration allowed experiments in all mixed convection regimes (laminar, turbulent, pure natural, pure forced and mixed convection) with Richardson numbers of $0.18 < \mathrm{Gr}/\mathrm{Re}^2 < \infty$. On the plate surface, the local temperature was measured at 105 points, each equipped with an array of three thermocouples[3]. Additionally, heat losses by conduction through the insulation at the back were evaluated though 26

[2] Rather than being evaluated at the arithmetic mean temperature $T_{\mathrm{prop}} = \frac{1}{2} \cdot (T_{\mathrm{W}} + T_{\infty})$, all dimensionless numbers in this publication were evaluated at ambient temperature T_{∞}. This results i.e. in a significantly higher Grashof number.

[3] At this point, it should be noted that today's high-resolution thermography methods were not available at the time.

additional thermocouples. Through energy balances, this constellation allowed to determine local convective heat transfer coefficients with an uncertainty of 6% to 10%.
Profiles for mean temperature and mean velocity within the boundary layer have been measured simultaneously. For this purpose, a traverse mechanism was used to precisely position a probe carrying a thermocouple and pressure sensing ports. The latter consisted of two tubes for the total pressure and two tubes for the static pressure, the difference of which was used to determine the local flow velocity. Furthermore, two yaw sensing tubes allowed to measure the flow angle with respect to the imposed horizontal flow. In order to ensure that the measured plate boundary layer profiles were unaffected by the developed boundary layers of the wind tunnel walls, a suction apparatus was installed at the plate leading edge.
As a result of his study, Siebers (1983) reported a smooth transition from forced to mixed and to natural convection with increasing Richardson number. The mixed convection regime was defined in the range $0.7 < \mathrm{Gr}/\mathrm{Re}^2 < 10$. Beyond the regime boundary, the heat transfer coefficient matched the values predicted by literature correlations for pure natural and pure forced convection on a flat plate to within ±3%. Within the regime boundary, the local distribution of the convective heat transfer coefficient was similar for the same characteristic Richardson number – however, the absolute values varied. When evaluating the measured heat transfer coefficients, the author found that the plate average value could be quantified by blending the forced convection heat transfer coefficient h_f and its natural convection counterpart h_nat:

$$\bar{h}_\mathrm{mix} = \left(\bar{h}_\mathrm{f}^{3.2} + \bar{h}_\mathrm{nat}^{3.2}\right)^{\frac{1}{3.2}} \tag{2.79}$$

However, applying the same procedure to the local values yielded only moderate agreement with the measurements to within ±10%.
The transition from laminar to turbulent flow conditions was investigated and found to be affected by the imposed free-stream velocity and the wall temperature. An increase in wall temperature initiated faster transition as the boundary layer was destabilized by buoyancy. Furthermore, Siebers investigated the influence of temperature-dependent thermophysical properties on the convective heat transfer. This effect became significant for high-velocity turbulent flows, where the heat transfer rate even decreased when increasing the wall temperature.
Within the inner 5% to 7% of the turbulent boundary layer, the measured flow angle profile was found to be constant. However, the magnitude of the flow increased with wall distance until a maximum occurred at the edge of the constant-angle region. This region appeared for all Richardson numbers and all across the plate. The measured angles varied from nearly 90° for buoyancy-dominated cases (in the upper downstream corner of the plate) to rather low angles for inertia-dominated cases, which underlines the three-dimensional nature

of the flow. Surprisingly, for the mixed convection experiments in the laminar regime, Siebers did not find the constant-angle region.
Finally, he found evidence that some of the momentum in vertical direction produced by the buoyant forces is transferred into the horizontal flow. The author suspects turbulence to be the driving mechanisms for this transfer. Unfortunately, given the low temporal resolution of the measurement techniques, the sampling of turbulence characteristics was not possible. This lack of information on turbulence is – from today's point of view – regrettable, as the detailed validation of simulations (i.e. when performing LES or DNS) using this dataset is not possible.

Since 1983, Sieber's experiment has been the starting point of several numerical studies: In a numerical work following up the experiments, Afshari (1989) developed a specialized turbulence model for the boundary layer. He succeeded in reproducing the measured results within the experimental uncertainty, i.e. the constant flow angle region. However, the size of the region was slightly smaller in the simulations. The author added to Sieber's findings, that the characteristics of the mixed convection flow depends rather on a fluid particle's residence time close to the wall than the flow distance from the inlet.
More recently, Evans et al. (2005) have numerically reproduced Sieber's experiment. Their study has already been discussed in the methods section in Section 2.2.2, as its main objective was the validation of different turbulence models. Consequently, no additional physical findings have been reported.

A number of additional studies on three-dimensional mixed convection flows has been published in the context of cooling applications in electronic components (Gadepalli and Rahman, 1996; Raghavan and Rahman, 1997, 1996). However, these flows are characterized by rather low Grashof and Reynolds numbers ($\mathrm{Gr} < 10^8$ and $\mathrm{Re} = 411$) and thus not relevant for the present work. The same is the case e.g. for the studies by Rahman and Carey (1986) and Evans and Plumb (1982) which exclusively cover laminar flows.

2.4. Chapter summary

This chapter gave an introduction to mixed convection, including the fundamentals of fluid dynamics, modeling approaches for turbulence, heat transfer, and boundary layer theory. The respective challenges in the experimental investigation (i.e. similarity and measurement resolution) and in the numerical simulation (i.e. boundary layer resolution, computational cost, turbulence, and stability) were highlighted and discussed. A literature review showed that detailed information is available on the two-dimensional mixed convection, where gravity points in a direction parallel to the imposed flow. In cases where buoyancy acts in the same direction as the imposed flow, an effect referred to as laminarization delays

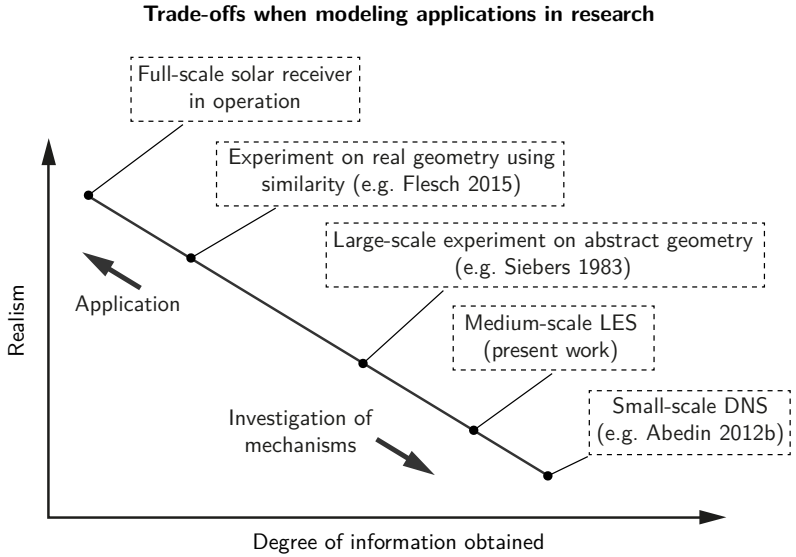


Figure 2.13.: Illustration of the trade-off between obtaining a high degree of information and a high degree of realism. While the upper part of the figure represents research focused on application, basic research is represented by the lower part.

the onset of turbulence with higher flow velocities. As a consequence, the heat transfer rate also decreases with increasing flow velocities in these cases. The explanation for this effect is that the difference in velocity between the updraft and the free stream reduces when the free-stream velocity increases, resulting in lower shear. In contrast to the broad range of investigations on two-dimensional mixed convection, few studies have been conducted on three-dimensional mixed convection where buoyancy acts perpendicular to the imposed flow. Literature on this subject mostly dates from the 1980's and – due to the lack of methods available at the time – gives very limited information on turbulence. For three-dimensional mixed convection, the availability of detailed knowledge on the two-dimensional flow cases is of little use, as there is only limited analogy expected.

The review of research on mixed convection allows to categorize the methods used as shown in Figure 2.13: Approaches such as large-scale experiments using real-size objects (e.g. solar receivers) allow research with a high degree of realism. However, the obtained results are then very specific and the degree of information on the mechanisms is therefore rather low. This type of research

would be categorized as applied science. On the other hand, extensive direct numerical simulations allow to gain insights into the smallest scales, but the computational domains are limited in size. This means for example that such a method cannot be used to simulate an entire solar receiver. This type of research is considered basic research. Several of the studies discussed in this chapter are located in the figure between these two extremes.

The present work is located in the region of basic research, however slightly towards the region where the scales investigated gain a certain relevance in real-life applications. This classification within the state of the art reveals the basic intention and the basic research question of this work. The subject of this study is the investigation of the processes related to the heat transfer in turbulent, three-dimensional mixed convection. This heat transfer mode and its associated flow is relevant i.e. for solar receivers (whose geometrical influence, think for example about cavities or the novel receiver design, is not the subject of the present work). For a variety of reasons, literature lacks insights into these mechanisms. The aim of this work is first, to close this scientific gap. This includes the investigation of boundary layer flows and turbulence in mixed convection, which both have a significant influence on the heat transfer. The present study also seeks to answer the question of how a change in flow velocity and a change in surface temperature influences mixed convection. The second aim is to provide a solid data base for future boundary layer modeling that includes the physical effects described by this work. The approach chosen is a numerical investigation using CFD, more specifically large eddy simulations. Several "lessons" were learned from literature that helped to tackle the challenges named above, i.e. not to use wall functions in the simulation and not to use the Boussinesq approximation. While this appears to be a constraint at first sight (meaning a limit in size and consequently a lower realism in Figure 2.13), it actually allows to gain insights into the boundary layer mechanisms that govern the heat transfer (meaning a position further to the right).

Chapter 3.

Computational methodology

All simulations in the present work were conducted using the C++-based CFD code OpenFOAM (Open Source Field Operation and Manipulation). Generally, a very attractive feature of open-source software is the possibility to adapt the code to the user's needs. In the case of OpenFOAM, the source code of any solver can be modified, e.g. by including new features, equations, or utilities. The software can thus be adapted to a very specific flow problem. Furthermore, the license limitations of commercial codes, which often hinder massively parallel computing, are not an issue when using open-source codes. Within this work, commercial CFD codes like CFX and Ansys Fluent were also tested. However, the advantages mentioned above were the decisive factor for using OpenFOAM. Throughout the entire study, version number 2.3 was used.

In the following sections of this chapter, the approaches used to overcome the challenges discussed in Chapter 2.2.2 (Numerical simulation methods) will be presented. This includes the modeling of turbulence and the thermophysical properties. Furthermore, an overview of the modified solvers will be given. Crutial for any simulation is the computational grid and the boundary conditions as well as the discretization schemes which will then be presented. The initialization strategy is the topic of the subsequent section, before the solver validation and the evaluation methods are discussed.

3.1. Modeling approach

When simulating fluid flows, the use of certain model assumptions is inevitable. This includes the treatment of turbulence effects and the description of the fluid's thermophysical properties. The following two sections will give details on the modeling used throughout the present work.

3.1.1. Large eddy simulation

In Chapter 2.1.3, three different approaches for the treatment of turbulence in CFD simulations were discussed: Fully resolving all scales of turbulence (DNS) would require a tremendous amount of computational resources. On the other hand, when investigating three-dimensional mixed convection, RANS modeling does not resolve any turbulent scale and does therefore not provide sufficient

information on the heat transfer and flow processes. Consequently, the approach chosen for this work is a large eddy simulation, as this method represents a decent compromise between RANS and DNS.

The subgrid-scale model for the LES in this work is the one-equation eddy viscosity model by Yoshizawa and Horiuti (1985) which was presented in Chapter 2.1.3. A similar model configuration was successfully used by de Villiers (2006). The main reason for this choice is the expected non-equilibrium of subgrid-scale turbulent kinetic energy production and dissipation. While this is generally the case in shear flows and boundary layers, it is especially true if the boundary layer is buoyancy-affected. Here, the algebraic Smagorinsky model would provide a less accurate description of the turbulent processes. The dynamic procedure to determine the Smagorinsky coefficient introduces the chance of producing values that are too low near the wall (Cabot et al., 1999), which would result in an underestimation of sgs viscosity. As the near-wall region is relevant for this work, the option of using the dynamic procedure was discarded.

In OpenFOAM, Yoshizawa's model is implemented as *oneEqEddy* model. The governing equation for the transport of subgrid-scale turbulent kinetic energy (Eqn. 2.46) and the associated closure of the filtered Navier Stokes equations (Eqn. 2.48) have been discussed above. In the present work, the two model constants are universally defined as the standard values, namely

$$C_\epsilon = 1.048, \qquad C_\mathrm{k} = 0.094 \tag{3.1}$$

The filtering operation generally used for LES in OpenFOAM is a so-called implicit filtering where the spacial discretization of the finite volume method itself effectively represents a filtering. This filtering basically corresponds to the use of the simple box (top-hat) filter. The filter width Δ consequently depends on the local grid. For the present work, the standard cube-root-volume Δ-function is used:

$$\Delta = \sqrt[3]{\Delta x \Delta y \Delta z}$$

This formulation imposes a certain degree of restraint to the mesh design, as it requires equilateral cells. If the length of one cell side exceeds the others, the resulting filter width no longer represents the smallest resolvable scale. Special care has thus been taken in the mesh creation: An inflation layer, where the cell side lengths decrease only in wall-normal direction, exists solely in the first 9 cells in direct wall proximity. In this region, the effect of turbulence is expected to be limited and – due to the small filter width – the error introduced does not have a significant influence. Furthermore, as filtering is achieved implicitly, the filter width only influences the dissipation rate of sgs turbulent kinetic energy

and sgs viscosity. The first tends towards zero at the wall (see Eqn. 2.46), as a fixed value of zero for k_{sgs} is a mandatory boundary condition. The same is the case for the sgs viscosity (see Eqn. 2.47).

Almost all effects of interest in the present work occur in the boundary layer at the wall. In order to gain insights into these processes and based on the wall-model testing by Ojofeitimi (2013), the concept of a wall-resolved LES without any modeling of wall effects was chosen. This requires a resolved boundary layer and implies in particular, that the sgs viscosity is not damped near the wall e.g. by the van Driest damping function. As the mesh size is dramatically reduced towards the wall (viz. the filter width Δ is very small), the sgs viscosity is expected to tend towards zero.

3.1.2. Thermophysical properties

The fluid flow investigated in the present work is considered to be incompressible, i.e. density ρ is not a function of pressure p. Therefore, no equation of state, like the ideal gas equation, can be used to describe the density. However, the precondition for the development of a buoyancy-driven flow is a variable and temperature-dependent density. Therefore, an idealized fluid based on the properties of water has been chosen as the working fluid in this study. Water satisfies both conditions in the relevant temperature range between 293 K and 373 K at the pressure of 1 MPa[1]:

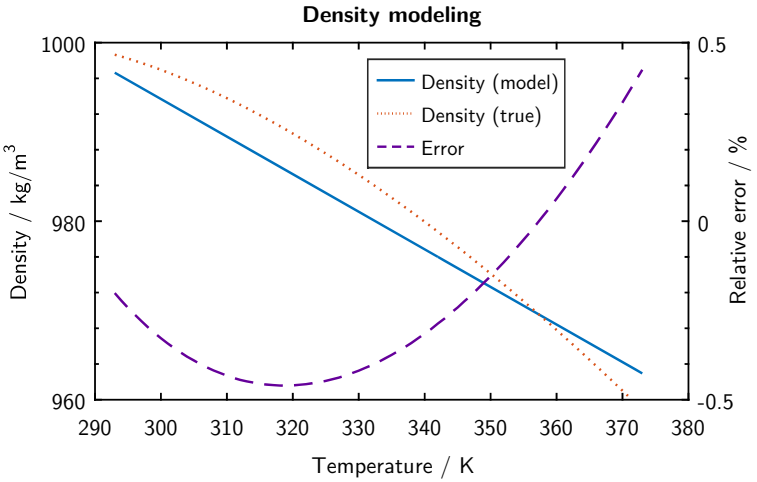
$$\frac{\partial \rho}{\partial p} = 0.4451 \cdot 10^{-3}\ \mathrm{kg/m^3Pa} \tag{3.2}$$

$$\frac{\partial \rho}{\partial T} = -0.5003\ \mathrm{kg/m^3K} \tag{3.3}$$

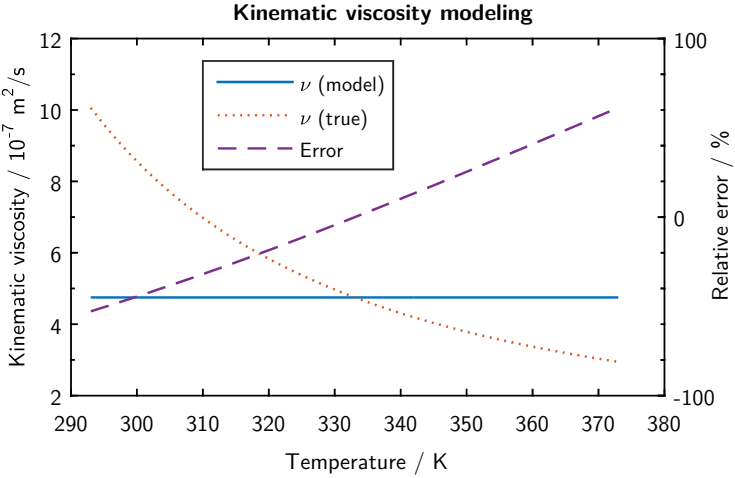
Additionally, water could serve as fluid in possible future experimental investigations, which could then be compared to the present study. Even though a broad range of measured thermophysical properties is available for water, some simplifications were made. For details on the implementation, please refer to Appendix D.

For the density ρ, a linear dependence on temperature was assumed. This simplification produces only a slight error of less than 0.5%, as shown in Figure 3.1(a). The main reason for this modeling choice is that it does not introduce additional non-linear effects. This is important, as the coupling of energy and momentum by the density is per se a source of numerical instability.

[1] All measured thermophysical fluid properties in this work are evaluated using data from Lemmon et al. (2004)

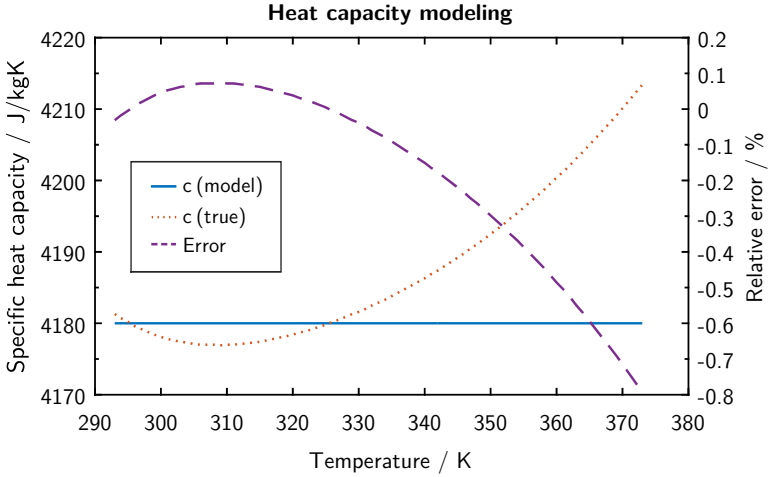


(a) Comparison of the modeled density (linear) and the measured density of water. For the temperature range investigated in this work, the error is below 0.5%.

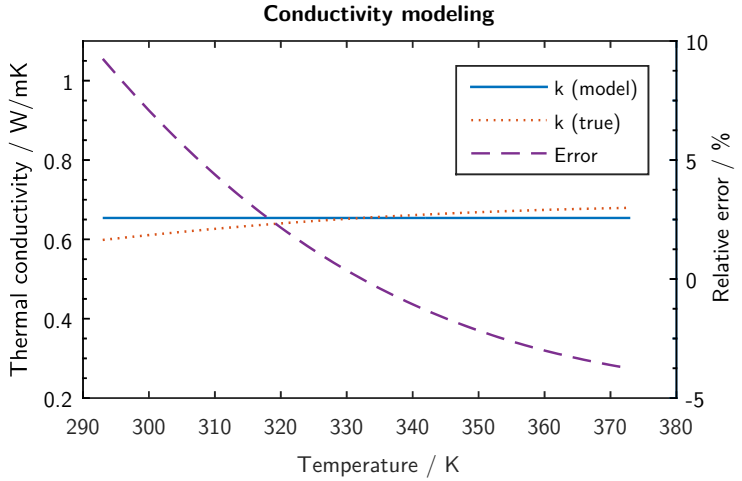


(b) Comparison of the modeled and the measured kinematic viscosity. Even though the assumption of constant viscosity does not represent the viscosity of water, it eliminates fluid-specific influences and thus allows general conclusions on mixed convection flows.

Figure 3.1.: Fluid properties required in the momentum equation. All measured thermophysical properties are listed by Lemmon et al. (2004).



(a) Comparison of a constant and the measured specific heat of water: The relative error is below 1%.



(b) Evaluation of the error introduced by assuming a constant molecular diffusivity of heat (thermal conductivity).

Figure 3.2.: Modeling of the fluid thermophysical properties related to heat transfer. Like in the preceding figure, the measured thermophysical properties are listed by Lemmon et al. (2004).

The second important fluid property, the kinematic viscosity ν, is defined as a constant. With the tensor

$$\boldsymbol{\tau} = \nu \nabla (\rho \boldsymbol{u})$$

describing the shear stress, which can also be interpreted as a flux of momentum, ν is the corresponding transport coefficient for momentum diffusion. With the variable density ρ, the kinematic viscosity ν instead of the dynamic viscosity $\mu = \nu\rho$ is set to be constant. Admittedly, this decision does not have a major impact, yet, any constant viscosity does not represent the actual fluid properties of water. As shown in Figure 3.1(b), the relative deviation is as high as 61%. However, aside from the pleasing effect of enhancing stability, a constant viscosity allows to draw general conclusions on mixed convection. Using the actual viscosity of water (which decreases with temperature) would produce fluid-specific effects that do not occur in air (where viscosity increases with temperature). The constant viscosity of $4.75 \cdot 10^{-7}\,\mathrm{m}^2/\mathrm{s}$ is evaluated at the very same temperature, the overall dimensionless numbers are calculated at.

The fluid properties related to heat transfer and transport are also considered to be constant. The specific heat c is set to the standard average value for water, 4180 J/kg K, which produces a maximum relative error of 0.8% in the investigated temperature range (see Figure 3.2(a)). The thermal conductivity k, diffusive transport coefficient for molecular diffusion of heat, is set to 0.654 W/m K. As the convective heat transfer is to a large extend determined by the fluid conductivity, its value is chosen to represent the temperature at which the dimensionless numbers are evaluated. Like the viscosity, the relative error introduced by this assumption is significant (up to 9.3%). However, setting the conductivity to a constant value independent of the temperature keeps further non-linear effects off the energy equation.

For the present simulations, the ratio of the coefficients for momentum transport and heat transport – the Prandtl number – is

$$\mathrm{Pr} = \frac{\nu \rho_\infty c}{k} = 3.02$$

with the density being evaluated at ambient temperature. This value corresponds roughly to the Prandtl number that water would have at a temperature of 60 °C.

3.2. Solution algorithm

All simulations in the present work were conducted using an iterative solution strategy featuring a segregated approach where the equations for velocity, energy and pressure are solved one after another. The solver has to deal with the errors

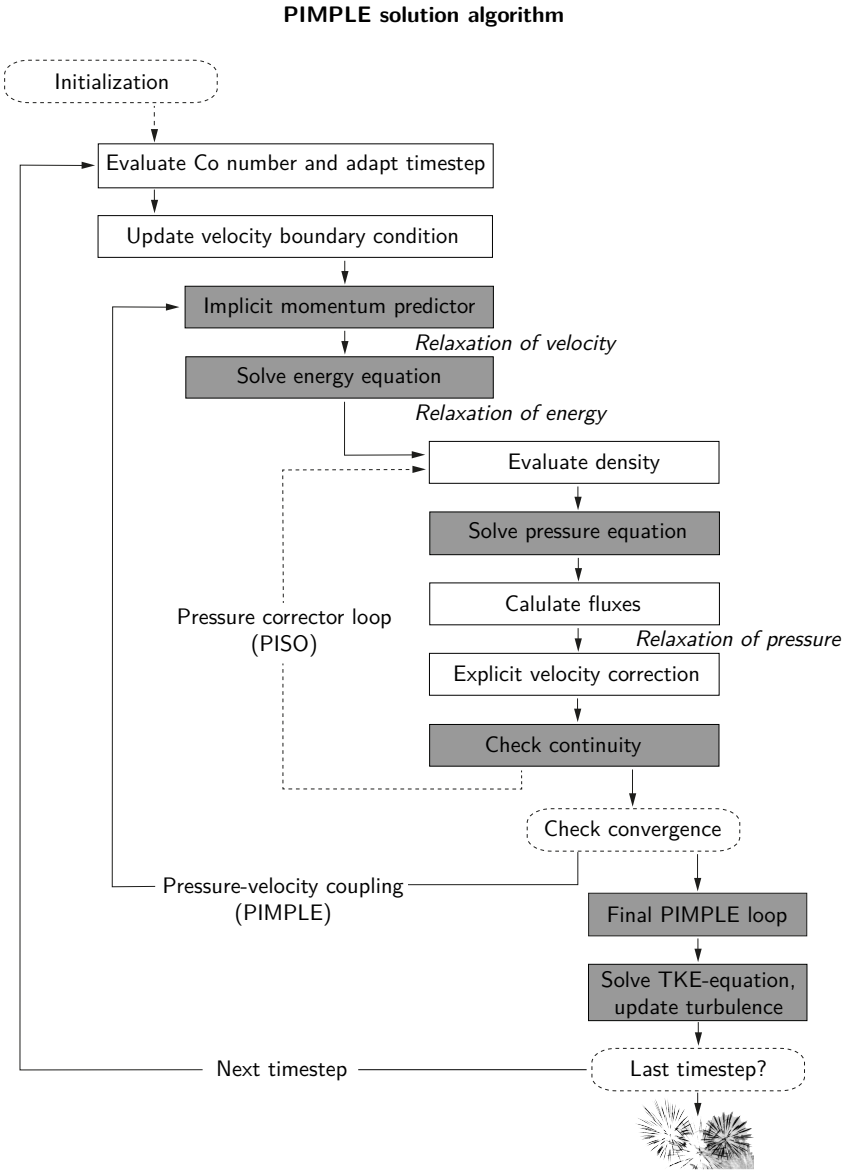


Figure 3.3.: Flow diagram of the PIMPLE (merged PISO-SIMPLE) algorithm in form of the *convectionFoam* solver. Each step in grey color features a linear solver.

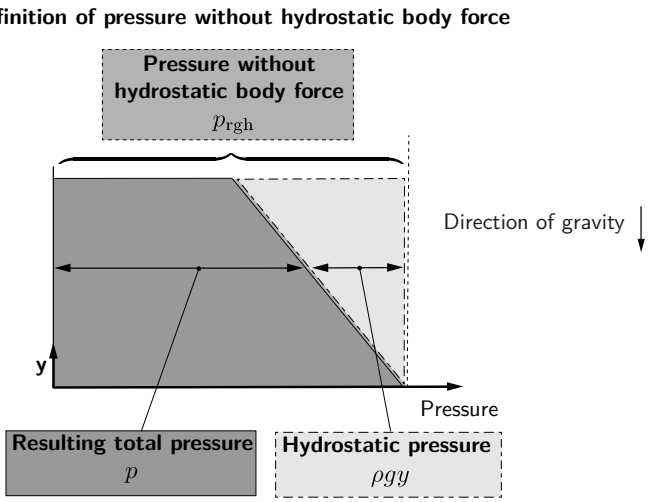


Figure 3.4.: Illustration of the relation between the pressure without hydrostatic pressure p_{rgh} and the total pressure p as introduced in Eqn. 3.4.

introduced by the linearization (as the flux from a previous iteration/timestep is used), by the discretization (discretization error), and by the fact that pressure and velocity are evaluated in sequence but actually are coupled (splitting error). In CFD, two different algorithms are commonly used: The SIMPLE (Semi-Implicit Method for Pressure-Linked Equations) algorithm introduced by Patankar and Spalding (1972) is for steady-state simulations and exhibits high numerical stability by taking advantage of under-relaxation. The PISO (Pressure Implicit with Splitting of Operator) algorithm by Issa (1986) is for transient simulations but allows only small timesteps for stability reasons.
The flow cases in the present work are transient, involve a large computational domain, and require the simulation of a relatively long period of time. For this application, neither PISO nor SIMPLE is a good choice. The present solution algorithm therefore is a combination of both, which is implemented in OpenFOAM as PIMPLE algorithm. The standard *buoyantPimpleFoam* solver has been used as a starting point, as it is intended for compressible fluids and does not use the Boussinesq approximation. Efficiency and the speed of convergence have been increased by adapting the solver to the incompressible, variable density flow setup, i.e. by removing all routines that treat compressibility effects. The solution procedure of the new *convectionFoam* solver is presented in Figure 3.3. For an in-depth discussion of the solution algorithm and the linear solvers used, please refer to Appendix A.

For the present cases where gravity is aligned in positive or negative y-direction, the pressure is divided into a part affected by flow and buoyancy and a part which includes the hydrostatic pressure. Instead of the pressure p, a new scalar field p_{rgh} for the pressure without the hydrostratic pressure is introduced. This procedure is proposed e.g. by Ferziger and Peric (2008) because it promotes solution efficiency.

$$\bar{p} = \bar{p}_{\mathrm{rgh}} + \bar{\rho} g y \tag{3.4}$$

Figure 3.4 illustrates the concept of p_{rgh}. The dark grey area is the resulting total pressure p, the hydrostatic pressure is shown in light grey. Consequently, no boundary condition is given for the pressure p in the present work. The boundary information required for the computation is solely given by a homogeneous p_{rgh} boundary condition, which significantly simplifies the simulation setup. In the momentum equation (Eqn. 2.5), the body force term (v) expressing the buoyancy is now included in the pressure term (iii). However, evaluating the pressure equation (Eqn. A.10) with $\bar{p}_{\mathrm{rgh}}$ instead of $\bar{p}$ introduces an additional term as

$$\nabla \cdot (\nabla \bar{p}_{\mathrm{rgh}}) = \nabla \cdot (\nabla \bar{p} - g y \nabla \bar{\rho} + g \bar{\rho}) = \nabla \cdot (\nabla \bar{p}) - \underbrace{\nabla \cdot (g y \nabla \bar{\rho})}_{\text{(i)}} \tag{3.5}$$

Consequently, the additional term (i) needs to be compensated.

3.3. Computational mesh and boundary conditions

While intense modeling of turbulence reduces computational costs, it fails to correctly describe all effects that influence heat transfer in mixed convection. Performing a wall-resolved large eddy simulation is a way to resolve all influential scales while modeling the non-relevant ones. However, this type of simulation also requires a high-quality computational mesh. Mesh generation therefore is a crucial step in the preprocessing and the mesh should be designed with great care. On one hand, the resolution of the boundary layer has to be sufficiently fine, on the other hand, the number of cells should not be excessive. In general, the size of a mesh element is expressed in the same way as the dimensionless wall distance

$$\Delta l^{+} = \frac{\Delta l u_{\tau}}{\nu} \tag{3.6}$$

where Δl is the cell size Δx, Δy or Δz (Eqn. 2.59). For an a priori evaluation of grid spacing, an estimation of the friction velocity (Eqn. 2.57) is needed:

$$u_{\tau} = \sqrt{\frac{\tau_{\mathrm{W}}}{\rho}}$$

As the wall shear stress depends on the velocity gradient in wall-normal direction

$$\tau_{\mathrm{W}} = \nu\rho \left(\frac{\partial u}{\partial z}\right)_{z=0} \tag{3.7}$$

it can only be computed after having performed the simulation. One way to find an estimate is to use the Schlichting skin-friction correlation for a flat plate (Schlichting, 1958):

$$C_f = (2\log \mathrm{Re}_x - 0.65)^{-\frac{2}{3}} \tag{3.8}$$

and estimate the wall shear stress

$$\tau_{\mathrm{W}} = C_f \frac{1}{2}\rho u_\infty^2 \tag{3.9}$$

The dimensionless cell size can then be determined using Eqn. 3.6. For a wall-resolved LES, Chapman (1979) advises a near-wall resolution of $\Delta x^+ = 100$ (streamwise direction), $\Delta y^+ = 20$ (spanwise direction), and a minimum of 10 cells in normal direction to resolve the viscous wall region. In their recent revision of Chapman's estimations, Choi and Moin (2012) came to a similar conclusion. However, applying this resolution requirement on the entire domain described in Chapter 4 would result in a vast number of cells.

The use of an unstructured mesh consisting of tetrahedrons would allow to resolve the near-wall region with very fine cells and grow to coarse cells in the free stream, thus meeting the requirements and still keeping the computational cost in an applicable dimension. However, this type of mesh introduces numerical diffusion and instabilities into the simulation that – due to the buoyancy effects – is inherently unstable. Problems in unstructured meshes are mainly caused by the skewness of mesh elements[2] and their non-orthogonality[3]. Both a high non-orthogonality and a high skewness cause a faulty interpolation onto the cell faces and thus numerical diffusion errors (see Jasak, 1996). For the present work, an unstructured test mesh meeting the resolution requirements has been created. The maximum skewness in this mesh was 1.1 and a severely high maximum non-orthogonality of 72°(with an average of 17°) was detected. As a rule of thumb, the mesh non-orthogonality for an LES should be less than 60°, which the tested mesh failed to comply with in any configuration.

[2] Skewness is the distance between the centroid of the common face of two neighboring cells and the point where the connecting line between the two cell centers crosses that face. OpenFOAM scales the skewness with the distance between the two cells.

[3] Non-orthogonality describes the angle between the normal of the common face and the line connecting the neighboring two cell centers.

To create a high-quality mesh and still limit the number of cells to a technically feasible dimension, structured zonal grids have proven to be good compromise. The approach of Kravchenko et al. (1996) used such a mesh with hexahedral cells for the computation of wall-bounded turbulent flows. Their LES of a turbulent pipe flow on a mesh consisting of five zones proved good agreement with experimental data. The near wall resolution in their work was $\Delta x^+ = 110$ (streamwise direction), $\Delta y^+ = 20$ (spanwise direction) and $0.6 \leq \Delta z^+ \leq 130$.

The computational mesh of the present work features this approach and uses a structured, zonal grid with eight zones. This way, all relevant regions of the boundary layer are resolved with appropriate resolution. The resolution in x-direction and y-direction is chosen to be identical, as the buoyant flow in the boundary layer makes a distinction between streamwise and spanwise direction difficult. Figure 3.5 shows the resulting mesh resolution: The ambient mesh, which resolves the free stream far away from the wall, consists of cubic cells with an edge length of $4 \cdot 10^{-3}\,\mathrm{m}$. This cell size corresponds to $\Delta l^+ = \Delta x^+ = \Delta y^+ = \Delta z^+ = 80$ for the simulation case of $u_\infty = 0.2\,\mathrm{m/s}$. The outer region of the boundary layer is refined one time, each cell is thus split into eight cells. This results in a total of 17 cell layers with an edge length of $2 \cdot 10^{-3}\,\mathrm{m}$ or $\Delta l^+ = 40$. As OpenFOAM is not able to run simulations on a mesh with hanging nodes (a node that is next to a cell face), the refined layer is connected to the ambient mesh by a layer of polyhedrons. These elements are cubic, hexahedral cells with one side face split into four sub-faces. For better distinctiveness in Figure 3.5, those mesh elements are illustrated as triangles. Towards the wall, the refined region is followed by seven cells which are refined for a second time ($\Delta l = 1 \cdot 10^{-3}\,\mathrm{m}$ or $\Delta l^+ = 20$). Connected through another layer of polyhedron elements, a layer of four cells with $\Delta l = 5 \cdot 10^{-4}\,\mathrm{m}$ or $\Delta l^+ = 10$ is refined three times. This resolution satisfies the requirements in span- and streamwise direction even for the cases with high imposed velocities. The cells closer to the wall are therefore not further refined in x and y direction, but split in z-direction for a better description of the near-wall gradients. This results in a total of four inflation layers instead of cubic cell layers. Accordingly, no polyhedron elements are required in the very near-wall region. In z-direction towards the wall, the inflation layers have two cells with $\Delta z = 2.5 \cdot 10^{-4}\,\mathrm{m}$ ($\Delta z^+ = 5$), two cells with $\Delta z = 1.25 \cdot 10^{-4}\,\mathrm{m}$ ($\Delta z^+ = 2.5$), three cells with $\Delta z = 6.25 \cdot 10^{-5}\,\mathrm{m}$ ($\Delta z^+ = 1.25$) and – adjacent to the wall – two layers with $\Delta z = 3.125 \cdot 10^{-5}\,\mathrm{m}$ ($\Delta z^+ = 0.625$). The final computational mesh consists of 53.6 million cells. Thereof, 98% are hexahedral cells and 2% are polyhedral elements in the connection layers. The maximum skewness of the latter is 0.33, while the maximum non-orthogonality is 25° with an average of 4°. The mesh exhibits an excellent quality and meets the resolution requirements with 92% of all cells having a size of $\Delta l^+ \leq 20$. In total, 98% of all cells are accumulated

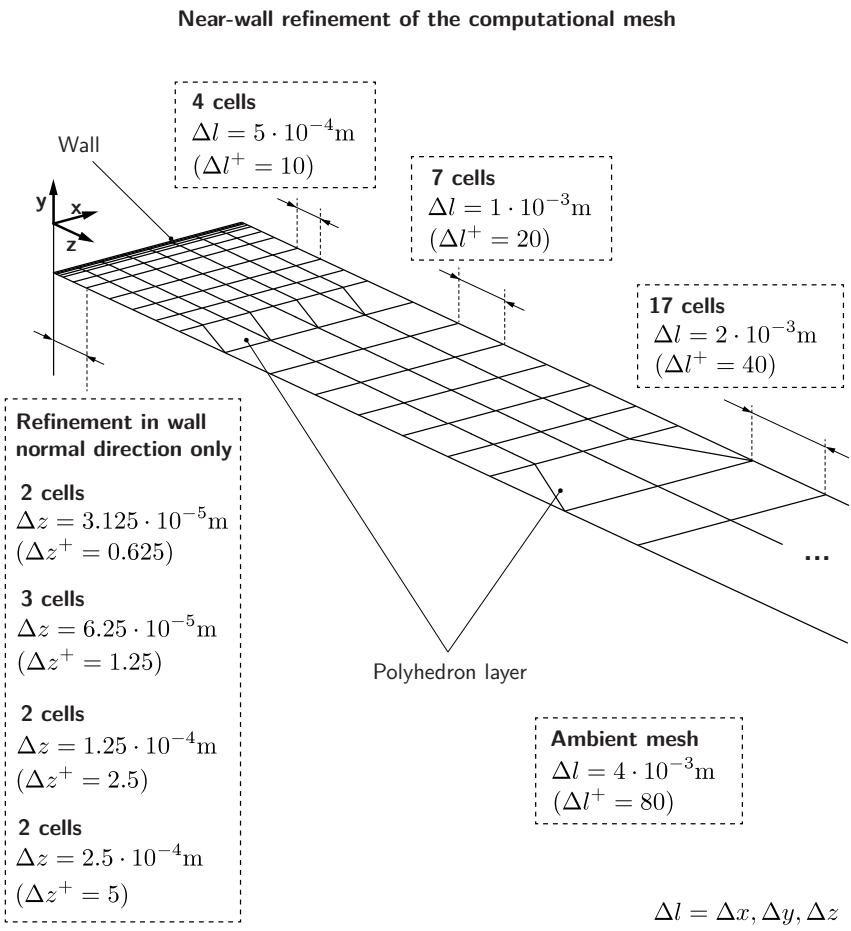


Figure 3.5.: Meshing concept in the near-wall region using the zonal grid approach (Kravchenko et al., 1996). The ambient mesh resolving the free stream is refined in seven zones towards the wall. The dimensionless mesh size is evaluated for the case of 0.2 m/s free-stream velocity.

in the refined boundary layer zones. The mesh used for the validation cases features the same mesh resolution and the same element distribution, but – as the computational domain has a smaller volume (see Section 3.6) – consists of only 41 million cells.

The large number of cells in the computational mesh requires the use of parallel computing, where the mesh and the associated field data are distributed to separate processors. The present mesh is decomposed into 16 to 504 partitions using scotch decomposition. This method attempts to keep the number of processor boundaries as low as possible. Consequently, all fields have to be reconstructed before the simulation results can be post-processed.

Figure 3.6 shows the boundary conditions imposed on the simulations of the three-dimensional flow cases. Physically, the computational domain is confined by a wall and five openings. The opening in upstream direction serves as inlet for the imposed flow. Accordingly, the opening in downstream direction is the outlet. The bottom and top openings are relevant for the flow induced by buoyancy. On the opposite side of the wall is the opening toward the free stream, which is referred to as channel. A set of Dirichlet boundary conditions is imposed on the inlet and the wall, while the downstream is described by Neumann boundary conditions. The channel, the bottom, and the top boundaries are a mix of both types.

The *wall* is set to a no-slip boundary condition for the velocity, which imposes a zero-velocity vector and also implies a turbulent kinetic energy of zero. The pressure at the wall is set to values that result in a no-flux condition, corresponding to the velocity boundary condition. The wall itself is divided into two regions: First, the bigger part of the plate is heated, which is implemented as a fixed-temperature boundary condition. The temperature is set according to the Grashof number of the respective case (e.g. to 365.15 K for $\mathrm{Gr} = 3.3 \cdot 10^{11}$). Second, a very small strip close to the bottom and inlet boundary conditions is kept adiabatic for reasons of numerical stability. This is implemented by setting the wall temperature to the ambient value of 298.15 K.

The *inlet* boundary condition is set to fixed values of 298.15 K for the temperature field and $1 \cdot 10^5$ Pa the pressure field. The velocity in y and z direction is set to zero, and in x according to the Reynolds number of the respective case (e.g. to 0.2 m/s for $\mathrm{Re} = 4.06 \cdot 10^5$). In order to trigger the transition from a laminar to a fully turbulent flow, a certain amount of turbulence has to be imposed on the flow at the inlet. As a starting point, the turbulence intensity I of the incoming flow, defined by

$$u' = I \cdot u_\infty \tag{3.10}$$

is estimated to be 5%, which is a common choice for a medium-turbulence flow (Marić et al., 2014). For this intensity, a total TKE at the inlet (on both resolved and modeled scales) can be determined. Hereof, in LES, the resolved share

$$k = \frac{3}{2} u'^2$$

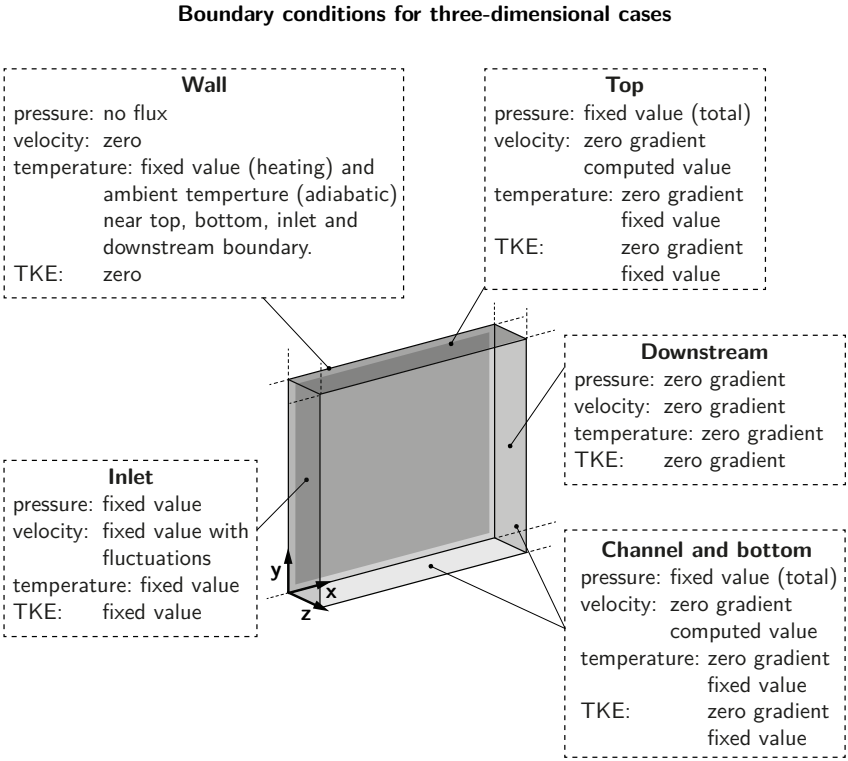


Figure 3.6.: Boundary conditions for three-dimensional flow cases.

should account for approximately 80%, while 20% can be modeled by the subgrid-scale turbulence model. Practically, this is implemented by setting a fixed sgs turbulent kinetic energy k_{sgs} (for the modeled turbulence) at the boundary condition, and by imposing isotropic fluctuations on the velocity (for the resolved turbulence). As the mesh at the inlet boundary exhibits different cell sizes in wall-normal direction, the use of plain white noise would cause severe numerical instabilities. Therefore, synthetic turbulent structures (vortex singularities or vortons) are generated by the so-called *InflowGenerator* of the open-source library LEMOS and imposed on the inlet velocity field. A detailed description of the method is given in Kornev and Hassel (2007); Kornev et al. (2008, 2007). As input, a characteristic length scale is set to approximately 4% of the plate length. Furthermore, the Reynolds stress tensor $\overline{\boldsymbol{u'u'}}$ (Eqn. 2.25) is required. As it is not a priori known, its values are estimated according to the 80% precondition.

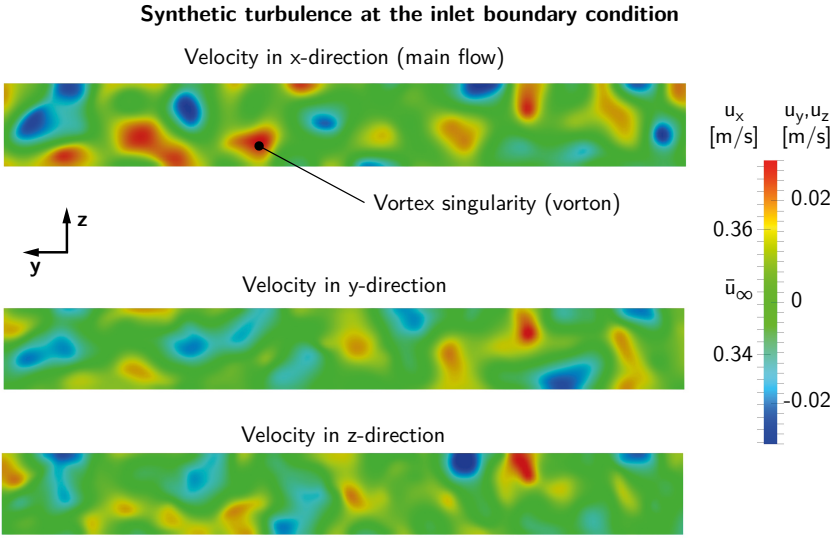


Figure 3.7.: Example of the instantaneous three velocity components at the inlet boundary condition showing the synthetic turbulent structures imposed.

The trace of the tensor $\overline{u_i' u_i'}$ defines the absolute value of the fluctuations. How the fluctuation in one direction correlates with the ones in the other directions is specified by the remaining entries $\overline{u_i' u_j'}$. Figure 3.7 illustrates the inlet flow field for a mean velocity of 0.35 m/s with imposed synthetic turbulence. The fluctuations are homogeneous and the vortons are weakly correlated.

The *channel*, *bottom*, and *top* boundaries are supposed to represent the free stream. As the Boussinesq-approximation is not used in the solver (see Section 3.2), the volume expansion of the incompressible fluid in the boundary layer is expected to cause a very small flow in z-direction. This prohibits the use of a fixed-velocity Dirichlet boundary condition at the channel (set to the free-stream conditions). The same is the case for the bottom boundary condition, where cold ambient fluid is expected to be entrained into the domain in order to compensate for the updraft leaving the domain in vertical direction. Consequently, at the top, fluid is generally expected to leave the domain. However, within coherent vortices and in the outer boundary layer, a reversed flow is possible. For these three boundaries, a zero-gradient Neumann boundary condition is suitable when fluid leaves the domain. For the opposite case, however, this condition would cause velocity streaks leading to the divergence of

the simulation. Therefore, a complex boundary condition (*pressureInletOutletParSlipVelocity*) is used with a zero-gradient for outflow and an imposed normal velocity for inflow. The latter value is obtained from the internal cell next to the boundary. In tangential direction, a slip (zero-gradient) condition applies. This boundary condition is self-stabilizing as the total pressure is set to a fixed value ($1 \cdot 10^5\,\mathrm{Pa}$). However, the pressure boundary condition (*totalPressure*) was modified to consider only the velocity component normal to the boundary ($p = p_0 - \rho u_n^2/2$). Without this change, the fluctuations imposed by synthetic turbulence would cause non-physical variations in the pressure boundary. If the local velocity vector points out of the computational domain, a zero gradient boundary condition is set for the temperature and for the subgrid-scale TKE, allowing advective transport over the system boundary. For a velocity pointing into the domain, the ambient temperature and the inlet k_{sgs} is imposed. In OpenFOAM, this choice is implemented as *inletOutlet* boundary condition.

For all fields, the *downstream* boundary condition is set to a zero gradient, as no reversed flow back into the domain is expected at this location.

3.4. Numerical schemes

The proper choice of numerical discretization schemes is crucial for large eddy simulations, as the schemes have to ensure numerical stability and to provide the required amount of precision. In the present work, all gradients are evaluated by applying the Gauss' theorem in its gradient form

$$\int_{\mathrm{V}^*} \nabla\phi \mathrm{d}V = \oint_{\partial \mathrm{V}^*} \mathrm{d}\boldsymbol{S}\phi = \sum \phi_f \boldsymbol{S}_f \tag{3.11}$$

which results in a vector for a scalar ϕ and in a tensor for a vector $\boldsymbol{\phi}$. The theorem in its divergence form

$$\int_{\mathrm{V}^*} (\nabla \cdot \boldsymbol{\phi})\, \mathrm{d}V = \oint_{\partial \mathrm{V}^*} \mathrm{d}\boldsymbol{S} \cdot \boldsymbol{\phi} = \sum \boldsymbol{\phi}_f \cdot \boldsymbol{S}_f \tag{3.12}$$

is used to evaluate divergence terms. Both evaluations require the value ϕ_f at the cell face, which is initially unknown. The value at the face f between the cells N and P must thus be interpolated from the cell values ϕ_c. The simplest interpolation scheme is central differencing (cd), where

$$(\phi_f)_{\mathrm{cd}} = w_{\mathrm{cd}} \phi_{c,P} + (1 - w_{\mathrm{cd}})\, \phi_{c,N} \tag{3.13}$$

The factor w_{cd} is a weighting factor for the linear interpolation. It expresses the distance between the face and the respective cell center, viz. for uniformly sized

cells $w_{\mathrm{cd}} = 0.5$. This scheme is second-order accurate but can only be bounded for a sufficient mesh resolution, i.e. a cell Reynolds number of $\mathrm{Re}_{\Delta l} < 2$. If this is not the case, the solution tends to non-physical oscillations (Patankar, 1980). The alternative upwind scheme (ud) uses the upwind cell value as face value

$$(\phi_f)_{\mathrm{ud}} = \phi_{c,i} \tag{3.14}$$

with $i = N$ or $i = P$ depending on the direction of flow. The scheme is bounded, therefore no oscillations will appear in the solution. Obviously, it is only first-order accurate and stability comes at the price of numerical diffusion, which smears the solution. Numerical diffusion is always problematic in an LES because is can easily outweigh the contribution of modeled subgrid-scale turbulent diffusion processes.

In a general form, both schemes can be rewritten as

$$\phi_f = w\,(\phi_{c,P} - \phi_{c,N}) + \phi_{c,N} \tag{3.15}$$

with the weighting factor

$$w = w_{\mathrm{cd}} = 0...1 \tag{3.16}$$

depending on the mesh for central differencing. For upwind differencing, the factor can be written as

$$w = w_{\mathrm{ud}} = \begin{cases} 0 & \text{for positive flux} \\ 1 & \text{for negative flux} \end{cases} \tag{3.17}$$

Jasak (1996) shows examples of numerical errors introduced by discretization, including inaccuracy by numerical diffusion for the upwind scheme and oscillations caused by central differencing. In order to prevent oscillations and still guarantee the precision required for LES, both schemes can be blended

$$\phi_f = (1-\gamma)\,(\phi_f)_{\mathrm{ud}} + \gamma\,(\phi_f)_{\mathrm{cd}} \tag{3.18}$$

where γ is the blending factor between upwind ($\gamma = 0$) and central differencing ($\gamma = 1$). In the general form of Eq. 3.15, this yields

$$\phi_f = \Big((1-\gamma)\,w_{\mathrm{ud}} + \gamma w_{\mathrm{cd}}\Big)\,(\phi_{c,P} - \phi_{c,N}) + \phi_{c,N} \tag{3.19}$$

In the present work, such a blending scheme is used for the interpolation of the velocity $\boldsymbol{u}$ when evaluating the divergence $\nabla \cdot (\rho \boldsymbol{u}\boldsymbol{u})$ and in the interpolation for $\nabla \cdot (\rho \boldsymbol{u} k_{\mathrm{sgs}})$. Both fields are important as they are used in the turbulence model and therefore influence the modeled subgrid-scale diffusion of energy and momentum. The scheme was originally introduced by Jasak et al. (1999) and successfully applied by de Villiers (2006) in large eddy simulations of wall-

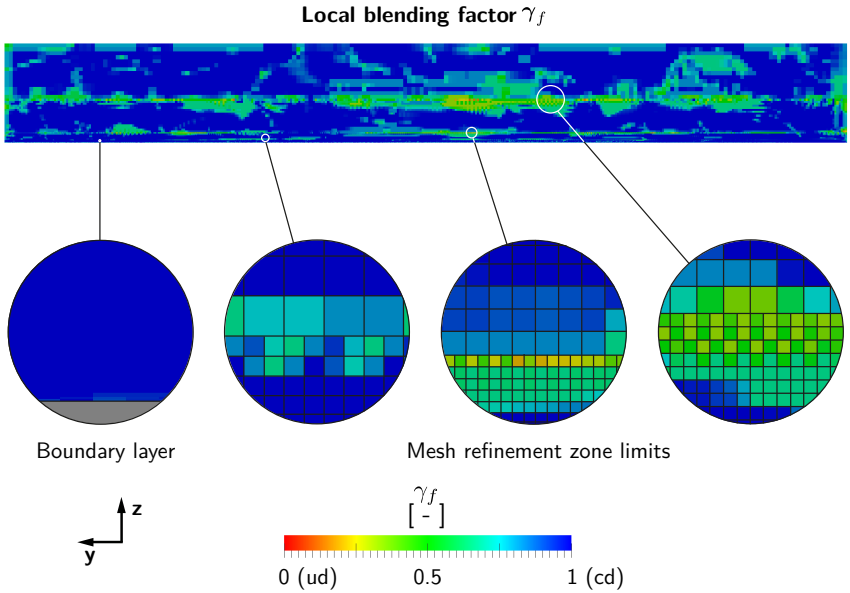


Figure 3.8.: Exemplary instantaneous distribution of the local blending factor γ_f for the velocity field between central differencing ($\gamma = 1$) and upwind differencing ($\gamma = 0$). Artifacts occurring at the limits of the mesh refinement zones are counteracted by the use of a higher share of upwind differencing. It is important to note, that the high share of central differencing within the boundary layer ensures accuracy.

bounded flows. In OpenFOAM, it is implemented as GAMMA-scheme. For each face, the local blending factor γ_f is evaluated. For this purpose, the dimensionless variable

$$\tilde{\phi}_c = \frac{\phi_{c,P} - \phi_{c,U}}{\phi_{c,N} - \phi_{c,U}} = 1 - \frac{(\nabla\phi)_f \cdot \boldsymbol{d}}{2\,(\nabla\phi)_{c,P} \cdot \boldsymbol{d}} \tag{3.20}$$

is evaluated from the values obtained in the previous timestep. The value $\phi_{c,U}$ is from the cell upstream of P and the vector $\boldsymbol{d}$ describes the distance between the respective cell centers. When the variable is $\tilde{\phi}_c < 0$ or $\tilde{\phi}_c > 1$, unboundedness has occured. As a function of $\tilde{\phi}_c$, the local blending factor is

$$\gamma_f = \begin{cases} 0 & \text{for } \tilde{\phi}_c \leq 0 \\ \frac{\tilde{\phi}_c}{\beta_\mathrm{m}} & \text{for } 0 < \tilde{\phi}_c < \beta_\mathrm{m} \\ 1 & \text{for } \beta_\mathrm{m} \leq \tilde{\phi}_c < 1 \\ 0 & \text{for } \tilde{\phi}_c \geq 1 \end{cases} \tag{3.21}$$

γ_f thus changes linearly when $0 < \tilde{\phi}_c < \beta_\mathrm{m}$, the latter of which is a globally defined constant. Throughout this work, its value is fixed to $\beta_\mathrm{m} = 0.2$. When looking at the actual implementation[4] in the code of OpenFOAM version 2.3, as shown in Appendix E, keep in mind that the input of a constant which is twice the value of β_m is required. At this point, it is worth noting, that the GAMMA scheme formulation is based on the Normalised Variables Diagram (NVD). Figure 3.8 illustrates an exemplary instantaneous distribution of the local blending factor: in most of the solution domain, surface values are interpolated using central differencing. Most notably, a maximum amount of accuracy is ensured in the boundary layer by the use of pure central differencing. Some artifacts and oscillations in the solution domain are counteracted by blending into upwind differencing. These instabilities inevitable occur at the limits of the mesh refinement zones. Nevertheless, the share of upwind differencing is kept as low as possible in order to avoid to the problems associated with numerical diffusion in LES. Note that Figure 3.8 shows cell values, which are obtained by calculating the face-weighted average for all faces adjacent to the respective cell center.

The interpolation for the advection of enthalpy in $\nabla \cdot (\rho \boldsymbol{u} h)$ is realized by the *limitedLinear* scheme, which is a Total Variation Diminishing (TVD) scheme. In general, this is the OpenFOAM implementation of a central differencing scheme stabilized by applying the limiter as introduced by Sweby (1984). The face value is calculated as described in Versteeg and Malalasekera (2007) (in general) and Jasak (1996) (in the context of OpenFOAM):

$$\phi_f = (\phi_f)_\mathrm{ud} + \psi(r) \left((\phi_f)_\mathrm{cd} - (\phi_f)_\mathrm{ud} \right) \tag{3.22}$$

This formulation is consistent with Eqn. 3.18. In this scheme, the flux limiter $\psi(r)$, corresponding to γ, is a function of

$$r = \frac{\phi_{c,P} - \phi_{c,U}}{\phi_{c,N} - \phi_{c,P}} = 2 \left(\frac{(\nabla\phi)_{c,P} \cdot \boldsymbol{d}}{\phi_{c,N} - \phi_{c,P}} \right) - 1 \tag{3.23}$$

and defined as

$$\psi(r) = 2r \tag{3.24}$$

Contrary to the GAMMA scheme, $\psi(r)$ has a lower limit of 0 (which corresponds to pure upwind differencing) and an upper limit of 1 (which corresponds to pure central differencing). Again, the implementation in OpenFOAM requires the

[4]It should be added that the implementation of the GAMMA scheme in OpenFOAM 2.3 did not yield the desired results as it does not entirely reflect the concept published in literature. For proper use in the present work, some corrections were required: In the case of $\tilde{\phi}_c > 1$, unboundedness was not detected and the scheme thus switched to full cd. This problem was fixed by multiplying $\tilde{\phi}_c$ with (-1) when larger than 1. See Appendix E for details.

input of a constant, which is chosen to obtain the formulation as described above.

All further surface interpolations are obtained by using pure central differencing. For the Laplacian terms, e.g. $\nabla \cdot (k\nabla T)$ in the energy equation, the transport coefficient is interpolated linearly and the surface normal gradient evaluated by

$$(\nabla\phi)_f = \frac{\phi_{c,N} - \phi_{c,P}}{d} \tag{3.25}$$

where d is the distance between the two cell centers. This method is applied to all orthogonal cells, which most of the grid in the present work consists of. For the non-orthogonal cells at the boundary of refinement zones, an additional explicit correction term is introduced. This term includes the cell center gradients from the previous iteration (see Jasak (1996) for details on the implementation in OpenFOAM).

For the temporal discretization of ϕ, Backward differencing is used:

$$\int_{\mathrm{V}^*} \frac{\partial(\rho\phi)}{\partial t}\mathrm{d}V = \frac{3(\rho\phi V)_t - 4(\rho\phi V)_{t-\Delta t} + (\rho\phi V)_{t-2\Delta t}}{2\Delta t} \tag{3.26}$$

While the alternative Euler implicit scheme is only first-order accurate, Backward differencing is second-order accurate. The price to pay is a significantly higher demand in memory, as all fields have to be stored twice – one field for the previous timestep $t - \Delta t$ and one field for the timestep $t - 2\Delta t$. The implementation of the Backward differencing scheme in OpenFOAM includes the possibility of time step modifications. The scheme reads as follows (Marić et al., 2014):

$$\int_{\mathrm{V}^*} \frac{\partial(\rho\phi)}{\partial t}\mathrm{d}V = \frac{c_t(\rho\phi V)_t - c_{t-\Delta t}(\rho\phi V)_{t-\Delta t} + c_{t-2\Delta t}(\rho\phi V)_{t-2\Delta t}}{\Delta t_t} \tag{3.27}$$

with the coefficients

$$c_{t-2\Delta t} = \frac{(\Delta t_t)^2}{\Delta t_{t-\Delta t}(\Delta t_t + \Delta t_{t-\Delta t})} \tag{3.28}$$

$$c_{t-\Delta t} = c_t + c_{t-2\Delta t} \tag{3.29}$$

$$c_t = 1 + \frac{\Delta t_t}{\Delta t_t + \Delta t_{t-\Delta t}} \tag{3.30}$$

yielding Eqn. 3.26 for uniform timesteps.

3.5. Initialization

For any numerical problem solved by iteration, initial conditions are required. Complex simulations are highly sensitive to small modifications in these initial conditions, see e.g. the famous work of Lorenz (1963) examining the feasibility of long-range weather predictions. Nevertheless, the numerical system in the present work is considerably more stable than meteorological simulations and can reach its quasi steady-state solution almost independently of the initialization. Using an initialization far from the final result, however, comes at high computational expenses. Generally, the most efficient way to reduce computational cost in a transient simulation is to start with a flow field that is as close to the final solution as possible. In practice, this can be achieved by using the results of a preliminary simulation, expected simulation results, or measurement data from an experiment. For the present work, a preliminary steady-state simulation for each flow case was performed. The resulting fields for velocity, temperature, and pressure were then used as initial condition for the actual transient LES. In order to avoid mapping data from one computational mesh to another, the same mesh as described in Chapter 3.3 was used for the initialization. This approach allowed the direct adoption of the respective solution vectors.

The preliminary simulations were initialized with a homogeneous velocity and temperature field, each defined by the respective inlet boundary condition. A major stability problem using this approach arose from the fact that the imposed wall temperature penetrates the computational domain at a very low speed. Consequently, as the density is a function of the temperature, a flow field mostly unaffected by buoyancy developed at first. When the lagging temperature field then started to locally influence the converging flow through buoyant effects, the solution of the momentum equation diverged. In order to avoid this problem, the coupling between energy and momentum equation was suppressed by starting the simulation with no gravity. After being en route towards convergence, i.e. when the temperature information had propagated through the boundary layer, gravity was slowly added to the case. Figure 3.9 shows the increase in gravity for the different cases. For a low Re and moderate Gr number, the temperature information penetrates the solution domain rather quickly. The increase in gravity could thus be started after 1000 iterations – however, due its high influence, at a moderate rate of $0.002\,\mathrm{m/s^2}$ per iteration. The same rate was applied for the case with moderate Re and high Gr numbers, stating after 1300 iterations. For high Re and moderate Gr numbers, the increase was also initiated after 1300 iterations. As the influence of buoyancy is limited, the increase rate could be considerably higher ($0.005\,\mathrm{m/s^2}$ per iteration). The strategy for the two-dimensional validation cases (which will be described in the following section) is also shown in Figure 3.9: For the case with gravity in

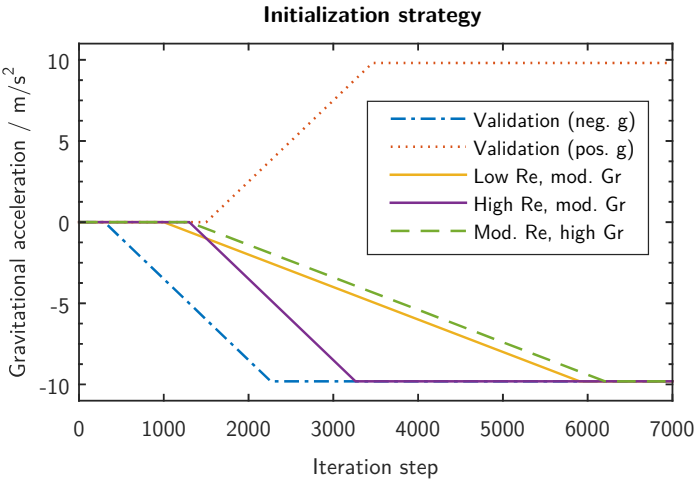


Figure 3.9.: Initialization strategy for the preliminary simulations. Depending on the flow configuration (Re and Gr number), gravity is increased at different rates and after a different numbers of iterations.

negative y-direction, the influence of buoyancy is in flow direction. This allowed a high increase rate at an early time. For the case with gravity in counter-flow direction, the increase was started after 1500 iterations with a rate of $0.005\,\mathrm{m/s^2}$ per iteration.

The modified solver used for the initialization is based on OpenFOAM's *buoyantSimpleFoam*. Figure 3.10 shows a flow diagram of the solver, whose sequence – in general – resembles the one shown above for the PIMPLE solver. However, as the initialization solver is steady-state, all temporal effects drop out. The implicit momentum predictor and the subsequent solution of the energy equation both use the PBiCG linear solver. In the pressure correction, after evaluating the thermodynamical density and updating $\boldsymbol{H}(\boldsymbol{u})$ and a_P (see Appendix A), the pressure equation is solved. For the reasons discussed in Appendix A, this operation is performed by the GAMG multi-grid solver. Fluxes and velocities are afterwards explicitly corrected for the next momentum predictor. During the calculations, all solution fields are under-relaxed with $\alpha = 0.3$. Without having an influence on the simulation, the continuity condition is evaluated and – as long as convergence would not be reached – the loop is repeated. The linear increase in gravity is incorporated within the SIMPLE loop. Before the momentum prediction is performed, the field of gh (in the present

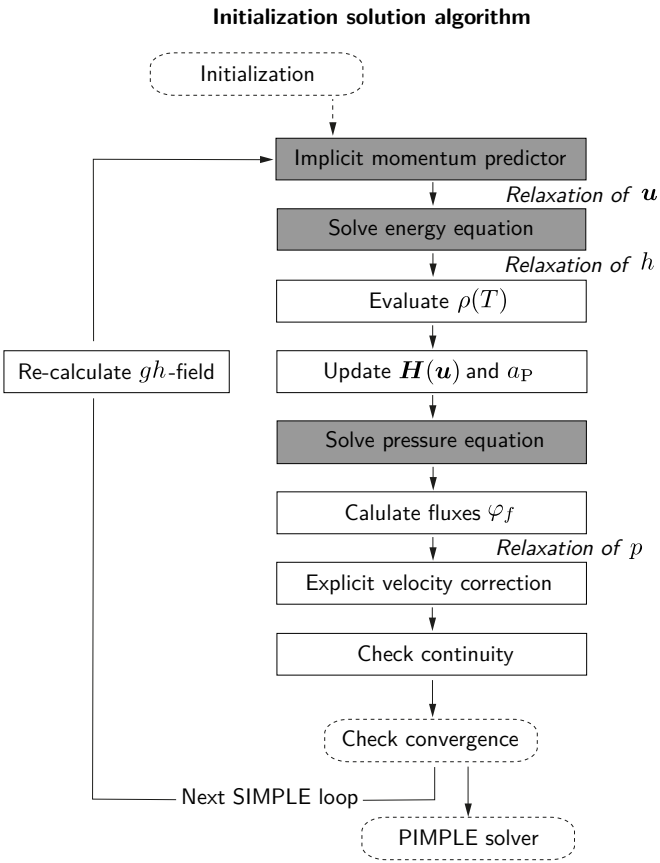


Figure 3.10.: Flow diagram of the modified SIMPLE solution algorithm used for the preliminary simulations. Each step featuring a linear solver is marked in grey.

coordinate system gy) is recalculated and stored. This implies that the field is reevaluated after each iteration during the linear rise of the gravity.

All preliminary simulations were conducted without any turbulence modeling. For the LES, the initial condition of the subgrid-scale turbulent kinetic energy field was estimated based on the final velocity field of the preliminary simulation. For this purpose, a turbulence intensity of 5% was presumed and the total turbulent kinetic energy evaluated for each cell (Eqns. 3.10 and 2.16). Hereof, a share of 20% was imposed as initial condition for k_{sgs}, consistent with the requirement of LES.

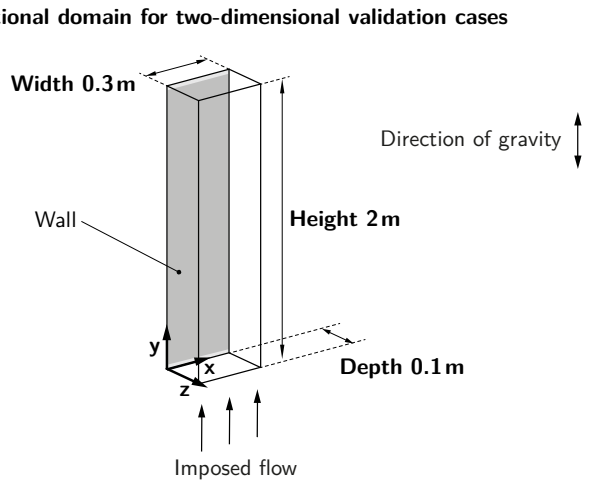


Figure 3.11.: Schematic of the computational domain for the two-dimensional flow cases.

3.6. Qualitative validation and evaluation methods

In this section, the question whether the numerical methods discussed in the previous sections are suitable for the investigation of mixed convection will be addressed. This includes in particular two points: The use of LES with the one-equation subgrid-scale model for the turbulence effects, and the grid resolution (equivalent to the LES filter width) in the near-wall region. The general approach for a validation is to apply the simulation method to a setup for which results are existent in literature. As discussed before, such results lack for three-dimensional mixed convection. Consequently, simulations of two-dimensional mixed convection were performed using the present computational methods. Three different approaches are used to evaluate their suitability: First, the DNS results of Abedin et al. (2012a) serve as a qualitative comparison. Second, the LES results are interpreted in terms of physical meaning, and third, the results are evaluated in terms of numerical consistency (i.e. whether all scales of relevance are resolved). A major advantage of using two-dimensional mixed convection is that this simpler flow also allows to determine the shortcomings and limitations of the simulation method. Consequently, the simulation results will be evaluated using the same methods as later on for the three-dimensional cases. The present section thus allows to introduce and discuss these evaluation methods by providing a look into the physics of the two-dimensional flow.

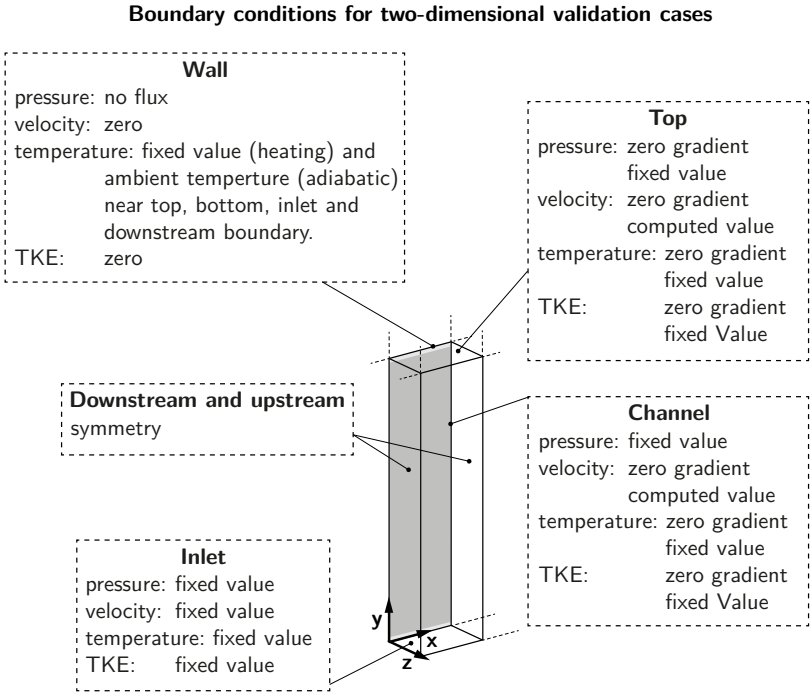


Figure 3.12.: Boundary conditions for the two-dimensional validation cases.

Even though the flow cases discussed in this section are two-dimensional, a three-dimensional computation is required to account for turbulence effects. Figure 3.11 illustrates the computational domain: The volume dimensions are 0.3 m in spanwise (x) and 0.1 m in wall-normal (z) direction, the latter corresponding to the depth of the three-dimensional simulation cases. A flow is imposed in vertical (positive y) direction and the constant-temperature wall stretches to a height of 2 m. This height is required to obtain high values of the Grashof number. For the LES, the disadvantage of an elevated height – apart from the large size of the mesh – is the long simulation time needed to reach a quasi steady-state condition. The effect of buoyancy is introduced to the simulation by adding gravity in vertical direction. Gravity being aligned in the flow direction results in an opposing flow, while gravity in negative y-direction causes an aiding flow.

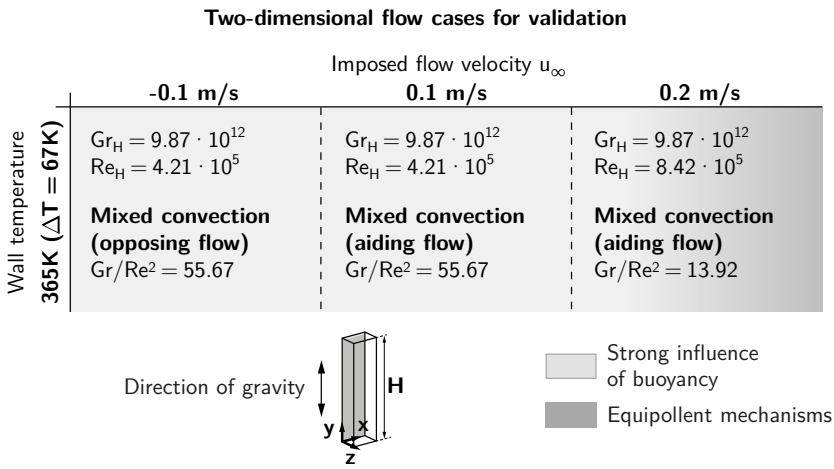


Figure 3.13.: Overview of the simulation cases for qualitative validation.

The numerical setup is identical to the three-dimensional cases, i.e. the near-wall grid resolution is the same as discussed in Chapter 3.3 and the thermophysical properties of Chapter 3.1.2, are used. However, due to the different nature of the flow, some boundary conditions had to be adapted (see Figure 3.12 for an overview): The two-dimensional flow case allows to replace the upstream and downstream boundary condition by symmetry. The imposed flow enters the domain through the bottom, which is referred to as the inlet. Contrary to the three-dimensional simulations, no synthetic turbulence is imposed on the flow of the validation cases, as this has also not been the case in the literature. For the opposing flow, fluid leaving the domain through the bottom is permitted by changing the boundary conditions to an inlet/outlet (fixed value/zero gradient) type. Fluid entering the domain through the top is taken into account through the same complex boundary condition used for the channel in the three-dimensional case.

Three simulations have been performed, as shown in Figure 3.13, each with a wall-fluid temperature difference of $\Delta T = 67\,\mathrm{K}$ (corresponding to $\mathrm{Gr} = 9.87 \cdot 10^{12}$ in the domain described above): One aiding flow case with a moderate imposed velocity of $0.1\,\mathrm{m/s}$ (corresponding to $\mathrm{Re} = 4.21 \cdot 10^5$), resulting in a Richardson number of 55.56. This case is thus classified as buoyancy-dominated. The setup has been duplicated for the second case, but the inlet velocity was doubled ($0.2\,\mathrm{m/s}$ or $\mathrm{Re} = 8.42 \cdot 10^5$). For the second case, the Richardson number is 13.92, indicating less influence of buoyancy. The third case is an opposing

flow case with the same parameters as the first aiding case. However, as buoyancy accelerates the boundary layer in the opposite direction, the Richardson number no longer is a valid measure for the influence of buoyancy. This flow case is expected to be dominated by turbulence due to the high shear stress between the boundary layer and the free stream. All dimensionless numbers in Figure 3.13 have been evaluated with the height as the characteristic length scale.

In Chapter 2.2.2, the challenges related to the numerical investigation of mixed convection were introduced. In the simulation of two-dimensional flow cases, the problem of different scales (large domain size and small boundary layer) can be addressed through two different approaches:

Time-developing boundary layers: Imposing periodic boundary conditions at the inlet and outlet (top and bottom) allows to reduce the computational domain to a minimum flow cell. Instead of considering a large fluid volume with a fixed coordinate system, the flow in a short fluid volume is simulated. The influence of the free stream is introduced either by imposing a moving-wall boundary condition or by adding a source term to the momentum equation. When running the simulation, the boundary layer in the small volume thus develops over time. Physically, this approach can be understood as the tracking of a fluid volume on its flow along a surface. However, for a given time, the varying velocity for different wall-normal positions in the boundary layer results in a different numbers of domain passes. From this numerical configuration follows that the height as the characteristic length scale is no longer available.

The work of Abedin et al. (2012a), used as a comparison for the present simulations, features the time-developing approach. The authors introduced the boundary layer integral thickness δ_1 (see Eqn. 2.56) as a characteristic length in all dimensionless numbers. Consequently, Re_{δ_1} not only describes the flow, but is severely influenced by the boundary layer thickness as well. Therefore, a growing boundary layer, e.g. caused by a higher influence of buoyancy, would increase the Reynolds number as well – an effect that is not present for Re_L. As a consequence, a certain Re_{δ_1} does not allow to draw conclusions concerning the actual flow velocity. Quantitatively comparing cases characterized by Re_{δ_1} is therefore only valid to show the relative influence of the flow within Abedin's study. The same applies to Gr_{δ_1} and Nu_{δ_1}.

Space-developing boundary layers: Here, the domain size is not reduced, the boundary layer development thus occurs spatially. This is the intuitive approach, as it numerically reproduces the physical setup required for the experimental investigation of mixed convection. The required domain size

is therefore significantly larger than for the time-developing approach. The case is characterized by $\mathrm{Re_L}$, $\mathrm{Gr_H}$, and $\mathrm{Nu_{LH}}$.

As discussed above, three-dimensional mixed convection flow cases cannot be reduced to a minimum flow cell. Consequently, all simulations of the present work – including the two-dimensional cases performed for the purpose of qualitatively validating the computational method – feature the space-developing approach as well.

In literature, no space-developing simulations of two-dimensional mixed convection suitable for the validation of the present computational method exist. Consequently, the time-developing results of Abedin et al. (2012a) are the best available option. Comparing their results to the ones of the present work therefore allows a qualitative, but no quantitative validation. In the following section, it will be shown that the present results are plausible and that all physical effects described by Abedin are correctly resolved in the LES. Quantitatively comparing the results of a space-developing and a time-developing simulation for validation would be problematic, mainly because of two reasons: First, the numerical approach to the physical problem is different, prohibiting a one-to-one comparison. Second, the characteristic numbers describing the problem are incompatible. A transformation of time-developing numbers (referred to δ_1) to space-developing results (referred to H) has been derived by Abedin et al. (2012a). This transformation, however, is based exclusively on natural convection experiments and furthermore only applies to the Grashof and Nusselt number, and not to the Reynolds number. The inverse transformation (from space-developing numbers to time-developing numbers) is generally possible by scaling to δ_1 as well. It should be noted, however, that the boundary layer thickness is not known a priori. Therefore, when setting up the two-dimensional cases of the present work, an educated guess for the required temperature difference, the flow velocity and the domain height was necessary. The maximum values that numerical stability and computational resources would permit were chosen, resulting in the characteristic numbers introduced above. It is evident that – due to the high influence of δ_1 – the values of Gr_{δ_1}, Re_{δ_1} and their ratio do not match the literature values.

3.6.1. Aiding flow

The results of the two simulation cases for two-dimensional mixed convection with an imposed aiding flow have been obtained in a sampling period of 17.5 sec duration. This period is long enough to ensure that the dataset is sufficiently large to perform a valid averaging. Besides convergence, a quasi steady-state of the simulations was reached before starting data sampling. At 21 different locations, set in a streamwise y-distance of 0.1 m, raw profiles in wall-normal direction of all relevant physical and numerical results $\phi = f\left(x_0, y_0, z, t_i\right)$ were

stored after each timestep i. This includes the local results of velocity, pressure, temperature, density, and k_{sgs}, which were all sampled at each cell in wall-normal direction. These profiles also allowed the derivation of wall-normal gradients $\partial\phi/\partial z$ and second derivatives $\partial^2\phi/\partial z^2$ through central differencing. For the evaluation of the corresponding gradients $\partial\phi/\partial y$ and $\partial\phi/\partial x$, additional profiles in $\pm 4\,\text{mm}$ streamwise and spanwise distance[5] from the sampling point were stored.

Figures 3.14 and 3.15 show instantaneous fields of the converged, quasi steady-state simulation results. The fields are the vertical velocity and the temperature on a slice at the center of the domain (see sketch for illustration). The imposed flow enters at the bottom and leaves at the top, the wall is located to the left. Figure 3.14 on the left side represents the low-velocity case, and Figure 3.15 on the right side the high-velocity case. In both cases, the coupling between temperature and vertical velocity through the buoyant updraft is obvious, as distinct structures in the temperature and velocity fields match (see left figure, where matching structures are pointed out).
In the low-velocity case, a stratified boundary layer for the temperature and the velocity is highlighted. For the temperature, the highest value occurs at the wall. Throughout the boundary layer, the temperature drops sharply until reaching the value of the free stream. The corresponding velocity at the wall is zero, complying with the no-slip condition. An acceleration due to the buoyant forces can be observed, with velocities exceeding the imposed velocity in the free stream. First instabilities in both fields start to develop at approximately 1/2 of the domain height ($y = 1\,\text{m}$, $\text{Re}_y \approx 2.1 \cdot 10^5$). They grow in intensity to about 3/4 of the domain height ($y = 1.5\,\text{m}$, $\text{Re}_y \approx 3.2 \cdot 10^5$), where the flow starts to transition into a turbulent state. The fields at the top of the domain clearly show a turbulent boundary layer.
The general image for the high-velocity case shown in Figure 3.15 is the same. However, no instabilities develop until the flow starts to transition at approximately 3/4 of the domain height (corresponding to $y = 1.5\,\text{m}$, $\text{Re}_y \approx 6.3 \cdot 10^5$). Obviously, the higher imposed flow velocity dampens the instabilities. This observation is in accordance with the findings from other authors, as discussed in Chapter 2.3.1, where this particular effect is referred to as laminarization. Compared to the low-velocity case, the transition to a fully turbulent state appears to occur at a faster rate, which is not surprising given the significantly higher Reynolds number.

The influence of buoyancy on the boundary layers of velocity and temperature is shown in the Figures 3.16 and 3.17. At the top, respectively, the local average vertical velocity is plotted as a function of wall-normal distance. Below, the

[5] This distance is defined by the resolution in the outer regions of the domain.

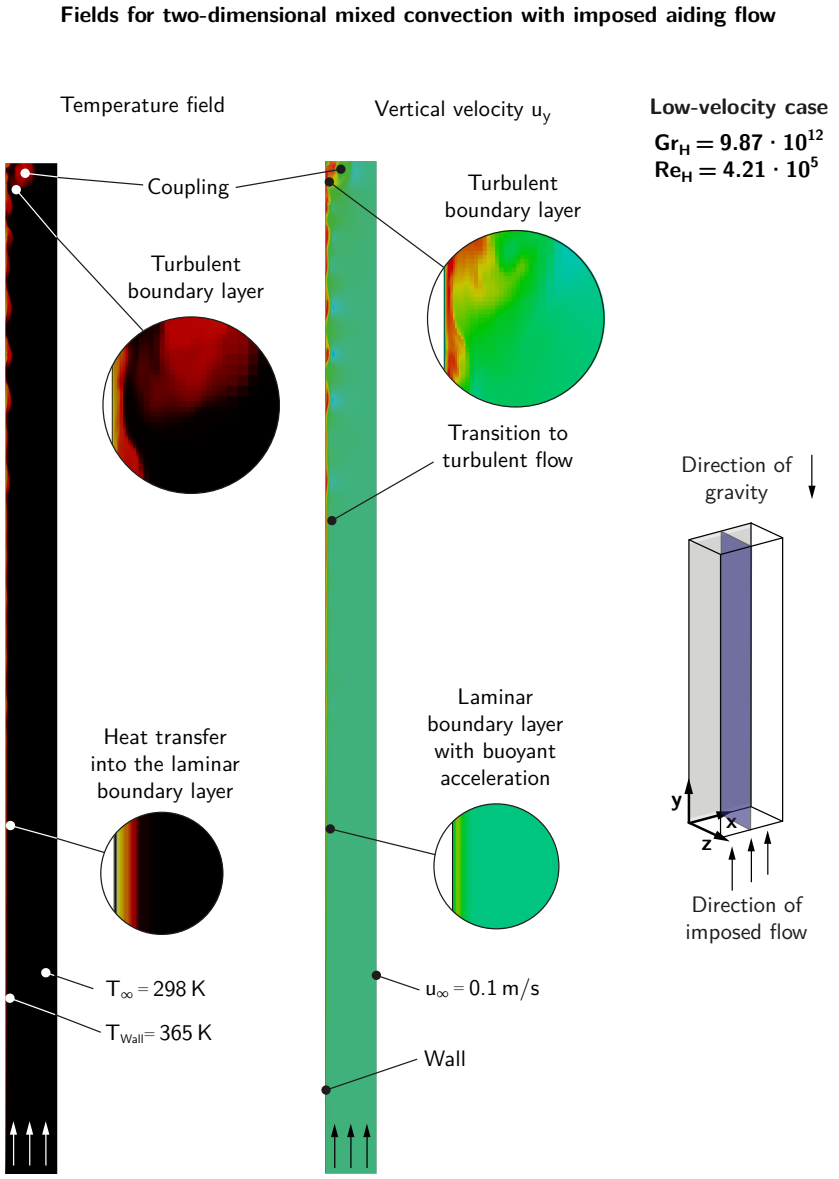


Figure 3.14.: Simulation results showing the instantaneous fields of temperature and velocity in a vertical slice at the center of the low velocity aiding flow case (*see figure on the right for the colormap legend*). Note the strong coupling between the two fields.

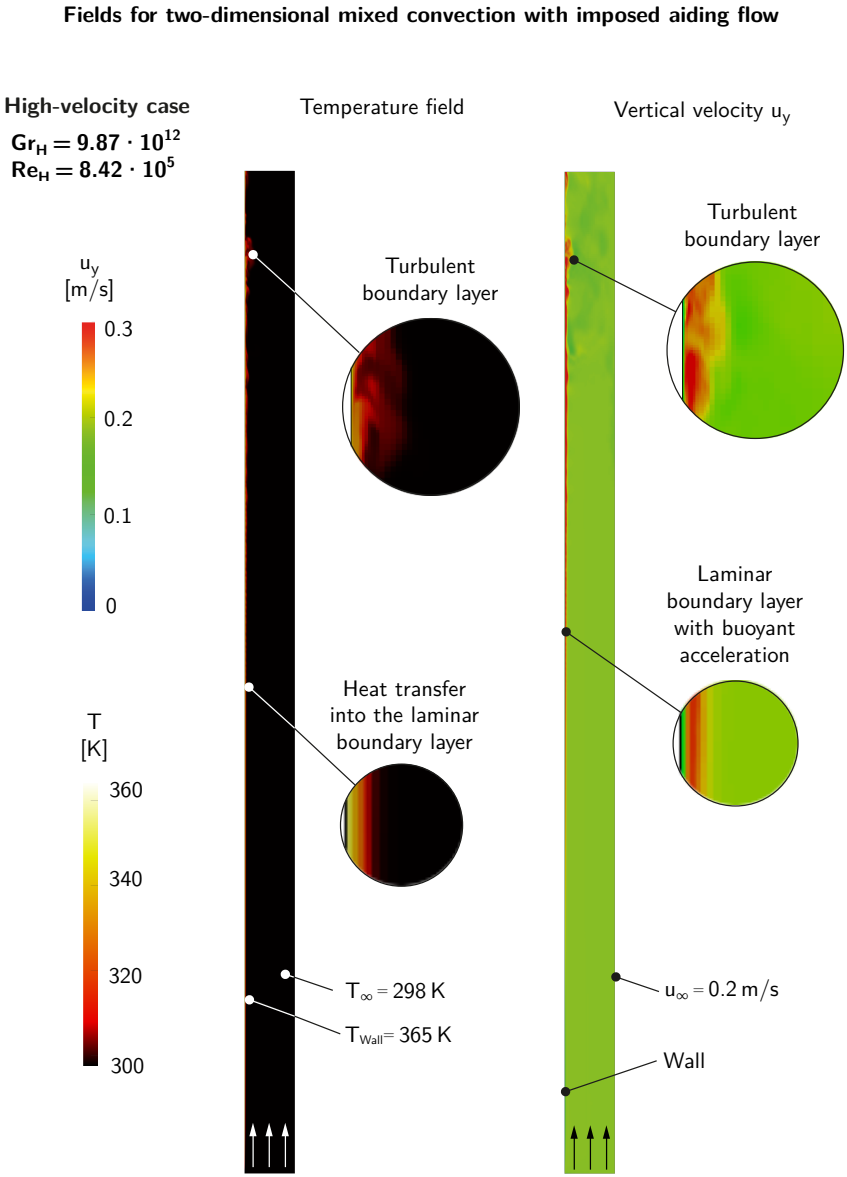


Figure 3.15.: The same fields as on the left side for the high-velocity aiding flow case. A comparison of the two cases clearly shows the laminarization effect where transition to a turbulent state is delayed for a higher velocity flow.

average temperature profile is shown. In both figures, the average is timestep-weighted:

$$\overline{\phi}_{\text{avg}} = \frac{\sum_i \phi \Delta t_i}{t_{\text{end}} - t_{\text{start}}} \tag{3.31}$$

Each line represents one distinct height from 0.1 m (close to the inlet at the bottom) to 1.9 m (close to the outlet at the top) in steps of 0.3 m.

The first set shows the boundary layer profiles for the low-velocity case. At the bottom of the domain (lowest line), the velocity is unaffected by buoyancy and exhibits the profile expected for a flow over a flat plate: The velocity at the wall is zero, then steeply increases. Its gradient $\partial u_y / \partial z$ steadily decreases with wall distance, until the flow eventually reaches free-stream velocity. At this position of the domain, the boundary layer is very thin as it just started to develop. The same is the case for the temperature boundary layer. The corresponding temperature profile therefore is very steep in wall proximity, which results in a high heat flux. This heat rapidly increases fluid temperature, causing a change in density and thus a buoyant force in vertical direction. However, the forces of this updraft act against the viscous forces that slow down the fluid at the wall. With growing height, the temperature increase propagates further away from the wall where the viscous forces have less influence. Consequently, a distinct hump in the vertical velocity starts to develop. As the temperature boundary layer grows in vertical direction, the velocity hump grows as well – both in intensity and size. Eventually, this region of the boundary layer exhibits velocities that outreach the free-stream velocity by a factor of 2.5. The transition to turbulence can be observed in both the temperature and the velocity profile: The magnitude of the velocity hump stops to increase and eventually even decreases. However, the boundary layer thickness massively grows. The same is observed for the temperature profile, where the temperature drops in the inner part of the boundary layer and rises in the outer part. Note that the near-wall temperature gradient significantly increases, resulting in a higher heat flux, which is well-known from literature. The shaded areas in the figures enclose all fluctuations $\phi' = \phi - \overline{\phi}_{\text{avg}}$ that ever occurred during the simulation at the top-end of the domain, clearly indicating a highly turbulent flow state.
The corresponding spatial boundary layer evolution for the high-velocity case is shown in Figure 3.17. In general, the profiles resemble the ones of the low-velocity case. However, some differences can be observed: Referred to the free-stream velocity, the peak in vertical velocity is less prominent. Also, it does not decrease when reaching turbulent flow state, which indicates that the mechanisms triggering the transition differ from the other case. Compared to the low-velocity case, fluctuations – both in velocity and in temperature – are less intense and both boundary layers are significantly thinner.

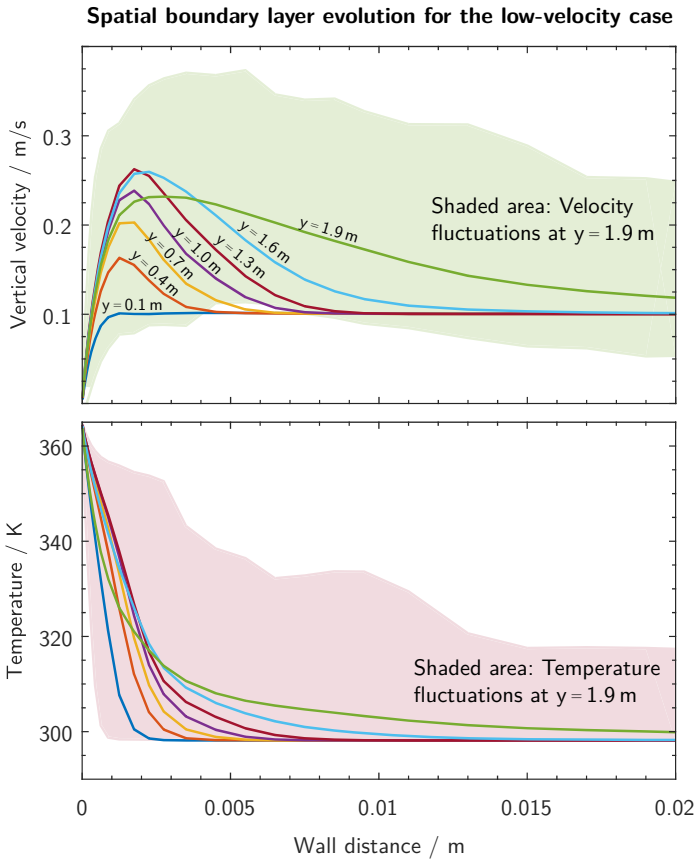


Figure 3.16.: Spatial evolution of the velocity and temperature boundary layer for the low-velocity case. Shown are the profiles between a height of 0.1 m and 1.9 m in steps of 0.3 m. The lines represent the time-averaged values and the shaded area the fluctuations at the upper end of the domain.

These observations lead to the following conclusion, which is backed by literature (see discussion in Chapter 2.3.1): The influence of buoyancy is significantly higher for the low-velocity case, even though the Grashof number is the same for both. This higher influence results in instabilities, which are reflected in the high magnitude of fluctuations and can also be observed in the flow fields above. Clearly, the cause of these instabilities is the high amount of shear created by the velocity difference between the hump and the free stream. The instabilities

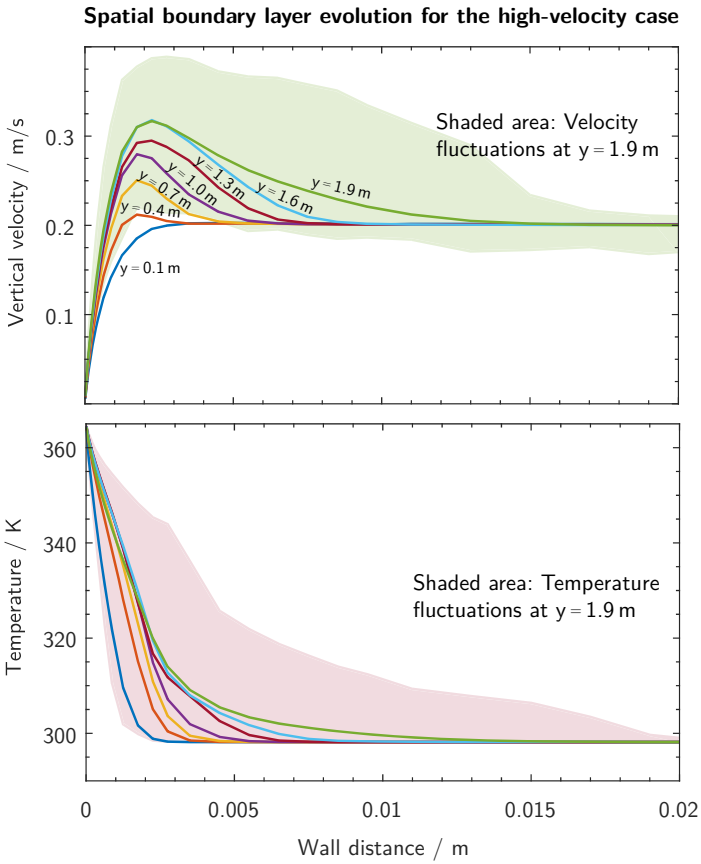
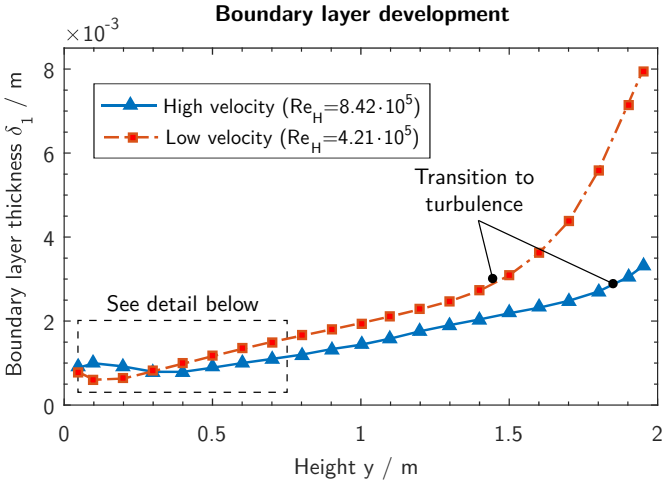
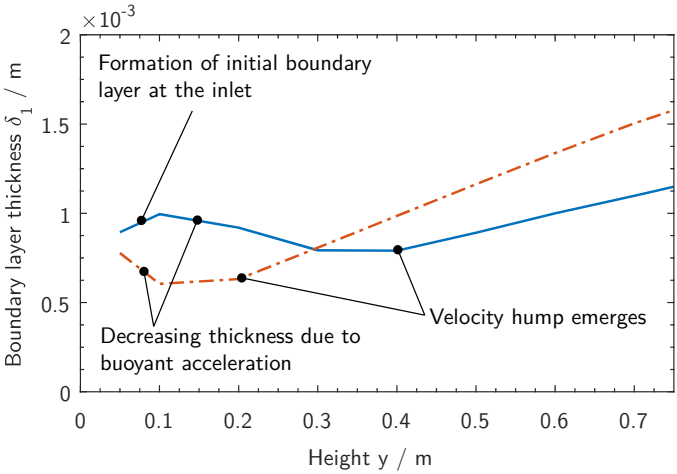


Figure 3.17.: Spatial evolution of the velocity and temperature boundary layer for the high velocity case. The choice of profiles and the coloring is the same as in Fig. 3.16. However, the fluctuations at the top of the domain are significantly less strong than in the low-velocity case.

are suppressed in the high-velocity case, where this velocity difference is less significant. Counterintuitively, this means that the higher velocity actually stabilizes the boundary layer. Further into the discussion of the results, it will be shown that this effect also reduces the heat transfer rate. From the velocity profiles, it can already be derived that the instabilities in the low-velocity case have an influence on the transition to turbulence (this will be reviewed in detail when turbulent coherent structures are discussed later on in this section).



(a) Evolution of the boundary layer over the entire plate



(b) Detail view of the decreasing boundary layer thickness near the inlet

Figure 3.18.: Evolution of the two-dimensional mixed convection velocity boundary layer: The high-velocity case exhibits a later transition to turbulence which is due to laminarization. The lower detail view shows the decrease in boundary layer thickness near the inlet for both cases, caused by buoyant acceleration. However, the boundary layers subsequently start to grow when the distinct hump in the velocity profile emerges (see following Figure 3.19).

In the following, the local thickness of the boundary layer will be used as a scaling parameter for the wall-normal distance. In order to have a physically meaningful measure, the displacement thickness δ_1 was introduced before (see Eqn. 2.56 and its discussion in Chapter 2.1.4). As the temperature and the velocity boundary layer interact, both will be scaled with the same parameter. Figure 3.18 shows the boundary layer thickness as a function of height for the high-velocity and the low-velocity case, respectively. The evolution of δ_1, shown in Figure 3.18(a) is in line with the velocity profiles discussed above, where transition to turbulence led to a significant increase in thickness. For the low-velocity case, this increase occurs at a lower height than for the high-velocity case. In general, the case with the higher influence of buoyancy – the low-velocity case – features a higher boundary layer thickness.

It may seem surprising at first sight that the boundary layer thickness decreases to a global minimum at the bottom of the domain before starting to increase again. Figure 3.18(b) provides a detail view of δ_1 this region. For the high-velocity case, the boundary layer thickness slightly grows within the first centimeters of the domain, which is attributed to the formation of a boundary layer at the inlet, where a uniform flow velocity was imposed[6]. At 0.1 m height, the boundary layer starts to thin. The onset of regrowth is located at approximately 0.4 m domain height. The same effect can be observed even more distinct for the low-velocity case at a domain height of $y = 0.1\,\mathrm{m}$ to $y = 0.2\,\mathrm{m}$.
In order to explain this rather unexpected behavior, a detailed look at the velocity profiles in this region is required. Figure 3.19 provides a detailed view of the average profiles close to the inlet. For both cases, the boundary layer flow within 2 mm of the wall experiences buoyancy-caused acceleration (compare profiles at 0.05 m and 0.1 m for the low-velocity case and profiles at 0.1 m and 0.3 m for the high-velocity case). The resulting higher velocity increases the mass flow in the boundary layer, which then is reflected in a lower displacement thickness. Also, when examining the velocity gradient $\partial u_y/\partial z$ in the figure, the reduction in boundary layer thickness becomes apparent, as the entire profile appears to move closer to the wall. This development eventually comes to a halt when parts of the boundary layer become faster than the free stream. Consequently, the distinct velocity hump emerges and the boundary layer starts to regrow.

In Figure 3.20, the characteristic numbers based on local boundary layer thickness are evaluated for the present space-developing simulations. The dashed line represents the values Abedin et al. (2012a) obtained in their time-developing simulation. The figure on top shows the Grashof number that scales with δ_1^3 and is thus very sensitive to the boundary layer thickness. The Reynolds number

[6] Unfortunately, the spatial sampling resolution for the average values does not allow to examine the same effect in the low-velocity case.

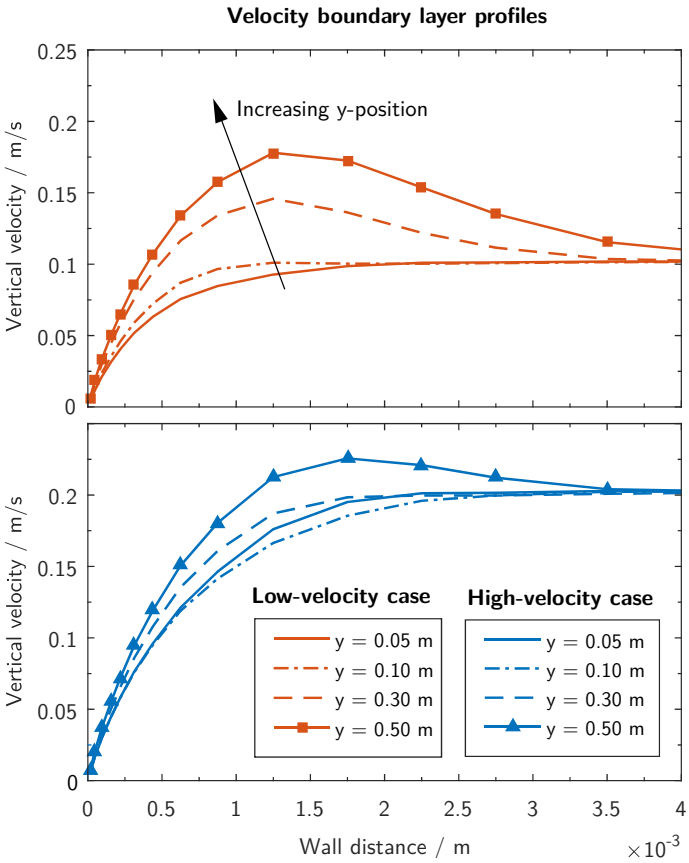


Figure 3.19.: Profiles of the vertical boundary layer velocity at the bottom region of the domain. The buoyant acceleration decreases the boundary layer thickness, before it regrows when the distinct hump starts to develop. In the high-velocity case, inlet effects cause an initial increase, before it eventually also decreases.

shown at the bottom scales linearly with δ_1 and is therefore less sensitive to variations in boundary layer thickness. The maximum Reynolds number obtained in both simulation cases at the top of the domain matches the values of Abedin's simulation. Please keep in mind that, when Re_{δ_1} of both cases match, the boundary layer thickness of the low-velocity case must be twice the value of the high-velocity case. The corresponding Gr_{δ_1} then varies by the factor of eight.

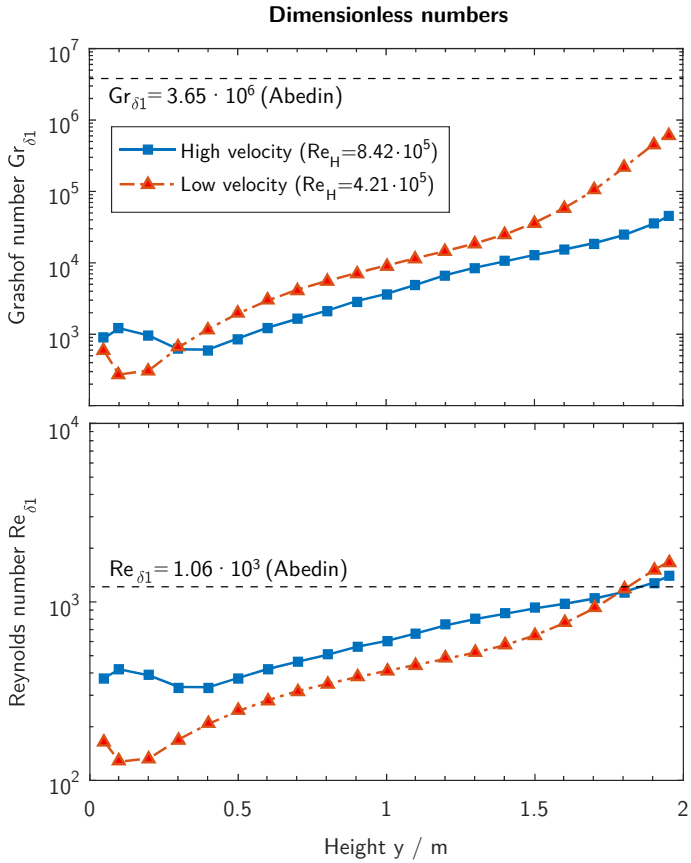


Figure 3.20.: The dimensionless Grashof number Gr_{δ_1} and Reynolds number Re_{δ_1} of the present space-developing simulations as a function of the height y. The values of the time-developing DNS simulations by Abedin et al. (2012a) are marked, showing that the studies differ in the Grashof number while the Reynolds numbers are in the same range at the top of the present domain.

In the following, the results of the present LES are compared to Abedin's DNS. Figure 3.21 presents the boundary layer profile for the average velocity in the low-velocity case (top) and in the high-velocity case (bottom). The velocity is scaled to the difference between the local maximum velocity and the local minimum velocity. The profile is a function of the dimensionless wall distance, scaled to the local boundary layer thickness δ_1. The velocity is sampled at

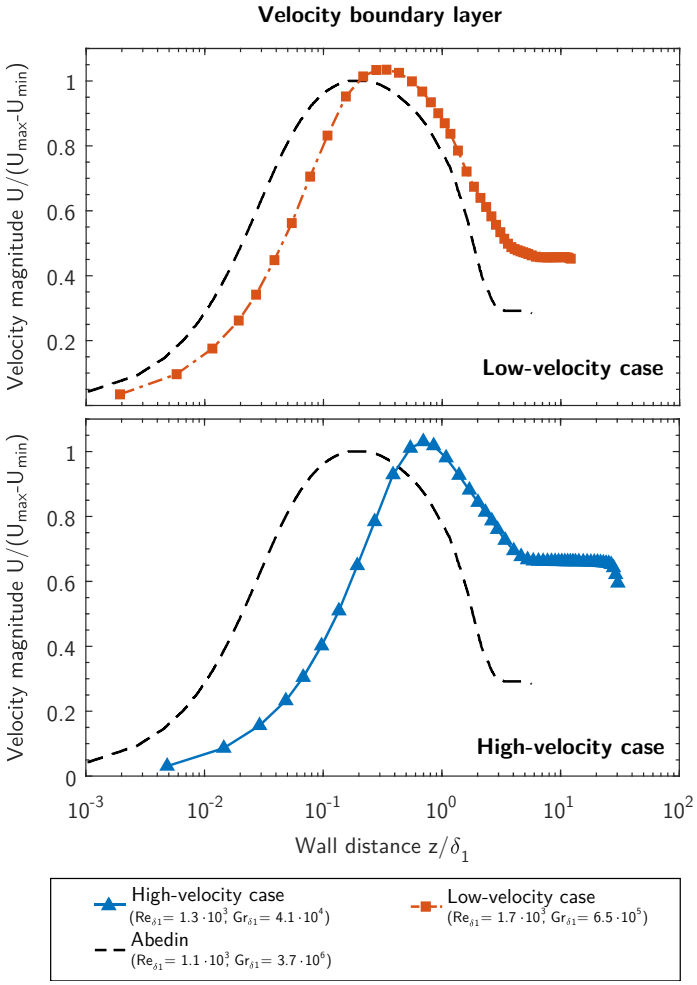


Figure 3.21.: The dimensionless boundary layer velocity as a function of the dimensionless wall distance for the low-velocity case (top) and the high-velocity case (bottom), for DNS (Abedin et al., 2012a) and the present LES.

the top of the domain, respectively. The markers on the lines indicate the respective cell centers and thus give an idea of the boundary layer resolution. The present simulations successfully reproduce the general profile shape of the DNS results, with a distinct hump formed by the buoyant acceleration. This

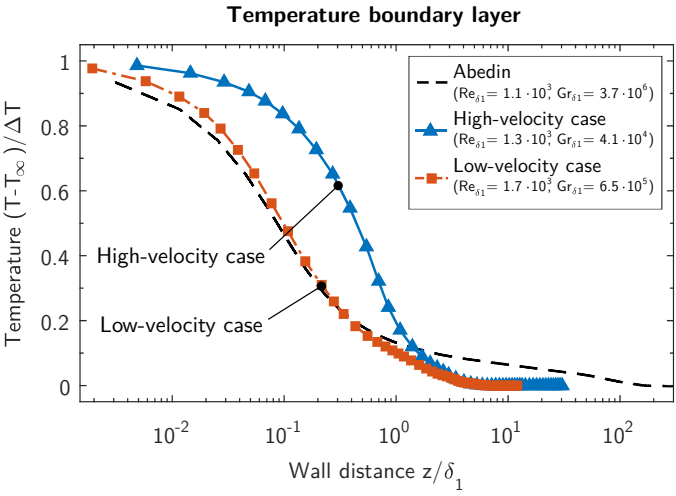


Figure 3.22.: Temperature profiles at the upper end of the domain in comparison to the DNS simulation by Abedin. The present simulation is capable of reproducing the general shape of the profile. However, as the turbulent boundary layer is not yet fully developed, deviations in the outer region occur.

hump features a high degree of symmetry in logarithmic scaling (i.e. for the low-velocity case). However, a general shift to the right is apparent. When looking at the low-velocity case, it can be observed that the LES and DNS profiles approach for smaller differences in Gr_{δ_1}, linking the shift to a difference in the boundary layer thickness.

The corresponding profiles for the temperature boundary layer (same positions, same legend) are shown in Figure 3.22. Here, the difference between the local temperature and the free-stream temperature is scaled to the maximum temperature difference. The strong influence of Gr_{δ_1} discussed above is underlined by the fact that the profile of the low-velocity case agrees very well with the DNS data. In the outer region, the typical bend caused by coherent structures in turbulent boundary layers, is captured by the LES. As the boundary layer for the high-velocity case has just transitioned into a fully turbulent state at the top of the domain, its temperature gradient deviates in the outer region. Like for the velocity boundary layer, the profile of the high-velocity case is shifted to the right, resulting in an apparently steeper gradient. However, keep in mind that the axis is logarithmic and dimensionless. Nevertheless, in the region close to the wall, the gradients of both cases seem to be less steep than for the DNS data. This could be an indication, that the subgrid-scale model adds diffusive

heat transport in that region – even though the transport coefficient should converge towards zero. Contributing is also the fact, that Abedin's fluid featured a Prandtl number of $\mathrm{Pr} = 6.0$ whereas the present simulation was performed for $\mathrm{Pr} = 3.02$ (see Chp. 3.1.2 for discussion).

Above, the profiles obtained by averaging over the entire sampling period have been presented and compared to the respective literature values. By the nature of averaging, fluctuations are not included, however, are of high relevance for turbulent flows. In the two-dimensional mixed convection cases, the fluctuations are evaluated in vertical and in wall-normal direction. Similar to Eqn. 3.31, the mean fluctuations are evaluated by

$$\overline{\phi}'_{\mathrm{avg}} = \frac{\sum_i \left(\phi - \overline{\phi}_{\mathrm{avg}}\right) \Delta t_i}{t_{\mathrm{end}} - t_{\mathrm{start}}} \tag{3.32}$$

Figure 3.23 shows the average value of the absolute fluctuations in vertical velocity $\overline{u}'_y$ (top) and in wall-normal velocity $\overline{u}'_z$ (bottom). The black dashed line shows the respective fluctuations in literature data. All profiles are scaled to the maximum difference in local average velocity and the wall distance is referred to the local boundary layer thickness. The general observation in the figure is that the present LES resolves the fluctuations to a similar extent as the DNS. Even though the numerical approach and the case setups are different, the general shape and size of the profiles, as well as the region of their occurrence are in qualitative agreement. Furthermore, the LES captures all relevant effects that can be derived from the DNS: $\overline{u}'_y$ is more intense and reaches further to the wall than $\overline{u}'_z$. Towards the wall, the magnitude of all fluctuations reduces and converges toward zero in the viscous sublayer.
Differences in this reduction occur at $z/\delta_1 \approx 4 \cdot 10^{-2} ... 2 \cdot 10^{-1}$ (vertical direction) and $z/\delta_1 \approx 2 \cdot 10^{-1} ... 10^{0}$ (wall-normal direction), where the DNS profiles decrease linearly while the LES profiles exhibit a more or less steeper decent. The reason for this difference is that the turbulent length scales in this region start to become smaller than the LES filter size. Consequently, small-scale fluctuations are not resolved, but their influence is taken into account through the subgrid-scale model. This is reflected in a local increase in the subgrid-scale turbulent kinetic energy (see Figure 3.32 and Eqn. 2.46 for the corresponding transport equation). As the TKE is a scalar and therefore includes the fluctuations in x, y and z directions, its value cannot directly be compared to the intensity of the fluctuations. Nevertheless, the elevated values in TKE point out the regions, where turbulent effects are modeled rather than being resolved.
In both directions, the fluctuations of the low-velocity case are higher than the ones of the high-velocity case. This reflects the occurrence of instabilities discussed above and shows their significant impact.

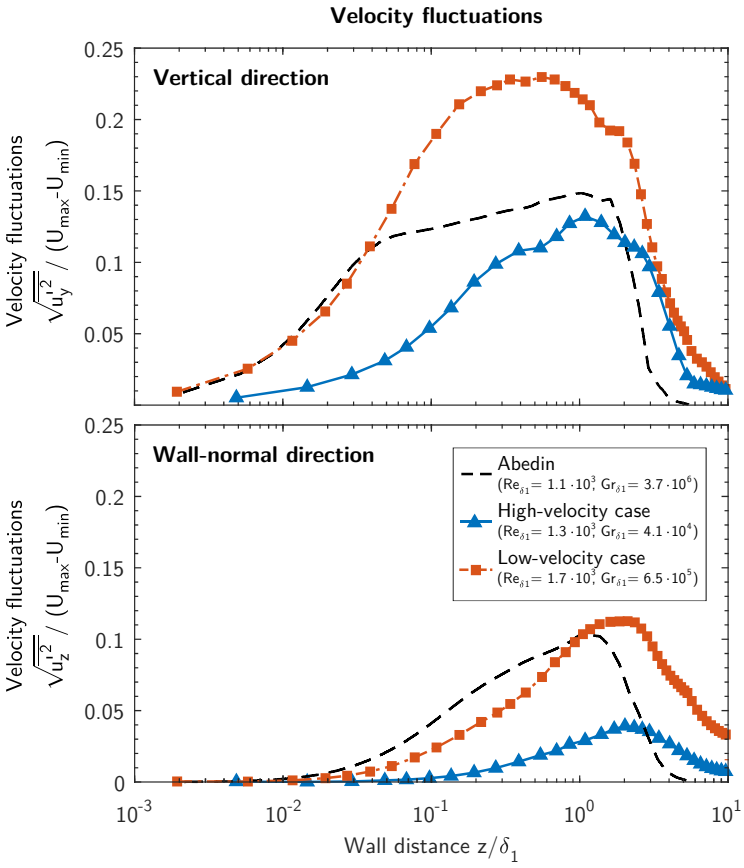


Figure 3.23.: Profile of the resolved average velocity fluctuations, compared to the time-developing DNS results by (Abedin et al., 2012a).

The average fluctuations in the temperature as a function of wall distance are shown in Figure 3.24. The profiles agree in shape and size, i.e. the slow decrease in the outer region as a result of coherent structures is reproduced by the LES. The shift to the right is not surprising as it has been observed in all profiles above. As discussed, the shift is the result of varying scaling and characteristic numbers caused by the different numerical approaches (space-developing vs. time-developing). Compared to the velocity fluctuations, the shift appears more prominent in the temperature fluctuations. This, however, is attributed to their occurrence at lower values of z/δ_1 and the logarithmic scaling in the figure.

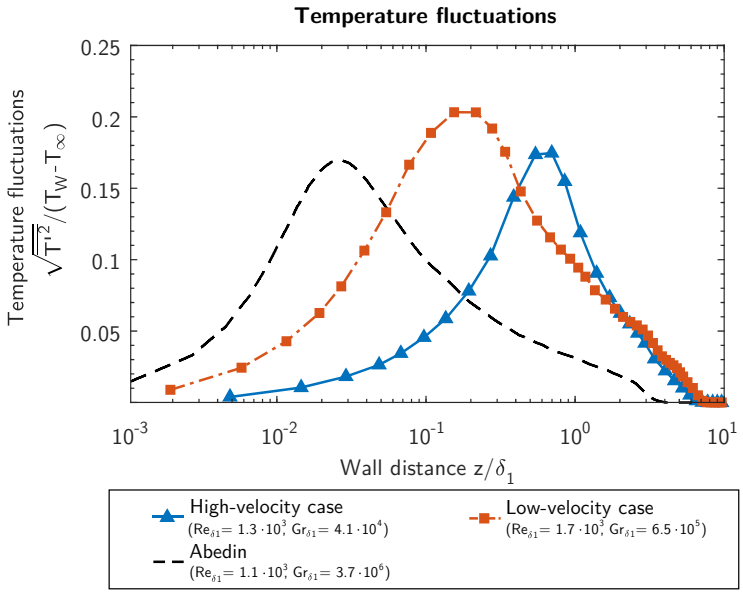


Figure 3.24.: Profile of average temperature fluctuations, in comparison to DNS (Abedin et al., 2012a). The shape of the profiles is in good agreement. However, a general shift to the right is the result of the different numerical approach and the resulting variation in characteristic numbers.

The set of curves in Figure 3.25 show the transport coefficients for momentum and heat on the subgrid scales. Both are put into relation to the effective coefficient, which, e.g. for the momentum is the sum of subgrid-scale and molecular viscosity ($\nu_{\text{sgs}} + \nu$). The first is defined as

$$\nu_{\text{sgs}} = C_{\text{k}} \Delta \sqrt{k_{\text{sgs}}} \tag{3.33}$$

by the sgs model (see Section 2.1.3). It is directly dependent on the filter size Δ, which corresponds to the mesh size in the present simulations. Consequently, the jumps in the profile are attributed to the meshing strategy where the cell size doubles at the refinement limits. It is interesting to note, that the value of the subgrid-scale viscosity is in the same order of magnitude as the molecular viscosity. The subgrid-scale heat diffusivity α_{sgs} is the transport coefficient for heat on the subgrid-scale level.

$$\alpha_{\text{sgs}} = \frac{\rho \nu_{\text{sgs}}}{\text{Pr}_{\text{t}}} = \rho C_{\text{k}} \Delta \sqrt{k_{\text{sgs}}} \tag{3.34}$$

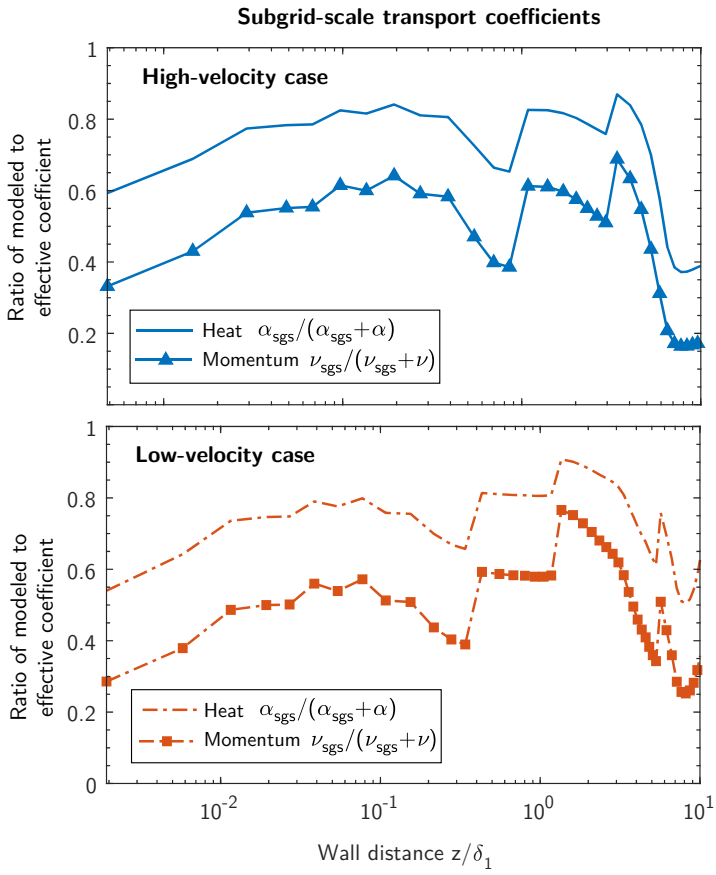


Figure 3.25.: The ratio of the subgrid-scale transport coefficients, sgs viscosity ν_{sgs} and sgs heat diffusivity α_{sgs}, to the effective coefficients.

Even though the turbulent heat transport in general is a convective transport mechanism, its modeled part is treated as a diffusive transport mechanism. It can therefore be compared to the effective transport coefficient, consisting of sgs diffusivity and the molecular diffusivity ($\alpha_{sgs} + \alpha$). The general level of subgrid-scale heat transport is high, and in most regions even outnumbers the molecular transport, which is reasonable given the convective nature of the transport. Nevertheless, this finding underlines the importance of a proper model selection.

Both coefficients differ only by the local density and are evaluated from time-averaged values. Following the definition, the profiles reduce in the wall proximity. However, a model influence remains in the first cell, i.e. indicating that the subgrid-scale model slightly overestimates near-wall turbulent heat transport, which already was suspected above when evaluating the average temperature profiles.

As stated in the introduction, the present work is motivated by the aim to gain insight into the mechanism that drives the convective heat losses on the surface of solar receivers. Therefore, the investigation of the heat transfer from the vertical wall into the fluid is in the focus of this work. In the following, the heat transfer rate, the mechanisms of heat transfer and transport in the boundary layer of the two-dimensional cases, and the associated evaluation methods will be discussed.
The local convective heat transfer rate is defined through the dimensionless local Nusselt number:

$$\mathrm{Nu}_y = \frac{\dot{q}''_\mathrm{w}}{\Delta T} \cdot \frac{y}{k} = \frac{k\frac{T_\mathrm{w} - T(\Delta z/2)}{\Delta z/2})}{\Delta T} \cdot \frac{y}{k} \tag{3.35}$$

where $\dot{q}''_\mathrm{w}$ describes the heat flux from the wall into the fluid. In theory, this flux would be defined by the temperature gradient in wall-normal direction at $z = 0$. However, in the present simulation, the temperature wall boundary condition is set to be a fixed value. Consequently, the gradient is not defined at this position, but can be evaluated at a wall-normal distance of $z = \Delta z/4$ (where Δz is the z-length of the first mesh cell at the wall). The equation above shows that the gradient is calculated using the central differencing sheme. As the heat transfer occurs at the wall, where no turbulence or advective transport in wall-normal direction is present, the heat flux $\dot{q}''_\mathrm{w}$ is solely defined by conduction on the resolved scales.

Figure 3.26 shows a plot of the instantaneous Nusselt number distribution at the wall, with the local height y used as a characteristic length scale. The comparison between the low-velocity case (left) and the high-velocity case (right) shows the strong impact that the instabilities have on the heat transfer. For the low-velocity case, the development of instabilities is clearly reflected in the heat transfer rate. This indicates that the vortices resulting from the instabilities transport cold fluid towards the wall which increases the local temperature gradient and thus results in a locally elevated Nu number. Furthermore, it can be observed that the nature of these instabilities is two-dimensional, indicating that they are Tollmien-Schlichting waves. At the top of the domain, the distribution becomes more complex with local spots where a high heat transfer rate occurs. This distribution is the result of a three-dimensional flow, and therefore

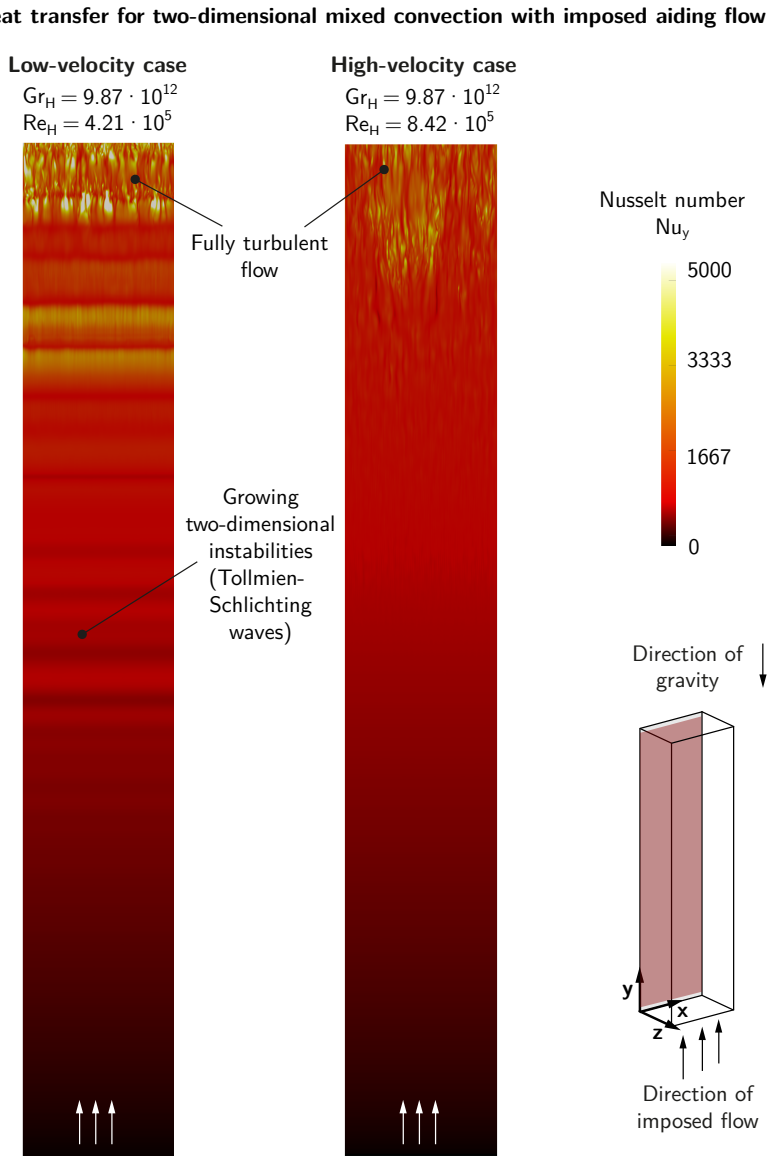


Figure 3.26.: Instantaneous field of the resolved heat transfer. The low-velocity case is characterized by growing instabilities that eventually burst into turbulence. The high-velocity case features lower Nu numbers and no characteristic instabilities.

indicates a fully turbulent state. The high-velocity case does not feature the characteristic instabilities. As noticed before, the laminarization effect caused by the higher imposed velocity suppresses instabilities, thus reduces mixing and consequently results in a generally lower heat transfer level. Like for the other case, the characteristic pattern at the top of the domain indicates a fully turbulent flow. It can also be observed that this pattern develops gradually, marking the zone where the flow transitions. Interestingly, this distinct zone does not occur for the low-velocity case. This finding backs the conclusion drawn before that different mechanisms trigger the transition: While the transition is "classical" for the high-velocity case, it is highly influenced by the instabilities in the low-velocity case. When looking carefully at the turbulent region of the low-velocity case, it can be found that the patterns are superimposed upon two-dimensional structures, which are the remains of the instabilities.

The figure discussed above presented an instantaneous snapshot of the Nusselt number distribution. In the following Figure 3.27, the time-averaged local Nusselt number as a function of the Grashof number is shown for both the high-velocity and the low-velocity case. Here, the Grashof number can be understood as a dimensionless height parameter. The heat transfer is in the same order of magnitude for both while the flows are laminar. At $\mathrm{Gr}_y \approx 3 \cdot 10^{12}$, the two cases separate with the average heat transfer of the low-velocity case being higher than the one of the high-velocity case. Nusselt number results obtained by Abedin et al. (2012a) as shown in Figure 2.12 are included for comparison (black lines). As discussed above, a one-to-one comparison of space-developing simulation results (present work) and time-developing simulation results (Abedin) is not valid – and not possible due to the lack in characteristic length scales i.e. in the Reynolds number. Qualitatively, the physical effects visible in the DNS are captured by the LES: Transition to turbulence results in a sharp increase in Nu. Comparing both cases, the higher imposed velocity delays the onset of turbulence, which is the case in the DNS as well. A higher velocity results in a higher Nusselt number throughout the laminar regime, which is true when comparing the DNS cases, and also when comparing the present low-velocity case to the present high-velocity case. The gradients in the laminar regime match the gradients of Abedin's work.

It is now of interest to determine which mechanisms are relevant for the heat transfer. Figure 3.28 therefore presents the evaluation of all major heat transport mechanisms, namely: Advective transport by the mean flow, molecular diffusion (heat conduction), resolved turbulent transport $\overline{\boldsymbol{u}'T'}$ (heat being transported through fluctuations), modeled turbulent transport on the unresolved scales (labeled "turbulent diffusion", as it is numerically implemented as a diffusion term, see Chp. 2.1.3), and turbulent dissipation. The latter is a source term

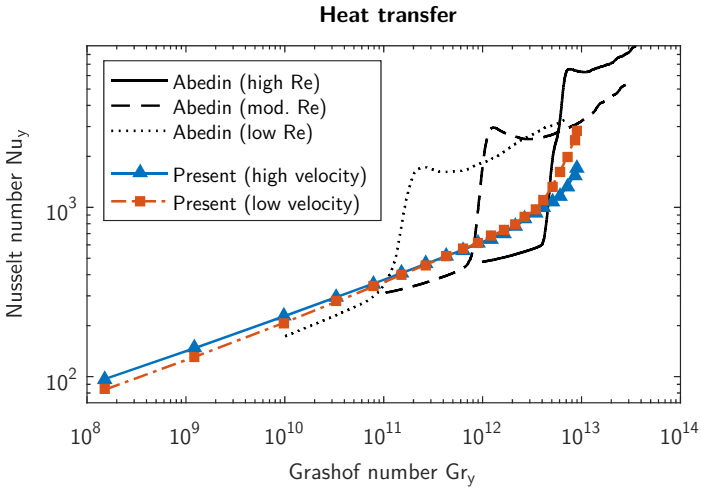


Figure 3.27.: Nusselt number Nu_y as a function of Grashof number Gr_y for the present case (LES, resolved part) compared to three literature (DNS) cases (Abedin et al., 2012a). This comparison, however, is only qualitative, as the numerical approach is different. Qualitatively, effects like a delay in the transition from laminar to turbulent state for a higher velocity is captured by the LES. Furthermore, in the laminar regime, the gradients are in good agreement with Abedin's data, as well as the fact that a higher velocity results in a higher laminar heat transfer rate.

which is the result of the viscous dissipation of small-scale turbulence (at the end of the Kolmogorov cascade) and is identical to the sink in the TKE transport equation (see Eqn. 2.18). For the complete equation of turbulent heat transport, please refer to Eqn. 2.9 and literature (e.g. Schlichting and Gersten, 2006).
The chosen representation is common for the investigation of boundary layer transport mechanisms, and has to be read in the following way: Imagine a small volume where heat is brought in and out by a certain transport mechanism. The difference between all inflows and outflows of this particular mechanism can be understood as the local change rate in thermal energy within the volume, or as a volumetric source[7]. Consequently, the net amount of heat that a certain mechanism introduces into or removes from the imaginary volume is shown. The shaded areas in the figure represent the different regions of the boundary layer as discussed in Chapter 2.1.4 and using Eqn. 2.59: The viscous sublayer (dark grey), the buffer layer (light grey), and the outer boundary layer. The evaluation is presented for the high-velocity case (top) and for the low-velocity case (bottom) at a vertical position of $y = 1.95\,\mathrm{m}$ (top of the domain).

[7] Mathematically, this is the divergence of the fluxes by a certain transport mechanism.

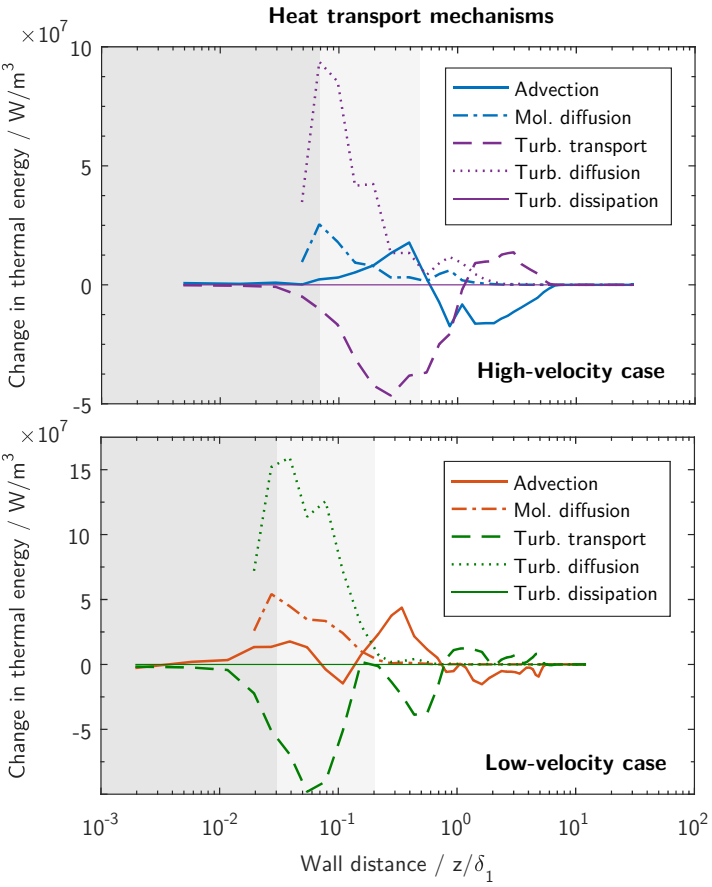


Figure 3.28.: Evaluation of the major heat transport mechanisms in the boundary layer for the high-velocity and the low-velocity case at the top of the computational domain ($y = 1.95\,\mathrm{m}$). The high influence of the turbulent transport, both on the resolved scales and on the modeled scales is apparent. The shading represents the viscous sublayer (dark), and the buffer layer (light).

For both cases, the heat transport is dominated by the turbulent mechanisms (both resolved and modeled). Starting from the wall, heat gets transfered through the viscous sublayer. Consequently, no heat sources are apparent in direct wall proximity, as no change in the heat transport mechanisms occurs. This finding is not surprising, as it is well-known from literature that molecular conduction is the only transport mechanism in this region. At the outer limit of the viscous

sublayer, the temperature gradient decreases, leading to the introduction of heat through the diffusive transport mechanisms. As noted before, the subgrid-scale model predicts a high share of turbulent transport on the small scales. Keep in mind that the diffusion is defined by the second derivative. Close to the wall, where the cells are very small, the numerical precision at which results are written thus has an influence. In post-processing, the evaluation of the second gradient in this region with small cell sizes and a high temperature gradient becomes numerically unstable, the curves for diffusive transport are therefore starting at $z/\delta_1 \approx 2 \cdot 10^{-2} ... 5 \cdot 10^{-2}$. This leads to the limitation that diffusive transport cannot be evaluated in the first three cells adjacent to the wall[8]. Further limitations are attributed to the fact, that all x and y-gradients are evaluated over a span significantly higher than in z-direction.
All over the buffer layer, with an introduction of heat through the diffusive transport processes in wall-normal direction, a strong resolved turbulent transport removes this heat and carries it into the outer boundary layer region. It is interesting to note, that in both cases, advection also introduces a net heat flow into this region. In order to explain this observation, a quick recapitulation of the spatial temperature boundary layer evaluation (Figure 3.17 and 3.16) is helpful: At the top of the domain (where the present figure is evaluated), the local temperature in the buffer boundary layer region decreases with height. As explained before, this is attributed to the transition to turbulence and the resulting redistribution of heat towards the outer region of in the boundary layer, as a consequence of which the temperature profiles become steeper. Hence, the fluid entering the volume in positive y-direction has a higher temperature than the fluid leaving the volume at the opposite side. This net heat flow in vertical direction is the cause of the advection peak.
In the outer boundary layer region, the introduction by diffusion further reduces with the wall distance and eventually reaches zero. From here on, the contribution of the advective transport sees a second peak in the low-velocity case, which is not the case in the high-velocity simulation. This peak is most likely related to the lack of diffusive transport in this region. Consequently, part of the heat transported to the outer regions by turbulence has to be supplied by advection. In the outer region, at $z/\delta_1 > 10^0$, which spatially covers the main part of the boundary layer (keep in mind the logarithmic scaling in the figure), this turbulent heat flux is then introduced into the imaginary cell and transported away by advection. The latter observation clearly shows the importance of turbulent transport in most of the boundary region. All across the boundary layer, turbulent dissipation only plays a minor role and its contribution is barely noticeable.

[8] This limitation applies only for post-processing, and not for the simulation itself, where results are internally handled with higher precision.

Having come to the conclusion that turbulent transport is a major mechanism for heat transfer, a detailed look at the coherent structures of turbulence is required. In Chapter 2.1.4, several ways to identify vortex structures have been presented. Thereof, a selection based on the second invariant of the velocity gradient tensor (Q-criterion) proved to be the most applicable measure for the present flow cases. An iso-surface plot showing all regions where $Q > 20$ is presented in Figure 3.29 (for the low-velocity case) and in Figure 3.30 (for the high-velocity case).

The plot for the low-velocity case approximately shows the upper third of the computational domain and thus covers the laminar-turbulent transition. Primary instabilities develop at the bottom of the figure. They are caused by the shear between the updraft and the free stream and are explained by primary stability theory (Schlichting and Gersten, 2006). The resulting periodically occurring two-dimensional vortices are an almost textbook example of Tollmien-Schlichting waves. They travel in vertical direction and exhibit a linear amplification along their path. When reaching the vertical center of the volume shown in the figure, they become subject to secondary instabilities, start to become three-dimensional, and eventually break apart, resulting in so-called Λ-structures (Boiko et al., 2011; Schlichting and Gersten, 2006). Comparison with this literature reveals that these structures are distorted in the present mixed convection case. This distortion is the result of the velocity peak, in which the legs of the Λ-structures are transported faster than their top. The transition into a fully turbulent flow state is finalized when the Λ-structures continue to grow into turbulent coherent structures like hairpin vortices. The turbulent flow on top of the domain clearly shows remains of the Tollmien-Schlichting waves. This observation conforms to DNS results in literature for aiding flows (Abedin et al., 2012a) and pure natural convection (Abedin et al., 2009), where the periodic vortices are referred to as plumes. The artifacts visible in the figure are the result of a faulty node-interpolation at the polyhedron layer next to the mesh refinement limit and are solely of visual nature.

The plot for the high-velocity case covers approximately half of the computational domain. Here, no trace of any large-scale instability is visible and no two-dimensional vortices like the Tollmien-Schlichting waves occur. Instead, the transition to turbulence happens in the way described in Chp. 2.1.4, with streamwise streaks being formed in the lower boundary layer region. Figure 3.30 highlights these streaks and also shows the formation of coherent vortices when moving further up the top of the domain (e.g. Λ-structures and wall-attached hairpin vortices). Like in the low-velocity case, the Λ-structures are distorted by the updraft near the wall. The fact that the Tollmien-Schlichting waves fail to appear when the imposed velocity is increased leads to the conclusion that the laminarization effect stabilizes the boundary layer. Consequently, the instabilities occurring in the low-velocity case are suppressed.

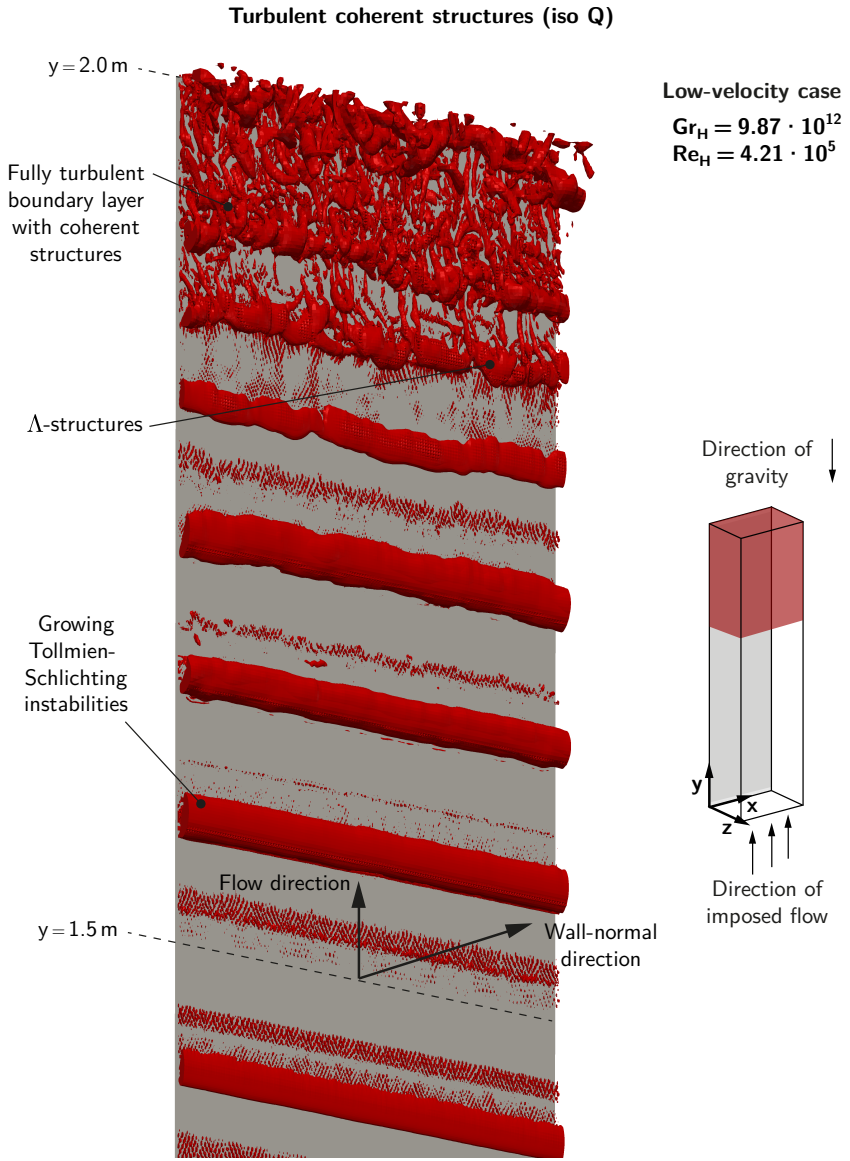


Figure 3.29.: Iso-surface plot of $Q = 20$ showing coherent turbulent structures in the upper domain of the low-velocity case. Two-dimensional structures caused by instabilities travel in vertical direction, grow three-dimensional and burst into turbulence.

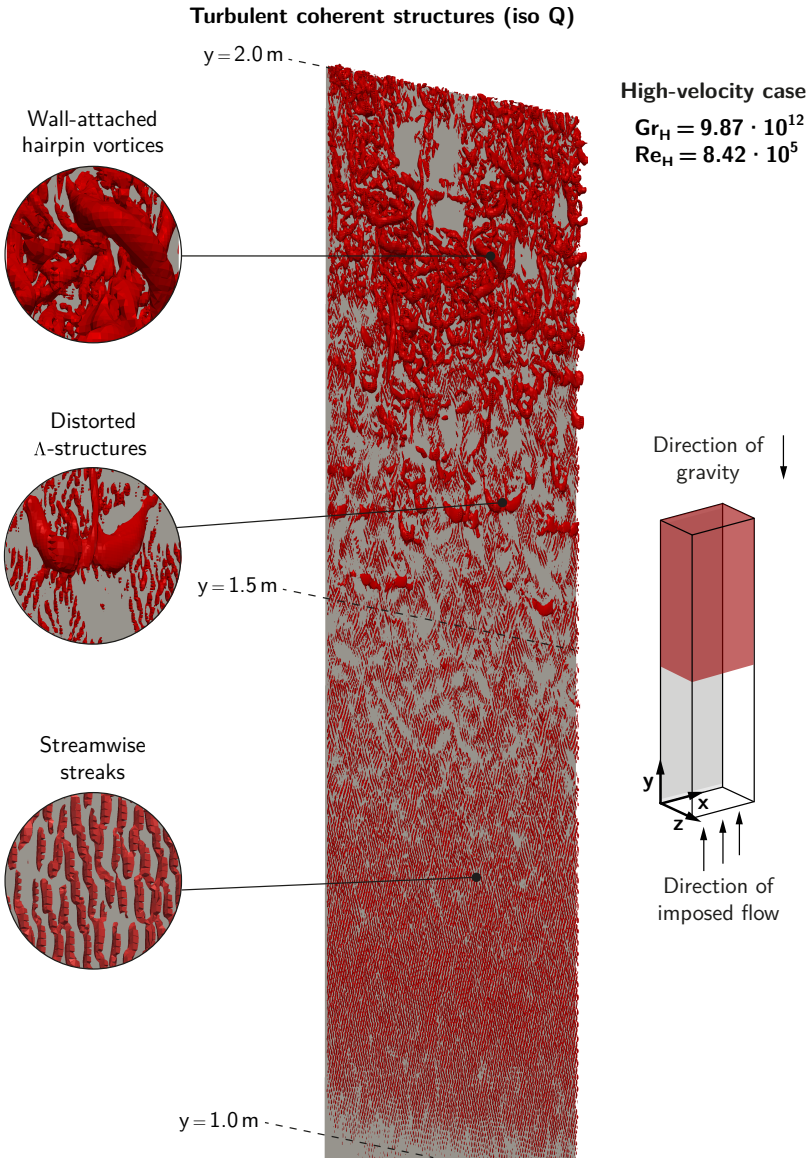


Figure 3.30.: The turbulent coherent structures in the high-velocity case show the lack of Tollmien-Schlichting instabilities. The transition to turbulence occurs with streaks that later on induce Λ-structures and the wall-attached hairpin vortices.

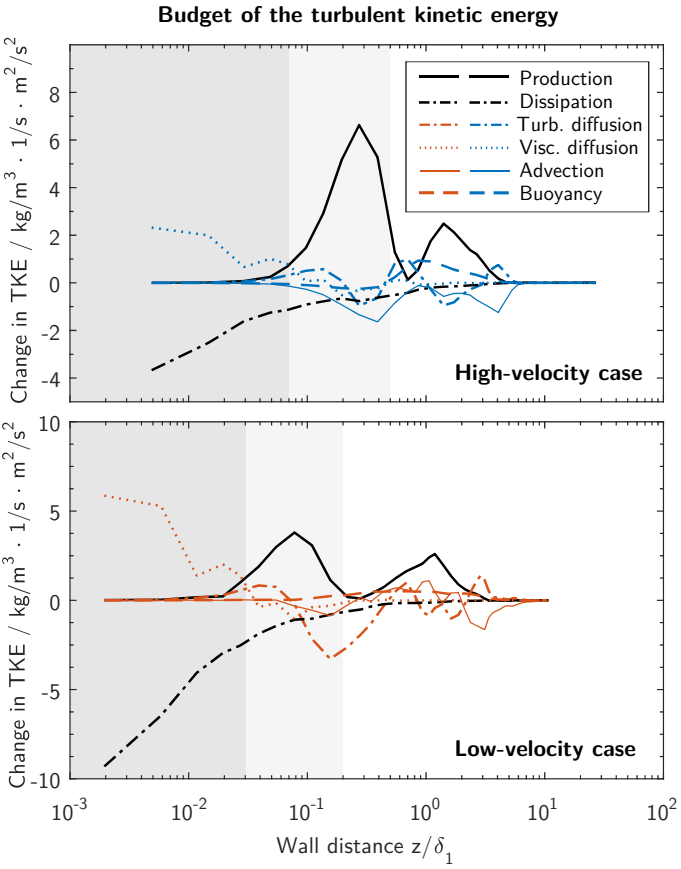


Figure 3.31.: Evaluation of the production, transport, and dissipation of turbulent kinetic energy on the resolved scales. Two peaks in production occur at each side of the velocity hump. The profiles are evaluated at the top of the computational domain ($y = 1.95\,\mathrm{m}$). The gray shading represents the viscous sublayer and the buffer layer.

In order to investigate the mechanisms that promote or reduce turbulence, the different terms of the transport equation for turbulent kinetic energy (see Eqn. 2.18) are evaluated in the following. This method allows to budget the TKE on the resolved scales and split the respective mechanisms into "loss" and "gain". The effects evaluated are: Production and dissipation of k, turbulent and viscous diffusion, advective transport, and production by buoyancy. The results presented in Figure 3.31 are read in a similar way as the diagram for the

different heat transport mechanisms: They show the change in TKE (kg m^2/s^2) per second and volume and were evaluated at a vertical position of $y = 1.95\,m$. The production of turbulent kinetic energy exhibits two distinct peaks in both cases. The fact that these peaks are located at each side of the region where the peak velocity occurs ($z/\delta_1 \approx 7 \cdot 10^{-1}$ for the high-velocity case and $z/\delta_1 \approx 3 \cdot 10^{-1}$ for the low-velocity case), points out that the production is dominated by the velocity gradient in $\overline{u'_y u'_z} \partial \overline{u_y} / \partial z$. A quick look at the average velocity profiles in Figure 3.16 and 3.17 allows to identify the regions characterized by high velocity gradients in z-direction and highlights the congruence of their position with the production peaks. In the high-velocity case, the peak at the wall side, where the velocity drops by 0.33 m/s, is consequently higher than the peak at the free-stream side where the drop is only 0.12 m/s. A similar connection between the production peaks can be drawn in the low-velocity case, where the velocity drop is 0.25 m/s at the wall side and 0.15 m/s at the free-stream side. As observed above in the spatial boundary layer evolution, this value has already decreased due to the transition to turbulence. In both simulation cases, it can be stated, that the production rate of k is more prominent at the wall side.
The turbulent kinetic energy is transported into the viscous sublayer by viscous diffusion where it is dissipated. Both mechanisms counterbalance each other. However, like for the heat transfer mechanisms discussed above, it should be kept in mind that numerical instabilities occur in the post-processing of this particular region due to the second gradient in the diffusion term. Both mechanisms, viscous diffusion and dissipation, play a major role in wall proximity, but are of low relevance throughout the rest of the boundary layer.
The transport by turbulent diffusion exhibits a characteristic pattern visible in both cases: TKE is removed from the region where the wall-peak in production is located and transported towards the wall and towards the region where the maximum velocity occurs. The same pattern appears at the other side near the second peak in production. While this can clearly be observed in the high-velocity case, oscillations occur in the low-velocity case. In the outer region of the boundary layer, the transport by turbulent diffusion is balanced with the advective transport. Keep in mind that the figure shows the local net amount of transport and does not resolve the transport in each direction.
Advective transport removes TKE rather than introducing it, while buoyancy has a positive contribution. The latter features a distinct peak in the high-velocity case. In the low-velocity case, its influence is less but covers a wider region.

In general, these profiles are in good agreement with the ones observed by Abedin et al. (2012b) in air. However, they exclusively cover the turbulent kinetic energy on the resolved scales and not on the subgrid scales. For the validation of the present simulation method, numerical consistency has to be ensured. This covers the main goal in LES to resolve at least 80% of the tur-

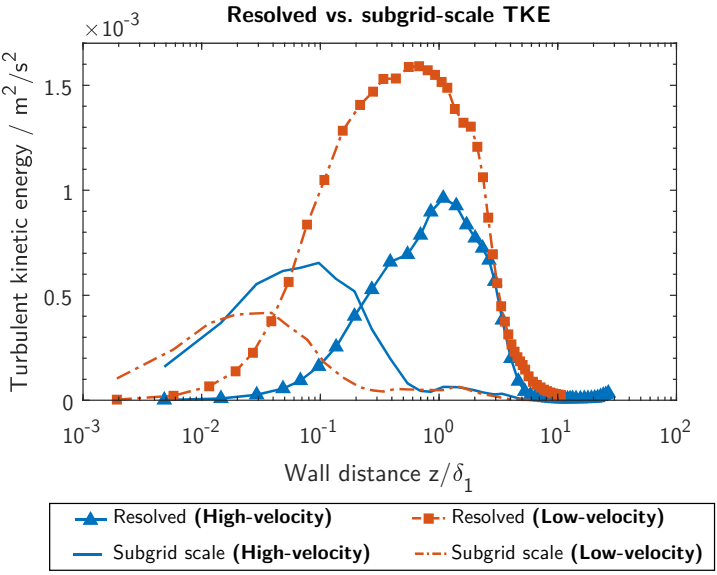


Figure 3.32.: Comparison of the resolved and the modeled (sgs) share of turbulent kinetic energy at $y = 1.95\,\mathrm{m}$ shows that the resolution requirement of LES is complied with. High values of k_{sgs} occur at the boundary of the viscous sublayer where the scales of turbulence are smaller than the mesh/LES filter size.

bulent energy, as well as the question, whether the turbulent spectra match theory (i.e. whether the energy cascade discussed in Chp. 2.1.3 can be observed). Figure 3.32 is a comparison of resolved and modeled (sgs) TKE at the same vertical position as the evaluation above. The profiles show that the bigger part of TKE is resolved and the goal of an LES thus achieved. The values of k_{sgs} solely increase in direct wall proximity. For both cases, the maximum of modeled TKE is at the outer boundary of the viscous sublayer. This behavior is not unexpected, as the scales of turbulence grow very small in this region. For both cases, the resolved part exceeds the modeled part in the buffer layer and in the outer boundary layer. Also, the figure repeats the observation from previous evaluations that the low-velocity case shows a significantly higher degree of turbulent fluctuations and thus exhibits a higher amount of turbulent kinetic energy.

While this figure evaluates the integral of turbulent energy with respect to all scales of turbulence, the two figures 3.33 and 3.34 show the corresponding spectral distribution. The top diagram illustrates the velocity signal in time-space for the first ten seconds of the sampling period (as stated above, the

actual sampling period is 17.5 sec). The lowest line is the velocity in direct wall proximity at $z = 4.7 \cdot 10^{-5}$ m and thus exhibits very low fluctuations. The uppermost line is the velocity in the region of the buoyant updraft (at a wall distance of $2.2 \cdot 10^{-3}$ m) where the highest velocities occur. The middle line is in the free stream, close to the channel boundary condition ($z = 0.074$ m), where the mesh resolution is coarse. For each of these three positions, the signal of the fluctuations is transformed from the time-space into the frequency-space through a fast Fourier transform (FFT) algorithm. As described by Schlüter and Pitsch (2005), a Hann-window is generated and multiplied with the input data in time-space. Since this evaluation is performed for a fixed position – defined vertical height and wall distance – the wavenumber κ is not a function of the respective length scale but of the corresponding time scale.
For both the high and low velocity case, the turbulent spectrum near the wall (right spectra) nicely follows the dashed line indicating the Kolmogorov law ($\kappa^{-5/3}$). In both cases, the LES is able to resolve the large-scale fluctuations (small wavenumbers) and a large number of small-scale fluctuations (large wavenumbers). The same is the case for the spectrum in the velocity hump (top figures). Note that the energy contained in the large scales is higher by several orders of magnitude compared to the spectrum evaluated at the wall. It does not come as a surprise that the spectra in the free stream indicate that the resolution of the LES at this location is insufficient. While the high-velocity case does not follow the $\kappa^{-5/3}$-law at all, the low velocity-case follows for a small number of scales (which is due to the lower flow velocity). This behavior has been anticipated and is the result of the mesh refinement strategy that focuses on the boundary layer. Consequently, it has to be ensured that all effects of influence for mixed convection occur within the region where the LES resolution is sufficient. While this has been the case for all simulations presented here, as well as all simulations of three-dimensional mixed convection, it did not apply to the simulation of the opposing flow (as will be discussed and shown in the following section).

3.6.2. Opposing flow

The results of the simulation case for two-dimensional mixed convection with imposed opposing flow illustrate the limits of the present computational method. A numerically converged, quasi steady-state solution was obtained. Figure 3.35 shows the instantaneous field for temperature and vertical velocity. The fluid inlet with cold fluid entering the domain is located at the top with a fluid flow towards the bottom. At the same time, a strong buoyant force accelerates the wall boundary layer in opposite direction, resulting in a boundary layer flow towards the top. This leads to the requirement, that the velocity boundary condition at the top needs to account for an entering flow (inlet) in the free stream and a leaving flow (outlet) near the wall. As can be observed in the

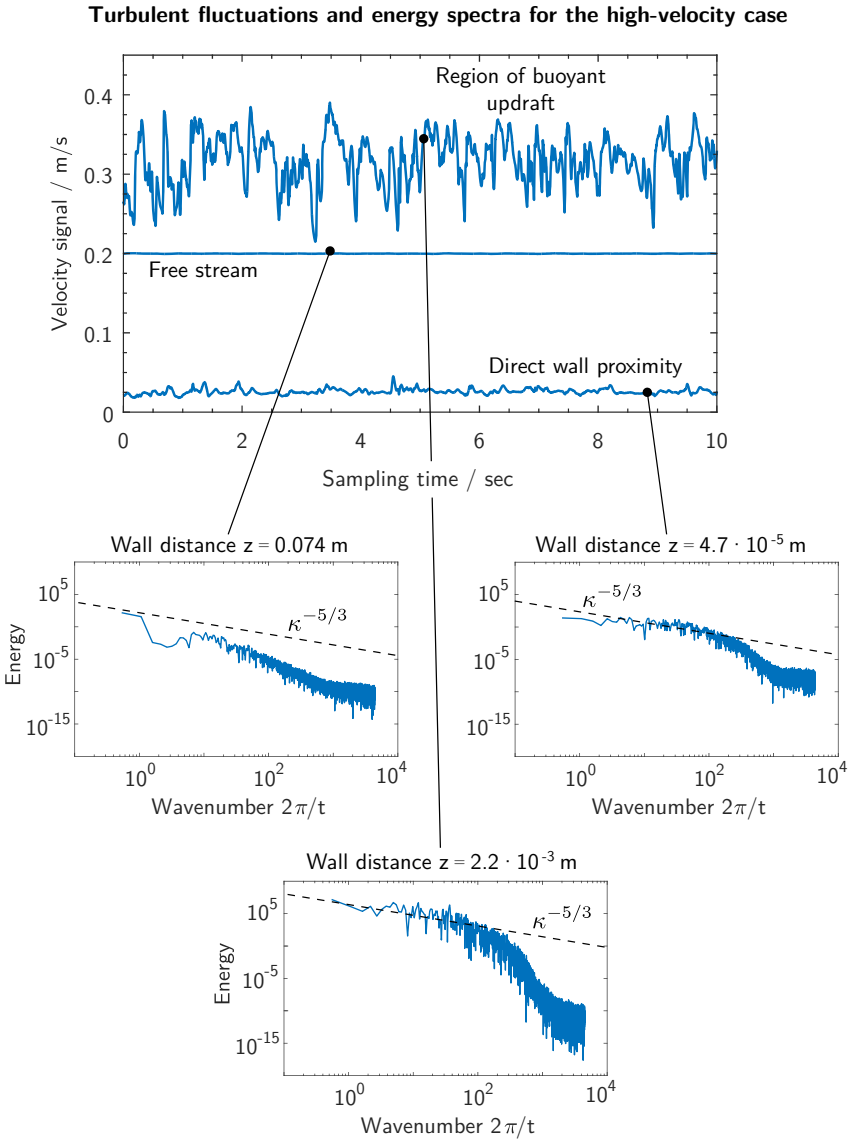


Figure 3.33.: Evaluation of the turbulent spectrum of the high-velocity case at two locations within the boundary layer and one location in the free stream. The fluctuations in frequency-space are shown at the bottom and the raw velocity signal in time-space is at the top. The present LES is capable of resolving all relevant scales, however, with the limitation that all relevant effects have to occur within the refined region.

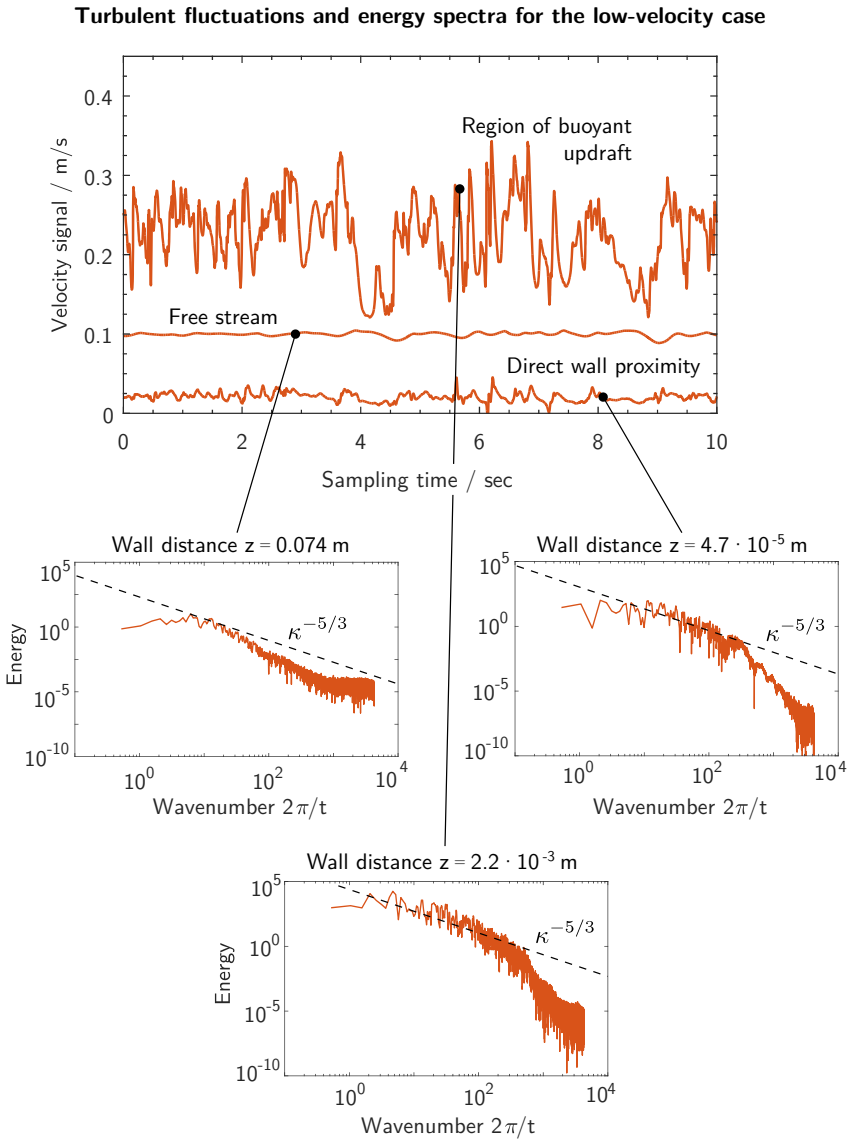


Figure 3.34.: The corresponding evaluation of the turbulent spectra for the low-velocity case (see Figure 3.33).

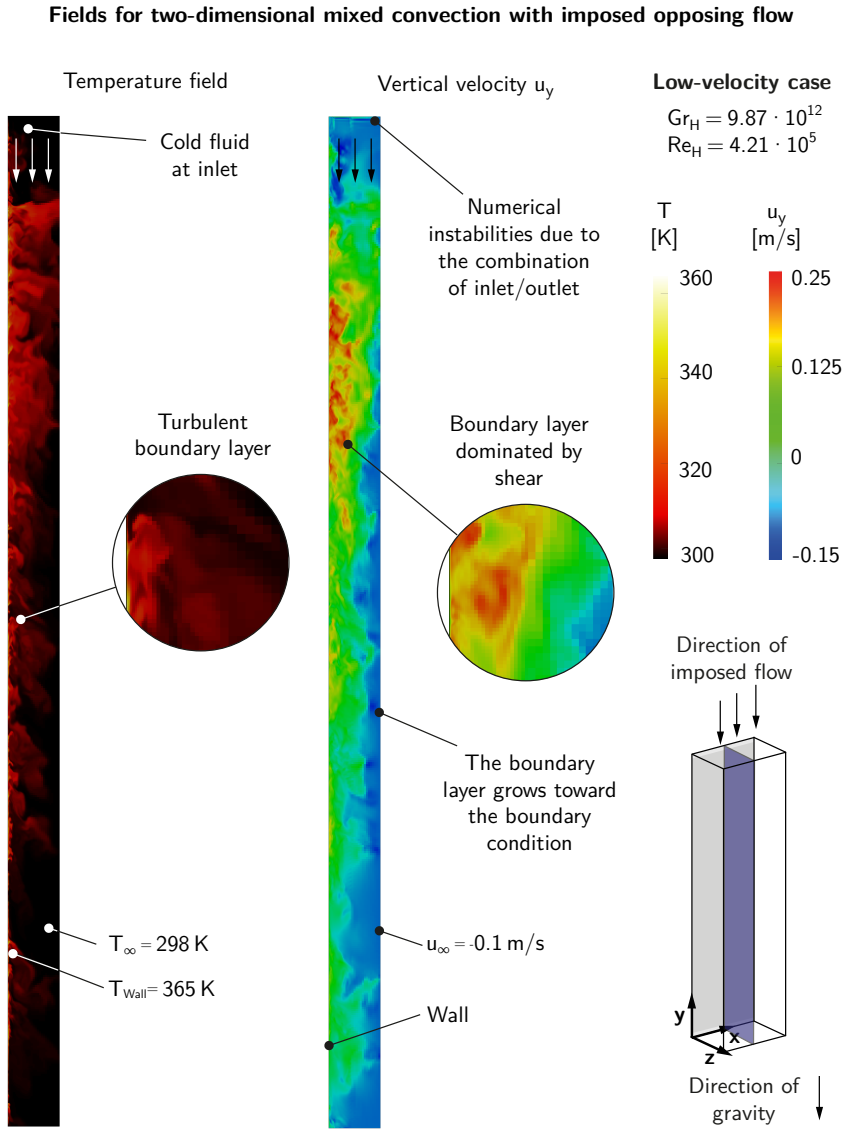


Figure 3.35.: Results obtained from the simulation of the opposing case showing the instantaneous field of temperature and vertical velocity. The flow is clearly dominated by buoyancy. Numerical problems arose from the boundary layer growing towards the boundary condition and from the combination of inlet and outlet at the top.

velocity flow field, this problem leads to numerical instabilities that manifest themselves in oscillations near the top of the computational domain. The flow fields also show that the boundary layer exhibits a high degree of turbulence throughout the entire height. The results of the aiding case showed an increase in turbulence when the shear caused by the velocity difference between the boundary layer updraft motion and the free stream was high. In the opposing case with its high velocity differences, shear consequently dominates the boundary layer, creating huge amounts of turbulence, as highlighted in the figure.

In the previous section, when the turbulent spectra were evaluated, it was shown that the LES does not resolve all relevant scales in the region far away from the wall. While this limitation did not pose any problem for the simulation of the aiding flow cases, it does for the opposing case. Figure 3.35 clearly shows that the boundary layer grows in size, eventually even reaching the boundary condition. This results in the occurence of relevant mechanisms in under-resolved mesh regions. Furthermore, the boundary condition has an undesirable influence on the boundary layer. The present case therefore shows the limits of the simulation method with the presented domain size and refinement strategy.

3.7. Chapter summary

This chapter presented the details of the computational methods used in the present work. While most turbulent scales are resolved in the LES approach, small scales are modeled using a subgrid-scale model. This model introduces an additional transport equation for subgrid-scale turbulent kinetic energy. The separation of resolved scales and modeled scales is obtained by using the local mesh as a filter. All thermophysical properties of the working fluid are set to be constant, except for the density which is a linear function of the temperature. It was shown in the chapter that the deviation resulting from this simplification is acceptable. The solution algorithm used in the simulations solves the transient, incompressible, variable-density transport equations of mass, momentum, and energy. A series of numerical methods is used to stabilize the simulation and obtain convergence, including a strategy for the initialization of all relevant fields. Special care was taken in the development of a mesh refinement strategy that would allow to perform a wall-resolved LES on a large computational domain at an acceptable computational cost. The resulting mesh features several refinement steps. The choice of boundary conditions is a compromise between ensuring numerical stability and not imposing a solution onto the simulation. The crucial selection of proper numerical discretization schemes ensures low numerical diffusion and low local instabilities in the flow fields, which was achieved through a blending scheme. Three simulation cases for two-dimensional mixed convection were set up for the purpose of proving the

suitability of the present computational method. The latter was performed on three levels: First, the results were compared to DNS results in literature, which, however, were obtained using a different numerical approach. This qualitative validation generally showed that all effects of relevance were correctly resolved. Second, a detailed interpretation of the physical results revealed that the present simulation method is capable of reproducing all effects described in literature (i.e. the prediction of instabilities, the laminarization effect, the heat transfer rates, the onset of turbulence, and its triggering mechanisms). Last, the results of the present LES were examined for numerical consistency, which lead to the conclusion that close to the wall, all relevant scales of turbulence were resolved. The limit of the present method was found in a case where the boundary layer grew large compared to the computational domain.
The conclusion drawn in this chapter is that the presented method of LES is suitable for the investigation of mixed convection.

Chapter 4.

Physical description of the investigation

This chapter presents the physical parameters for the simulations of three-dimensional turbulent mixed convection on a vertical plate. The geometry of a plate has been chosen because it represents a simple setup where the occurring mechanisms can be investigated without any geometrical influence. As it would be the case for an actual flow experiment, a spatial domain needs to be specified for the numerical experiment. Figure 4.1 shows a schematic of this setup.

The plate extends 1.02 m in positive x-direction (length) and 0.82 m in positive y-direction (height). Hereafter, the plate is referred to as wall, as it represents the closure of the domain to one side. The origin of the coordinate system is set to the lower left-hand corner of the plate. A fluid flow is imposed in positive x-direction at varying flow velocities. Contrary to a real-life experiment, the imposed flow does not exhibit any boundary layer, which allows the investigation of the boundary layer evolution along the plate. In order to include the entire zone of wall influence on the flow, the computational domain stretches 0.1 m into the free stream. Varying surface temperatures are imposed onto the vertical plate. As gravity is in negative y-direction, a buoyant updraft in positive y-direction within the temperature boundary layer is expected.

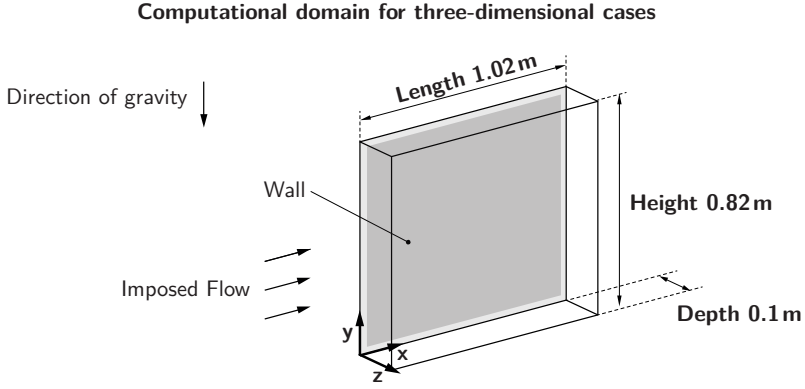


Figure 4.1.: Schematic of the computational domain for the three-dimensional flow cases showing all relevant geometric parameters.

As discussed in Chapter 2.2, a three-dimensional mixed convection flow is characterized by two dimensionless numbers: Reynolds number (for the forced convection part) and Grashof number (for the influence of buoyancy). The characteristic length scale for Re is the plate length L as it represents the dimension in direction of the imposed flow. Accordingly, Gr is scaled to the height H. For the heat transfer, however, neither the horizontal x nor the vertical y are a valid characteristic length scale, as both buoyancy and free stream have an influence. In Chapter 2.2, the length LH for the average Nusselt number was briefly discussed. In the present work, a blending of height and length will be used. This approach was successfully applied by Siebers et al. (1983), where – as a major downside – it required profound knowledge of the flow field in form of a maximum flow angle. As these informations are not available, e.g. when evaluating a Nusselt-correlation, the use of the characteristic Richardson number ($\mathrm{Ri} = \mathrm{Gr}/\mathrm{Re}^2$) as a parameter to describe the relative influence of buoyancy is more reasonable. The resulting length scale is

$$lh\,(x,y,\mathrm{Ri}) = \sqrt{y^2 \sin^2\left(k\frac{\pi}{2}\right) + x^2 \cos^2\left(k\frac{\pi}{2}\right)} \tag{4.1}$$

with the coefficient

$$k = \begin{cases} 0 & \text{for } \mathrm{Ri} < 0.3 \\ \frac{\mathrm{Ri}-0.3}{16-0.3} & \text{for } 0.3 \leq \mathrm{Ri} \leq 16 \\ 1 & \text{for } \mathrm{Ri} > 16 \end{cases} \tag{4.2}$$

The regime boundaries $\mathrm{Ri} = 0.3$ and $\mathrm{Ri} = 16$, as defined by Sparrow et al. (1959), are used to separate mixed convection from pure natural convection and pure forced convection. Accordingly, the heat transfer into a vertical flow (pure natural convection) would be characterized by Nu_y while a horizontal flow (pure forced convection) would result in a heat transfer described by Nu_x.

As introduced in Chapter 3.1.2, an incompressible fluid, comparable to water, is used as the working fluid in the simulations. Contrary to real-life experiments, the temperature-dependence of thermophysical fluid properties can easily be eliminated in numerical simulations. This also eliminates the significant fluid-specific influence on the results (see Siebers, 1983), and thus allows to draw more general conclusions. As one goal of the present work is the generation of a base for future modeling, non-specific flow results are essential.

The Richardson number allows to classify the flow case in a regime map. Pure forced convection (driven by flow inertia) and pure natural convection (driven by buoyancy) mark the boundaries of the mixed convection regime with equipollent mechanisms (buoyancy and intertia). For the simulations in this work,

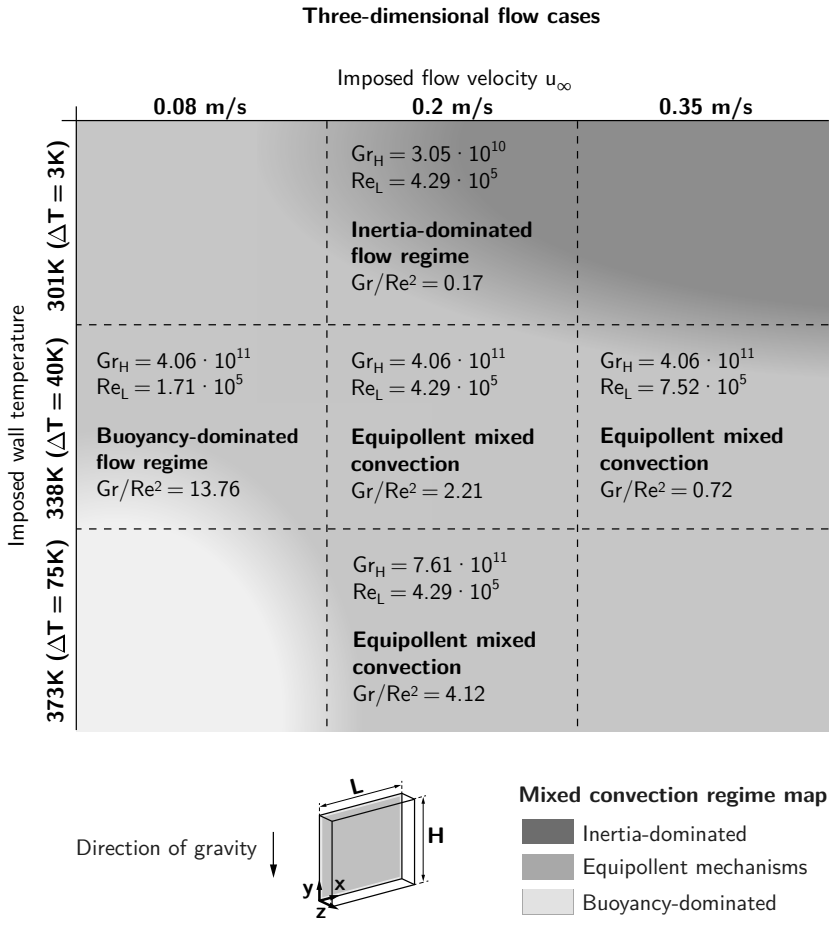


Figure 4.2.: Overview of the simulation cases in a matrix showing the mixed convection flow regimes, defined according to Sparrow et al. (1959) (see Chp. 2.2).

two parameters have been varied in order to obtain different flow cases: First, the imposed flow velocity u_∞ defining Reynolds number $\mathrm{Re_L}$. Three different values have been investigated: a low velocity of 0.08 m/s ($\mathrm{Re_L} = 1.71 \cdot 10^5$), a medium velocity of 0.2 m/s ($\mathrm{Re_L} = 4.29 \cdot 10^5$), and a high velocity of 0.35 m/s ($\mathrm{Re_L} = 7.52 \cdot 10^5$). The second parameter is the wall temperature and accordingly

the difference ΔT between wall and fluid temperature, which has an impact on the Grashof number $\mathrm{Gr_H}$. Presuming an ambient temperature of 298 K, a small temperature difference of 3 K results in $\mathrm{Gr_H} = 3.05 \cdot 10^{10}$. A higher influence of buoyancy is obtained by a temperature difference of 40 K (wall temperature of 338 K and $\mathrm{Gr_H} = 4.06 \cdot 10^{11}$). The maximum plate temperature in the present work is set to 373 K (75 K temperature difference and $\mathrm{Gr_H} = 7.61 \cdot 10^{11}$), which would be slightly below the boiling point of water. Even though phase change is not relevant for the present simulations, staying below this critical temperature would allow the comparison of the results with future experimental data.

This setup results in a simulation matrix with 3 times 3 entries, as shown in Figure 4.2. When evaluating the Richardson number, most of the matrix is located in the mixed convection regime as defined above ($0.3 < \mathrm{Ri} < 16$). For low temperatures, the regime changes from inertia-dominated mixed convection to pure forced convection. On the other hand, the low-velocity, high-temperature cases result in a transition from the buoyancy-dominated side of the mixed convection regime to pure natural convection. Taking into consideration the computational cost of each simulation, performing a large number of simulations in the same flow regime is not reasonable. Therefore, a careful design-of-experiment was conducted. The matrix in Figure 4.2 gives an overview of the resulting simulation cases in the context of the regime map. One extreme case is considered pure forced convection, however a small influence of buoyancy is expected. Further digging into this pure forced convection or into pure natural convection without considering the influence of the other mechanism is not wise, as those flows have been subject to decades of experimental and numerical research. In the mixed convection regime, one case covers domination by buoyancy and three cases investigate equipollency of both driving mechanisms.

The reason for this particular case setup is that the simulation case in the center of the matrix (in the equipollent regime) will be used as a reference case. Comparison with the cases featuring an identical Grashof number, but higher and lower Reynolds numbers, will allow to asses the influence of the free stream. Within this series of simulations, transition between buoyancy-dominated and equipollent mechanisms regime will occur. The influence of buoyancy can be evaluated by comparing the results of the reference case to the ones featuring a higher and lower Grashof number. Within this series, transition from interia-dominated to equipollent mechamisms regime will take place. This design-of-experiment results in the “cross” of cases on the regime map (Figure 4.2). The following three sections will discuss the resulting five cases in the context of their respective flow regime before a chapter summary is given.

4.1. Buoyancy-dominated mixed convection

The case is characterized by a large Richardson number, which suggests that flow conditions are mainly dominated by buoyancy. To ensure this, Reynolds number is kept at the minimum value of this study (with the numerical values as defined above). The simulation was performed for a medium-range Grashof number. With a Richardson number of 13.76, the case is located close to, nevertheless still within, the boundaries of the mixed convection flow regime. The aim of this simulation is to investigate a buoyancy-dominated mixed convection flow where the influence of flow inertia is small but still noticeable. Given these conditions, a strong updraft in the near-wall region is expected. Towards the free stream, the velocity magnitude is expected to reduce to the free-stream velocity while the flow direction is supposed to turn from the y-direction (updraft) to the x-direction (free stream). Using the similarity approach, this constellation can be transferred to the motivating real-life problem of a solar receiver. Presuming a surface temperature of 600 °C, the case would result in a receiver height of 3.8 m and an outer diameter of 3 m. The receiver represented by this setup is thus smaller than the concepts shown in Chapter 1. In order to obtain the intended Re number, the wind speed would be at a moderate level of 3 m/s. Note that these figures and the ones yet to follow for the other cases are evaluated using actual thermodynamic data for the air fluid properties (Lemmon et al., 2004).

4.2. Inertia-dominated mixed convection

The domination by inertia is represented by one case with the medium Reynolds number and the small Grashof number. The resulting Richardson number is 0.17, the flow can thus be classified as pure forced convection. However, limited to the direct wall proximity, a small influence of buoyancy is anticipated, as the case is located close to the regime boundary at $\mathrm{Ri} = 0.3$. The simulation is therefore supposed to investigate the transition towards the forced convection flow regime. It is expected that the imposed flow suppresses or severely delays the development of a turbulent boundary layer flow. Contrary to the buoyancy-dominated case discussed above, no real transfer to a solar receiver is possible. The small Grashof number would merely correspond to a receiver height of 1.5 m. Supposing a characteristic length of 3 m, the wind speed would be 7.2 m/s.

4.3. Mixed convection with equipollent mechanisms

Three cases investigate a flow setup where neither buoyancy nor inertia is the dominating mechanism. In Figure 4.2, those cases are denominated as equipollent mixed convection, as they are located at the center of the mixed convection regime.

The first case is characterized by the high Reynolds number and the medium Grashof number. Evaluating the Richardson number for this case yields a rather low value of 0.72. A real-life flow with these dimensionless numbers could thus occur at a solar receiver of 3.8 m height and 3 m diameter, when a stiff breeze of 13 m/s blows.
Featuring a Richardson number of 4.12, a higher influence of buoyancy is investigated by the second case. Here, the Grashof number is set to the maximum value of the present study, while the Reynolds number remains at a moderate level. Compared to the first case with equipollent mechanisms, a higher level of turbulence is expected in the buoyancy-influenced boundary layer. The lower flow inertia is not expected to significantly suppress disturbances. When transferring the flow setup to reality, this case represents the conditions at a medium-sized solar power plant, with a 4.7 m high and 3 m wide receiver in an ambient airflow of 7.2 m/s.
The third case combines the characteristics of both previous cases: The Grashof number is set to the medium value of the first case while the Reynolds number has the same moderate value as in the second case. Consequently, the resulting Richardson number of 2.2 ranges between the values of the previous cases. As mentioned above, when evaluating the results of all simulations, this case will serve as the reference case. The influence of the free stream is analyzed by comparing the results of this case to the ones featuring a higher and lower Reynolds number. Accordingly, the influence of buoyancy will be shown by comparing the reference case to the ones featuring a higher and lower Grashof number.

4.4. Chapter summary

This chapter provided a physical description of the simulation setup. The geometry is a flat, vertical plate of roughly 1 m width and 0.8 m height. The imposed flow over this surface has velocities that range between 0.08 m/s and 0.35 m/s. The plate is uniformly heated to wall-fluid temperature differences between 3 K and 75 K. The resulting Reynolds numbers are in the range of $10^5 ... 10^6$ and the resulting Grashof numbers are $10^{10} ... 10^{12}$. Consequently, transition to a turbulent flow state is expected. The flow regimes are characterized by the Richardson number. They cover buoyancy-dominated mixed convection (high Ri number), inertia-dominated mixed convection (low Ri number) and mixed convection with equipollent mechanisms. One case with a medium velocity and a moderate wall temperature is defined as the reference case of this study. It will serve as a reference in the comparison with the other cases, which are characterized by a higher or a lower influence of buoyancy and flow inertia. This procedure will allow to assess to what degree three-dimensional mixed convection is affected by buoyancy and the free stream, respectively.

Chapter 5.

Simulation results

The present work seeks to investigate the mechanisms of three-dimensional mixed convection, where an imposed horizontal flow interacts with a buoyant updraft. The latter is the result of heat being transferred into the fluid from a hot, vertical wall. Here, in particular the influence of buoyancy and the free stream on the flow field, the boundary layer, the turbulence characteristics, and the heat transfer is of relevance. For the simulations, the computational methodology presented in Chapter 3 was applied. Starting from initialization, 1.2 domain flow passages were simulated for each case, until a quasi steady-state condition was assumed. This assumption proved to be valid due to the good initialization. Depending on the imposed flow velocity, the physical time to reach this state were 3.4 sec (for the high-velocity case), 6 sec (for the medium-velocity cases), and 15 sec (for the low-velocity case). For the computation, the domain was partitioned and the simulation was run in 16, 32, 48, 64, or 504 parallel processes. The methods used to evaluate the results have been presented in Chapter 3.6. After reaching the steady-state condition, the entire flow fields were exported every 250 time steps. Additionally, local profiles in z-direction of all relevant physical and numerical parameters were sampled for each timestep. The sampling positions stretched horizontally and vertically across the domain in steps of 0.1 m, respectively. As discussed above, each position had four additional profiles written in 4 mm x and y distance for the evaluation of local gradients.

As previously discussed in Chapter 4, a reference simulation case with moderate Grashof and Reynolds numbers is defined. The following Section 5.1 shows and discusses the simulation results of this case. Based on these findings, varying the Reynolds number while maintaining a constant Grashof number allows to assess the influence of the free stream, which will be discussed in Section 5.2. Gradually increasing Reynolds number brings the flow from the buoyancy-dominated regime to the regime with equipollent mechanisms. The same approach is consequently used to evaluate the influence of buoyancy, where – starting from the reference case – Grashof number is decreased for one case and increased for another case, while Reynolds number remains constant. The corresponding transition takes place from the intertia-dominated regime to the regime with equipollent mechanisms. The associated findings are presented and discussed in Section 5.3. Additional numerical solution parameters can be found in Appendix C.

5.1. Reference case

The reference case features a horizontal flow characterized by a Reynolds number of $\mathrm{Re_L} = 4.29 \cdot 10^5$ and a buoyant updraft near the vertical wall characterized by a Grashof number of $\mathrm{Gr_H} = 4.06 \cdot 10^{11}$. This constellation results in a Richardson number $\mathrm{Gr_H}/\mathrm{Re_L^2} = 2.21$, which locates the case in the flow regime of equipollent mixed convection (see Chapter 4). As the present section discusses spatial developments within the domain – rather than featuring a comparison to other flow cases – the dimensionful coordinates x, y, and z will be used to describe a horizontal, vertical, and wall-normal location (instead of $\mathrm{Re_x}$ and $\mathrm{Gr_y}$).

5.1.1. Flow fields

A general introduction to three-dimensional mixed convection can be given by discussing the flow fields of the reference case. The following Figures 5.1 and 5.2 show an instantaneous field of the velocity components in horizontal and vertical direction and hence give an overview of the typical flow situation. The figures consist of a horizontal plane situated at the vertical center ($y = 0.4\,\mathrm{m}$ or $\mathrm{Gr_y} = 4.7 \cdot 10^{10}$) and three vertical planes located near the inlet ($x = 0.25\,\mathrm{m}$ or $\mathrm{Re_x} = 1.1 \cdot 10^5$), at the horizontal center ($x = 0.5\,\mathrm{m}$ or $\mathrm{Re_x} = 2.1 \cdot 10^5$), and near the outlet ($x = 0.75\,\mathrm{m}$ or $\mathrm{Re_x} = 3.2 \cdot 10^5$). In the first, the wall is located at the bottom, in the latter ones on the left side, respectively. The illustration at the bottom of the figures provides a small aid to identify the location of each plane.

The horizontal velocity u_x is shown in Figure 5.1 with the imposed flow entering the domain from the left side. Velocity fluctuations in the free stream at some distance from the wall are the result of the imposed synthetic turbulence. Some qualitative conclusions can be drawn from observing the instantaneous flow field, even without further in-depth analysis: First, the location where the boundary layer flow transitions from a laminar into a turbulent state can be identified at approximately $x = 0.35\,\mathrm{m}$. At this point, the typical stable, stratified velocity boundary layer – as highlighted in the left plane – starts to exhibit vortex structures and significantly grows in visual size. Interestingly, as will also be shown later, the flow transitions along a straight vertical line. Additionally, at the bottom, transition also occurs along a horizontal line at approximately $y = 0.1\,\mathrm{m}$. This detail leads to the conclusion, that a critical local Reynolds number (corresponding to a horizontal path length) as well as a certain critical local Grashof number (corresponding to a vertical path length) are a prerequisite for the laminar-turbulent transition. Second, the u_x boundary layer spatially develops exclusively in horizontal direction. Little variation in vertical direction can be observed, except for the fact that no transition to turbulence is visible at the bottom of the domain. Third, unsurprisingly, the lowest u_x occurs at the wall (no-slip condition) and the highest in the free stream (u_∞).

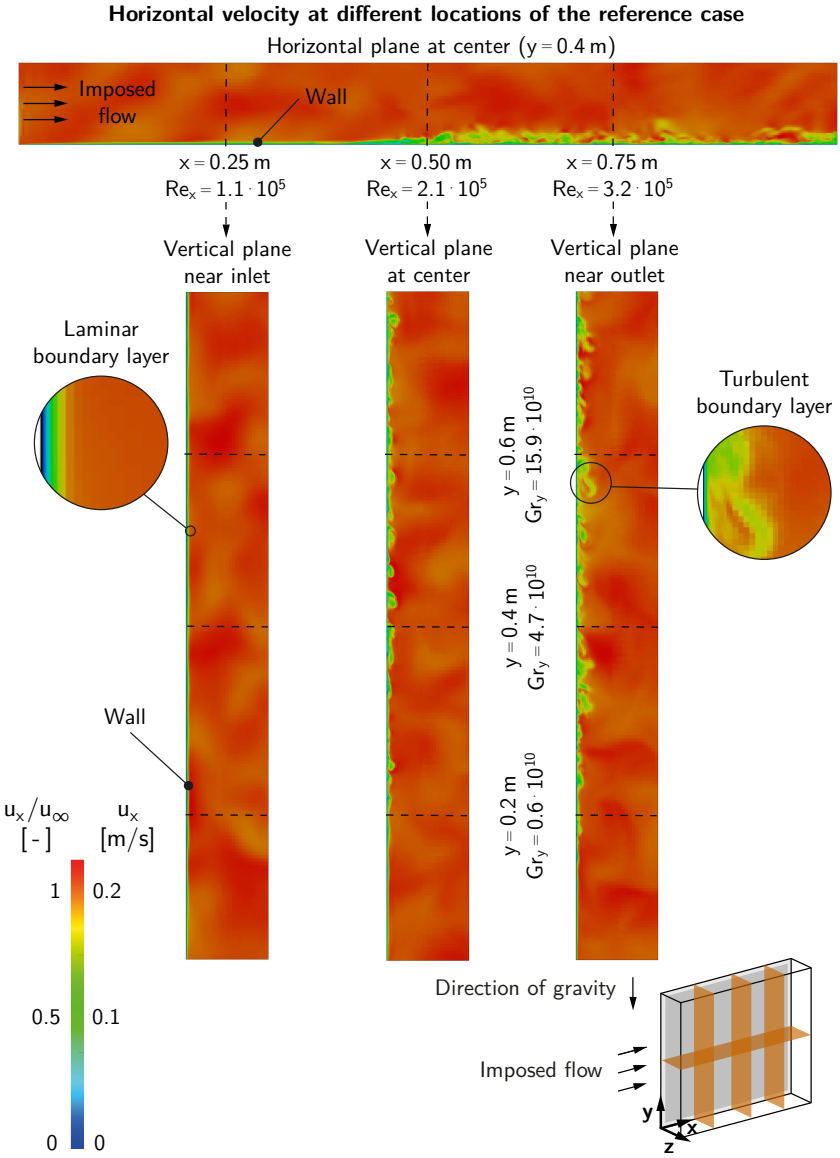


Figure 5.1.: Instantaneous field of the horizontal velocity at different locations of the domain showing a laminar boundary layer near the inlet and near the bottom and its transition to a fully turbulent boundary layer.

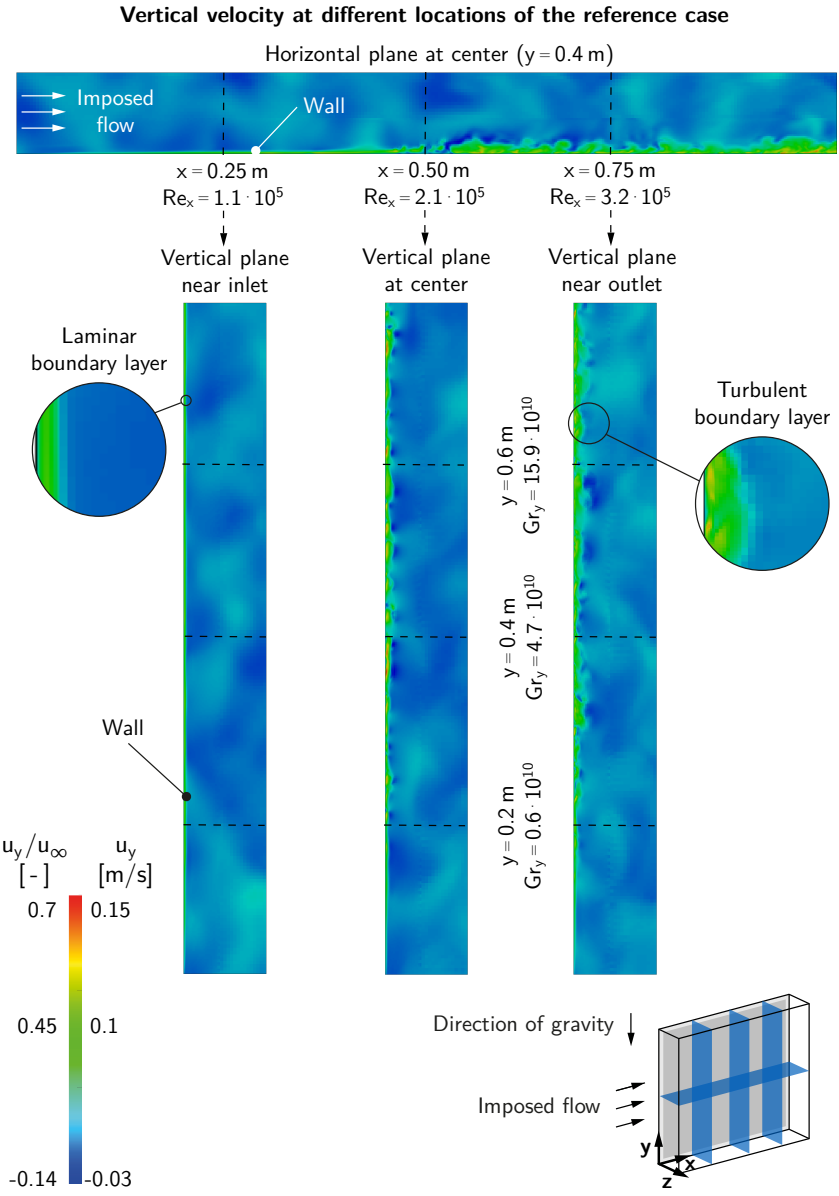


Figure 5.2.: The instantanous vertical velocity field on locations corresponding to the ones in Figure 5.1.

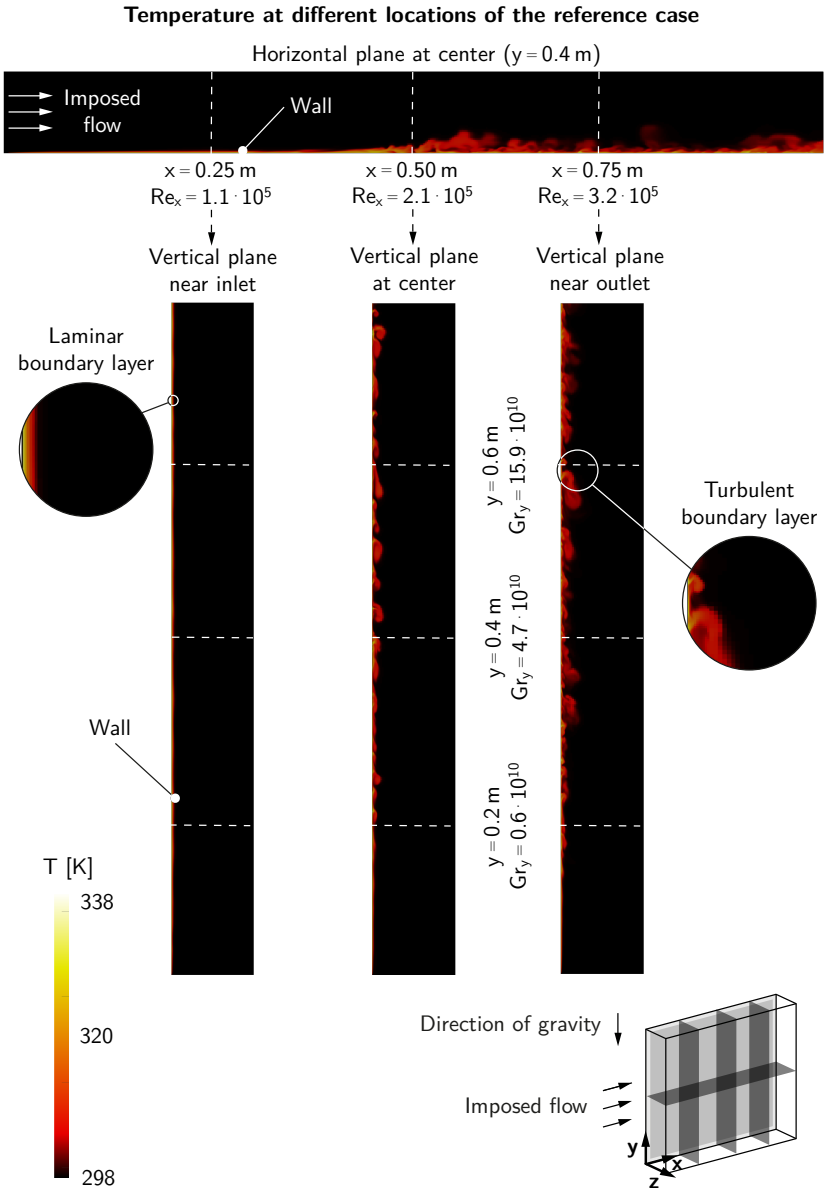


Figure 5.3.: The instantaneous temperature field on locations corresponding to the ones in Figure 5.1. The free-stream temperature is 298 K and the imposed wall temperature is 338 K.

The velocity in vertical direction u_y is the result of the buoyant updraft caused by the local increase in fluid temperature next to the wall. In the case of two-dimensional mixed convection, the buoyant updraft and the imposed velocity added up. In the present three-dimensional case, the vertical velocity u_y is mostly independent of the imposed u_x, see Figure 5.2. In the left plane (laminar flow state), starting from the zero-velocity at the wall, an increase in velocity can be observed in wall-normal z-direction. After reaching its maximum value, the velocity drops back to zero in the free stream (instead of the imposed value in the two-dimensional cases). Interestingly, the size of both u_y and u_x boundary layers matches. In the vortices of the turbulent flow, local patches are vertically accelerated to velocities of up to 0.7 times the value of the imposed flow. It is worth noting, that each patch of very high u_y near the wall corresponds to a patch of negative u_y in the outer boundary layer (see i.e. at the central plate). Furthermore, the patches also coincide with regions of low u_x (compare Figure 5.1). Both correlations are attributed to mass continuity.

Buoyancy strongly couples features in the temperature and in the vertical velocity field (see Figure 5.3). The center and the right plane in the figure show the same turbulent structures in the temperature field that have been observed in the flow fields before. The higher rate of momentum transport, compared to the transport of heat, is reflected in steeper gradients at the edge of these features in the temperature field. The highest temperature occurs near the wall, where the no-slip condition restrains the updraft.

All fields show the respective values at the center of each cell of the computational mesh. Hence, the varying resolution as a result of the mesh refinement strategy is visible in the figures. It can also be observed, that turbulent structures stretch across the refinement boundaries, however, without being disturbed. The presence of small numerical oscillations at small velocities near the outer refinement limit (e.g. in the vertical velocity) occurs in sufficient distance from the relevant boundary layer.

5.1.2. Boundary layers

The following section discusses the temperature and velocity boundary layers of the reference case with a focus on their respective spatial development. Therefore, profiles in wall-normal direction have been sampled at three locations: One at the zone where the flow transitions from a laminar to a turbulent flow state ($x = 0.35\,\mathrm{m}$), one in the turbulent flow regime ($x = 0.65\,\mathrm{m}$), and one in the turbulent flow at the outlet ($x = 1.00\,\mathrm{m}$). As stated before, little variation occurs in the vertical direction, which is the reason, why all profiles are at the vertical center.

Figure 5.4 shows the temperature and Figure 5.5 the velocity profiles within the boundary layer. As noted above, the boundary layer thickness δ_{99} – defined as the point at which the velocity has mostly reached free-stream values – is almost identical for the horizontal and vertical velocity.

In the first diagram, respectively, the profiles at the laminar-turbulent transition are shown. All lines represent the time-averaged values and the shaded area encloses all fluctuations. The mean temperature exhibits a steep gradient, dropping from the wall temperature to the temperature of the free stream. The corresponding laminar velocity profiles have a typical form: The horizontal velocity (green semicolon line) steeply rises from the zero velocity at the wall to the imposed free-stream velocity. The profile of the vertical velocity (solid red line) resembles the one discussed for two-dimensional mixed convection with a distinct peak in its course. In the first figure, this peak is still symmetric in its appearance, with steep gradients on both sides. The average velocity in wall-normal direction (dashed blue line) is near zero – however a very slight hump is visible, which is due to the thermal expansion of the fluid and the onset of turbulence. Interestingly, fluctuations in the lower temperature boundary layer are already prominent, while fluctuations in the velocity are mostly attributed to the imposed vortons. This synthetic turbulence can be identified by the size of the shaded area, which is identical for all velocity components and does not vary with z. Keep in mind, that no numerical fluctuations are imposed on the temperature field. Consequently, the small fluctuations in the wall-normal velocity, in combination with the steep temperature gradient, are sufficient to generate noticeable temperature fluctuations. This finding indicates, that the resulting fluctuation in the buoyant force plays a major role in the laminar-turbulent transition.
In the turbulent flow regime (second and third diagram in Figures 5.4 and 5.5), both the temperature and velocity boundary layers clearly grow in size. Compared to the transitional regime, the distinct peak in the vertical velocity is no longer symmetric, but exhibits a significantly less steep decent towards the free-stream side. The magnitude of the peak is considerably lower than in the first diagram at $x = 0.35\,\mathrm{m}$. The reason for this behavior is the transition to turbulence: Hereby, momentum is transported into the outer boundary layer, where it is used to accelerate the fluid in vertical direction. This results in a velocity increase in some wall distance and consequently in a lower velocity near the wall. The profile of the horizontal velocity features a near-wall gradient that is steeper than the one in the transitional regime. However, when reaching a velocity of $0.15\,\mathrm{m/s}$, the gradient sharply decreases, resulting in a moderate increase in velocity. The temperature gradient near the wall grows steeper, increasing the heat flow from the wall, which is an expected behavior in the laminar-turbulent transition. At some distance from the wall, however, the steeply descending temperature profile exhibits a bend and continues to decrease

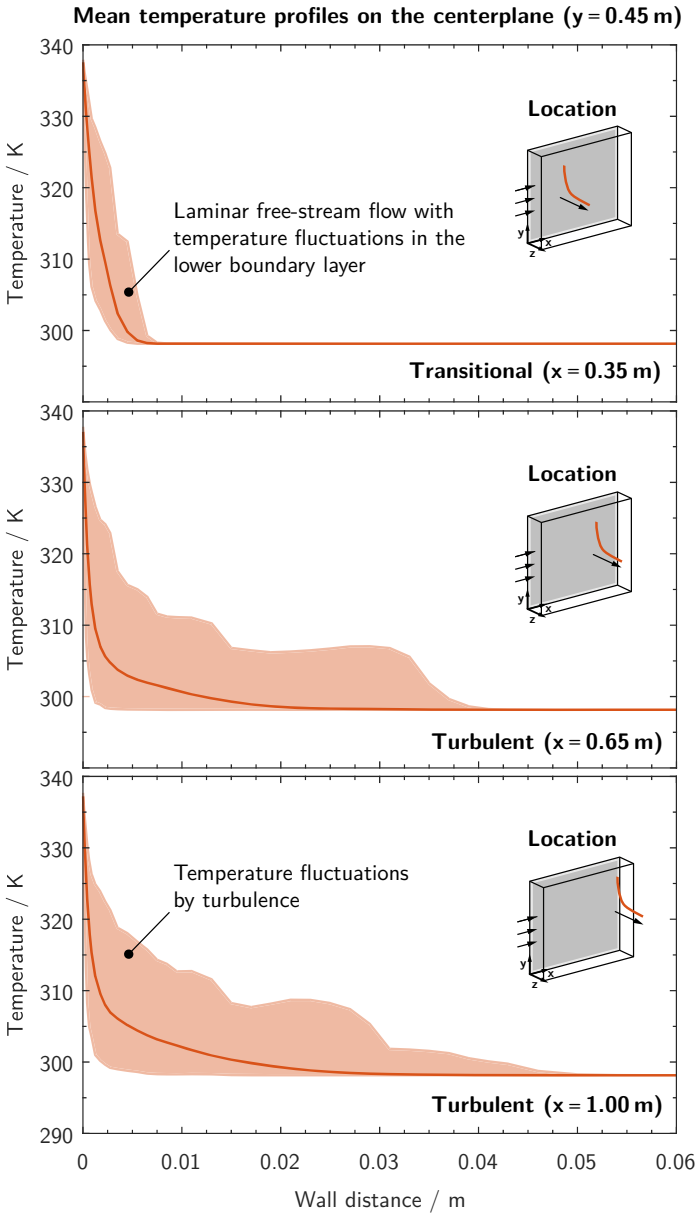


Figure 5.4.: Wall-normal profiles of the mean temperature (solid line) and temperature fluctuations (shaded area) at three locations along the horizontal centerplane. The profiles show the spatial development of a fully turbulent temperature boundary layer.

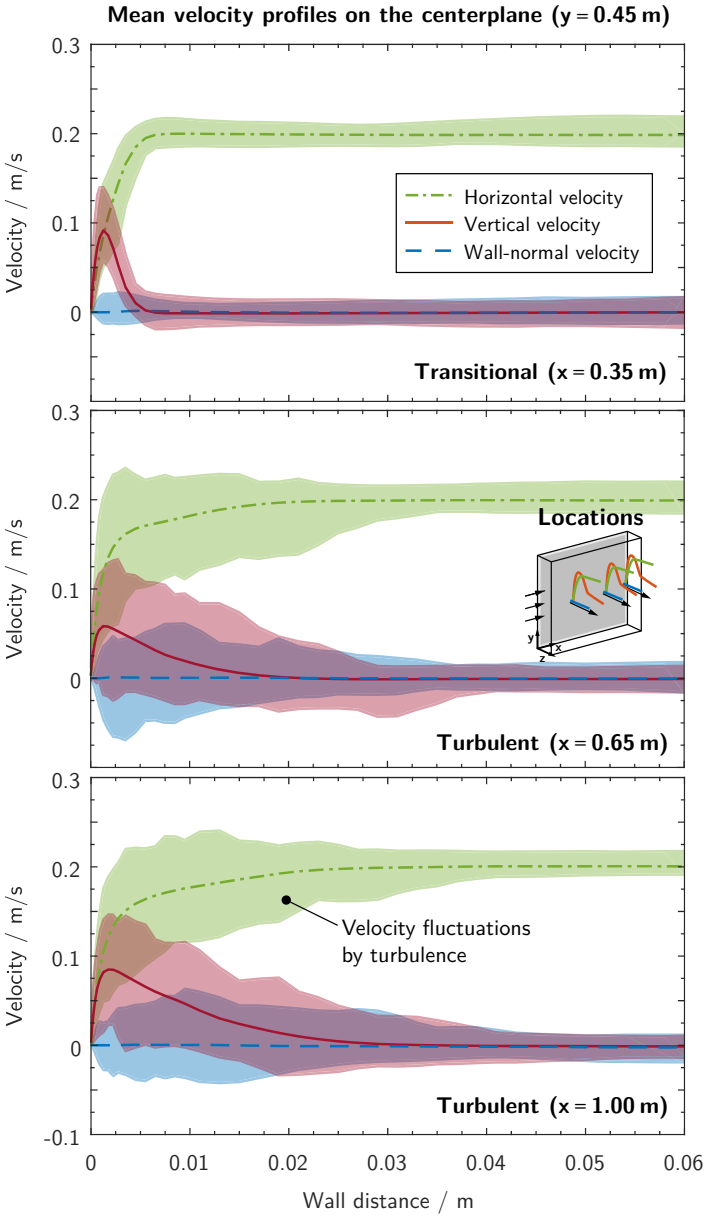


Figure 5.5.: Wall-normal profiles of all three average velocity components (lines) and their fluctuations (shaded area) at three locations along the horizontal centerplane.

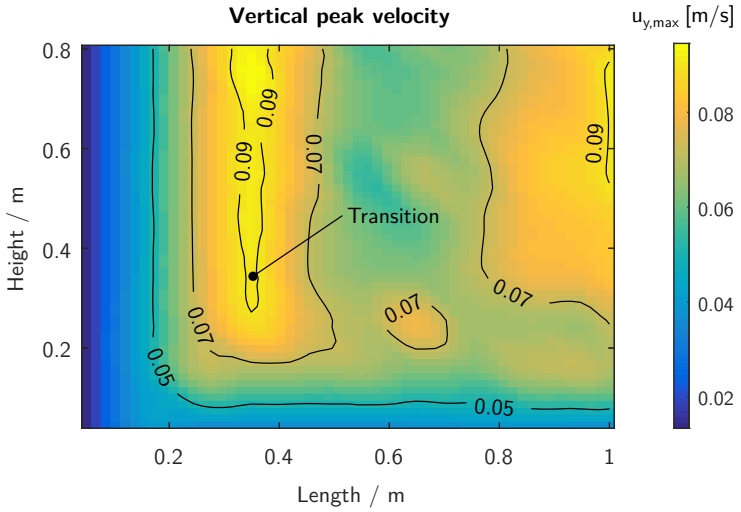


Figure 5.6.: Contour plot of the maximum average velocity in vertical direction showing the location of the laminar-turbulent transition in the reference case.

less dramatically – a clear indication that different mechanisms are responsible for the heat transport (as will be discussed later). Fluctuations in temperature and all three velocity components grow in intensity, increasing the turbulent kinetic energy in the flow.

The finding that the vertical velocity peak starts to decrease at the laminar-turbulent transition allows to precisely determine the position of the latter by evaluating the maximum u_y. Figure 5.6 confirms the location of $x = 0.35\,\mathrm{m}$, visually determined in the flow fields. In the laminar regime and below a height of 0.2 m, the maximum velocity does not depend on the vertical position. After the transition, the maximum velocity continues to decrease before it eventually starts to increase again at approximately $x = 0.6\,\mathrm{m}$. The fact that only a small peak is present at the bottom of the domain and its dependence on the vertical position indicates the entrainment of cold fluid near the wall at the bottom boundary: The influence of buoyancy grows with the temperature and the cold fluid has to travel a certain distance in order to heat up.

Evaluating the boundary layer profiles in a dimensionful way – as done in Figure 5.4 and 5.5 – does not allow to distinguish between the boundary layer growth and other effects like a growing influence of buoyancy. In order to compare the shape of profiles at different locations, the wall distance needs to

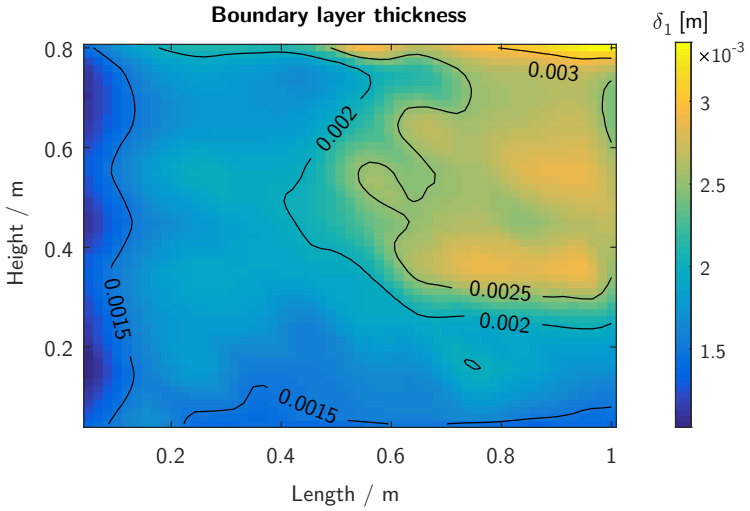


Figure 5.7.: Contour plot of the boundary layer displacement thickness δ_1, which will be used as a scaling parameter for the dimensionless wall distance z/δ_1.

be scaled to the boundary layer thickness. As discussed in Chapter 3.6, the displacement thickness δ_1 is used as scaling parameter for the dimensionless wall distance z/δ_1. Figure 5.7 is a surface plot showing the local δ_1 of the reference case. The region where high vertical velocities occur (in the first section of the plate) coincides with a lower displacement thickness, as the flow within the boundary layer is faster. In the turbulent region, the boundary layer has been found to visually grow, with a deviation from the free-stream velocity stretching far into the flow. Consequently, evaluating the δ_1-integral leads to higher values.

The curves in Figure 5.8 are the dimensionless form of the mean temperature profiles discussed above: Shown is the dimensionless temperature $(T - T_\infty)/\Delta T$ as a function of the dimensionless wall distance z/δ_1. The sampling locations are identical to those in the figures above (one in the transitional and two in the turbulent regime). One additional turbulent profile is located at the top near the outlet (see illustration in the figure). The figure shows that, once the flow has reached the turbulent flow state, the profiles show little dependence on the x and y location. Consequently, the temperature profile at the center, at the outlet, and at the top lie on top of each other. This implies that the temperature gradients decrease with x, as the wall distance in the figure is referred to a varying δ_1. The profiles stretch far into the outer boundary layer and show the bend typical of turbulent temperature profiles (indicating the region where heat

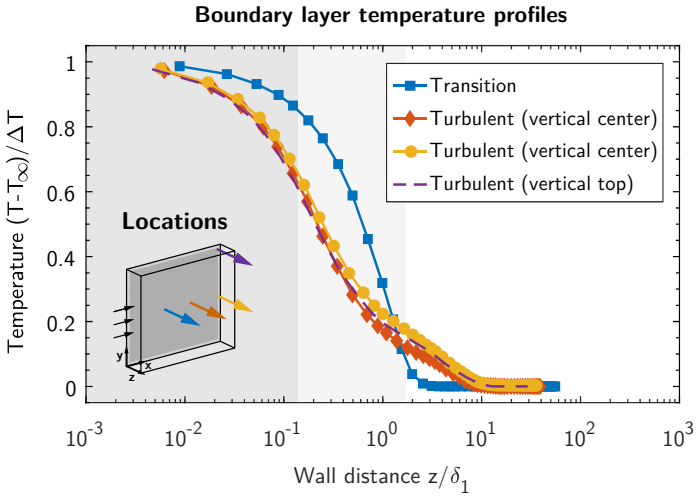


Figure 5.8.: Mean temperature profiles in the boundary layer of the reference case showing the dimensionless temperature as a function of the dimensionless wall distance. The shaded areas indicate the regions: viscous sublayer, buffer layer, and outer boundary layer. The locations are identical to those in Figure 5.5. One additional location is in the turbulent regime at the top of the domain (near the outlet). Within the turbulent flow regime, the profiles show little variation, neither in vertical nor in horizontal direction.

is no longer transported by conduction, but by advection and turbulence). Even though the flow case is different from the work of Abedin et al. (2012a), the general shape of the turbulent temperature profiles in the reference case are in good agreement (compare to Figure 3.22 in Chapter 3.6).
There are clear differences between the profiles in the transitional and in the turbulent regime: Even considering the smaller scaling factor δ_1, the near-wall temperature gradient of the former is less steep. As heat in this region is transported exclusively by gradient-dependent diffusive processes, this difference will also be reflected in the heat transfer. Furthermore, the transitional profile does not feature any bend – which is an indication of little variation in the heat transport mechanisms across the boundary layer.

In Figure 5.5, the average velocity in wall-normal direction was found to be zero. This allows to reduce the mean velocity to its two components u_x and u_y. Consequently, the profiles can be translated into a polar plot for the dimensionless representation of the velocity boundary layer. This translation results in one profile for the angle γ between the flow direction and the horizontal reference, shown in the top of Figure 5.9. Each flow angle is associated with a

dimensionless velocity magnitude $|\boldsymbol{u}|/u_\infty$ (bottom of the figure). An illustration of this definition is shown in the figure. Like in the temperature profiles above, the wall distance is expressed in dimensionless form z/δ_1 and the sampling locations correspond to the ones in the preceding figure. While Figure 5.5 gave an impression of the general profile shape, it failed to give further insights into the processes in the velocity boundary layer. The dimensionless velocity profile, however, allows to evaluate the mechanisms occurring in three-dimensional mixed convection and to assess the impact of buoyancy on the flow. Due to the latter, the velocity profiles have to be interpreted in conjunction with the dimensionless temperature profiles (Figure 5.8) .

The profiles in Figure 5.9 show this influence with the highest flow angles occurring in the wall proximity while the free stream on the outer side of the domain remains undisturbed. As stated before, most of the spatial boundary layer evolution occurs in horizontal direction (from line with squares to line with diamonds to line with circles). The flow shows little variation in vertical direction (compare the line with circles to the dashed line). Contrary to the two-dimensional flow case, no overshoot in the magnitude to values larger than the imposed free-stream velocity emerges from the vertical peak. This observation, however, is case-specific and flow cases with higher Richardson-numbers will feature this overshoot.

Within the velocity boundary layer of the reference case, a number of effects can be observed. For the sake of clarity, three distinct regions are classified using the definitions in Chapter 2.1.4, (i.e. Eqn. 2.59):

Outer boundary layer (no shading): In this region, the flow angle γ steadily grows with the x-coordinate. Two effects provoke this growth:

First, during laminar-turbulent transition, momentum from this region is transferred towards the wall by turbulent transport. When comparing the velocity magnitude in the transitional regime (line with squares) to the magnitude in the turbulent regime (other lines), the reduction in momentum is clearly visible. The region in which momentum is reduced stretches far into the free stream (keep in mind the logarithmic scaling in the figure), resulting in a significant amount of momentum being transferred. The flow in the free stream is predominantly in horizontal x-direction. As the angle can be understood as the relation between vertical and horizontal velocity, the reduction of the horizontal momentum leads to an increase in γ. Consequently, within the regions closer to the wall, where the momentum is reintroduced, the flow angles decreases.

Second, the turbulent transport of heat into the outer boundary layer raises the fluid temperature. This increase in the turbulent regime can clearly be seen in the temperature profiles above. Accordingly, with increasing horizontal x-position, the buoyant updraft intensifies and the vertical

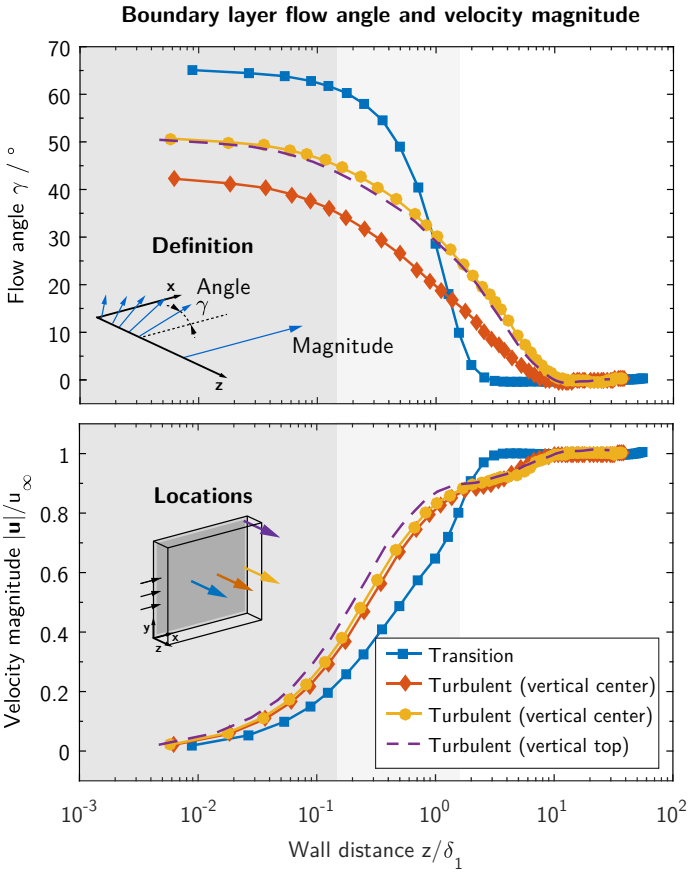


Figure 5.9.: Polar representation of the velocity in boundary layer with viscous sublayer and the buffer layer indicated by shading. The locations are identical to those in Figure 5.5. One additional location shows the profile in the turbulent regime at the top of the domain (near the outlet). Each polar plot consists of a profile for the local flow angle and a profile for the velocity magnitude.

velocity peak grows further into the free stream. This is then reflected in a higher flow angle (compare line with diamonds to the line with circles). Interestingly, while the flow angle grows in horizontal direction, the velocity magnitude remains almost constant. This finding suggests that – in the outer boundary layer – the flow is deflected rather than being accelerated.

Buffer layer (light shading): Within this region, wall friction does not yet play a significant role. The peak in vertical velocity occurs here and is clearly visible in the bottom figure at $z/\delta_1 \approx 10^0$ in the turbulent regime. Note that, in form of a slight bend, it is also recognizable in the magnitude profile for transitional flow. Two independent mechanisms cause this region to continuously gain momentum:

First – as described above – during the laminar-turbulent transition, momentum from the outer boundary layer is transferred into the inner boundary layer. In the velocity magnitude, this introduction compensates the reduction in peak velocity during transition caused by the vertical acceleration of a growing boundary layer (see corresponding discussion of Figure 5.6). The resulting increase in momentum is reflected in a sudden growth of the velocity magnitude during transition. Consequently, as the momentum introduced is in x-direction, thus resulting in higher u_x, and as the vertical velocity decreases, the flow angle drastically drops (compare line with squares to line with diamonds).

Second, after transition, the influence of buoyancy increases in this region as well. The peak in vertical velocity regrows (see Figure 5.6). Consequently, the flow angle grows in horizontal direction (compare line with diamonds to line with circles), however without exhibiting a significant change in magnitude (flow deflection). In vertical direction, the angle remains constant (compare line with squares to dashed line) with a slight increase in magnitude (flow acceleration).

Viscous sublayer (dark shading): In this region, viscous effects dominate the flow and wall friction plays an important role. In the first numerical cells of the boundary layer, a low horizontal velocity u_x coincides with a high fluid temperature, the latter provoking an updraft. Even though the resulting vertical velocity is small because of the viscous effects restraining the flow, u_y is in the same order of magnitude as u_x. This slight updraft in the viscous sublayer thus results in high flow angles. Siebers (1983) described this part of the boundary layer as constant-angle region. In the present work, no constant flow angles can be observed in any simulation result (keep in mind the logarithmic scaling). However, the viscous sublayer features the high values of γ that were observed by Siebers.

The same effects as in the buffer boundary layer cause the flow angle to decrease during transition and regrow in the turbulent flow regime. While their absolute impact on the magnitude is very limited (due to the generally low level in this region), major changes occur in the flow angle.

While the polar representation of the boundary layer flow is most suitable for the evaluation of spatial developments and allows to assess the influence of the

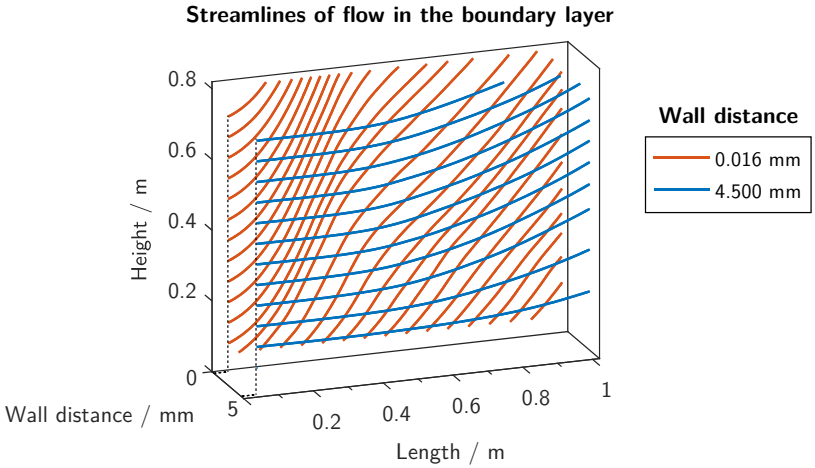


Figure 5.10.: Visualization of the streamlines in the viscous sublayer (wall distance of 0.016 mm or $z/\delta_1 \to 0$) and beyond the velocity peak (4.5 mm or $z/\delta_1 > 1.5 \cdot 10^0$).

respective mechanisms, it is rather difficult to access at first sight. Figure 5.10 therefore shows an alternative visualization of the flow angle γ in form of three-dimensional streamlines. The lines next to the wall represent the flow in the viscous sublayer (high-angle region, $z/\delta_1 \to 0$). The streamlines at 4.5 mm ($z/\delta_1 > 1.5 \cdot 10^0$) are located further into the free stream beyond the vertical velocity peak. In this representation, the entrainment of cold fluid in the viscous sublayer at the bottom – which was briefly discussed above – becomes visible. Comparing the plot with the measurements of Siebers (1983) reveals qualitative agreement for the streamlines at 4.5 mm[1].

Evaluating the profiles of temperature and velocity in Figure 5.8 and 5.9 with respect to the question whether they are self-similar, reveals that the temperature exhibits the latter to some degree. For the velocity magnitude, the profiles appear to show self-similarity. However, a complete description of the boundary layer velocity, the flow angle profiles ought to be self-similar as well. Even when scaling the γ-profiles to a reference angle, e.g. $\gamma/\gamma_{\max}$, the resulting profiles do not exhibit the same course (i.e. the profile with diamonds differs). The mechanisms occurring in the boundary layer prove to be too complex, which poses a challenge for a possible future development of mixed convection wall functions.

[1] Measurement results of flow angles at a wall distance as low as 0.016 mm were not available using Sieber's measurement techniques.

5.1.3. Heat transfer

The heat transfer in three-dimensional mixed convection is of particular interest, as it fuels the buoyant updraft within the boundary layer. Therefore, the investigation of the heat transfer rates, their spatial distribution, and the driving mechanisms is one major focus of the present work.

Figure 5.11 shows the instantaneous heat transfer rate in form of the dimensionless local Nusselt number Nu_{lh} as defined in Equation 3.35 and 4.1. The figure reveals the high degree of interaction between turbulence and heat transfer: After entering on the left side, the imposed horizontal flow passes the laminar region. Here, Nu is low and no variation occurs. During transition, low-velocity streaks are formed in the flow (see next section on turbulent coherent structures). As these streaks interact with the viscous sublayer, they result in locally increased heat transfer rates, which can be observed as elongated patches in the figure. Subsequently, in the fully turbulent flow regime, the streaks form turbulent coherent structures, locally enhancing the Nusselt number. The flow angle γ is made visible by the orientation of this pattern: The footprint of the streaks features a steeper angle than the one of the other turbulent coherent structures, which shows that the streaks are located closer to the wall (compare to the profiles and streamlines in Figure 5.9 or 5.10). In horizontal direction, the heat transfer enhancement grows, leading to small patches of Nusselt numbers as high as 4000.
The entrainment of cold fluid at the bottom causes a small region of elevated heat transfer rates. In the inner boundary layer, this fluid continues its laminar flow in vertical direction (as shown in Figure 5.10) and heats up. The corresponding reduction in the Nusselt number can be seen in the figure. Eventually, the flow starts to transition along the horizontal line identified above, exhibiting the same streaks as the main flow along the vertical transition line. The reference case is equipollent mixed convection with a moderate Richardson number of $\mathrm{Ri} = 2.21$. Following the definition above, the spatial scale lh for the given case is essentially identical to the horizontal path length. Consequently, the Nusselt number grows in horizontal x-direction rather than in vertical y-direction. This explains, why the effect of high heat transfer rates is not visible at the inlet, where cold ambient fluid makes first contact with the hot wall: While heat transfer is present, the length scale lh is near-zero due to $x \approx 0$. Note that, at the top near the inlet, a small increase in Nu_{lh} becomes visible – the large y at this position has an impact on the length scale leading to a non-zero value of lh.

While the figure above shows the instantaneous heat transfer (in other words: a "snapshot"), the time-averaged local Nusselt number Nu_{lh} is presented in Figure 5.12. As a result of the laminar-turbulent transition, the mean heat transfer rises steeply. Within the turbulent regime, Nu grows in horizontal direction.

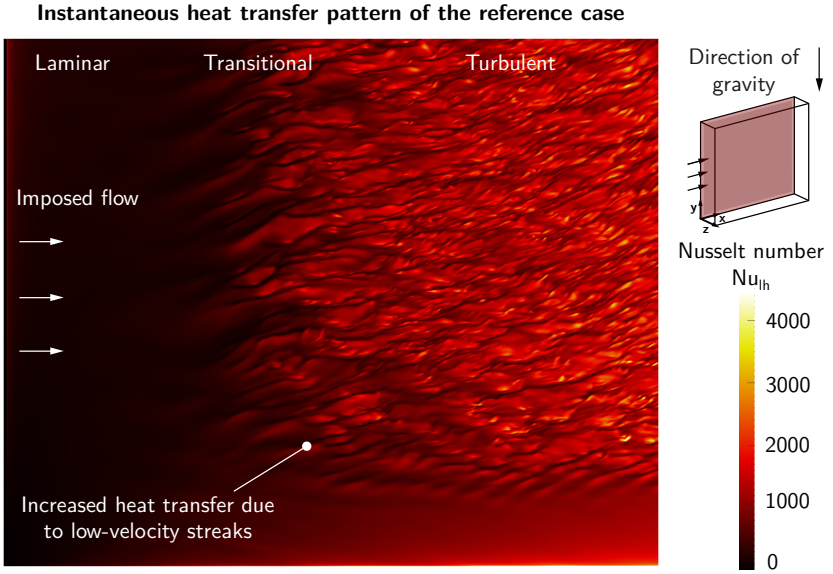


Figure 5.11.: Instantaneous local Nusselt number Nu_{lh} of the reference case describing the heat transfer from the wall into the flow. The flow regimes laminar, transitional, and turbulent are clearly reflected in the heat transfer rates.

From the observation that this growth is not linear follows a decrease in the dimensionful heat transfer coefficient h ($\mathrm{W/m^2K}$). This represents an expected behavior for a flow with growing boundary layers and is in line with the reducing temperature gradients in Figure 5.8. As noted before, no clear dependency of the mixed convection with the height can be observed for the reference case. At the bottom, the high heat transfer rate due to cold fluid entrainment and due to the horizontal transition can be seen. Even though the flow setup of the reference case is different from the work of Siebers (1983) (i.e. his Richardson number being $\mathrm{Ri} = 3.0$), the effects discussed above have been observed in his results as well. Yet, Sieber's observation of a decreasing heat transfer coefficient is more pronounced than for the present result. This difference is mainly provoked by his use of real air as a working fluid instead of an ideal incompressible fluid, which inherently involves different temperature-dependent thermophysical properties.

Contrary to the experimental work of Siebers (1983), the use of highly resolved LES in the present study allows a detailed analysis of the heat transfer. Figure 5.13 presents the spatial evaluation of the major heat transfer mechanisms along the centerplane of the reference case. The sampling positions in the

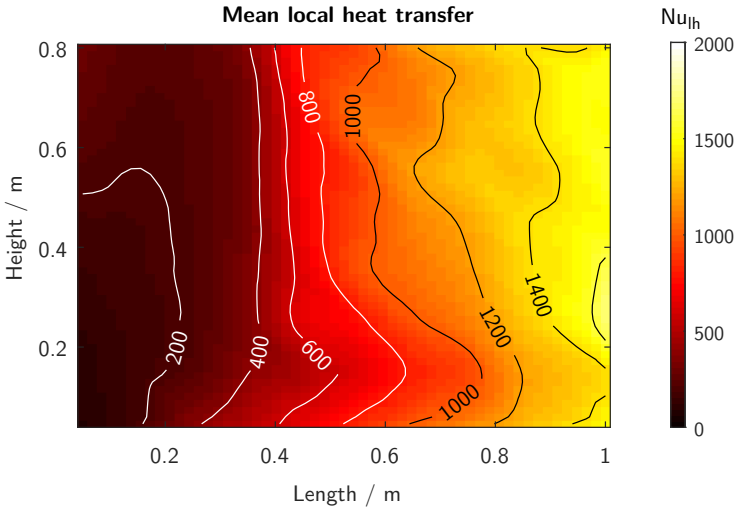


Figure 5.12.: Time-averaged mean heat transfer (Nusselt number) for the reference case.

transitional and turbulent regime are identical to the figures above. As described in Chapter 3.6, where the evaluation method was introduced, the figure can be interpreted as a net heat flow or a local source/sink term associated to the respective transport mechanism.
In the transitional regime (top), the turbulent transport of heat only plays a minor role. As for the cases of two-dimensional mixed convection, heat gets introduced into the viscous sublayer (dark shading) exclusively by diffusive transport in wall-normal direction – most of which is conduction (molecular diffusion) and some is the modeled flux on the subgrid scale (turbulent diffusion). The peak in vertical velocity in the buffer layer (light shading) represents a net introduction of heat by advection. It is counterbalanced by turbulent transport. In the outer boundary layer, this image is reversed with heat being led away by advection and introduced by turbulent fluctuations and by diffusive transport. Keep in mind that the evaluation of all diffusive terms tends to be numerically instable due to the limitations discussed in Chapter 3.6.
Comparing the general source/sink strength in all three diagrams shows the substantial increase in the heat transfer rate between the transitional and turbulent regime (first to second graph), and the slight decrease within the latter (second to third graph). The size of the boundary layer region influenced by heat transfer significantly grows after transition.
Unsurprisingly, at both sampling locations in the turbulent regime, turbulent

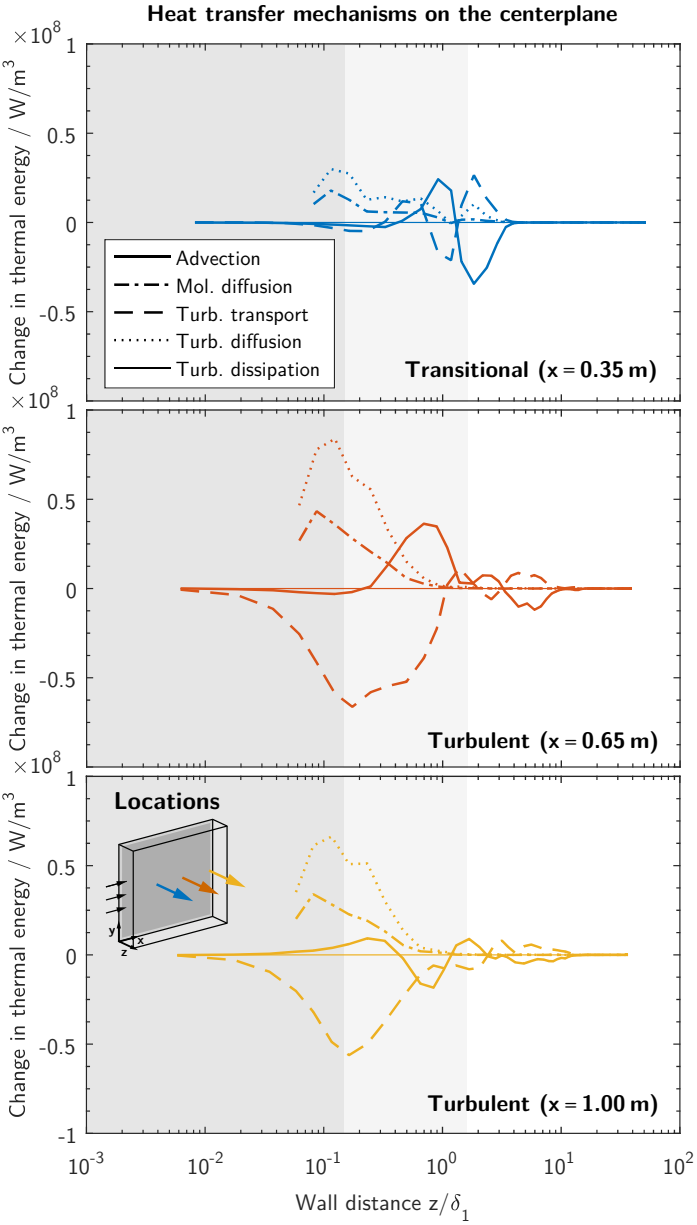


Figure 5.13.: Evaluation of the different heat transport mechanisms within the transitional and turbulent boundary layer of the reference case. Dark shading represents the viscous sublayer and light shading the buffer layer.

transport has a major impact. In the buffer layer, the net drain of heat is almost entirely by turbulent transport, counterbalancing the introduction of heat by the diffusive mechanisms. Thereof, molecular diffusion is exceeded by its modeled counterpart on the subgrid scale, showing the influence of the turbulence model in the inner boundary layer. While at $x = 0.65\,\mathrm{m}$, the local change rate by advection of heat through the vertical velocity peak is positive, it turns negative at $x = 1.00\,\mathrm{m}$. At the same time, the magnitude reduces. Recapitulating the boundary layer thickness (Figure 5.7) shows that the first position is in a region where δ_1 exhibits an increase, whereas in the second, it stagnates. This indicates that the turbulent temperature boundary layer is still in a phase of development at $x = 0.65\,\mathrm{m}$. In the outer boundary layer, at both positions, turbulent transport and advection counterbalance one another at different prefixes. Due to the logarithmic scaling of the figure, this state describes most of the boundary layer.

5.1.4. Turbulence

The previous section has pointed out the strong interaction between turbulence and the heat transfer. Following up this discussion, Figure 5.14 presents the turbulent coherent structures of the reference case, in form of the second invariant of the velocity gradient tensor ($Q > 10$), see Chapter 2.1.4. The laminar-turbulent transition can easily be identified in the figure: Here, elongated low-velocity streaks develop, the footprint of which on the instantaneous Nusselt number has been described above. As noted before, the transition occurs along a vertical and along a horizontal line. The fact that the flow does not transition into a turbulent flow state at the bottom of the domain gives an indication that a certain Gr_y is a premise for turbulence, underlining the impact of buoyancy. The orientation of the streaks is in streamwise direction. However, due to the buoyant updraft, the local boundary layer flow is not necessarily horizontal, but follows the local flow angle shown in Figure 5.9. This allows to derive the approximate wall distance of each structure by evaluating its flow angle and comparing it to the above-mentioned figure. Conforming with theory (see Section 2.1.4), the angle between 30° (bottom) and 39° to 41° (left side) locates the streaks in the buffer layer. The observation that the orientation of each distinct streak remains virtually constant, leads to the conclusion that the streaks do not significantly change their wall distance. While they appear stable at first, they soon exhibit instabilities, and further turbulent coherent structures emerge. Some aspects of the streak-vortex interaction seen here have been discussed in Section 2.1.4. Boiko et al. (2011) suggests various mechanisms as a cause for their disintegration, including interaction with Tollmien-Schlichting instabilities (which, however, are not visible here). Compared to the streaks, the resulting structures exhibit lower flow angles (up to almost horizontal orientation), showing their position in the outer boundary layer. The figure highlights the example of a wall-attached hairpin vortex. In the context of its orientation, it is noticeable

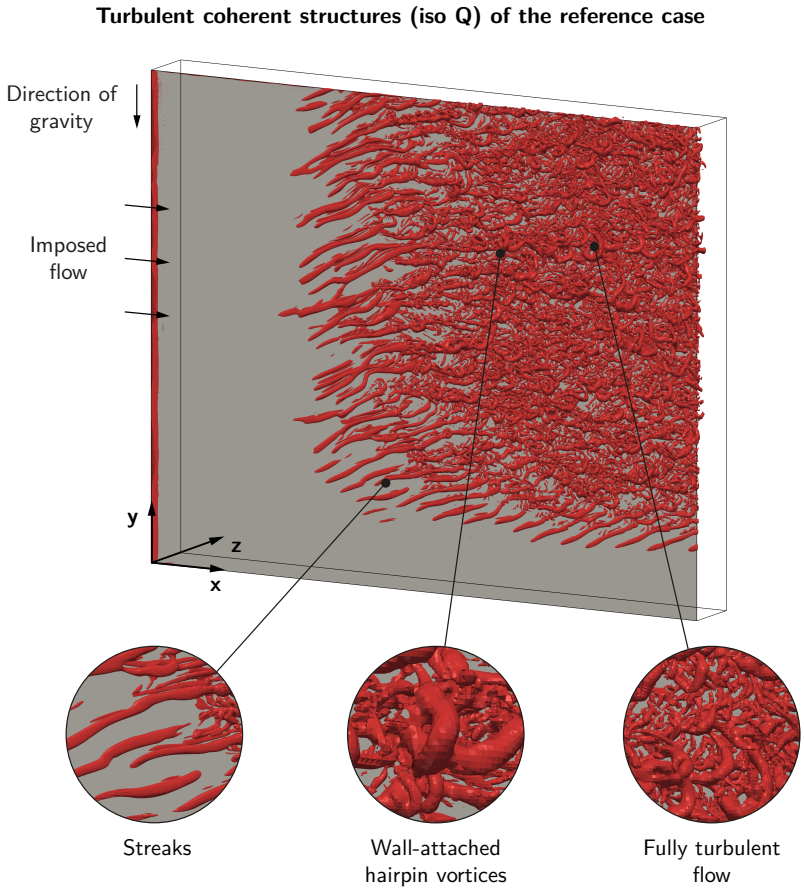


Figure 5.14.: Iso-surface representation of the turbulent coherent structures ($Q = 10$) of the reference case. The laminar-turbulent transition along a vertical and a horizontal line can easily be recognized in form of low-velocity streaks, eventually forming coherent structures like wall-attached hairpin vortices.

that the vortex is not symmetric. While its top is far away from the region influenced by buoyancy, thus traveling with the horizontal flow, the movement of its wall-attached bottom exhibits a strong vertical component. Furthermore, the Q-field in the turbulent regime confirms the observation, that – for the reference case – little variation occurs in vertical y-direction. It should be noted that the transition visually neither resembles the high-velocity case of two-dimensional

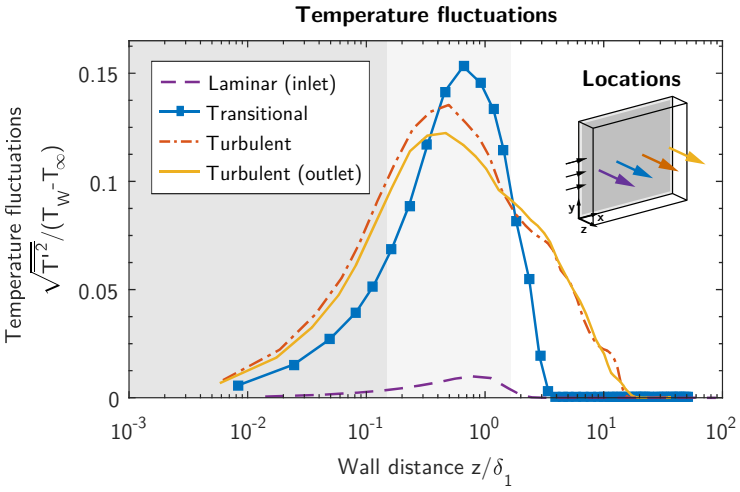


Figure 5.15.: Temperature fluctuations at the three locations discussed above and one addition location near the inlet (laminar regime).

mixed convection – as the streaks are larger in size for the present case – nor the low-velocity case – as the present case does not exhibit the characteristic Tollmien-Schlichting instabilities ahead of the transition zone. This supports the hypotheses that, even though both setups cover turbulent mixed convection, the flows are vastly different.

The scaled temperature fluctuations in the boundary layer are shown in Figure 5.15. One sampling location at the inlet ($x = 0.05\,\mathrm{m}$) has been added to the ones used above, providing some kind of laminar baseline. While temperature fluctuations are virtually non-existent at this location, they literally explode during transition. Here, the highest fluctuations occur in the buffer layer at a dimensionless wall distance of $z/\delta_1 \approx 0.8$, which is precisely the location of the vertical velocity peak. The presence of these intense fluctuations during transition is very surprising, as the average temperature profile (see Figure 5.4) did not exhibit much indication of changing heat transport mechanisms at $z/\delta_1 \approx 0.8$ – nor did the evaluation of the mechanisms in Figure 5.13 show much turbulent transport. This leads to the conclusion (being confirmed by the following profiles) that velocity fluctuations – which are required for $\boldsymbol{u}'T'$, the turbulent transport of heat – are not yet elevated at this location. Hence, during the transition, significant temperature fluctuations occur before velocity fluctuations are fully developed. This finding proves, that the resulting fluctuation in buoyant force and the instability it introduces into the boundary layer

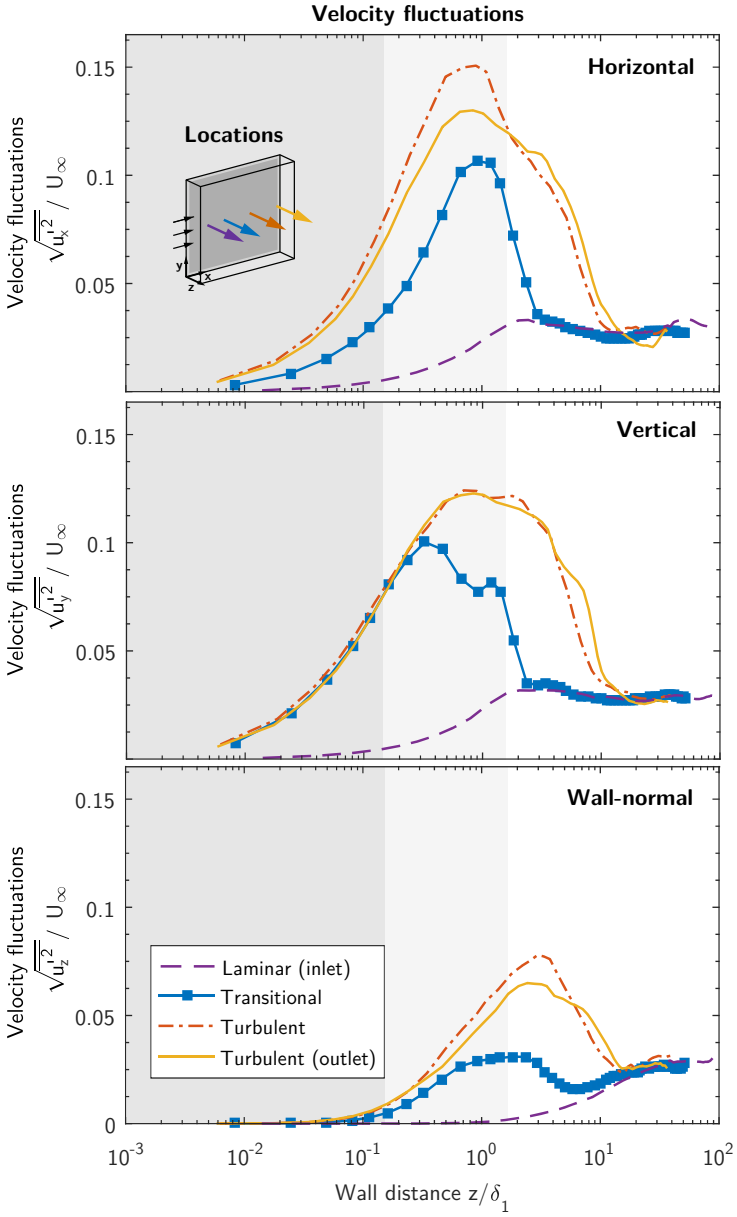


Figure 5.16.: Velocity fluctuations at the three locations discussed above and one addition location near the inlet (laminar regime).

plays a major role in the onset of turbulence. At the end of this chapter, the influence of buoyancy will be investigated, and the hypothesis that buoyancy actually triggers the laminar-turbulent transition in three-dimensional mixed convection will be confirmed.
After transition, the magnitude of the temperature fluctuations decreases, which is consistent with the finding that the general heat transfer rate decreases as a result of a growing boundary layer. This growth and the turbulent transport of heat in the outer boundary layer is reflected in the presence of fluctuations in the outer boundary layer (up to $z/\delta_1 \approx 20$) for both locations in the turbulent regime. Comparing the profile to the mean temperature profile (Figure 5.8) shows that the location where the mean profiles exhibit a bend is congruent with the location where the highest fluctuations occur. Also, the region in the outer boundary layer where turbulent transport and advective transport of heat alternate (see discussion of heat transfer mechanisms in Figure 5.13) stretches out to the wall distance of $z/\delta_1 \approx 20$ mentioned above.

Figure 5.16 shows the corresponding fluctuations in each of the three velocity components, scaled to the imposed velocity u_∞. The magnitude is highest in horizontal direction, being in the same range as the scaled temperature fluctuations. The vertical velocity fluctuations are slightly lower and the fluctuations in wall-normal direction exhibit the lowest intensity. This distribution is expected, as the highest absolute velocity occurs in x-direction, followed by y and z. The laminar baseline is the dashed line in the figure and shows no fluctuations except for those imposed through synthetic turbulence at the inlet boundary condition. For this reason, all profiles (all components at all locations) converge to a scaled magnitude of $\sqrt{u'^2}/u_\infty = 0.025$ in the free stream, where the wall does not influence the flow. As suggested above, when discussing T', the fluctuations u'_x and u'_z are still low at the location of transition, grow in the turbulent regime, until they slightly reduce toward the outlet. This slight reduction is attributed to a lower production of turbulent kinetic energy (see the following Figure 5.17). In vertical direction, u'_y grows during transition as well, however, remains on a constant level throughout the turbulent flow regime. Accordingly, buoyancy fuels these fluctuations. For the horizontal and the vertical direction, the wall-normal position of the peaks in temperature and velocity fluctuations are found at the same dimensionless wall-distance (compare Figure 5.15). For the wall-normal direction, the peak in T' is located closer to the wall that the peak for u'_z. Even though the position of the peaks hardly coincides, there is still some overlapping in the profiles, i.e. in the outer boundary layer. This combination of velocity and temperature fluctuation results in turbulent heat transport in wall-normal direction (see the discussion of heat transfer mechanisms where the turbulent transport alternates with advective transport in the outer boundary layer).

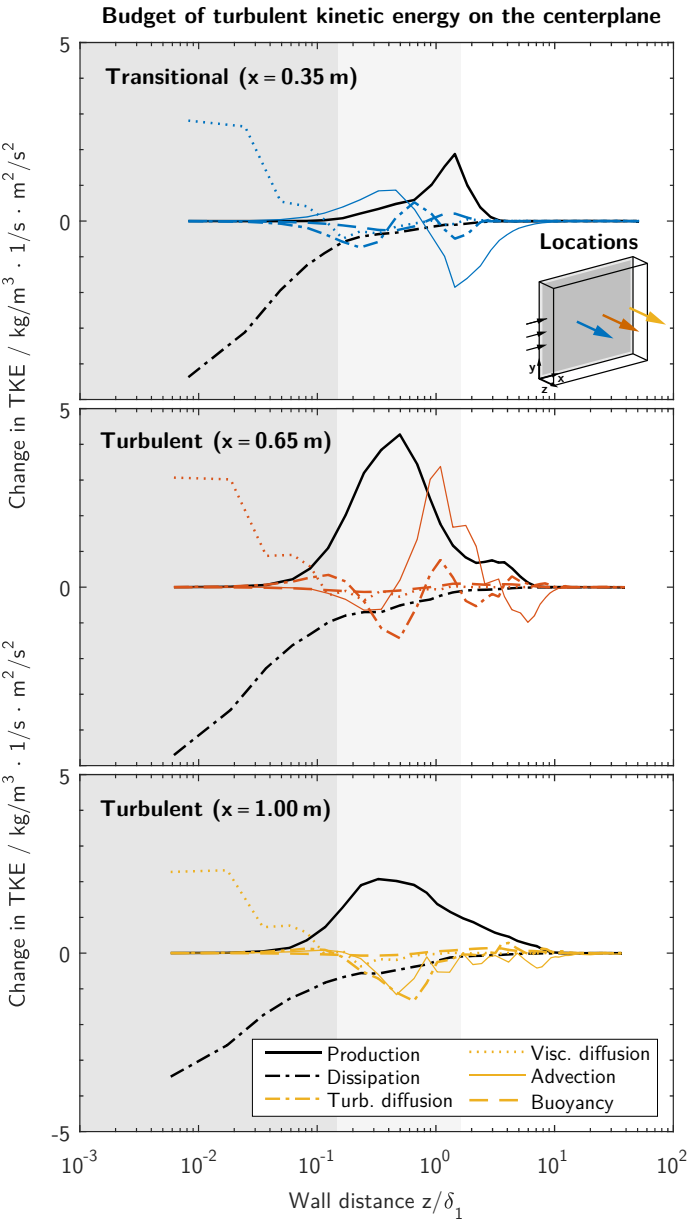


Figure 5.17.: Evaluation of the TKE budget equation at three locations across the domain.

Evaluating the budget equation for turbulent kinetic energy (Eqn. 2.18) produces Figure 5.17, showing the different mechanisms involved in the transport, production, and dissipation of resolved TKE.
The production rate for the two-dimensional validation cases discussed in Chapter 3.6 exhibited two peaks. In the three-dimensional reference case, for all locations evaluated, only one single peak is present. The reason for this difference is the different form of the $|\boldsymbol{u}|$-profile: In the two-dimensional cases, the velocity magnitude increases until it peaks and drops to the free-stream value. In the present three-dimensional case, the velocity magnitude continuously grows until its highest value is reached in the imposed free stream. As production depends on the change rate $\partial|\overline{\boldsymbol{u}}|/\partial z$, its profile can only exhibit one single peak. Consequently, the production reflects the profiles of the velocity magnitude in Figure 5.9: First, a narrow peak for the production rate at the transition. Second, a higher production rate in the turbulent regime (as $\partial|\overline{\boldsymbol{u}}|/\partial z$ is significantly higher). Third, there is little variation in the dimensionless representation of the mean velocity magnitude throughout the turbulent regime. However, the growth in boundary layer thickness reduces the gradient $\partial|\overline{\boldsymbol{u}}|/\partial z$, resulting in a lower strain rate and thus in a lower TKE production (compare the rate at $x = 0.65\,\mathrm{m}$ to the one at $x = 1.00\,\mathrm{m}$). Fourth, the $|\overline{\boldsymbol{u}}|$-profile at $x = 0.65\,\mathrm{m}$ grows steeper at $z/\delta_1 \approx 3$, which is reflected in a small "secondary hump" in the corresponding TKE-production rate.
The profiles for viscous diffusion and dissipation are almost identical to those of two-dimensional mixed convection: TKE is transported towards the wall, where it dissipates. The production of by buoyancy is almost constant at low level across the turbulent regime and slightly elevated during transition. For most of the outer boundary layer, advective transport and turbulent diffusion counterbalance one another. As the turbulent transport is low during transition, the TKE produced is removed by advection. This characteristic appearance of peaks in advective and turbulent transport at the outer flank of the production zone has also been observed in literature for other turbulent flows (Laval et al., 2012).

5.2. Influence of the free stream

In order to investigate the role of the free stream in three-dimensional mixed convection, simulations with varying flow conditions were conducted. While the case Grashof-numbers (and thus the wall temperature) remained constant at moderate level, a change in imposed velocity led to varying Reynolds numbers. In the following, the simulation results of the reference case (equipollent mixed convection) are compared to the results of two other cases: First, a simulation featuring a low imposed velocity ($\mathrm{Re_L} = 1.71 \cdot 10^5$), which – for the given Grashof number – is a flow in the buoyancy dominated regime ($\mathrm{Gr_H}/\mathrm{Re_L^2} = 13.76$). Second, a simulation featuring a high velocity ($\mathrm{Re_L} = 7.52 \cdot 10^5$), however, still representing the equipollent mixed convection regime ($\mathrm{Gr_H}/\mathrm{Re_L^2} = 0.72$). [2]As the present and the following section compare different flows, the case-specific measure for a horizontal position is the dimensionless Reynolds number Re_x. Accordingly, vertical positions are referred to by the Grashof number Gr_y.

5.2.1. Flow fields

The influence of an increasing free stream on the flow fields is presented in Figures 5.18 to 5.20. The fields are located on a horizontal plane at the vertical center of the domain (0.4 m) with the inlet on the left side. As the wall temperature is identical in all three cases, this location translates into a constant Grashof number of $\mathrm{Gr}_y = 4.7 \cdot 10^{10}$. Each of the figures compares the low-velocity case (top), the reference case (center), and the high-velocity case (bottom).

Figure 5.18 is the instantaneous horizontal velocity u_x. Since the magnitude varies over a broad range between the cases, the values are scaled to the respective u_∞, resulting in a homogeneous appearance of the free stream. In the boundary layer, however, the three cases exhibit major differences. Most striking is the location of the laminar-turbulent transition: When increasing the velocity, the transition zone travels in streamwise direction, delaying the development of a fully turbulent flow. For the low-velocity case, the onset of turbulence becomes visible at $\mathrm{Re}_x \approx 0.3 \cdot 10^5$. Increasing the velocity to the value of the reference case moves that threshold to $\mathrm{Re}_x \approx 1.5 \cdot 10^5$. In the high-velocity case, transition is observed as late as $\mathrm{Re}_x \approx 4.5 \cdot 10^5$. This behavior is counterintuitive at first sight, as for standard plate flows, increasing the flow velocity accelerates the onset of turbulence. However, the observed effect is well-known from two-dimensional mixed convection, being referred to as laminarization (see Chapter 2.3 for literature and Chapter 3.6 for the present two-dimensional simulations). The figure proves that the laminarization effect also occurs in three-dimensional mixed convection.

[2]Please refer to Chapter 4 for a detailed physical description.

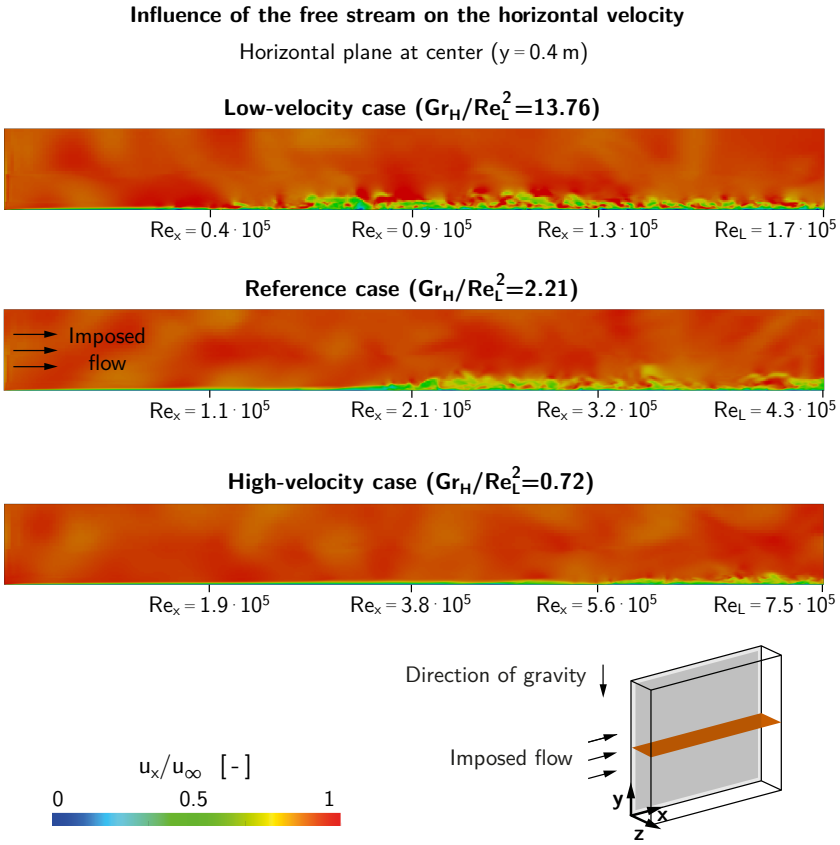


Figure 5.18.: The instantaneous horizontal velocity fields for different imposed velocities, illustrating the influence of the free stream on three-dimensional mixed convection. The top field is a case featuring a low imposed velocity, the center field is the reference case, and the bottom field is a high-velocity case. The velocity is scaled to the respective imposed velocity u_∞. The onset of turbulence occurs earlier for lower velocities, proving that the laminarization effect discussed for two-dimensional mixed convection occurs in three-dimensional flow as well.

In the preceding section, it was shown that the instability which is introduced to the boundary layer by buoyancy is a key factor in the laminar-turbulent transition. Consequently, reducing the relative influence of buoyancy (expressed by the Richardson number $\mathrm{Gr}/\mathrm{Re}^2$), stabilizes the boundary layer, which explains the presence of the laminarization effect in three-dimensional mixed convection. At

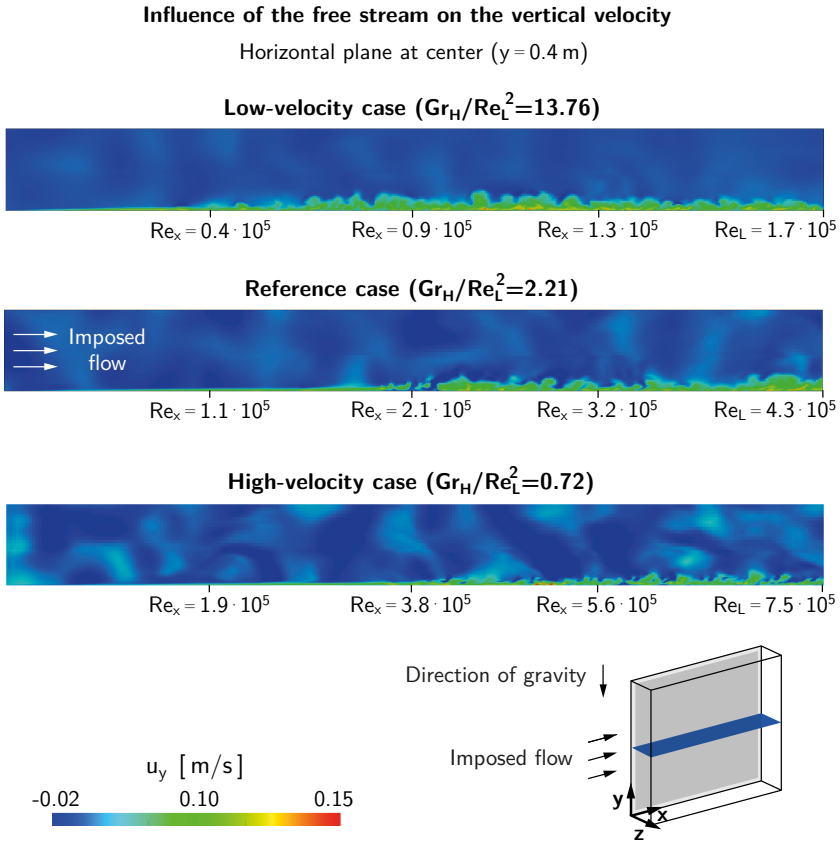


Figure 5.19.: The instantaneous vertical velocity fields (corresponding to Figure 5.18) shows that the buoyant updraft is strongest for the lowest imposed velocity.

this point, it is elucidating to have a look at the instantaneous fields of vertical velocity. The fact that the increase in imposed velocity reduces the relative influence of buoyancy is clearly reflected in the u_y-boundary layer: In the low-velocity case, dominated by buoyancy, the vertical velocity grows high in the inner boundary layer. Increasing the free-stream velocity brings the flow in the equipollent mechanisms regime, which clearly results in significantly lower vertical velocities. Note that – contrary to the first figure – the vertical velocity is expressed in absolute values, which is due to the lack of a physically reasonable scaling parameter. Consequently, the same colormap applies to all three fields. For this reason,

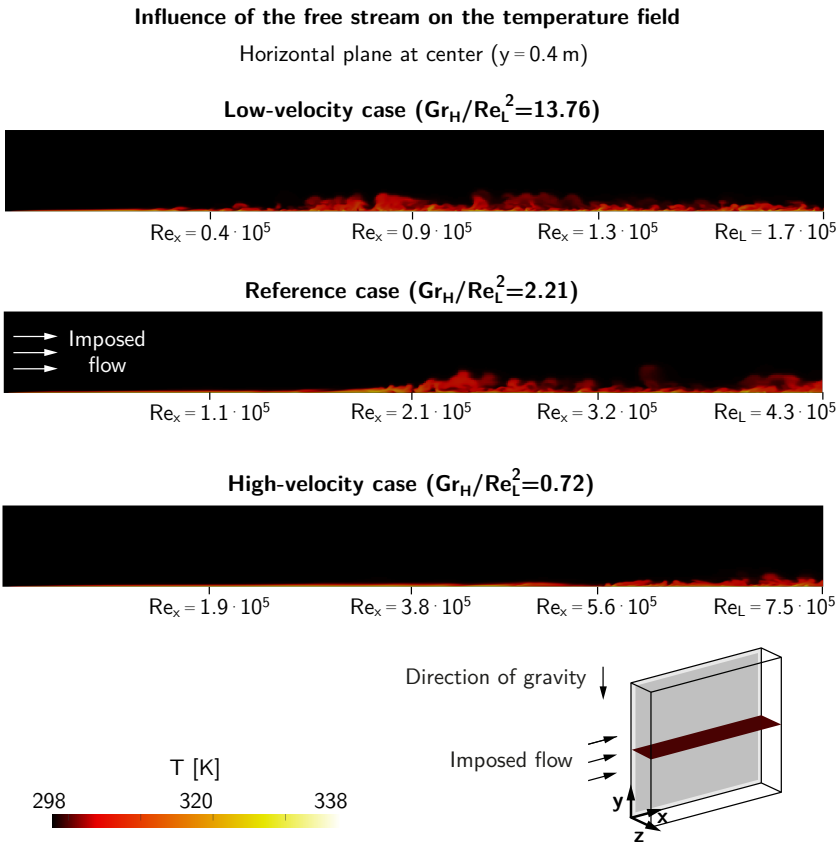


Figure 5.20.: The instantaneous temperature fields (corresponding to Figure 5.18) showing the same effects as for the velocity boundary layers.

the free-stream fluctuations by synthetic turbulence, whose magnitude depends on the imposed velocity, become considerably more apparent for higher velocities.

Both fields shown have in common that the turbulent boundary layer is thinner for higher velocities. One particular effect occurs in the low-velocity case: After transition, both boundary layers grow, reach a maximum thickness, and start to shrink again. This effect is specific for the case characterized by a high Richardson number. Here, it only appears around the centerplane, and will be discussed later on.

As the wall temperature is not changed in this part of the study, the scaling of the corresponding temperature fields (Figure 5.20) is absolute. As it has been discussed above for the reference case, distinct features in the fields of the vertical velocity (e.g. vortices) are present in the temperature fields as well, underlining the strong coupling of both fields due to buoyancy. In general, the temperature fields show precisely the same effects as the velocity fields, with respect to the influence of free-stream velocity, boundary layer development, and the visibility of the laminar-turbulent transition.

5.2.2. Boundary layers

The contour plot of the local boundary layer displacement thickness δ_1 (shown in Figure 5.21) allows to identify the location of the laminar-turbulent transition. The end of this zone, where the flow has reached fully turbulent state, is characterized by a steep growth in δ_1. The respective mixed convection regime is clearly reflected in the spatial development of the boundary layer: In the equipollent regime (high-velocity and reference case), δ_1 grows in horizontal direction ($\delta_1 \sim \mathrm{Re}_x$). Also, very little variation of the thickness with an increasing free-stream velocity can be observed. Compared to the reference case, the boundary layer of the high-velocity flow is just slightly less thick. When buoyancy dominates (low-velocity case), δ_1 grows with Re_x as well throughout the laminar regime. After transition to turbulence, the growth continues in horizontal direction ($\delta_1 \sim \mathrm{Re}_x$) but also exhibits some dependency on the vertical position ($\delta_1 \sim \mathrm{Gr}_y$). The resulting distribution grows towards the upper corner at the outlet. This simulation case exhibits by far the highest thickness, which is the result of a low imposed u_∞, a strong updraft $u_y > u_\infty$, and thus a large δ_1-defining velocity difference $|u_\infty - |\boldsymbol{u}||$. The latter is integrated over a wide boundary region influenced by the updraft (see Eqn. 2.56).
All cases have fairly thin boundary layers at a low y. As discussed for the reference case, this is caused by the entrainment of fluid though the bottom, compensating the buoyant updraft in the boundary layer. As this flow enters the domain through a defined boundary condition, it encounters the plate without having formed a boundary layer. Furthermore, when discussing the velocity field of the low-velocity case, a spatial reduction in the boundary layer thickness within the turbulent regime was observed. This visual perception is confirmed in Figure 5.21 (top) for a horizontal line along the vertical center. Later in this section, this effect will be linked to the entrainment as well.

Based on the following figures, the influence of the free stream on the temperature and velocity boundary layer profiles will be discussed. For each of the three cases introduced above, the profiles were evaluated at three locations: In the transition zone, at a position within the turbulent flow regime, and at the top near the outlet. While the third location is fixed and lies within the

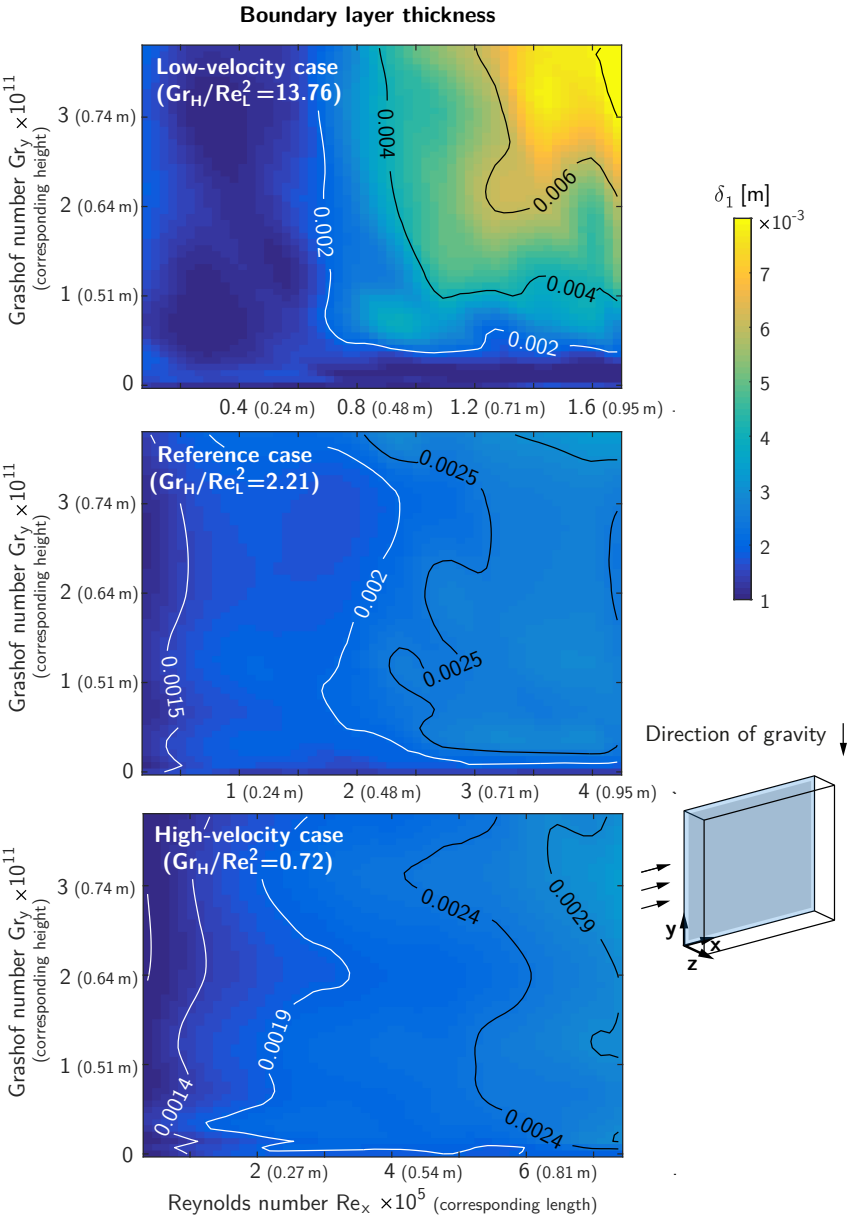


Figure 5.21.: Influence of increasing free-stream velocity on the boundary layer displacement thickness δ_1.

Table 5.1.: Overview of sampling locations for the evaluation of the free-stream influence.

Case	Location		
	Transitional	Turbulent (vertical center)	Turbulent (vertical top)
Low-velocity			
Reynolds number Re_x	$0.25 \cdot 10^5$	$0.58 \cdot 10^5$	$1.67 \cdot 10^5$
Grashof number Gr_y	$6.71 \cdot 10^{10}$	$6.71 \cdot 10^{10}$	$3.77 \cdot 10^{11}$
x-location	0.15 m	0.35 m	1.00 m
y-location	0.45 m	0.45 m	0.8 m
Reference			
Reynolds number Re_x	$1.05 \cdot 10^5$	$2.31 \cdot 10^5$	$4.21 \cdot 10^5$
Grashof number Gr_y	$6.71 \cdot 10^{10}$	$6.71 \cdot 10^{10}$	$3.77 \cdot 10^{11}$
x-location	0.25 m	0.55 m	1.00 m
y-location	0.45 m	0.45 m	0.8 m
High-velocity			
Reynolds number Re_x	$3.32 \cdot 10^5$	$7.37 \cdot 10^5$	$7.37 \cdot 10^5$
Grashof number Gr_y	$6.71 \cdot 10^{10}$	$6.71 \cdot 10^{10}$	$3.77 \cdot 10^{11}$
x-location	0.45 m	1.00 m	1.00 m
y-location	0.45 m	0.45 m	0.8 m

fully turbulent flow for all cases, the first two locations vary depending on the flow itself (i.e. where the onset of turbulence occurs, see Table 5.1). Again, the approximate location of the viscous sublayer and the buffer layer for the three cases are indicated by shading.

The dimensionless mean temperature profiles are presented in Figure 5.22. A clear difference between the transitional and the turbulent flow is evident for all imposed velocities: In the profiles of the transition zone, the temperature continuously decreases until it reaches the free stream value. The profiles of all cases exhibit the same shape, but are shifted sideways due to the difference in the scaling parameter δ_1. In the turbulent flow, the profiles are virtually identical for the two cases in the equipollent mixed convection regime (line with square and line with diamond makers). They show the characteristic bend at $z/\delta_1 \approx 5...7 \cdot 10^{-1}$ marking the region where diffusive transport of heat is replaced by turbulent transport. The third profile of the buoyancy-dominated case (line with triangles) generally has a similar shape. However, in the turbulent profile of the center figure, its δ_1 is smaller than for the other cases, resulting in a shift to the right. In the turbulent profile of the bottom figure, δ_1 of the low-velocity case is considerably larger as a result of the strong buoyancy. The resulting shift to the left can clearly be recognized in the location of the first marker, which shows the position of the wall-adjacent cell.

The two Figures 5.23 and 5.24 show the influence of the free stream on the local flow angle γ and the scaled velocity magnitude $|\boldsymbol{u}|/u_\infty$. The reduction

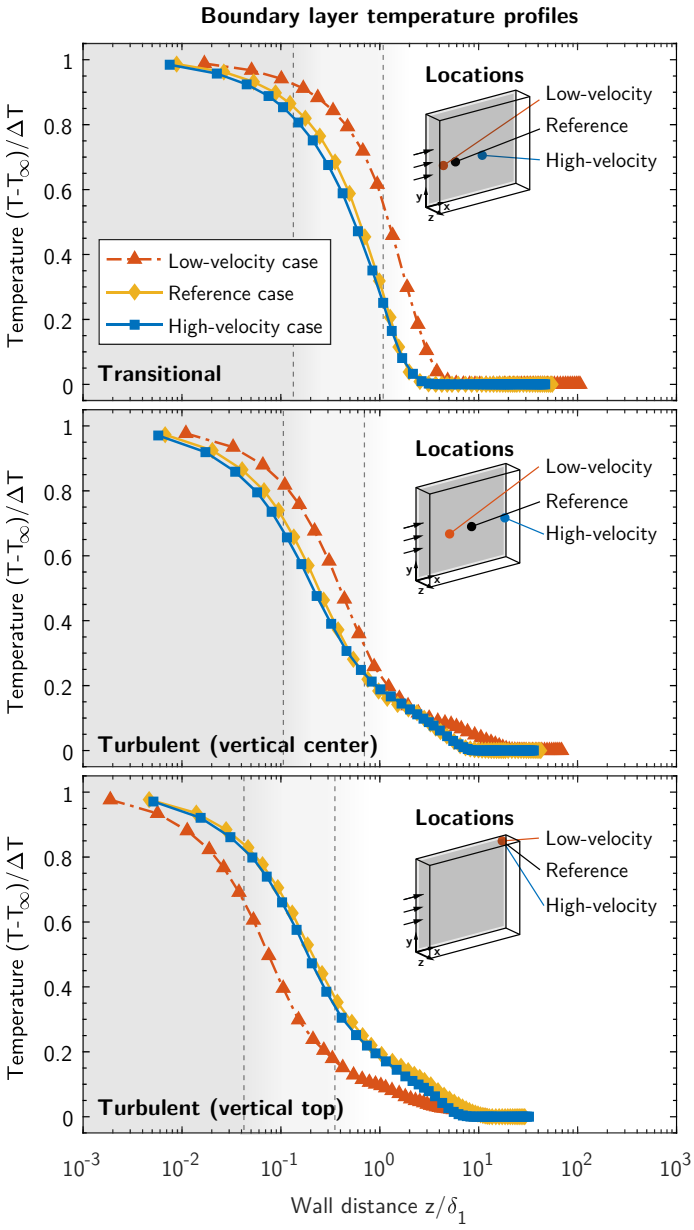


Figure 5.22.: Mean temperature boundary layer profiles for the three cases at the location of transition, in the turbulent regime, and at the top near the outlet. The shading indicates the approximate location of the viscous sublayer and the buffer layer.

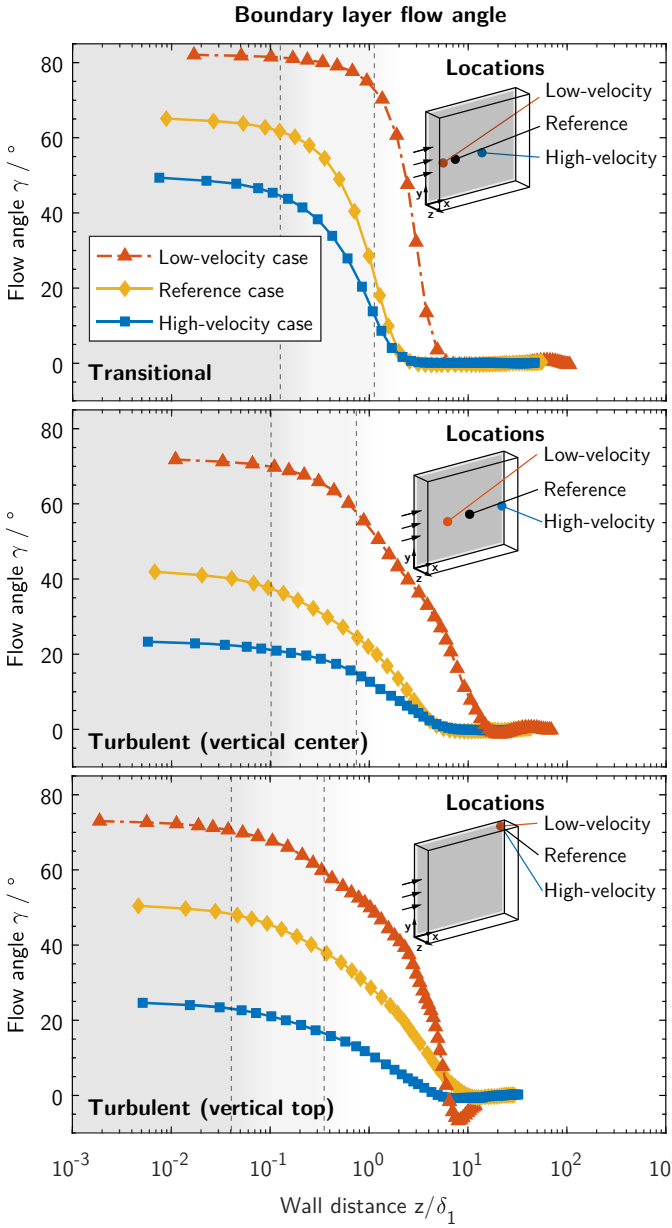


Figure 5.23.: Profiles of the flow angle for the polar representation of the velocity boundary layer for the three simulation cases investigated in this part of the study.

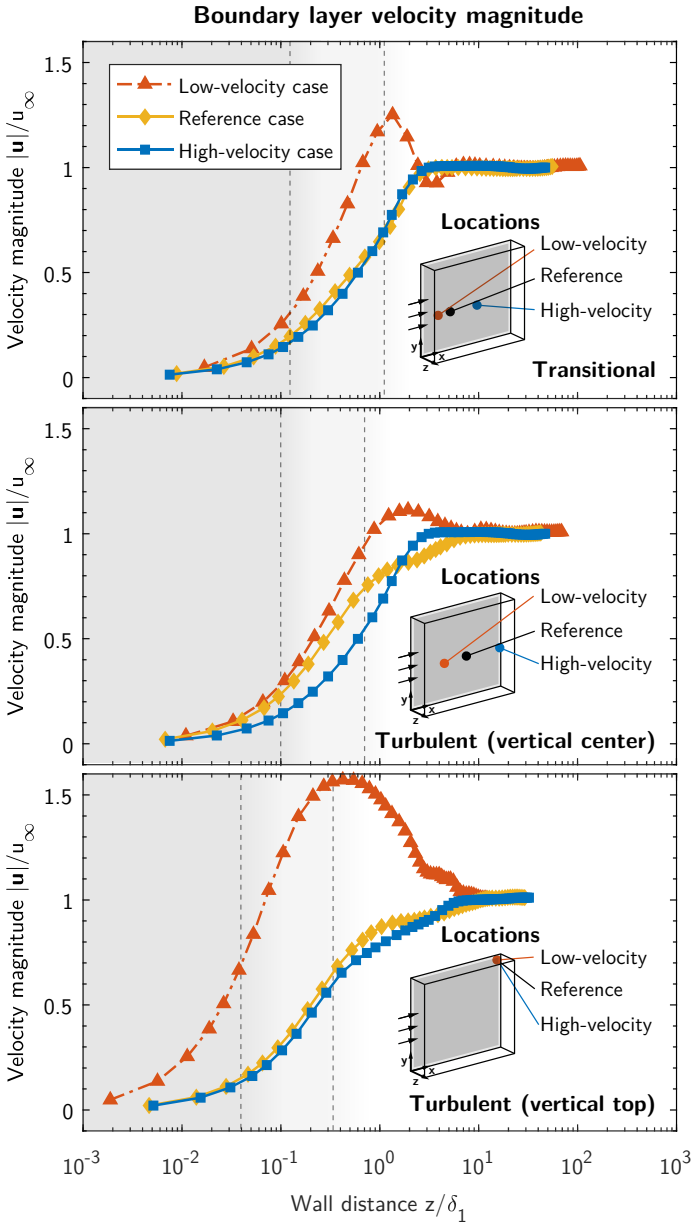


Figure 5.24.: The scaled velocity magnitude, corresponding to the flow angle in the preceding Figure 5.23.

in γ during transition, as discussed above, is again apparent in all three cases. Unsurprisingly, the velocity profiles are significantly different for the two mixed convection regimes:

Equipollent mixed convection regime (line with diamonds for the reference case and line with squares for the high-velocity case): As for the temperature above, the velocity boundary layer exhibits little variation between the two cases in the equipollent mechanisms regime. The profiles only differ in three points: First, the intensity of the buoyant updraft is lower for the high-velocity (low-Richardson number) case, which is reflected in a lower flow angle γ. Second, for the high-velocity case, no transport of momentum into the buffer layer (see discussion of the reference case) is recognizable at the first turbulent location. For this reason, the scaled magnitude of the high-velocity case is higher than the one of the reference case for $z/\delta_1 > 2 \cdot 10^0$. As the momentum is not removed from the outer boundary layer, it certainly cannot be reintroduced in the buffer layer. Here, its contribution lacks, resulting in a lower velocity magnitude. This absence of momentum transfer is related to the late onset of turbulence compared to the reference case. Consequently, for the second turbulent location on top of the domain, where the higher influence of buoyancy (higher local Grashof number, see Table 5.1) boosts turbulence, the momentum transport can be observed in both cases. Third, the peak in u_y, reflected in a slight bend in magnitude, is significantly less prominent for the high-velocity case (see bottom figure). In the turbulent profile at the vertical center, where turbulence was found to be less intense for this case, it is even virtually undetectable (see center figure).

Buoyancy-dominated mixed convection regime (line with triangles): Unsurprisingly, the buoyancy-induced vertical velocity plays an important role in this flow case. In the transitional regime, where the highest angle γ occurs, the flow in the viscous sublayer is almost vertical with $\gamma \approx 82^\circ$. The velocity peak is extremely prominent at all three locations, as shown in the plot of the velocity magnitude profiles. At the top, the maximum magnitude reaches a value of 1.5 times the imposed free-stream velocity. Here, the peak is impressive in size, dominating both the buffer layer and the outer boundary layer.

In the discussion of the instantaneous velocity fields of the reference case, patches of negative vertical velocity were noted in the outer boundary layer and attributed to mass continuity. As the low-velocity case exhibits an intense updraft, these patches grow strong enough to be reflected in the mean velocity profiles of the case. In the turbulent flow angle profile at the vertical center (Figure 5.23), a slight negative hump is visible at $z/\delta_1 \approx 2 \cdot 10^1$. In the γ-profile at the top, the negative flow even causes an undershoot. The occurrence of

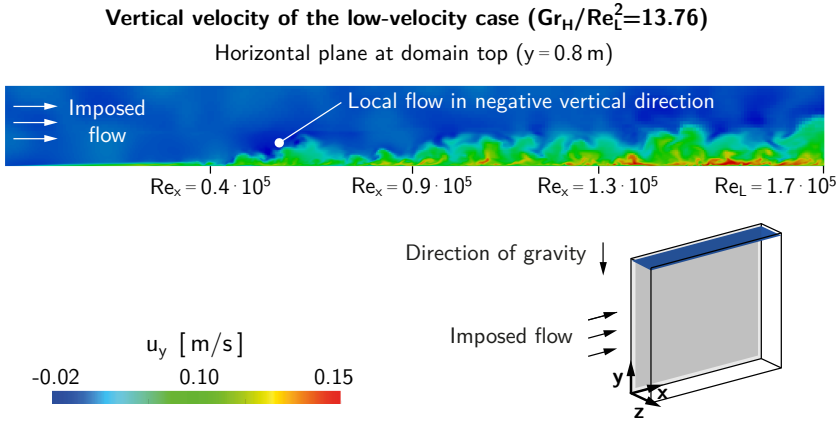


Figure 5.25.: Instantaneous vertical velocity field of the low-velocity case. The location of the plane is near the top of the domain at $y = 0.8\,\mathrm{m}$ or $\mathrm{Gr}_y = 3.77 \cdot 10^{11}$. The second turbulent profile of the preceding figures is thus at the far right of the plane. The field provides an example of the negative velocity patches discussed below.

this undershoot in a region where the horizontal flow component is already strong points out the high intensity of this effect. As a negative vertical flow increases the total velocity magnitude, its profile exhibits an elevation in the outer boundary layer (see bottom of Figure 5.24). Serving as an illustration, Figure 5.25 shows the local negative flow in the instantaneous u_y-field at the top of the domain. Note the sheer size of the boundary layer and the regular patches of negative u_y at this edge. The effect is very distinct in, however, not limited to the buoyancy-dominated flow. At the vertical top location, a very slight undershoot is visible in both profiles for equipollent mixed convection as well.

Figure 5.26 is the alternative representation of the flow angle γ. The streamlines in wall proximity almost point in vertical direction for the low-velocity case (top), illustrating the dominant nature of buoyancy in the inner boundary layer. Its effect, however, reaches far into the free stream. Even at some wall distance, the flow still shows a strong influence of buoyancy. The figure finally explains, why the boundary layer thickness δ_1 decreases with Re_x at the centerplane of the low-velocity case: The updraft grows so strong that – at some point – the fluid in the outer buffer layer no longer originates from the inlet, but is entirely entrained from the bottom instead. The fact that this fluid has flown a significantly shorter distance along the plate, and thus a lower temperature, causes a reduction in the buoyancy-induced turbulence. The lower degree of turbulence is then reflected in

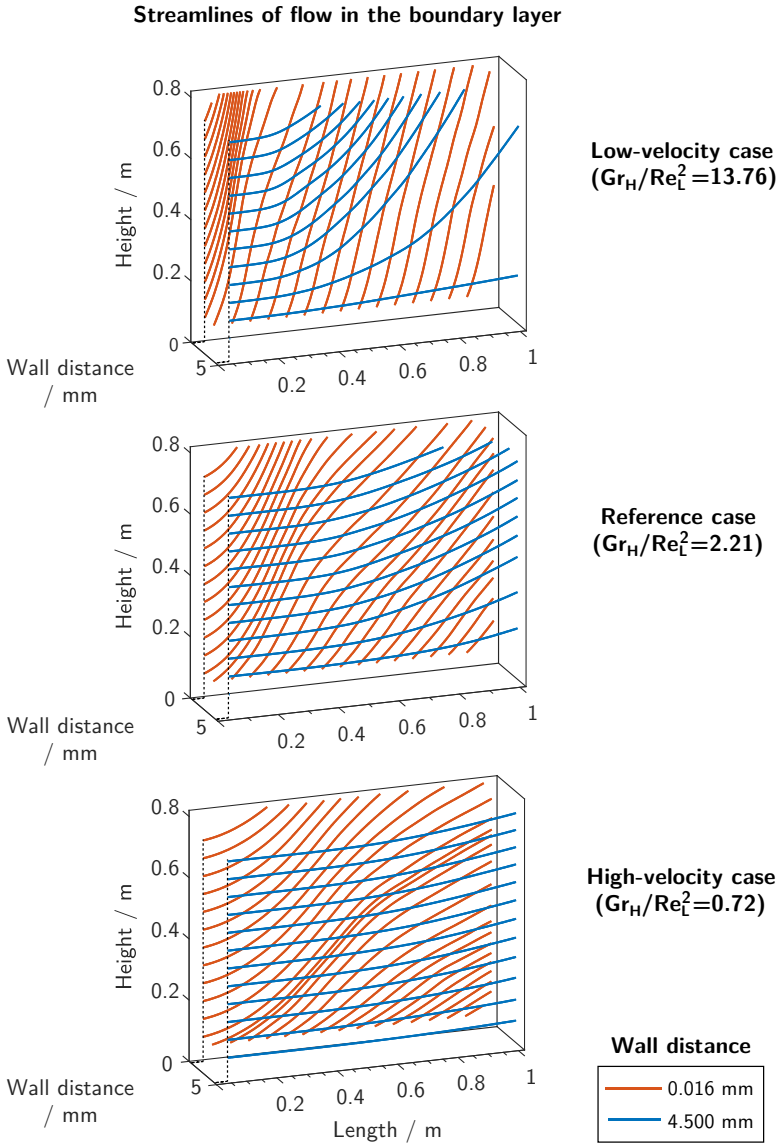


Figure 5.26.: Streamlines for the three different flow cases discussed in this section. The wall distances are 0.016 mm ($z/\delta_1 \to 0$) and 4.5 mm ($z/\delta_1 > 1.5 \cdot 10^0$). The growing influence of buoyancy with lower flow velocities can clearly be observed.

a lower δ_1. For the other cases, the figure illustrates the findings of the velocity profiles, where the influence of buoyancy in the outer boundary layer reduces with higher flow velocities.

5.2.3. Heat transfer

Given the strong influence of the free stream on the flow fields and the boundary layer profiles, it does not come as a surprise that this influence can also be observed in the heat transfer characteristics. Figure 5.27 shows the instantaneous heat transfer pattern in form of the dimensionless Nusselt number Nu_{lh}. Two interesting observations can be derived from the figure: First, a higher imposed flow velocity increases the heat transfer, leading to higher local Nusselt numbers. While the low-velocity case has relatively little elevated Nu_{lh}-values in the turbulent patches, scattered peaks are found in the reference case, and many appear in the turbulent heat transfer of the high-velocity case. Second, the onset of turbulence is significantly delayed for a high velocity. Consequently, the steep increase in heat transfer associated with the transition occurs later in the flow (compare i.e. the reference to the high-velocity case). These two effects – in part – counterbalance each other: While the heat transfer rate in the turbulent regime is lower in the low-velocity case, the onset of turbulence occurs earlier. For higher velocities, the heat transfer rate in the turbulent regime is higher, however, transition occurs later. This leads to the surprising situation where the area-weighted Nusselt number of the high-velocity case ($\overline{\mathrm{Nu}}_{lh} = 770$) is even lower than the one of the reference case ($\overline{\mathrm{Nu}}_{lh} = 780$) – with the case Reynolds number of the first one being 1.75 times larger. Due to the same effect, the area-weighted Nusselt number of the reference case ($\overline{\mathrm{Nu}}_{lh} = 780$) is just slightly higher than the one of the low-velocity case ($\overline{\mathrm{Nu}}_{lh} = 570$) – even though the corresponding Reynolds number is more than 2.5 times larger.
As discussed before, the turbulent coherent structures (i.e. vortices and low-velocity streaks) are reflected in the heat transfer rate, resulting in local peaks. When comparing the footprint of these structures (viz. their orientation) to the flow direction in the viscous sublayer and the buffer layer (see Figure 5.26), almost perfect agreement can be noticed.

The characteristic length scale of the Nusselt number was introduced and discussed above. For the low-velocity case, lh approaches y, whereas for the cases with higher imposed velocity, lh approaches x.
For the latter, the two cases in equipollent mixed convection regime, the dependency $\mathrm{Nu}_{lh} \sim \mathrm{Re}_x$ holds true, as little variation of the heat transfer in vertical direction can be found in Figure 5.28. The high heat transfer rate at the inlet, caused by the presence of cold fluid, is eliminated due to $lh \approx x \to 0$. On the contrary, the high heat transfer rate at the bottom is reflected in a Nusselt number that rises with x.

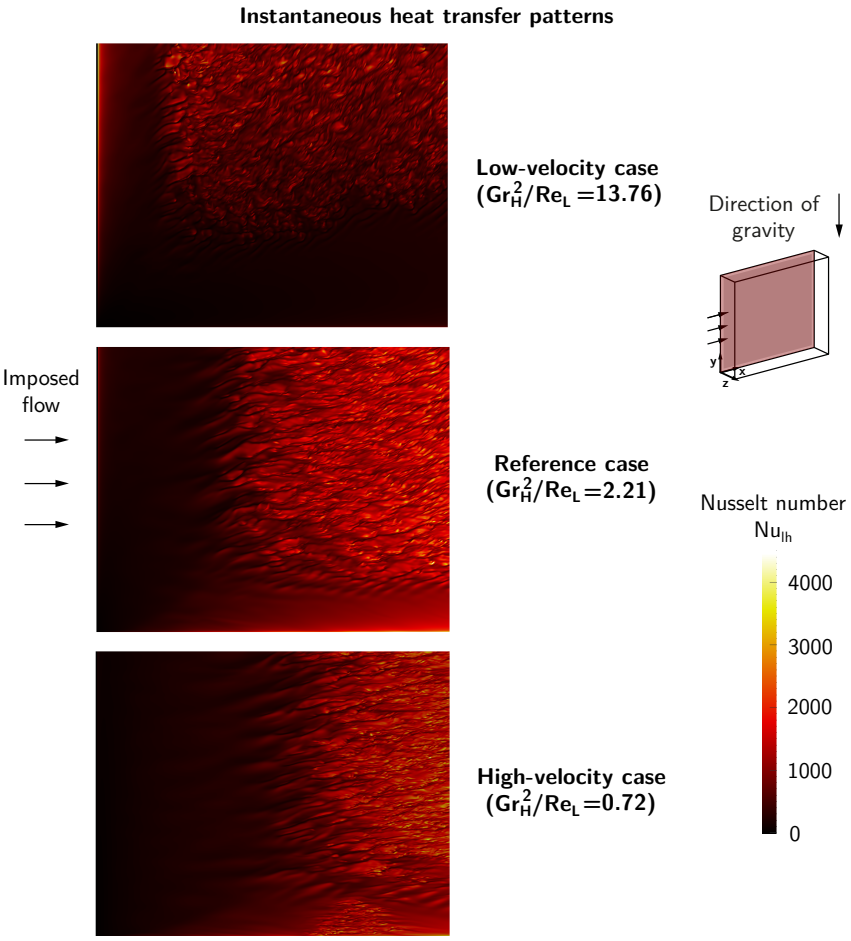


Figure 5.27.: The instantaneous fields of the Nusselt number Nu_{lh} for different free-stream velocities. The onset of turbulence can easily be identified by the appearance of structures. While the maximum heat transfer rate is higher for the high-velocity case, the area exhibiting this high rate is considerably smaller.

For buoyancy-dominated mixed convection (low-velocity case), the time-averaged Nusselt number exclusively is a function of Gr_y after transition, and no variation in horizontal direction is visible. As the onset of turbulence occurs at a low Reynolds-number, $\mathrm{Nu}_{lh} \sim \mathrm{Gr}_y$ correctly describes the heat transfer on most of the domain. Accordingly, an elevated Nu_{lh} appears at the inlet, while the heat

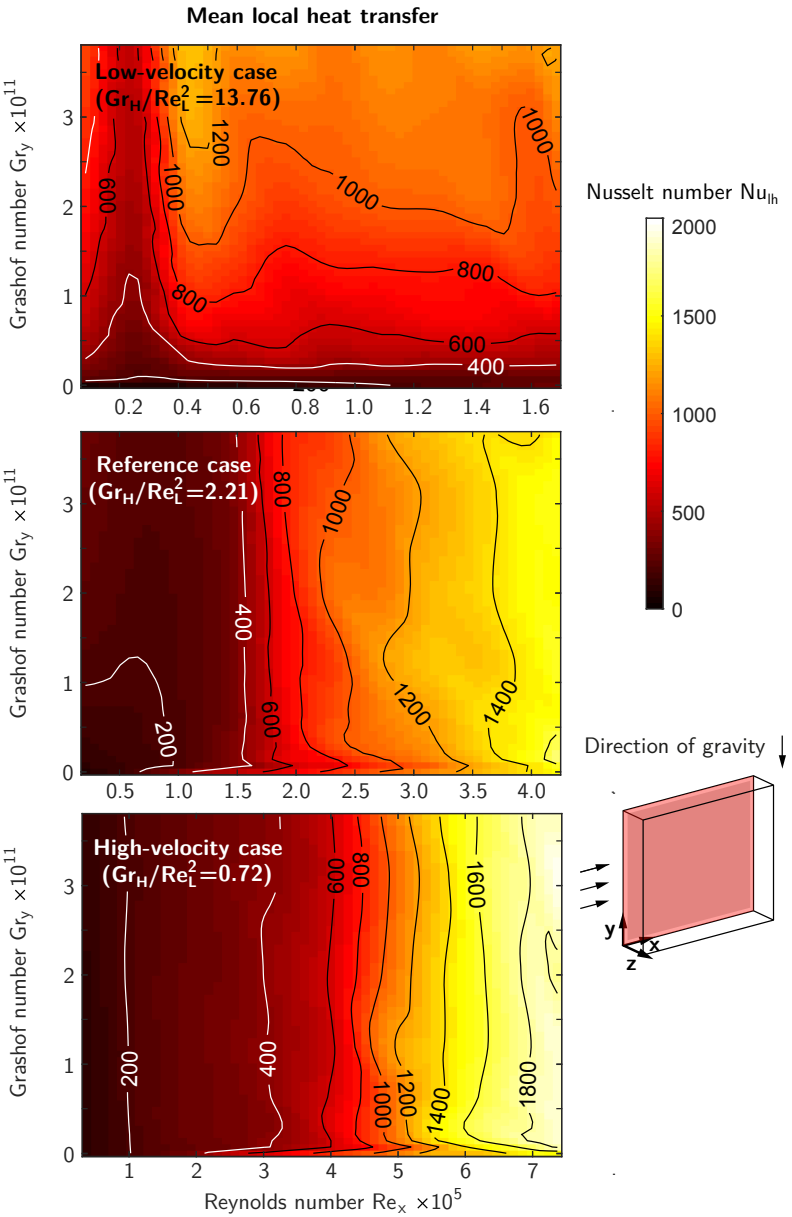


Figure 5.28.: Time-averaged Nusselt number for the three simulation cases showing the influence of the free stream on the heat transfer.

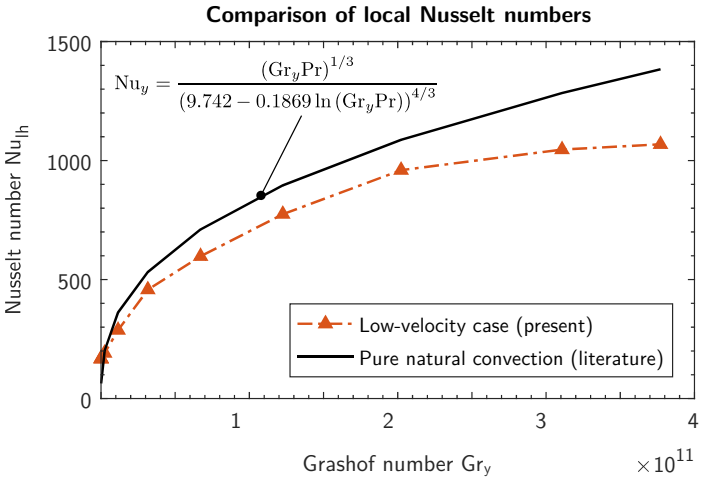


Figure 5.29.: The Nusselt-correlation by Balaji et al. (2006) for pure turbulent natural convection in comparison to the present low-velocity case where $lh \approx y$, showing that imposing a free stream can reduce the heat transfer.

transfer at the bottom boundary is not reflected in the Nusselt number. Note that one exception to this rule can be observed in the figure, namely the region close to the outlet. Here, the heat transfer locally reduces as a result of a lower degree of turbulence caused by entrainment (see discussion of Figure 5.26).

The finding of $\mathrm{Nu}_{lh} \sim \mathrm{Gr}_y$ for the low-velocity case suggests a comparison of this buoyancy-dominated mixed convection case with pure turbulent natural convection. In Figure 5.29, the Nusselt-correlation of Balaji et al. (2006) is used as a reference. The figure shows that imposing a weak horizontal flow onto pure natural-convection, thus making the problem three-dimensional, can actually decrease heat transfer. The profile of the present computed Nusselt number has slightly lower absolute values but exhibits a similar trend as the literature correlation. This is in line with the behavior of turbulent two-dimensional flow cases (see literature, e.g. Figure 2.12).

5.2.4. Turbulence

It has been noted before in this chapter that the imposed velocity severely impacts the level of turbulence of the flow. Figure 5.30 shows all turbulent coherent structures characterized by $Q > 10$ in form of an iso-surface plot. Comparing

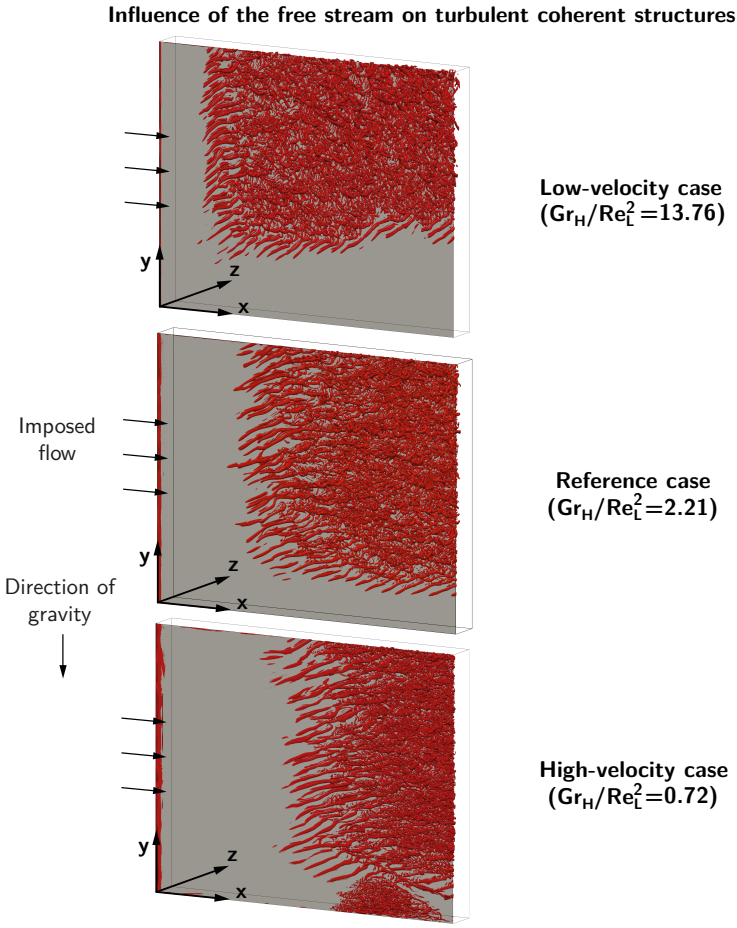


Figure 5.30.: Turbulent coherent structures (iso-surface representation with $Q = 10$) for increasing free stream velocity, showing the delay in transition due to laminarization.

the three flow cases confirms the observation that the onset of turbulence is delayed for high flow velocities. This laminarization effect manifests in a continuous horizontal shift of the transition zone towards the outlet. Consequently, the critical Reynolds number, describing the horizontal location of transition, actually increases for higher velocities.
All three cases feature the transition along a vertical and a – more or less –

horizontal line. When discussing the flow fields of the reference case, this finding has been linked to the prerequisite of a critical path length, allowing the fluid to develop the updraft. Consequently, fluid entering the domain at the inlet reaches this distance at the critical Reynolds number. The entrained cold fluid features a strong vertical component (due to the fact that it feeds a vertical updraft), and therefore travels this critical distance in a more vertical direction (critical Grashof number). A varying magnitude of the vertical flow component between the cases (see Figure 5.26) is reflected in the varying vertical distance of the horizontal transition line: The entrainment in the high-velocity case for example features a lower u_y-component. Consequently, the flow travels the critical path length mostly in horizontal x-direction. Accordingly, the horizontal transition line is closer to the bottom that for the other cases. An exception to this rule can be observed in the low-velocity case: Towards the outlet, the transition line no longer is horizontal, but moves to higher vertical locations. For an explanation, a brief look at the streamlines in Figure 5.26 is required: In the two cases of equipollent mixed convection, the vertical component of the entrained flow varies very little in horizontal direction. Following the logic above, the vertical distance of transition does not change, and the onset of turbulence thus occurs along a straight horizontal line. In the buoyancy-dominated case, however, large updraft-caused variations in the flow angle with x are observed, i.e. in the outer boundary layer. As a consequence of this variation, the vertical component of the critical path length grows larger with x, which results in a larger vertical distance of the transition from the bottom. Consequently, as can be seen in Figure 5.30, transition no longer occurs along a straight line. In this context, keep in mind that the streamlines in the buffer layer, relevant for the effect discussed here, are not represented in Figure 5.26. They are rather situated in between the red and the blue lines.

As discussed for the reference case, the transition is initiated by the formation of low-velocity streaks. Evaluating the orientation of these streaks shows consistency with the local flow angle in the buffer layer (Figure 5.23). The observation in the reference case, where the coherent turbulent structures change their direction of travel when emerging from the streak-breakup (as a result of increasing wall distance) also applies for the low-velocity and the high-velocity case.

At the bottom of the high-velocity case, a second mechanism of laminar-turbulent transition appears. Here, buoyancy does not have a significant effect on the flow, as the updraft has not yet developed at this location. Consequently, the transition occurs due to the "classic" mechanism. The difference from the buoyancy-triggered transition is expressed in the lack of low-velocity streaks. The flow at this point is in an instable state close to its critical Reynolds number of $\mathrm{Re}_{x,\mathrm{crit}} \approx 5 \cdot 10^5$ (Schlichting and Gersten, 2006), where the rate of dissipation

of turbulence is the same as the rate of production. Most likely, the flow reacts on a small numerical disturbance by the bottom boundary condition. As in the figure, Schlichting and Gersten (2006) describe the occurrence of typical wedge-shaped turbulent spots during transition at random locations and their downstream travel. In this context, keep in mind that Figure 5.30 represents an instantaneous Q-field.

5.3. Influence of buoyancy

Contrary to the previous section, where the influence of the free stream on three-dimensional mixed convection was investigated, the present section seeks to provide some insights on the influence of buoyancy. Therefore, the results of the reference case are compared to the results of a simulation case with a low wall temperature, characterized by a low Grashof number ($\mathrm{Gr_H} = 3.05 \cdot 10^{10}$). Given this number, buoyant effects are expected to be rather minor, locating the case in the inertia-dominated flow regime ($\mathrm{Gr_H/Re_L^2} = 0.17$). Additionally, the results of a high-temperature case ($\mathrm{Gr_H} = 7.61 \cdot 10^{11}$) serve as an example for a buoyancy-affected flow within the equipollent mixed convection regime ($\mathrm{Gr_H/Re_L^2} = 4.12$). All three cases feature the same imposed flow velocity ($\mathrm{Re_L} = 4.29 \cdot 10^5$). Consequently, all differences between the cases are the direct or indirect result of an increase in wall temperature, which thus allows to evaluate the influence of buoyancy.

5.3.1. Flow fields

As in the previous section, the flow and temperature fields located in a horizontal plane at the vertical center of the domain are compared for the three simulation cases (Figures 5.31 to 5.33). The vertical position of $y = 0.4\,\mathrm{m}$ is a dimensionless location of $\mathrm{Gr}_y = 0.35 \cdot 10^{10}$ (low-temperature case, at the top of the figure), $\mathrm{Gr}_y = 4.7 \cdot 10^{10}$ (reference case, center), and $\mathrm{Gr}_y = 8.8 \cdot 10^{10}$ (high-temperature case, bottom). The dimensionless horizontal positions are indicated in the figure and identical in all three cases due to the same imposed flow conditions.

The fields in Figure 5.31 are the instantaneous horizontal velocity in absolute values. The figure is well-suited to highlight the role of buoyancy in the laminar-turbulent transition: The boundary layer flow in the low-temperature case remains stable for most of the domain. Merely towards the outlet, some instabilities become visible. In a standard flow along a plate, unaffected by destabilizing buoyancy, laminar-turbulent transition would be expected at a critical Reynolds number of $\mathrm{Re}_{x,\mathrm{crit}} \approx 5 \cdot 10^5$ (Schlichting and Gersten, 2006). As the Reynolds number at the outlet is still slightly below this critical value, and given the inertia-dominated nature of the flow, it is not surprising that the low-temperature case does not develop a fully turbulent state. It can thus be stated, that this flow case exhibits the behavior of pure forced convection, which is in agreement with the regime boundaries discussed in Chapter 2.2. The increased wall temperature of the reference case leads to the onset of turbulence at $\mathrm{Re}_x \approx 1.5 \cdot 10^5$. When further raising the wall temperature to the value of the high-temperature case, transitions occurs even earlier, at $\mathrm{Re}_x \approx 1.1 \cdot 10^5$. Comparing the three cases shows that adding some buoyancy to a formerly

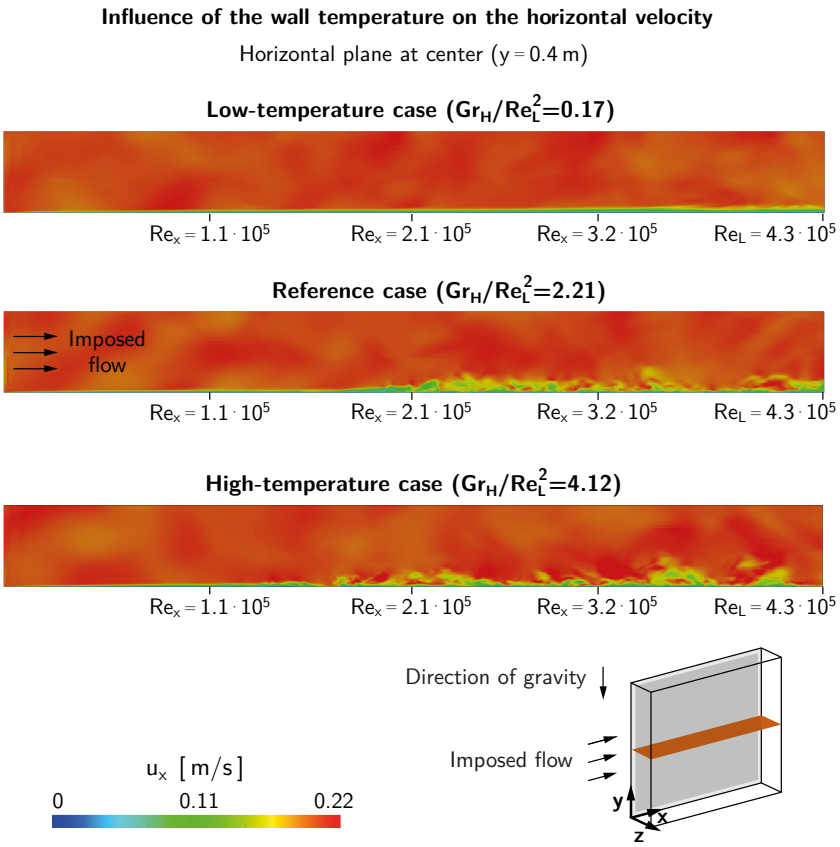


Figure 5.31.: The instantaneous horizontal velocity fields at the vertical center for different wall temperatures. The top field clearly shows very little influence of buoyancy, with a flow barely reaching the beginning of the laminar-turbulent transition. The boundary layer at the center (reference case) and at the bottom (high-temperature case) are clearly affected by turbulence. The figure illustrates that the instability introduced by buoyancy triggers the transition of a formerly stable boundary layer flow.

stable boundary layer flow introduces a sufficient amount of instability to trigger the onset of turbulence.

Figure 5.32 presents the instantaneous vertical velocity fields. As expected, the low wall temperature does not cause a significant updraft. The vertical velocity ranges in the same magnitude as the imposed synthetic free-stream turbulence. The slight instabilities towards the outlet, observed in the field

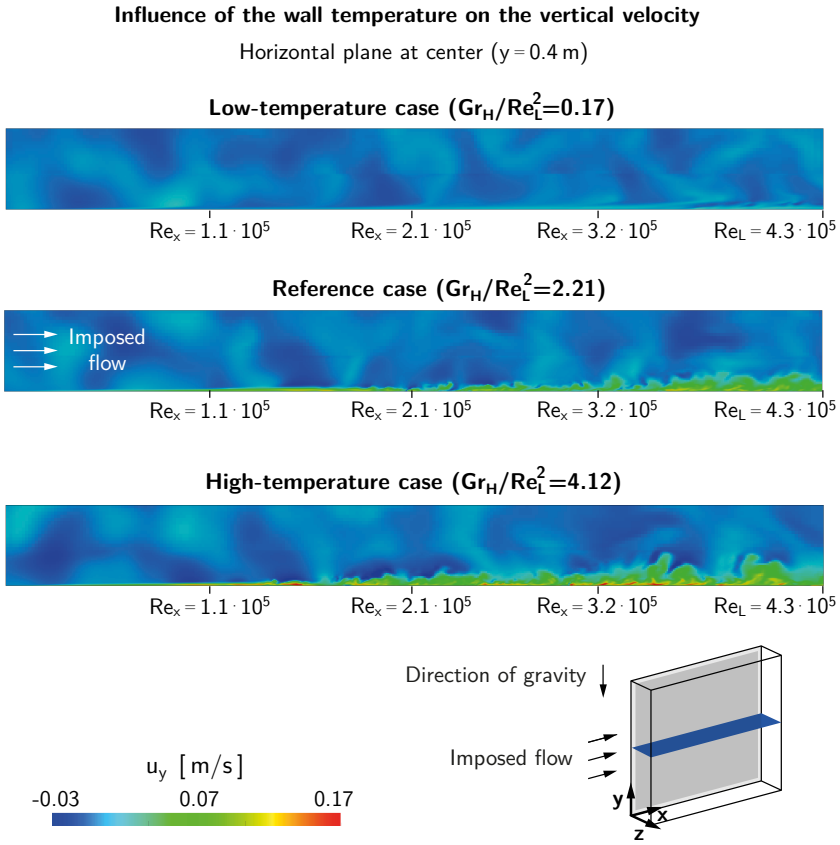


Figure 5.32.: The instantaneous fields of the vertical velocity (corresponding to Figure 5.31), show a strong increase in u_y with increasing Richardson number.

of the horizontal velocity, also have an influence on the vertical field. The corresponding increased mixing rate transports vertical momentum to the outer boundary layer. However, this effect is by far smaller than for the other two cases, where a notable vertical flow starts to develop even in the laminar regime. After transition, the corresponding boundary layers grow in size and cover a significant part of the domain in wall-normal direction. The increasing effect of buoyancy within the equipollent mixed convection regime is clearly reflected in a growing velocity magnitude. In the high-temperature case, u_y reaches values of 0.17 m/s even in some wall distance. This elevated velocity is in the same

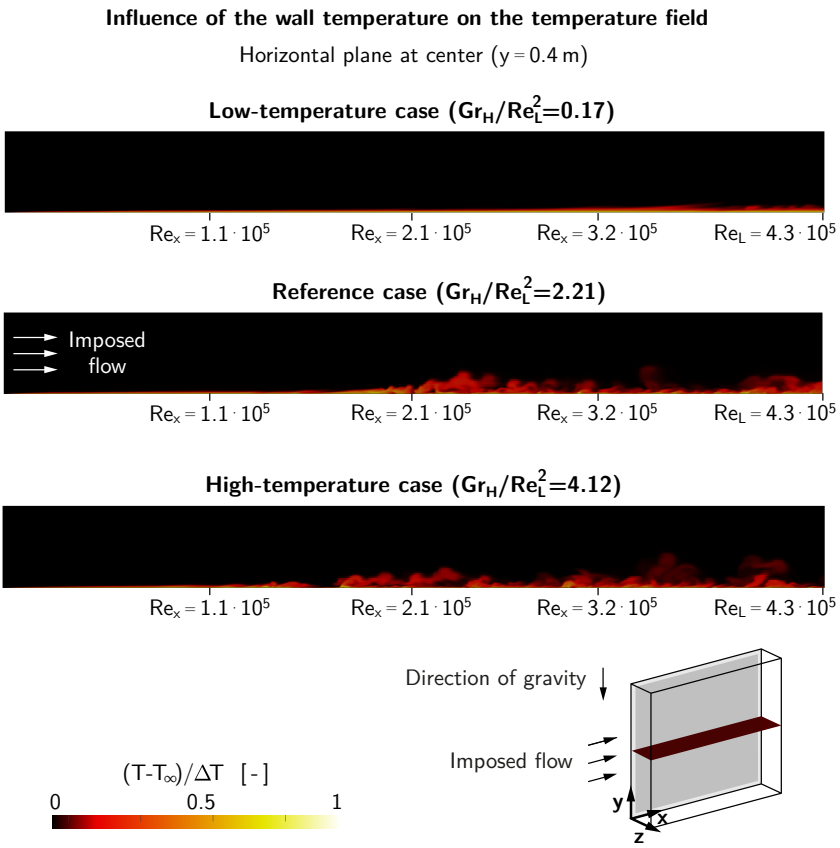


Figure 5.33.: The temperature fields corresponding to Figure 5.31. Note that the temperature is referred to the respective wall temperature.

range as the imposed horizontal free-stream velocity u_∞ and exceeds the vertical velocity of the low-temperature case by roughly one order in magnitude.

The temperature fields in Figure 5.33 mostly reflect the flow state in the preceding figures. The reason why the fields for the reference case and for the high-temperature case resemble each other is the relative scaling $(T - T_\infty)/(T_W - T_\infty)$ of the figure that takes into account the respective wall temperature .

5.3.2. Boundary layers

The boundary layer displacement thickness δ_1 for the three present simulation cases is shown in Figure 5.34. The general image is that, with rising Grashof numbers, the displacement thickness reduces. While this observation does not correspond with the visual perception of the velocity boundary layer thickness in the fields presented above, it is consistent with the definition (see Eqn. 2.56) and the physical interpretation of δ_1 – describing the displacement of streamlines due to the boundary layer formation: A higher mass flow within the boundary layer results in less displacement and thus in a reduction of δ_1.
In the low-temperature case, the flow does not transition into a fully turbulent state. Consequently, the boundary layer thickness grows with $\delta_1 \sim \mathrm{Re}_x$. The three exceptions from this rule (see yellow regions near the outlet) are – as will be shown when evaluating the turbulent coherent structures – related to isolated patches of developing turbulence. As the vertical velocity in the boundary layer is low, no significant fluid entrainment occurs. In line with the discussion in the preceding section, no reduced δ_1 can be found at the bottom of the domain. As discussed before, the dependency $\delta_1 \sim \mathrm{Re}_x$ is valid for the reference case as well. The transition into a fully turbulent flow is reflected in a steep increase in boundary layer thickness. In the high-temperature case, $\delta_1 \sim \mathrm{Re}_x$ is true in the laminar regime. For most of the region characterized by turbulent flow, no significant variation in boundary layer thickness occurs. Furthermore, no clear dependence of the boundary layer thickness with any direction can be found. The case Richardson number locates the case between the reference case (where $\delta_1 \sim \mathrm{Re}_x$) and the buoyancy-dominated case (see Figure 5.21 where $\delta_1 \sim \mathrm{Re}_x, \mathrm{Gr}_y$). Consequently, the field can be read as follows: the buoyant updraft is strong, but $|\boldsymbol{u}| < u_\infty$ – consequently, δ_1 reduces compared to the reference case. In both equipollent mechanism mixed convection cases, the entrainment of fluid at the bottom locally reduces the thickness.

Following the scheme of the preceding part of the study, the influence of buoyancy on the temperature and velocity boundary layer will be discussed in the following. Therefore, profiles in the transition zone, the turbulent zone and on the domain top at the outlet will be evaluated. As these regimes occur at different locations for the three cases, the sampling positions diver as well. The positions are illustrated in the figures and Table 5.2 gives the precise locations.

Above, similar temperature fields for the high-velocity and the reference case have been noticed. Accordingly, Figure 5.35 shows that the mean temperature profiles exhibit self-similarity for a constant case Reynolds number. When comparing the profiles, the only major difference is caused by the flow state. In the transitional regime (top), the profiles of all three cases are identical. In the turbulent regime (center), the two equipollent cases have identical temperature

Table 5.2.: Overview of sampling locations for the evaluation of the buoyant influence.

Case	Location		
	Transitional	Turbulent (vertical center)	Turbulent (vertical top)
Low-temperature			
Reynolds number Re_x	$2.73 \cdot 10^5$	$4.21 \cdot 10^5$	$4.21 \cdot 10^5$
Grashof number Gr_y	$0.50 \cdot 10^{10}$	$0.50 \cdot 10^{10}$	$2.8 \cdot 10^{10}$
x-location	0.65 m	1.00 m	1.00 m
y-location	0.45 m	0.45 m	0.8 m
Reference			
Reynolds number Re_x	$1.05 \cdot 10^5$	$2.31 \cdot 10^5$	$4.21 \cdot 10^5$
Grashof number Gr_y	$6.71 \cdot 10^{10}$	$6.71 \cdot 10^{10}$	$3.77 \cdot 10^{11}$
x-location	0.25 m	0.55 m	1.00 m
y-location	0.45 m	0.45 m	0.8 m
High-temperature			
Reynolds number Re_x	$1.05 \cdot 10^5$	$2.31 \cdot 10^5$	$4.21 \cdot 10^5$
Grashof number Gr_y	$1.26 \cdot 10^{11}$	$1.26 \cdot 10^{11}$	$7.07 \cdot 10^{11}$
x-location	0.25 m	0.55 m	1.00 m
y-location	0.45 m	0.45 m	0.8 m

profiles. As discussed before, these profiles exhibit the bend characteristic for a turbulent temperature boundary layer. However, the profile for the low-temperature case is mostly identical to its version in the transition region, confirming the observation that the flow has not turned fully turbulent at the outlet. The same is the case for the location at the top of the domain (bottom figure). Here, the profile for the low-temperature case still does not show any characteristics of a turbulent boundary layer. The two profiles for equipollent mixed convections are again mostly identical. Some minor variations occurs in the outer boundary layer, where the temperature for the high-temperature case is slightly elevated.

The influence of buoyancy on the velocity in the boundary layer is presented in the two Figures 5.36 and 5.37 and further illustrated in the streamlines in Figure 5.38. Again, the boundary layer profiles are in polar representation consisting of the flow angle γ and the scaled velocity magnitude $|\boldsymbol{u}|/u_\infty$. Major differences are visible for the two mixed convection regimes:

Inertia-dominated mixed convection regime (line with triangles): The fact that buoyancy only plays a minor role in the low-temperature flow case becomes apparent in the profile of the flow angle. Generally, compared to the other flow cases, the angle is low, barely reaching 20° in the high-angle region near the wall. The resulting near-horizontal flow in the viscous sublayer is a clear prove that the updraft is weak. Contrary to the other cases, there is little variation of γ with the location. Also, the point in the outer

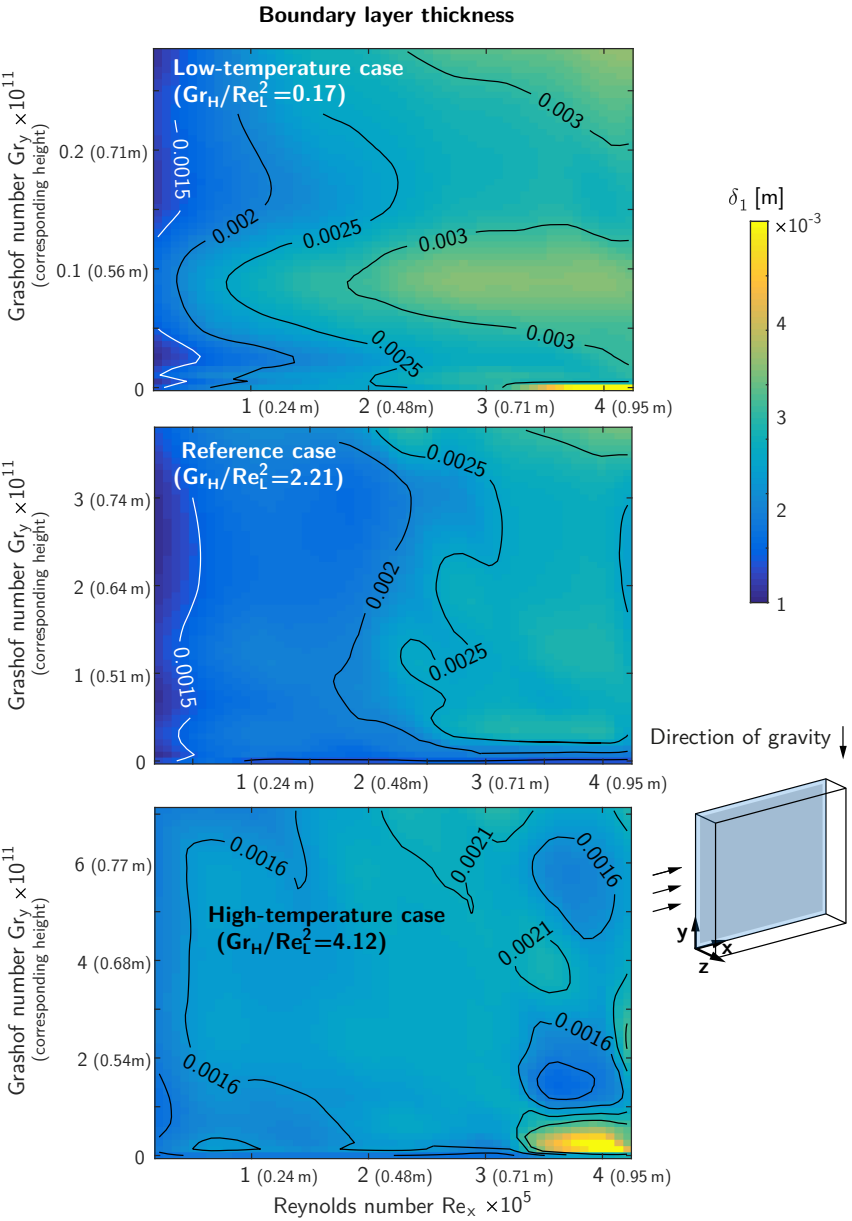


Figure 5.34.: Influence of increasing wall temperature on the boundary layer displacement thickness δ_1.

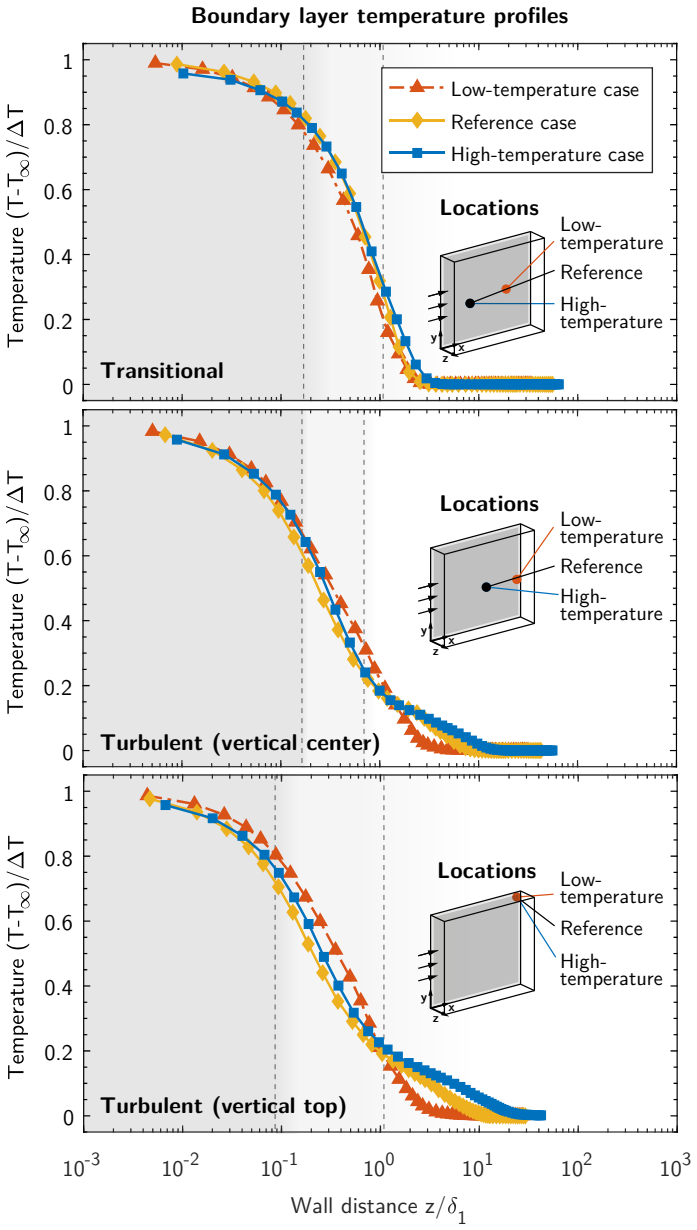


Figure 5.35.: Mean temperature boundary layer profiles at the three sampling points discussed above with the approximate location of the viscous subrange and the buffer layer.

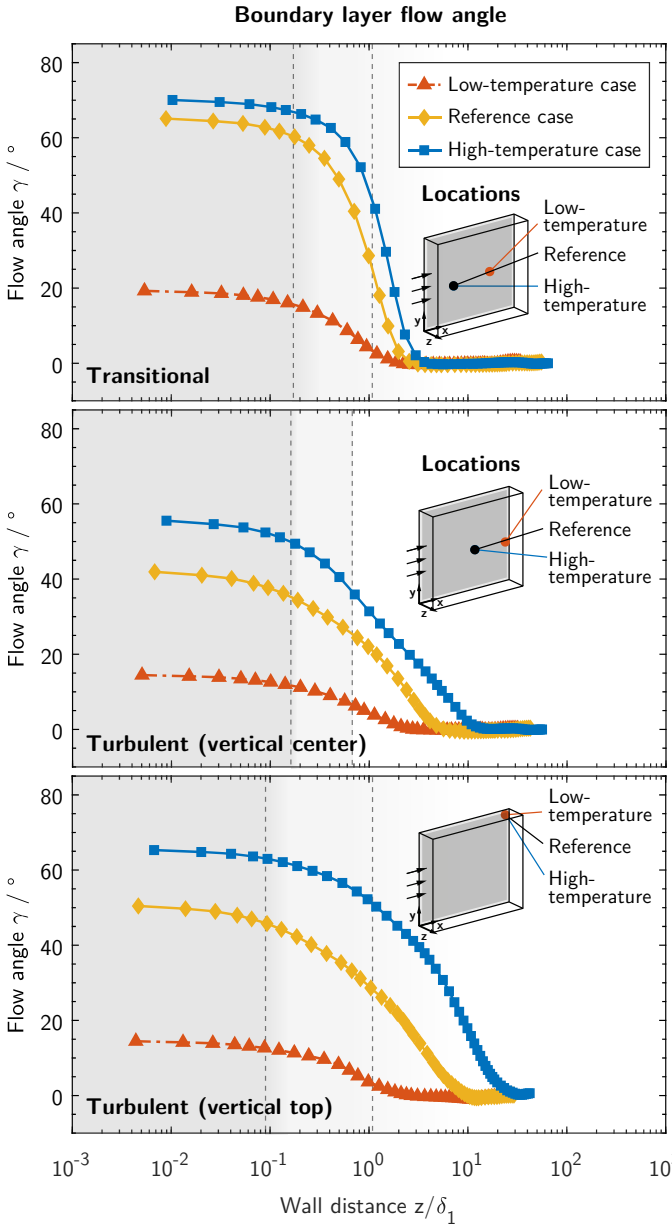


Figure 5.36.: Polar representation of the velocity boundary layer (flow angle) for increasing wall temperature.

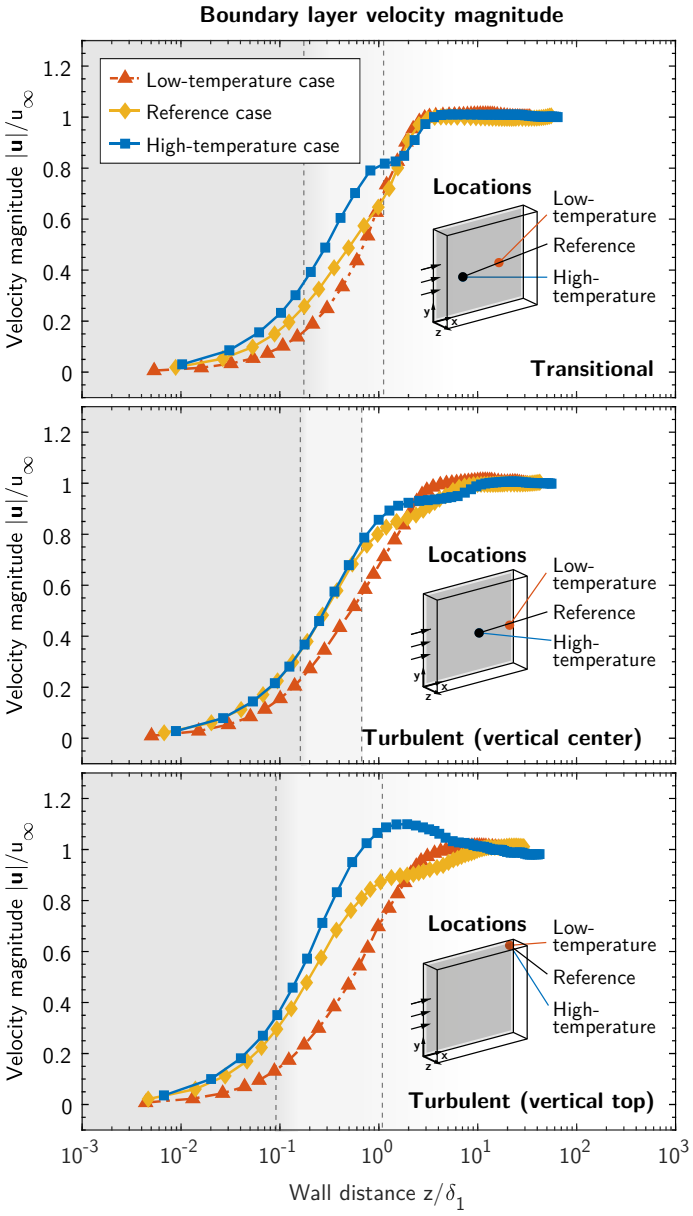


Figure 5.37.: The scaled velocity magnitude, completing the description of the velocity boundary layer in Figure 5.36.

boundary layer, where the angle-profile reaches free-stream conditions ($\gamma \approx 0°$) remains at the same wall distance of $z/\delta_1 \approx 2$. This finding is in good agreement with the observation that the flow does not transition. In this context, the absence of significant momentum transfer from the outer boundary layer towards the wall does not surprise. Admittedly, a slight reduction in magnitude in the outer boundary layer can be detected when comparing the profile at the transitional location to the profiles at the turbulent locations. As this reduction is not as significant as for the other cases, it is most likely attributed to diffusive transport of momentum instead of turbulent transport. The general shape of all profiles remains the same for all three figures, i.e. no velocity peak develops.

Equipollent mixed convection regime (line with diamonds and line with squares): The increasing effect of buoyancy is reflected in an increasing flow angle. Consequently, for all positions and throughout the entire boundary layer, the angles in the high-temperature case are larger than the angles of the reference case. All mechanisms discussed for the reference case, i.e. the reduction in γ and the transport of momentum during and after transition, are present in the high-temperature case as well. Despite the fact that both γ-profiles are close to each other near the transition, they exhibit a major difference in the turbulent regime. Here, unsurprisingly, the high-temperature case features a higher flow angle due to the higher influence of buoyancy. Like it was the case in the buoyancy-dominated mixed convection regime (see Chapter 5.2), the γ-profile travels outward for higher Richardson numbers. In this context, it is remarkable, that the region affected by buoyancy is approximately ten times larger in the high-velocity case than in the low-temperature case.

The development of the velocity peak nicely illustrates the strong influence of buoyancy. It is easily detectable in all equipollent mixed convection profiles, i.e. when comparing the velocity magnitude profiles to the one of the low-temperature case. Here, as discussed before, it is visible in form of a slight hump in the outer/buffer layer of the reference case. For the high-temperature case, the hump is very prominent, even at the transition. In the turbulent regime, the peak further evolves. At the vertical top, its magnitude even outpasses the free stream. At this location, the vertical updraft has grown intense enough to introduce momentum into the region that was subject to the removal of momentum by turbulence before. However, compared to the low-velocity case discussed in the preceding chapter, the peak is by far less intense.

Note that a slight undershoot in γ is apparent in the turbulent equipollent mixed convection profiles in this part of the study as well – yet, it does not appear in the inertia-dominated case, as the causing updraft is not significant.

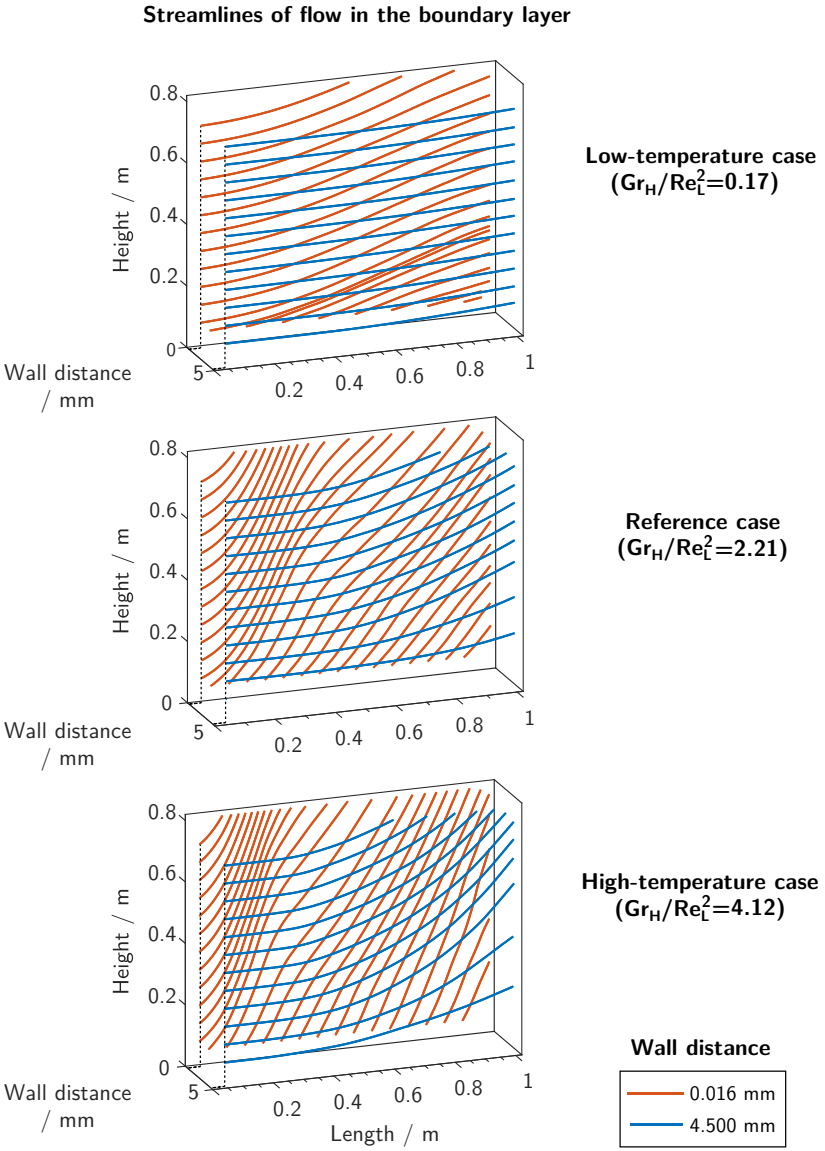


Figure 5.38.: Streamlines for the three different flow cases showing the increasing influence of buoyancy with increasing wall temperature. As before, the wall distance is 0.016 mm ($z/\delta_1 \to 0$) and 4.5 mm ($z/\delta_1 > 1.5 \cdot 10^0$).

The alternative representation in form of streamlines (Figure 5.38) visualizes how little the flow of the low-temperature case (top) is affected by buoyancy. For the two equipollent cases, the streamlines next to the wall illustrate the observation discussed above, that both flow angle profiles are almost identical during transition. In the turbulent regime, however, the high-temperature case features a significantly stronger vertical velocity component than the reference case.

5.3.3. Heat transfer

The heat transfer patterns shown in Figure 5.39 allow to draw the following conclusion concerning the dependency of the Nusselt number (heat transfer rate) with the Grashof number (wall temperature): Increasing the wall temperature results in significantly higher area-weighted Nusselt numbers. This is due to two effects: First, the instabilities introduced to the boundary layer by a growing buoyant updraft provoke an earlier onset of turbulence. While the low-temperatur case does not transition to a fully turbulent flow, thus exhibiting generally low heat transfer rates with some patches of high rates, high Nusselt numbers occur in the turbulent regimes of the other cases. Second, the turbulent heat transfer is enhanced by the increasing updraft itself. These findings are backed by the surface-plot of the time-averaged Nusself number in Figure 5.40. When comparing the overall values for the three cases, keep in mind the rather moderate variation with the free-stream velocity observed in the preceding section. Clearly, the influence of buoyancy on the heat transfer exceeds the influence of the free stream by far.

Again, the respective occurrence of non-zero values for the Nusselt number at the bottom and inlet reflects the characteristic length scale lh. However, in the Nusselt map of the high-temperature case, no clear dependency of the horizontal or vertical direction can be seen. The characteristic length scale for flow cases similar to this one should therefore be reconsidered in future work. For the low-temperature and the reference case, the time-averaged heat transfer in Figure 5.40 justifies the choice of $lh \approx x$. Here, the heat transfer is virtually unaffected by the height, with $\mathrm{Nu}_{lh} \sim \mathrm{Re}_x$. For the low-temperature case, this offers the option to compare the heat transfer of intertia-dominated mixed convection to pure forced convection (see Figure 5.41): The Nusselt number shows the same course as laminar forced convection, however, at slightly higher values and at a larger growth rate. This difference reflects the influence of buoyancy and is consistent with the comparison of the results for the three cases within this part of the study. Near the outlet, the computed Nusselt number increases as a result of the turbulent spots, tending towards the correlation for turbulent forced convection. However, as the present flow does not reach a fully turbulent state, a comparison with this correlation would not be valid.

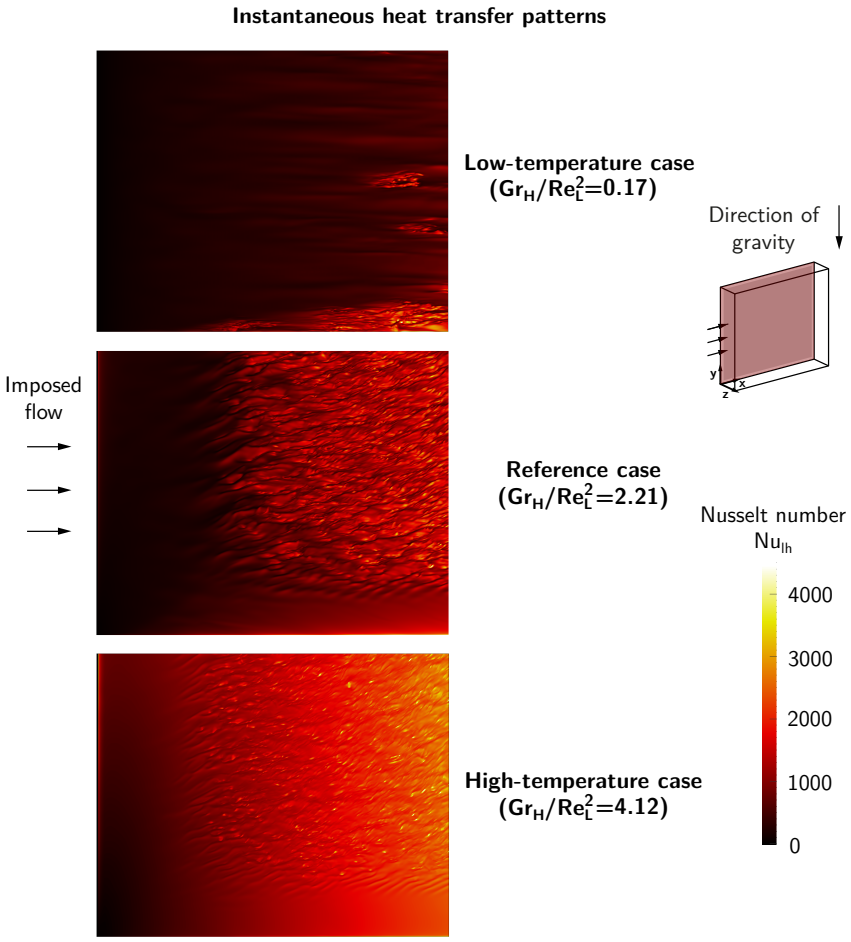


Figure 5.39.: The instantaneous field of the Nusselt number Nu_{lh} for increasing wall temperatures. The heat transfer in the low-velocity case is low, as the flow does not fully transition to turbulence. The highest Nu_{lh} occurs for high wall temperatures.

5.3.4. Turbulence

The conclusion that – when increasing the wall temperature – the heat transfer is highly affected by a growing turbulent transport raises further interest in the turbulence. Figure 5.42 shows all turbulent coherent structures characterized by $Q > 10$. From the figure, the following conclusions can be drawn:

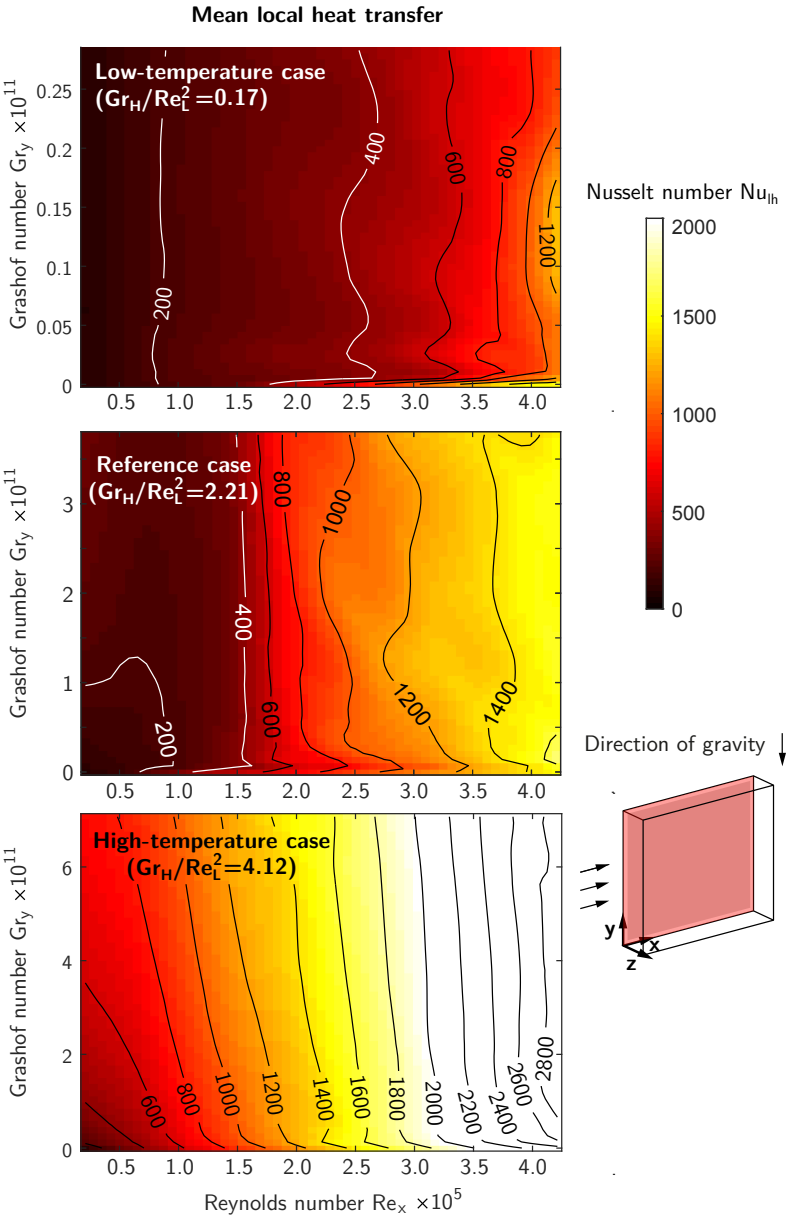


Figure 5.40.: Time-averaged Nusselt number for the three simulation cases showing the influence of buoyancy on the heat transfer.

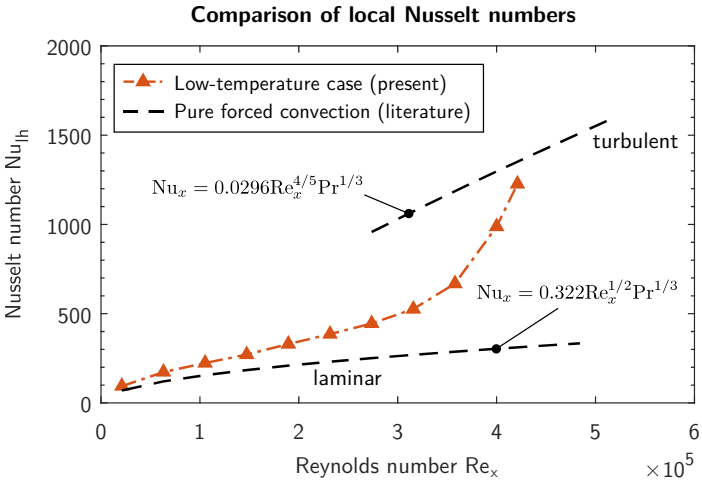


Figure 5.41.: The present low-temperature case is compared to Nusselt-correlations for pure forced convection (Incropera et al., 2007). As observed when comparing cases within the present study, the presence of buoyancy enhances the heat transfer.

First, for the given free-stream flow condition, the onset of turbulence is exclusively triggered by the instability introduced by buoyancy. The top figure shows the low-temperature case, where buoyancy does not play a major role. As suggested before, the flow does not transition into a fully turbulent state. Instead, isolated patches of a turbulent flow at random locations can be observed. This occurrence shows that, concerning turbulence, the flow has an intermittent character. The patches are rather small-scaled and – note that the figure shows an instantaneous field – are transported by advection towards the outlet. From these observations can be followed that the turbulent dissipation exceeds the turbulent production, preventing the flow from transitioning. However, as discussed by Schlichting and Gersten (2006), a laminar-turbulent transition is a stability problem, which implies that turbulent spots can form even before the flow fully transitions (e.g. caused by the synthetic free-stream turbulence or the boundary condition). As for the Q-field of the high-velocity case (see Section 5.2), the shape of these spots in the low-temperature case is similar to the patches shown in Schlichting's book. Note that – contrary to the onset of turbulence in all other cases – no streaks form at the beginning of each patch, indicating that the triggering mechanism for these spots is different. The two cases in the equipollent mechanisms regime (center and bottom) experience transition. As the free stream in these two cases is subject to the exact same conditions as in the low-velocity case, the onset must be related to buoyancy.

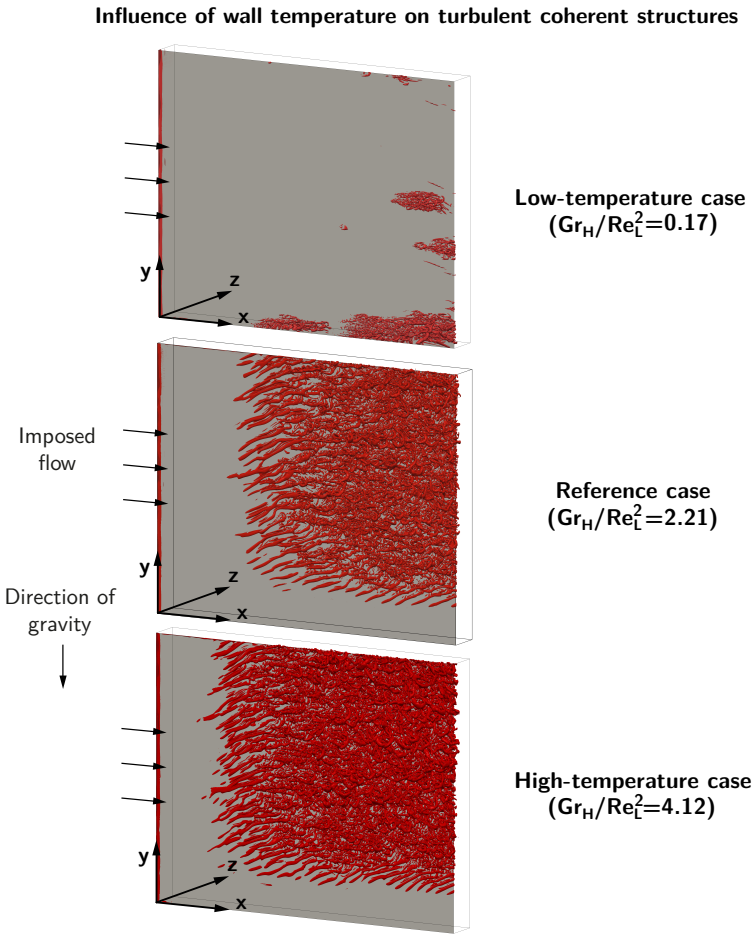


Figure 5.42.: All turbulent coherent structures characterized by $Q > 10$. When increasing the influence of buoyancy from top to bottom, the flow changes from not transitioning to a fully turbulent flow. Further increasing the wall temperature results in an earlier onset of turbulence.

Second, both cases in the equipollent mechanisms regime exhibit a clear transition along a vertical and horizontal line. When increasing the wall temperature, the vertical line travels upstream (to lower Re_x). As the heat transfer rate increases with the wall temperature, the path that a fluid parcel needs to travel

before the buoyancy-induced instabilities reach a critical value decreases. Consequently, the critical Reynolds number exhibits inverse proportionality with the wall temperature. The same is true for the cold fluid entrained at the bottom, which is reflected in a slight downwards shift of the horizontal transition line. Third, like in the Q-field in Section 5.2, the orientation of the streaks at the laminar-turbulent transition reflects the flow angle γ in the buffer layer. Note that the orientation of coherent structures in the high-temperature case almost reaches the free-stream value of $\gamma = 0°$, which is a nice illustration of the large boundary layer size for flow cases with a high influence of buoyancy.

5.4. Chapter summary

Three-dimensional mixed convection is the superposition of a buoyancy-induced updraft and an imposed free-stream flow. Consequently, two factors have an impact on the processes: The Reynolds number (reflecting the free-stream velocity) and the Grashof number (reflecting the wall temperature). By varying these parameters, the influence of buoyancy and the influence of the free stream were evaluated in the present work. The underlying physical mechanisms were investigated in a reference case (moderate Re / moderate Gr). The following effects were found to be characteristic for three-dimensional mixed convection:

Regimes: In preparation of the present simulations, three different regimes were defined: Inertia-dominated mixed convection, where buoyancy plays a minor role. Buoyancy-dominated mixed convection, where buoyancy has a major impact. Equipollent-mechanisms mixed convection where both mechanisms have an influence. The regime boundaries were defined by a threshold in the Richardson number ($\mathrm{Gr}/\mathrm{Re}^2$) expressing the relative influence of buoyancy. Within one regime, the flow fields, boundary layer profiles, heat transfer characteristics and the onset of turbulence varies. However, when crossing the regime boundaries, dramatic changes can be observed. This behavior was expected and justifies the classification of three-dimensional mixed convection in the three distinct regimes.

Instabilities by buoyancy: The onset of turbulence is triggered by instabilities caused by fluctuations in the buoyant force. Consequently, buoyancy plays a major role in the laminar-turbulent transition. Among others, this hypothesis is proven by the fact, that no transition occurs for the simulation case with a low wall temperature (low Gr). On the other hand, higher wall temperatures (medium and high Gr) result in an early onset of turbulence. For the investigated geometry – a vertical, flat plate – transition occurs along a vertical line. Additionally, the buoyancy-induced updraft entrains fluid at the bottom of the plate. This flow transitions along a horizontal line. The reason for these two sharp transition zones is that the cold fluid needs to travel a "critical" path length (corresponding to a critical Reynolds and Grashof number) in order to accumulate sufficient heat for the buoyancy-driven instabilities to become influential.

Laminarization: A high velocity suppresses turbulence. In the present study, a delay in the transition to turbulence was seen for increasing imposed velocities. Consequently, three-dimensional mixed convection with a high free-stream velocity exhibits less turbulence than with a low free-stream velocity. This laminarization effect has been described in literature for two-dimensional mixed convection. The present work shows, that it occurs for three-dimensional mixed convection as well.

Heat transfer: Almost all the heat introduced into the viscous sublayer and the buffer layer is removed by turbulent transport. In the outer boundary layer, turbulent transport and transport by advection counterbalance each other. These findings emphasize the role of turbulence in heat transfer. Consequently, the heat transfer rate is subject to a steep increase during transition. Once the flow has reached a turbulent state, the relations known from buoyancy-unaffected plate flows are valid: A higher flow velocity results in a higher heat transfer rate. Additionally, the heat transfer was found to increase with case Grashof number. This finding is not surprising, as the buoyant updraft in the boundary layer increases with the wall temperature. Accordingly, the lowest local heat transfer rates were found for low velocity / low wall temperature. The highest local heat transfer rates occurred for high wall temperature / high velocity. However, due to laminarization, the onset of turbulence is delayed for high velocities. This leads to the un-intuitive situation that the area-weighted Nusselt number can actually decrease with increasing velocity as the flow remains stable and laminar over a larger area. Clearly, the influence of buoyancy on heat transfer exceeds the influence of the free stream by far. It should be noted that the dimensionless heat transfer (Nusselt number) does not directly correlate with the Richardson number in any form.

Updraft in the boundary layer: The buoyant updraft changes the flow angle in the boundary layer. In direct wall proximity, a high-angle region is formed with its maximum value at the wall. Here, the flow varies from near-horizontal (low Ri number) to near-vertical (high Ri number). The local flow angle can be understood as the relation between the horizontal velocity component and the vertical component. The transport of momentum from the outer boundary layer towards the wall by turbulence is always reflected in a reduction of the flow angle, as the momentum introduced mostly points in horizontal direction. Consequently, the highest flow angles occur right before the laminar-turbulent transition. When buoyancy plays a major role (i.e. in cases characterized by a high Ri number), a distinct velocity peak becomes apparent in the velocity magnitude. This peak can have an influence far into the free stream, resulting in a deflection of the imposed horizontal flow.

Spatial boundary layer development: All cases in the equipollent mixed convection regime exhibit little variation of the flow characteristics in vertical direction. Instead, most of the boundary layer evolution occurs in horizontal direction. This includes the velocity and temperature profiles, the Nusselt number, and the boundary layer growth. Interestingly, when evaluating a distinct boundary layer for the horizontal and the vertical velocity, the visual thickness δ_{99} is identical for both.

Turbulent coherent structures: During the laminar-turbulent transition, elongated vortices (so-called streaks) in streamwise direction develop. Evaluating their orientation in combination with the local flow angle narrows the location of these structures down to the buffer layer. After remaining stable for a certain time, the streaks experience secondary instabilities and further turbulent coherent structures emerge. This includes wall-attached hairpin vortices. As this vortex extends from the inner boundary layer (where the flow is characterized by high flow angles) into the outer boundary layer (where the flow exhibits low flow angles), it is subject to distortion. It is interesting to note, that the simulation results do not show signs of "classic" transition mechanisms, e.g. primary instabilities like Tollmien-Schlichting waves. This finding, however, is in agreement with the conclusion, that the triggering instabilities in three-dimensional mixed convection are related to buoyancy.

Chapter 6.

Discussion

Three-dimensional turbulent mixed convection is a flow state emerging from heat transfer into a horizontal flow. It is a textbook example of complex thermo-fluid interaction and has to date not been subject to significant research activities. Therefore, the aim of this work was to gain insights into the underlying mechanisms of heat transfer, the boundary layer flow, and the onset of turbulence. The approach chosen to answer these research questions was the conduction of wall-resolved large eddy simulations (LES).

The use of this simulation method proved to be successful and meaningful results were obtained. A summary of these results and the corresponding physical interpretation was provided in Chapter 5.4. The mesh resolution chosen for the LES was sufficiently fine to resolve all relevant effects. Nevertheless, the computational costs of the simulations were acceptable – albeit the use of high-performance computing was required. The refinement strategy for the computational grid resulted in a lower resolution mesh for the regions in the outer boundary layer. While a number of interesting effects occur in this region, their influence on the heat transfer at the wall is limited. However, the effect that three-dimensional mixed convection has on the flow in this region should be subject to further research (see below). A huge dataset of simulation results (i.e. the entire flow fields and boundary layer profiles) has been generated and will be available for further investigations.

The resolution of the present simulations approaches the level of DNS for most of the boundary layer, with the resolved share of the total turbulent kinetic energy $k/(k + k_{\mathrm{sgs}})$ being far higher than the 80% required for LES. In direct wall proximity, where the turbulent scales inherently become small, the present simulation method falls back to the modeling approach. Consequently, the coefficients for the subgrid-scale transport of momentum ν_{sgs} and heat α_{sgs} increase. When choosing the simulation method, these values were expected to tend towards zero. Indeed, a decrease was shown in Chapter 3.6. However, the near-wall values still indicate a model influence. In future simulations, this influence could be reduced by refining the near-wall mesh cells, or by imposing the van Driest damping function.

In the present work, turbulence and the associated transport mechanisms were found to locally dominate the heat transfer. This imposes certain challenges on the use of a "simpler" turbulence treatment (e.g. in RANS simulations).

If the boundary layer profiles could be described by wall functions with sufficient precision, a reduction of the near-wall resolution would be possible, permitting the simulation of mixed convection without the use of expensive high-performance computing. The main prerequisite for wall functions is the existence of self-similarity. In the present work, self-similarity was found for the temperature profile within the turbulent regime. Unfortunately, the velocity profiles exhibit major variations throughout the domain, and little self-similarity was found. It is understood that describing the temperature by a function, while resolving the flow, does not make sense as the governing equations for both fields are solved on the same computational mesh.

For the use in technical applications, the description of the heat transfer by three-dimensional mixed convection through a correlation would be useful. The corresponding correlation would describe the heat transfer in form of the dimensionless Nusselt number. The influence of buoyancy on the heat transfer was found to exceed the influence of the free stream. Therefore, even in a first-order approximation, mixed convection should not be treated as pure forced convection. Consequently, a problem-specific correlation would be required. The major dependencies are: First, the horizontal location (Re_x). Second, the vertical location (Gr_y). Third, the mixed convection regime ($\mathrm{Gr}_\mathrm{H}, \mathrm{Re}_\mathrm{L}, \mathrm{Ri}$). Fourth, the thermophysical properties (Pr). A challenge in this modeling would be the choice of a representative characteristic length scale. In the present work, a scale $lh = f\,(x, y, \mathrm{Ri})$ was used – an approach that is consistent with the nature of mixed convection for all but one simulation case. Consequently, for this particular case (characterized by a high wall temperature), the present choice of the characteristic length scale should be reconsidered. A further challenge would be the dependency on Re_x and Gr_y which varies for the different flow and turbulence regimes, making the existence of single correlations rather unlikely. Nevertheless, the present work features too little supporting points for the derivation of a heat transfer correlation. Furthermore, as this work was focused on the physical mechanisms, the influence of temperature-dependent thermophysical properties (except for the density) has been neglected.

This last aspect points out the need for further research: The influence of real-life thermophysical properties on mixed convection, particularly with regard to the viscosity is an important issue. In the inner boundary layer, viscosity plays a significant role in dampening turbulent fluctuations. Consequently, the question whether instabilities can grow depends (at least in part) on a

temperature-dependent property – in a boundary layer region that is severely affected by heat transfer. While for liquids (i.e. water), the viscosity reduces with increasing temperature – thus fueling instabilities, the opposite is the case for gases (i.e. air). It can therefore be expected, that the mechanisms triggering the laminar-turbulent transition vary for different types of fluid. A further field requiring research is the behavior of turbulent coherent structures (i.e. the wall-attached hairpin vortices) in the outer region of the boundary layer. While their "legs" are affected by the buoyant updraft, their "top" travels with the free stream. These two movements result in a distortion of the structures. While literature describes these vortices as symmetric, the present simulation produced asymmetric structures.

Regarding the motivating occurrence of three-dimensional mixed convection in solar receivers, potential for a reduction of the heat losses by convection has been shown in the present work. Increasing the free-stream velocity over hot surfaces, e.g. through "air curtains", could decrease the influence of buoyancy. As the wall temperature cannot be reduced, this strategy is the only option to reduce the Richardson number. By making use of the laminarization effect discussed in the present work, transition into a turbulent flow state could potentially be delayed by this approach. In this context, the present simulation method is well-suited for the investigation of more complex geometries than a vertical plate. For solar receivers, i.e. the geometry of membrane walls, exhibiting "dead water zones", would be an interesting subject of future simulations.

Bibliography

Abedin, M. Z., Tsuji, T., Hattori, Y., 2009. Direct numerical simulation for a time-developing natural-convection boundary layer along a vertical flat plate. International Journal of Heat and Mass Transfer 52 (19-20), 4525 – 4534.

Abedin, M. Z., Tsuji, T., Hattori, Y., 2010. Direct numerical simulation for a time-developing combined-convection boundary layer along a vertical flat plate. International Journal of Heat and Mass Transfer 53 (9-10), 2113 – 2122.

Abedin, M. Z., Tsuji, T., Lee, J., 2012a. Effects of freestream on the characteristics of thermally-driven boundary layers along a heated vertical flat plate. International Journal of Heat and Fluid Flow 36, 92–100.

Abedin, M. Z., Tsuji, T., Lee, J., 2012b. Turbulence characteristics and vortical structures in combined-convection boundary layers along a heated vertical flat plate. International Journal of Heat and Mass Transfer 55 (15-16), 3995–4002.

Abu-Mulaweh, H. I., Armaly, B. F., Chen, T. S., 1992. Measurements of laminar mixed convection adjacent to a vertical plate – uniform wall heat flux case. Journal of Heat Transfer 114 (4), 1057–1059.

Abu-Mulaweh, H. I., Chen, T. S., Armaly, B. F., 2000. Effects of free-stream velocity on turbulent natural-convection flow along a vertical plate. Experimental Heat Transfer 13 (3), 183–195.

Adrian, R., Meubhart, C., Tomkins, C., 2000. Vortex organization in the outer region of the turbulent boundary layer. Journal of Fluid Mechanics 422, 1–54.

Adrian, R., Westerweel, J., 2011. Particle Image Velocimetry. Cambridge University Press.

Adrian, R. J., 2007. Hairpin vortex organization in wall turbulence. Physics of Fluids 19 (4), 041301.

Afshari, B., 1989. Computation of three dimensional turbulent mixed convection boundary layers. Ph.D. thesis, Stanford University.

Alfonsi, G., 2006. Coherent structures of turbulence: Methods of eduction and results. Applied Mechanics Reviews 59, 307–323.

Avila, K., Moxey, D., deLozar, A., Avila, M., Barkley, D., Hof, B., 2011. The onset of turbulence in pipe flow. Science 333, 192–196.

Balaji, C., Hölling, M., Herwig, H., 2008. A temperature wall function for turbulent mixed convection from vertical, parallel plate channels. International Journal of Thermal Sciences 47 (6), 723 – 729.

Balaji, C., Hölling, M., Herwig, H., 2006. Nusselt number correlations for turbulent natural convection flows using asymptotic analysis of the near-wall region. ASME Journal of Heat Transfer (129), 1100–1105.

Barhaghi, D. G., Davidson, L., 2009. Large-eddy simulation of mixed convection-radiation heat transfer in a vertical channel. International Journal of Heat and Mass Transfer 52, 3918 – 3928.

Bergan, N. E., 1986. Testing of the molten salt electric experiment solar central receiver in an external configuration. Tech. rep., Sandia National Laboratories (SAND86-8010).

Blasius, H., 1907. Grenzschichten in Flüssigkeiten mit kleiner Reibung. Zeitschrift für Mathematik und Physik 56, 1–37.

Bünger, F., Herwig, H., 2009. An extended similarity theory applied to heated flows in complex geometries. Zeitschrift für angewandte Mathematik und Physik 60 (6), 1095–1111.

Boer, G., Shepherd, T., 1982. Large-scale two-dimensional turbulence in the atmosphere. Journal of the Atmospheric Sciences 40, 164–184.

Boiko, A., Dovgal, A., Grek, G., Kozlov, V., 2011. Physics of transitional shear flows: instability and laminar-turbulent transition in incompressible near-wall shear layers. Fluid Mechanics and Its Applications. Springer.

Burgaleta, J. I., Arias, S., Ramirez, D., 2012. Gemasolar, the first tower thermosolar commercial plant with molten salt storgae. In: SolarPACES Conference, Marrakech, Morocco.

Cabot, W., Jiménez, J., Baggett, J., 1999. On wakes and near-wall behavior in coarse large-eddy simulation of channel flow with wall models and second-order finite-difference methods. Center for Turbulence Research Annual Research Briefs, 343–354.

Cebeci, T., Broniewski, D., Joubert, C., Kural, O., 1990. Mixed convection on a vertical flat plate with transition and separation. Journal of Heat Transfer 112, 144–150.

Chapman, D., 1979. Computational aerodynamics development and outlook. AIAA Journal 17 (12), 1293–1313.

Chen, T. S., Armaly, B. F., Ali, M. M., 1987. Turbulent mixed convection along a vertical plate. Journal of Heat Transfer 109 (1), 251–253.

Choi, H., Moin, P., 2012. Grid-point requirements for large eddy simulation: Chapman's estimates revisited. Physics of Fluids 24 (1), 011702.

de Villiers, E., 2006. The potential of large eddy simulation for the modeling of wall bounded flows. Ph.D. thesis, Imperial College of Science, Technology and Medicine,.

Eitel-Amor, G., Örlü, R., Schlatter, P., Flores, O., 2015. Hairpin vortices in turbulent boundary layers. Physics of Fluids 27, 025108.

Evans, G., Greif, R., Siebers, D., Tieszen, S., 2005. Turbulent mixed convection from a large,high temperature,vertical flat surface. International Journal of Heat and Fluid Flow 26, 1–11.

Evans, G. H., Plumb, O. A., 1982. Laminar mixed convection from a vertical heated surface in a crossflow. Journal of Heat Transfer 104, 554–558.

Ferziger, J. H., Peric, M., 2008. Numerische Strömungsmechanik. Springer-Verlag.

Flesch, R., Stadler, H., Uhlig, R., Hoffschmidt, B., 2015. On the influence of wind on cavity receivers for solar power towers: An experimental analysis. Applied Thermal Engineering 87, 724 – 735.

Freund, S., 2008. Local heat transfer coefficients measured with temperature oscillation IR thermography. Ph.D. thesis, Helmut-Schmidt-Universität / Universität der Bundeswehr Hamburg.

Fröhlich, J., 2006. Large Eddy Simulation turbulenter Strömungen. Vol. 1. Teubner Verlag.

Fureby, C., Gosman, A., Tabor, G., Weller, H., Sandham, N., Wolfshtein, M., 1997a. Large eddy simulation of turbulent channel flows. Turbulent shear flows 11, 28–13.

Fureby, C., Tabor, G., Weller, H., Gosman, A. D., 1997b. A comparative study of subgrid scale models in homogeneous isotropic turbulence. Physics of Fluids 9, 1416–1429.

Fureby, C., Tabor, G., Weller, H. G., Gosman, A. D., 1997c. Differential subgrid stress models in large eddy simulations. Physics of Fluids 9 (11), 3578–3580.

Gadepalli, P., Rahman, M., 1996. Conjugate mixed convective heat transfer in electronic equipment. American Society of Mechanical Engineers, Heat Transfer Division 333, 219–225.

Garbrecht, O., 2014. Solarturmkraftwerk-Solarempfänger, Patent EP2520872 B1, Solar Millennium AG.

Garbrecht, O., Al-Sibai, F., Kneer, R., Wieghardt, K., 2013. CFD-simulation of a new receiver design for a molten salt solar power tower. Solar Energy 90, 94–106.

Garnier, E., Adams, N., Sagaut, P., 2009. Large eddy simulation for compressible flows. Springer.

Gebhart, B., Jaluria, Y., Mahajan, R. L., Sammakia, B., 1988. Buoyancy-induced flows and transport. Hemisphere Publishing Corporation, New York.

Gerasimov, A. V., 2003. Development and validation of an analytical wall-function strategy for modelling forced, mixed and natural convection flows. Ph.D. thesis, University of Manchester Institute of Science and Technology.

Germano, M., Piomelli, U., Moin, P., Cabot, W. H., 1991. A dynamic subgrid-scale eddy viscosity model. Physics of Fluids A 3, 1760–1765.

Hall, W., Price, P., 1970. Mixed forced and free convection from a vertical heated plate to air. In: Fourth International Heat Transfer Conference, Paris-Versailles, Vol. IV, NC3.3.

Hattori, Y., Tsuji, T., Nagano, Y., Tanaka, N., 2000. Characteristics of turbulent combined-convection boundary layer along a vertical heated plate. International Journal of Heat and Fluid Flow 21, 520–525.

Hattori, Y., Tsuji, T., Nagano, Y., Tanaka, N., 2001. Effects of freestream on turbulent combined-convection boundary layer along a vertical heated plate. International Journal of Heat and Fluid Flow 22, 315–322.

Incropera, F., DeWitt, D., Bergman, T., Lavine, A., 2007. Fundamentals of heat and mass transfer. Vol. 6. John Wiley.

Issa, R. I., 1986. Solution of the implicitly discretized fluid flow equations by operator splitting. Journal of Computational Physics 62, 40–65.

Jasak, H., 1996. Error analysis and estimation for the finite volume method with applications to fluid flows. Ph.D. thesis, Imperial College of Science, Technology and Medicine.

Jasak, H., Weller, H., Gosman, A., 1999. High resolution NVD differencing scheme for arbitrarily unstructured meshes. International Journal for Numerical Methods in Fluids 31, 431–449.

Jeong, J., Hussain, F., 1995. On the identification of a vortex. Journal of Fluid Mechanics 285, 69–94.

Jin, Y., Herwig, H., 2010. Application of the similarity theory including variable property effects to a complex benchmark problem. Zeitschrift für angewandte Mathematik und Physik 61 (3), 509–528.

Kasagi, N., Nishimura, M., 1997. Direct numerical simulation of combined forced and natural turbulent convection in a vertical plane channel. International Journal of Heat and Fluid Flow 18 (1), 88 – 99.

Keitzl, T., Mellado, J. P., Notz, D., 2016. Impact of thermally driven turbulence on the bottom melting of ice. Journal of Physical Oceanography 46 (4), 1171–1187.

Kim, W.-W., Menon, S., 1995. A new dynamic one-equation subgrid-scale model for large eddy simulations. In: AIAA, 33rd Aerospace Sciences Meeting and Exhibit, Reno, USA.

Kis, P., 2011. Analyse turbulenter gemischter Konvektion auf der Basis von DNS-Daten. Ph.D. thesis, TU Hamburg-Harburg.

Kitamura, K., Inagaki, T., 1987. Turbulent heat and momentum transfer of combined forced and natural convection along a vertical flat plate – aiding flow. International Journal of Heat and Mass Transfer 30, 23–41.

Kolmogorov, A. N., 1941. The local structure of turbulence in incompressible viscous fluid for very large reynolds numbers. Doklady Akademiya Nauk SSSR 30, 299–303.

Kornev, N., Hassel, E., 2007. Method of random spots for generation of synthetic inhomogeneous turbulent fields with prescribed autocorrelation functions. Communications in Numerical Methods Engineering 23 (1), 35–43.

Kornev, N., Kröger, H., Hassel, E., 2008. Synthesis of homogeneous anisotropic turbulent fields with prescribed second-order statistics by the random spots method. Communications in Numerical Methods in Engineering 24, 875–877.

Kornev, N., Kröger, H., Turnow, J., Hassel, E., 2007. Synthesis of artificial turbulent fields with prescribed second-order statistics using the random-spot method. Proceedings in Applied Mathematics and Mechanics 7 (1), 2100047–2100048.

Kravchenko, A., Moin, P., Moser, R., 1996. Zonal embedded grids for numerical simulations of wall-bounded turbulent flows. Journal of Computational Physics 127 (2), 412 – 423.

Krishnamurthy, R., Gebhart, B., 1989. An experimental study of transition to turbulence in vertical mixed convection flows. Journal of Heat Transfer 111 (1), 121–130.

Körner, M., 2014. An experimental method for the investigation of indoor airflows in a reduced scale model room: Development and application. Ph.D. thesis, TU Ilmenau.

Lance, B., 2015. Experimental validation data for CFD of steady and transient mixed convection on a vertical flat plate. Ph.D. thesis, Utah State University.

Lata, J. M., Rodríguez, M., Álvares deLara, M., 2008. High flux central receivers of molten salts for the new generation of commercial stand-alone solar power plants. Journal of Solar Energy Engineering 130, 021002.

Lau, G., Sanvicente, E., Yeoh, G., Timchenko, V., Fossa, M., Ménézo, C., Giroux-Julien, S., 2012. Modelling of natural convection in vertical and tilted photovoltaic applications. Energy and Buildings 55, 810 – 822.

Launder, B., Spalding, D., 1974. The numerical computation of turbulent flows. Computer Methods in Applied Mechanics and Engineering 3 (2), 269 – 289.

Laval, J.-P., Marquillie, M., Ehrenstein, U., 2012. On the relation between kinetic energy production in adverse-pressure gradient wall turbulence and streak instability. Journal of Turbulence 13, 1–19.

Lemmon, E., Huber, M., McLinden, M., 2004. NIST Standard Reference Database 23: Reference Fluid Thermodynamic and Transport Properties-REFPROP, Version 7.1. National Institute of Standards and Technology, Standard Reference Data Program.

Leonard, A., 1974. Energy cascade in large-eddy simulations of turbulent fluid flows. Advances in Geophysics 18A, 237–248.

Lesieur, M., 2008. Turbulence in Fluids. Vol. 4. Springer.

Li, F., Wang, D., Kawaguchi, Y., Hishida, K., 2004. Simultaneous measurements of velocity and temperature fluctuations in thermal boundary layer in a drag-reducing surfactant solution flow. Experiments in Fluids 36 (1), 131–140.

Li, X., Kong, W., Wang, Z., Chang, C., Bai, F., 2010. Thermal model and thermodynamic performance of molten salt cavity receiver. Renewable Energy 35, 981–988.

Lilly, D. K., 1992. A proposed modification of the Germano subgrid-scale closure method. Physics of Fluids A 4, 633–636.

Lorenz, E. N., 1963. Deterministic nonperiodic flow. Journal of the Atmospheric Sciences 20, 130–141.

Marić, T., Höpken, J., Mooney, K., 2014. The OpenFOAM Technology Primer. Sourceflux UG.

Marquillie, M., Ehrenstein, U., Laval, J.-P., 2011. Instability of streaks in wall turbulence with adverse pressure gradient. Journal of Fluid Mechanics 681, 205–240.

Menon, S., Yeung, P. A. K., W.-W., 1996. Effect of subgrid models on the computed interscale energy transfer in isotropic turbulence. Computers & Fluids 25, 165–180.

Moukalled, F., Mangani, L., Darwish, M., 2015. The Finite Volume Method in Computational Fluid Dynamics: An Advanced Introduction with OpenFOAM and Matlab. Springer.

Nakao, K., Hattori, Y., Suto, H., 2016. Numerical investigation of a spatially developing turbulent natural convection boundary layer along a vertical heated plate. International Journal of Heat and Fluid Flow, in press.

Ojofeitimi, A., 2013. On the computation of buoyancy affected turbulent wall flows using large eddy simulation. Ph.D. thesis, University of Maryland.

Oosthuizen, P. H., 1974. Turbulent combined convection flow over a vertical plane surface. In: Proceedings of the 5th International Heat Transfer Conference, Tokyo, Japan. pp. 129–133.

Oosthuizen, P. H., 2010. A numerical study of laminar and turbulent mixed convective flow over a vertical isothermal plate. In: Proceedings of the 14th International Heat Transfer Conference, Washington, USA. pp. 233–239.

Patankar, S., Spalding, D., 1972. A calculation procedure for heat, mass and momentum transfer in three-dimensional parabolic flows. International Journal of Heat and Mass Transfer 15, 1787.

Patankar, S. V., 1980. Numerical heat transfer and fluid flow. Hemisphere Publishing Corporation.

Patel, K., Armaly, B., Chen, T., 1996. Transition from turbulent natural to turbulent forced convection adjacent to an isothermal vertical plate. American Society of Mechanical Engineers, Heat Transfer Division, Publication 324, 51–56.

Piomelli, U., 1999. Large-eddy simulation: achievements and challenges. Progress in Aerospace Sciences 35, 335–362.

Plumb, O. A., Kennedy, L. A., 1977. Application of a k-epsilon turbulence model to natural convection from a vertical isothermal surface. Journal of Heat Transfer 99 (1), 79–85.

Pope, S. B., 2000. Turbulent flows. Cambridge University Press.

Prandtl, L., 1904. Über Flüssigkeitsbewegung bei sehr kleiner Reibung. In: Verhandlungen des III. Internationalen Mathematiker-Kongresses, Heidelberg.

Raghavan, J., Rahman, M., 1997. Analysis of mixed convective cross flow near protruding heat sources on a vertical circuit board. American Society of Mechanical Engineers, Heat Transfer Division, Publication 351, 337–342.

Raghavan, J., Rahman, M. M., 1996. Transient response of discrete heat sources on a conducting board in the presence of cross flow mixed convection. In: Proceedings of the Intersociety Energy Conversion Engineering Conference. Vol. 2. pp. 1384–1389.

Rahman, M. M., Carey, V., 1986. Steady and transient mixed convection near a vertical uniformly heated surface exposed to horizontal fluid flow. Numerical Heat Transfer 10, 327–347.

Reynolds, O., 1883. An experimental investigation of the circumstances which determine whether the motion of water shall be direct or sinuous, and of the law of resistance in parallel channels. Proceedings of the Royal Society of London 35, 84–99.

Rietz, M., Garbrecht, O., Rohlfs, W., Kneer, R., 2014. Combined three-dimensional flow- and temperature-field measurement using digital light field photography. In: Proceedings of the 15th International Heat Transfer Conference, Kyoto, Japan.

Schlichting, H., 1958. Grenzschichttheorie. Verlag G. Braun.

Schlichting, H., Gersten, K., 2006. Grenzschicht-Theorie. Vol. 10. Springer.

Schlüter, J., Pitsch, H., 2005. Antialiasing filters for coupled Reynolds-averaged/large-eddy simulations. AIAA Journal (43), 608–615.

Siebers, D. L., 1983. Experimental mixed convection heat transfer from a large, vertical surface in a horizontal flow. Ph.D. thesis, Stanford University.

Siebers, D. L., Kraabel, J. S., 1984. Estimating convective energy losses from solar central receivers. Tech. rep., Sandia National Laboratories (SAND84-8717).

Siebers, D. L., Schwind, R. G., Moffat, R. J., 1983. Experimental mixed convection heat transfer from a large,vertical surface in a horizontal flow. Tech. rep., Sandia National Laboratories (SAND83-8225).

Smagorinsky, J., 1963. General circulation experiments with the primitive equations. i. the basic experiment. Monthly Weather Review 91, 99–164.

Sparrow, E. M., Eichhorn, R., Gregg, J. L., 1959. Combined forced and free convection in a boundary layer flow. Physics of Fluids 2 (3), 319–328.

Sweby, P. K., 1984. High resolution schemes using flux limiters for hyperbolic conservation laws. SIAM Journal on Numerical Analysis 21, 995–1011.

Taylor, G., 1935. Statistical theory of turbulence. Proceedings of the Royal Society of London A151, 421.

Thess, A., Wagner, C., 2008. Verfahren und Anordnung zur Nachbildung einer Raumluftströmung, Patent DE102006009646 B4.

Tsuji, T., Kajitani, T., 2006. Turbulence characteristics and heat transfer enhancement of a natural convection boundary layer in water along a vertical flat plate. In: Proceedings of the 13th International Heat Transfer Conference, Sydney, Australia.

Tsuji, T., Nagano, Y., 1989. Velocity and temperature measurements in a natural convection boundary layer along a vertical flat plate. Experimental Thermal and Fluid Science 2 (2), 208 – 215.

Versteeg, H. K., Malalasekera, W., 2007. Computational fluid dynamics – The finite volume method. Pearson Education Limited.

Vreman, B., Geurts, B., Kuerten, H., 1995. A priori tests of large eddy simulation of the compressible plane mixing layer. Journal of Engineering Mathematics 29, 299–327.

Wang, J., Li, J., Jackson, J., 2004. A study of the influence of buoyancy on turbulent flow in a vertical plane passage. International Journal of Heat and Fluid Flow 25 (3), 420 – 430.

Wilcox, D. C., 2006. Turbulence Modeling for CFD. DCW Industries, Inc.

Yan, Z., Nilsson, E., 2005. Large eddy simulation of natural convection along a vertical isothermal surface. Heat and Mass Transfer 41, 1004–1013.

Yeh, K. C., Hughes, G., Lovegrove, K., 2005. Modelling the convective flow in solar thermal receivers. In: Proceedings of the 43rd Conference of the Australia and New Zealand Solar Energy Society, Dunedin, New Zealand.

Yoshizawa, A., Horiuti, K., 1985. A statistically-derived subgrid-scale kinetic energy model for the large-eddy simulation of turbulent flows. Journal of the Physical Socienty of Japan 54, 2834–2839.

Appendix A.

Solution algorithm and linear solvers

The general approach for numerically solving the Navier-Stokes equations was briefly presented in Chapter 2.1.2. After the integration over a control volume (e.g. a cell in the computational grid), Gauss's theorem can be used to express gradients and divergences in the transport equations as the sum of the cell's surface values. As OpenFOAM works with collocated grids, where all variables are stored at cell centers, the surface values have to be obtained by interpolation. The corresponding method used in the present work will be discussed later in this chapter. The goal of this discretization procedure is to obtain a linear equation of the form:

$$a_{\mathrm{P}}\phi_{\mathrm{c,P}} = \sum_{\mathrm{N}} a_{\mathrm{N}}\phi_{\mathrm{c,N}} + K \tag{A.1}$$

for each cell. The index P denotes the cell itself, the index N the neighbor cells it interacts with. The index c underlines the fact that cell values are used – as opposed to face values. The term K includes all sources that are independent of the conservative scalar ϕ. The two coefficients a depend on the original transport equation and the applied interpolation scheme.
For the entire solution domain, a system of linear equations can be formed:

$$\boldsymbol{A}\boldsymbol{\phi} = \boldsymbol{K} \tag{A.2}$$

where $\boldsymbol{A}$ is a sparse matrix that includes the coefficients a_{P} (on the diagonal) and a_{N} (off-diagonal), $\boldsymbol{\phi}$ is a vector for the values of ϕ in each cell and $\boldsymbol{K}$ a vector containing the independent source terms and boundary information.

When applying this procedure to the momentum equation (Eqn. 2.5), two general problems arise: First, the equation contains the non-linear convection term $\nabla\cdot(\rho\boldsymbol{u}\boldsymbol{u})$ and second, the knowledge of the pressure gradient is a prerequisite. Considering the additional complexity that a solver for a system of non-linear differential equations would add to the solution routine, linearization of this term seems to be the lesser of two evils. The integration is thus rewritten

$$\int_{\mathrm{V}^*} \nabla\cdot(\rho\boldsymbol{u}\boldsymbol{u})\,\mathrm{d}V = \sum_{\mathrm{V}^*} \rho\boldsymbol{u}_f\boldsymbol{u}_f S_f = \sum_{\mathrm{V}^*} \varphi_f\boldsymbol{u}_f \tag{A.3}$$

where the flux φ_f over the cell surface S_f replaces one of the velocity terms. Linearization is achieved by using the flux value calculated in the previous timestep or in the previous iteration. After linearization, the discretization procedure is straightforward, as described above. Concerning the second issue, when simulating a compressible flow, the combination of density and temperature allows to calculate a pressure field using the equation of state. However, in the present work, no relation between pressure and density exists, as the flow is considered incompressible and the density thus exclusively depends on the temperature. For this case, an additional pressure equation for the pressure-velocity coupling must be derived.

The discretized, linearized, Favre-filtered (see Chp. 2.1.3) momentum equation in the form used in the present work reads as follows:

$$a_{\mathrm{P}}\tilde{\boldsymbol{u}}_{\mathrm{c,P}} = \boldsymbol{H}\left(\tilde{\boldsymbol{u}}\right) - \nabla\bar{p} \tag{A.4}$$

Again, a_{P} includes all factors for the cell (P) velocity, i.e. the coefficients from the temporal discretization, the convection, diffusion and (turbulent) stress term, and also the density. $\boldsymbol{H}\left(\tilde{\boldsymbol{u}}\right)$ includes the velocity of the neighbor (N) cells, the associated coefficients a_{N}, and a_{M} that combines the coefficient from the temporal discretization and additional sources:

$$\boldsymbol{H}\left(\tilde{\boldsymbol{u}}\right) = \sum_{\mathrm{N}} a_{\mathrm{N}}\tilde{\boldsymbol{u}}_{\mathrm{c,N}} + a_{\mathrm{M}} \tag{A.5}$$

A simple rearrangement of Eqn. A.4 yields an explicit expression for the velocity field in the cell centers and allows its interpolation onto the cell surfaces:

$$\tilde{\boldsymbol{u}}_{\mathrm{c,P}} = \frac{\boldsymbol{H}\left(\tilde{\boldsymbol{u}}\right)}{a_{\mathrm{P}}} - \frac{\nabla\bar{p}}{a_{\mathrm{P}}} \tag{A.6}$$

$$\left(\tilde{\boldsymbol{u}}\right)_f = \left(\frac{\boldsymbol{H}\left(\tilde{\boldsymbol{u}}\right)}{a_{\mathrm{P}}}\right)_f - \left(\frac{1}{a_{\mathrm{P}}}\right)_f \left(\nabla\bar{p}\right)_f \tag{A.7}$$

The cell face flux can thus be calculated by

$$\varphi_f = \bar{\rho}\left(\boldsymbol{S}_f \cdot \left(\tilde{\boldsymbol{u}}\right)_f\right) = \boldsymbol{S}_f \cdot \left(\left(\bar{\rho}\frac{\boldsymbol{H}\left(\tilde{\boldsymbol{u}}\right)}{a_{\mathrm{P}}}\right)_f - \left(\frac{\bar{\rho}}{a_{\mathrm{P}}}\right)_f \left(\nabla\bar{p}\right)_f\right) \tag{A.8}$$

In the next step, spatial discretization of the continuity equation (Eqn. 2.4) in its Favre-filtered form yields

$$\frac{\partial\bar{\rho}}{\partial t} + \sum_f \left[\bar{\rho}_f\left(\boldsymbol{S}_f \cdot \left(\tilde{\boldsymbol{u}}\right)_f\right)\right] = 0 \tag{A.9}$$

which, when inserting $(\tilde{\boldsymbol{u}})_f$ from Eqn. A.7, finally produces the pressure equation

$$\sum_f \left[\boldsymbol{S}_f \cdot \left(\left(\frac{\bar{\rho}}{a_\mathrm{P}} \right)_f (\nabla \bar{p})_f \right) \right] = \sum_f \left[\boldsymbol{S}_f \cdot \left(\bar{\rho} \frac{\boldsymbol{H}(\tilde{\boldsymbol{u}})}{a_\mathrm{P}} \right)_f \right] + \frac{\partial \bar{\rho}}{\partial t} \qquad \text{(A.10)}$$

In the present work, a standard PIMPLE algorithm in OpenFOAM has been adapted to the mixed convection flow studied. The solution procedure of the new *convectionFoam* solver is shown in Figure A.1:

Initialization: The case initialization is crucial for any CFD simulation. The choice of a good starting point is the most efficient action that can be taken in order to reduce the physical simulation time required to reach quasi steady-state conditions. Great care was taken to find a good intialization. The corresponding process is in-depth described in Section 3.5.

Evaluate Courant number: The dimensionless Courant number (Co) is a measure of how fast a particular flow feature propagates through the computational grid. For an arbitrary cell (P) with volume $V^* = \Delta x \Delta y \Delta z$, it is defined as

$$\mathrm{Co}_{\mathrm{c,P}} = \frac{1}{2} \Delta t \left(\frac{1}{V^*} \sum_\mathrm{N} \frac{|\varphi_f|}{\bar{\rho}} \right) \qquad \text{(A.11)}$$

Consequently, $\mathrm{Co} = 1$ is the case for a feature traveling through one single cell per timestep Δt. In the present code, the timestep is evaluated based on a maximum Co number, which is chosen between 0.6 and 0.85 for the three-dimensional mixed convection cases and 0.5 to 0.65 for the two-dimensional validation cases. Generally, the under-relaxation performed in the PIMPLE solution algorithm results in higher numerical stability and thus allows for larger timesteps than the PISO algorithm would. The larger timesteps significantly reduce the computing time without negatively influencing the accuracy of the results.

Update velocity boundary condition: In the next step, the velocity boundary conditions are updated. This action is necessary as the imposed velocity at the inlet is modulated by an algorithm which generates synthetic turbulence (see Chp. 2.1.4).

Implicit momentum predictor: The momentum predictor implicitly solves the Favre-filtered momentum equation (Eqn. 2.40) for each coordinate direction. As described above, the values computed in the previous iteration or timestep are used for the pressure gradient and for the fluxes required to linearize the convection term. The resulting set of linear equations is

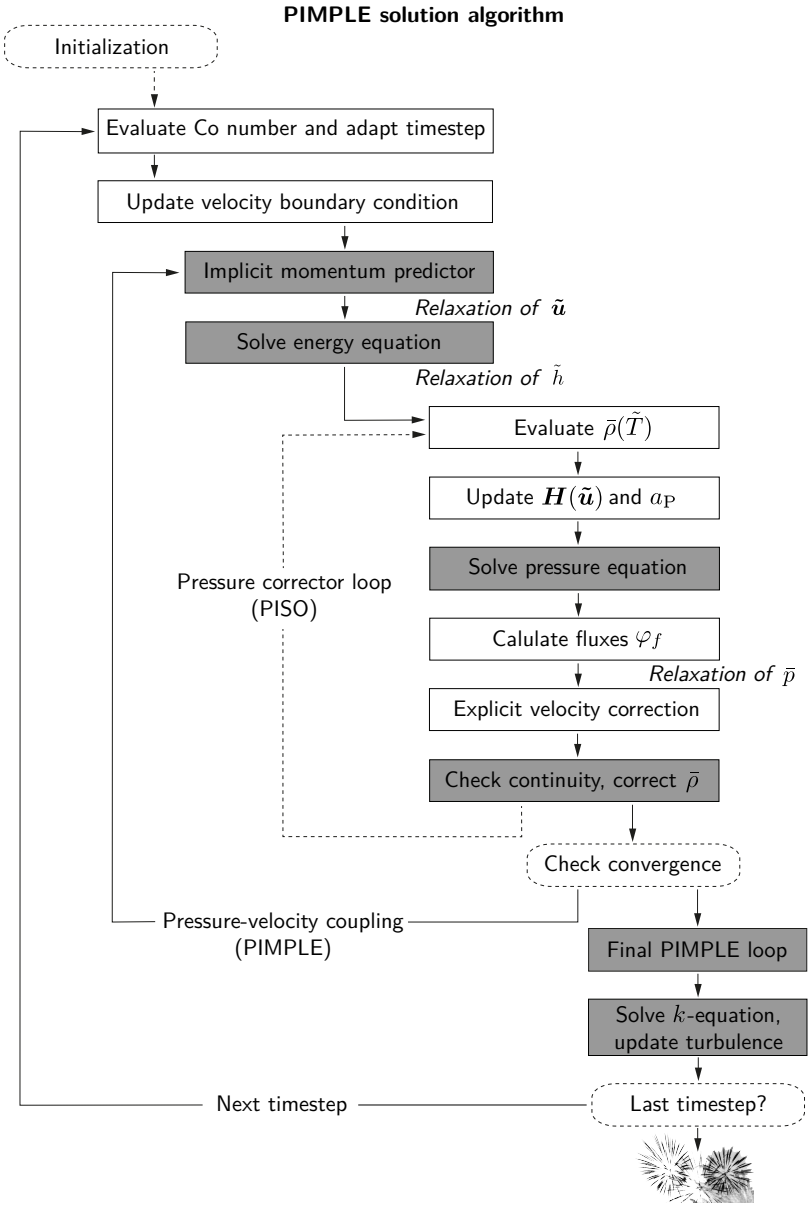


Figure A.1.: Flow diagram of the PIMPLE (merged PISO-SIMPLE) algorithm in form of the *convectionFoam* solver. Each step in grey color features a linear solver.

solved through iteration. However, the convergence rate of this solution method reduces on finer meshes (Versteeg and Malalasekera, 2007). It can therefore be useful to reduce the mesh resolution. Here, convergence is accelerated by gradually mapping from a fine mesh onto a coarse one and back. This concept of multi-grid solvers is implemented in OpenFOAM in form of the *generalised geometric-algebraic multi-grid solver* (GAMG). For the present work, this linear solver proved to be numerically stable and yet faster than other linear solvers – even taking into account the time required for solving the momentum equation more often and the time required for solution mapping. As the simulations in this study are without exception performed using parallel computing, a sufficient number of cells on each computational core has to be ensured at any time. Therefore, the number of cells in the coarsest level was set to be 5000 cells, which results in a sufficient average of 78 cells per core (when solving on 64 cores). High-frequency errors are smoothed using the Gauss-Seidel method. For further reading on multi-grid solution techniques, refer to Versteeg and Malalasekera (2007).

Any iterative solution method produces residuals which – when having the matrix $\boldsymbol{A\phi} = \boldsymbol{K}$ for of a set of equations in mind – are

$$\mathbf{Res} = \boldsymbol{K} - \boldsymbol{A\phi} \tag{A.12}$$

For the momentum predictor, the solution is considered to be converged when the relative tolerance (between the initial and the final residual) is 0.05 or the absolute residual is 10^{-5}. If, in the course of several PIMPLE loops, the initial residual is already below this value, the momentum predictor is skipped.

The resulting solution of the velocity field is under-relaxed. The general form is

$$\phi_{n+1} = (1 - \alpha)\, \phi_n + \alpha \phi_{\text{solver}} \tag{A.13}$$

where – for the velocity field – the new value is $\tilde{\boldsymbol{u}}_{n+1}$, the field resulting from the solver is $\tilde{\boldsymbol{u}}_{\text{solver}}$, and the value from the previous iteration $\tilde{\boldsymbol{u}}_n$. The under-relaxation factor is set to $\alpha_{\tilde{u}} = 0.3$. Under-relaxation is often considered to be the last resort for numerical stability. The procedure prevents divergence of the solution, however, at the price of a significant increase in computing time. This applies in particular for the present work, as the flow investigated is numerically challenging.

Due to the assumptions made above, the velocity field does not necessarily satisfy continuity. Therefore, an explicit velocity correction is performed later in the solution algorithm.

Solve energy equation: The energy equation (Eqn. 2.9) in its Favre-filtered form is solved using the *preconditioned bi-conjugate gradient solver for asymmetric matrices* (PBICG). Preconditioning the matrix is required for solvers using the conjugate gradient method in order to ensure fast convergence. This operation, which basically transfers the set of linear equations into a more suitable form is provided by *diagonal incomplete lower-upper factorization* (DILU). The convergence criteria and under-relaxation factors are the same as for the momentum predictor.

Evaluate density: The evaluation of the density marks the beginning of the pressure corrector (PISO) loop. The function used to describe the density $\rho \sim T$ has already been presented in Chp. 3.1.2.

Update $\boldsymbol{H}(\tilde{\boldsymbol{u}})$ and $\boldsymbol{a}_{\mathbf{P}}$: The operator $\boldsymbol{H}(\tilde{\boldsymbol{u}})$ (Eqn. A.5) and the matrix coefficients a_{P} are reassembled in this step using the velocity field calculated before (either by the momentum predictor in the first PISO loop or by the velocity correction in any succeeding loop).

Solve pressure equation: The pressure equation (Eqn. A.10) is solved using the GAMG multi-grid linear solver. This choice is mainly motivated by the consideration, that the pressure solver accounts for the lion's share of the computational cost. Literature (e.g. de Villiers, 2006) therefore suggests the use of efficient multi-grid algorithms for the solution of the pressure equation. The solver settings are identical to those used in the momentum predictor. The results are subsequently under-relaxed for the use in the velocity correction after the fluxes are calculated in the next step. The under-relaxation factor depends on the stage the simulation is running in. After initialization, it is set to a low value of $\alpha_p = 0.3$, promoting stability. In an advanced convergence stage, it is increased to values as high as 0.75. Contrary to the choice of $\alpha_{\tilde{u}}$ in the momentum predictor above, the value of α_p has a high influence on the overall simulation convergence speed. This is due to the fact that the pressure residual generally drops significantly slower than the residual of the energy or the momentum equation. The pressure equation is therefore always the last equation to reach converge and thus defines the number of iterations in the PIMPLE loop.

Calculate fluxes: By solving Eqn. A.8, and considering the updated pressure field, the surface fluxes are determined. The resulting field is subsequently used for the linearization of the convection term in the next PIMPLE loop.

Explicit velocity correction: In order to ensure that the continuity condition is satisfied, the velocity field is corrected explicitly using Eqn. A.6.

Check continuity: As all surface fluxes are now known, the discretized continuity equation (Eqn. A.9) allows to calculate a new density. For this operation,

the diagonal solver in OpenFOAM is used, which directly produces an exact solution (no iterations are needed). Ideally, the density computed in this step does not deviate from the thermodynamical density, which is evaluated as a function of the temperature. By substracting both densities from each other and referring the result to the total mass within the domain, the continuity errors are computed. In this solution algorithm, three different kinds of errors are determined: The sum of the magnitude of all local errors within the domain, the scaled global deviation and the cumulative error, which keeps track of the error throughout the entire simulation.

The continuity check marks the end of the PISO loop, which can then be repeated for a predefined number of times. However, for the simulations in the present work, a larger number of PISO runs did not result in faster convergence. The pressure correction is thus performed only one time per PIMPLE loop.

Check convergence: A convergence criterion has already been introduced for the linear solvers. Yet, a second set is required in order to determine whether the PIMPLE loop has to be repeated. In the given cases, the loop is rerun if the residua in the momentum equation are above $5 \cdot 10^{-3}$ or the residuum in the pressure equation is above $5 \cdot 10^{-4}$.

Final PIMPLE loop: When the solution is converged, the solver performs the final run of the PIMPLE loop. This last run differs from the previous runs in two aspects: First, no under-relaxation and second, significantly tighter convergence criteria for the linear solvers. Furthermore, the absolute residuals are the only measure used to evaluate convergence. As the converged solution from the previous loop serves as a starting point, the lack of under-relaxation increases the convergence speed without provoking instability. A higher degree of accuracy is achieved in this final loop by requiring tighter convergence, which – in the final run – results in a larger number of iterations required by the linear solvers.

Update turbulence: Before initiating the calculations for the next timestep, the influence of the subgrid-scale turbulence model needs to be updated. This requires the solution of the transport equation for subgrid-scale turbulent kinetic energy (Eqn. 2.46). Like for the momentum equation, the multigrid solver is used. The resulting field is used to evaluate the subgrid-scale turbulent viscosity (Eqn. 2.47) and update the subgrid-scale stress tensor $\boldsymbol{\tau}_{\mathrm{sgs}}$ (see Eqn. 2.48) for the implicit momentum predictor in the next timestep.

Appendix B.

Numerical solution parameters

The following Table B.1 presents the solution details of all five simulations cases of the present work, including the physical time, the number of sampling points and the number of probe locations.

Table B.1.: Solution details of the three-dimensional mixed convection simulation cases.

Inertia-dominated	Physical time initialization	sampling	Number of sampling points	probe locations
$Gr/Re^2 = 0.17$	6.5148 sec	14.7880 sec	19,750	990
Equipollent	Physical time initialization	sampling	Number of sampling points	probe locations
$Gr/Re^2 = 0.72$	4.3553 sec	7.5885 sec	16,850	990
$Gr/Re^2 = 2.21$	6.1488 sec	14.5428 sec	14,862	990
$Gr/Re^2 = 4.12$	6.5608 sec	20.9020 sec	24,907	990
Buoyancy-dominated	Physical time initialization	sampling	Number of sampling points	probe locations
$Gr/Re^2 = 13.76$	16.3157 sec	11.7404 sec	10,580	990
$Gr/Re^2 = 25.80$				990

In Section 3.3, the computational mesh used for the simulations in this work was presented. When defining the general meshing concept, the target for the dimensionless wall distance as defined in Eqn. 3.6, was $\Delta z^+ = 0.6$. However, estimations were needed as the wall shear stress is a priori unknown. Before analyzing the simulation results, it is therefore important to prove that the mesh complied with this target in the actual simulations.
Figure B.1 shows the dimensionless wall distance for the $u_\infty = 0.35\,\mathrm{m/s}$, $\Delta T = 40\,\mathrm{K}$ case. As this setup features the highest flow velocity, it represents the „worst case“ concerning the wall distance. Throughout most of the domain, z^+ is below the anticipated value. At the inlet (left side of the figure), the lack of a developed boundary layer results in a high wall shear stress and thus in higher values of z^+. However, the inlet is the only region, where $z^+ > 1$ occurs (as emphasized by the black color in the figure). The turbulent structures that grow within the boundary layer result in an increasing shear stress at the wall. Near the outlet, the value of the dimensionless wall distance locally slightly exceeds 0.6. While the figure shows a plot for the high-velocity case mentioned above, the surface average for all other relevant flow conditions, including those featuring

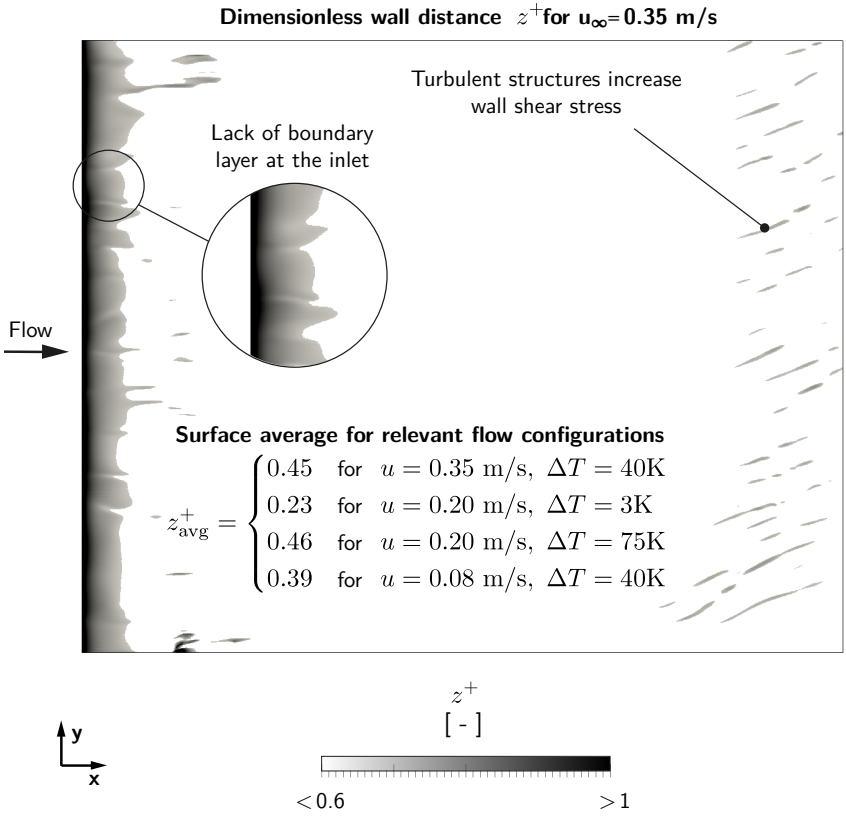


Figure B.1.: The dimensionless wall distance z^+ for an imposed velocity of $u_\infty = 0.35\,\text{m/s}$. The surface average for this case is $z^+_{\text{avg}} = 0.45$ and thus lower than the anticipated value of 0.6. A higher wall distance is observed at the inlet (left side) where the non-existing boundary layer causes a high wall shear stress. As turbulent structures develop across the domain, the resulting wall shear stress locally pushes z^+ to values higher than 0.6 (right side). However, the inlet is the only region where the value of 1.0 is exceeded.

a high wall temperature, is listed. For the case with a moderate imposed flow velocity and a low influence of buoyancy, the average z^+_{avg} ranges as low as 0.23. For the cases with high flow velocities and/or a high influence of buoyancy, the values are in the range of 0.45, which satisfies the requirement.

Appendix C.

Heat transfer mechanisms

The evaluation of the respective heat transport mechanisms has provided some insights into the heat transfer by three-dimensional mixed convection (see Chapter 5.1). Figure C.1 investigates, how an increasing free-stream velocity modifies the underlying mechanisms. The sampling location is at the top of the domain near the outlet, as the flow at this location is fully turbulent for all three cases. In general, there is little variation in the mechanisms involved. However, the observation that the local heat transfer rate increases with the velocity is confirmed by the magnitude of the source/sink terms, which is considerably higher for the high-velocity case. In all flow cases, advection is counterbalanced by turbulent transport in the outer boundary layer. In the high-velocity case, a higher level of advective heat transport can be observed. When increasing the velocity, the magnitude of the turbulent transport in the inner boundary layer continuously grows. This is due to the fact, that this mechanism compensates the heat introduced by diffusion. It is interesting to note that, in this region, both equipollent-mechanism cases also show a more or less prominent introduction of heat by advection. In the buoyancy-dominated case, however, the same flow removes heat. Also, the share of modeled transport (diffusion on the subgrid scale) increases with the imposed velocity. Yet, this finding is not surprising, given the observation that the resolved turbulent transport increases as well.

Figure C.2 presents the heat transport mechanisms in the boundary layer at the top of the domain near the outlet for a varying wall temperature. Comparing the mechanisms for the three cases allows to evaluate how the heat transport changes with increasing Grashof number and thus, how buoyancy affects the heat transfer: First, the turbulent intensity, and therefore the turbulent transport (on the resolved and on the modeled scales) significantly increases, which is reflected in the magnitude of the respective source/sink terms. For the low-temperature case, these terms are about 25 times lower than for the reference case, which is the consequence of the non-turbulent flow state. In the corresponding figure, the scale has been adapted to match these low values. Here, turbulent transport is virtually non-existent.
Second, the boundary layer region influenced by heat transfer grows. Note that the counterbalancing of advective and turbulent transport is still present at $z/\delta_1 \approx 30$ in the high-temperature case, which is roughly one order in magnitude larger than for the low-temperature case.

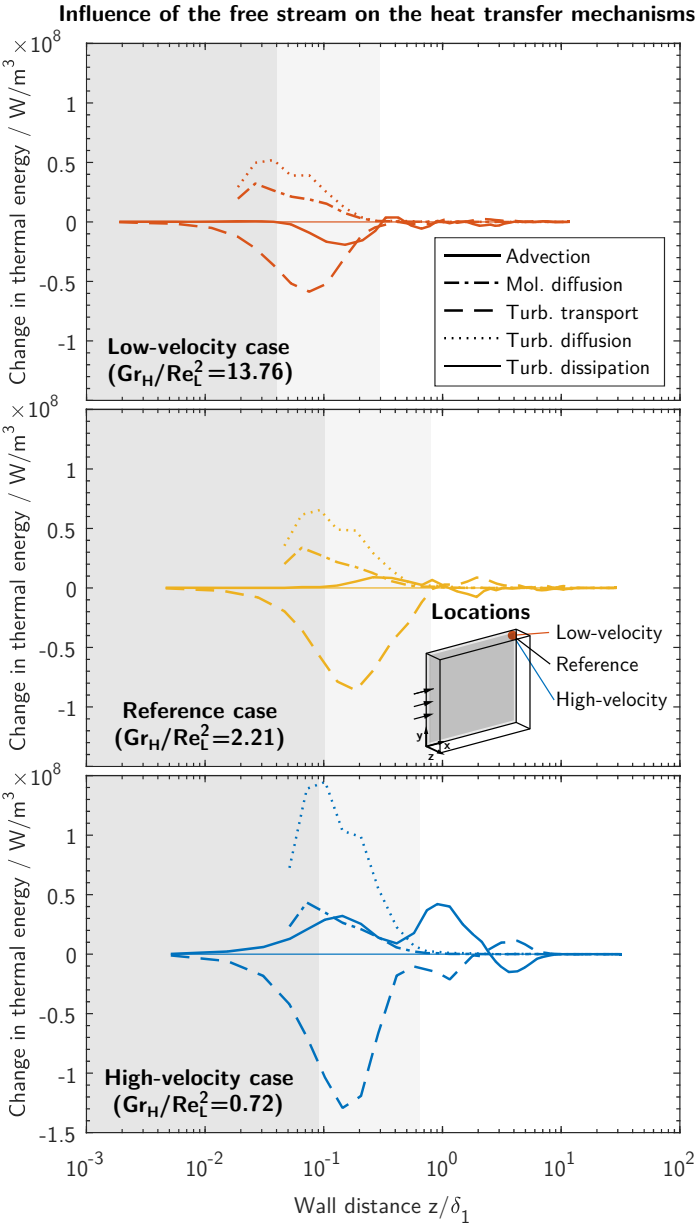


Figure C.1.: Evaluation of how an increase in free-stream velocity influences the heat transport mechanisms in the boundary layer. Again the shading represents the boundary layer regions for the respective case.

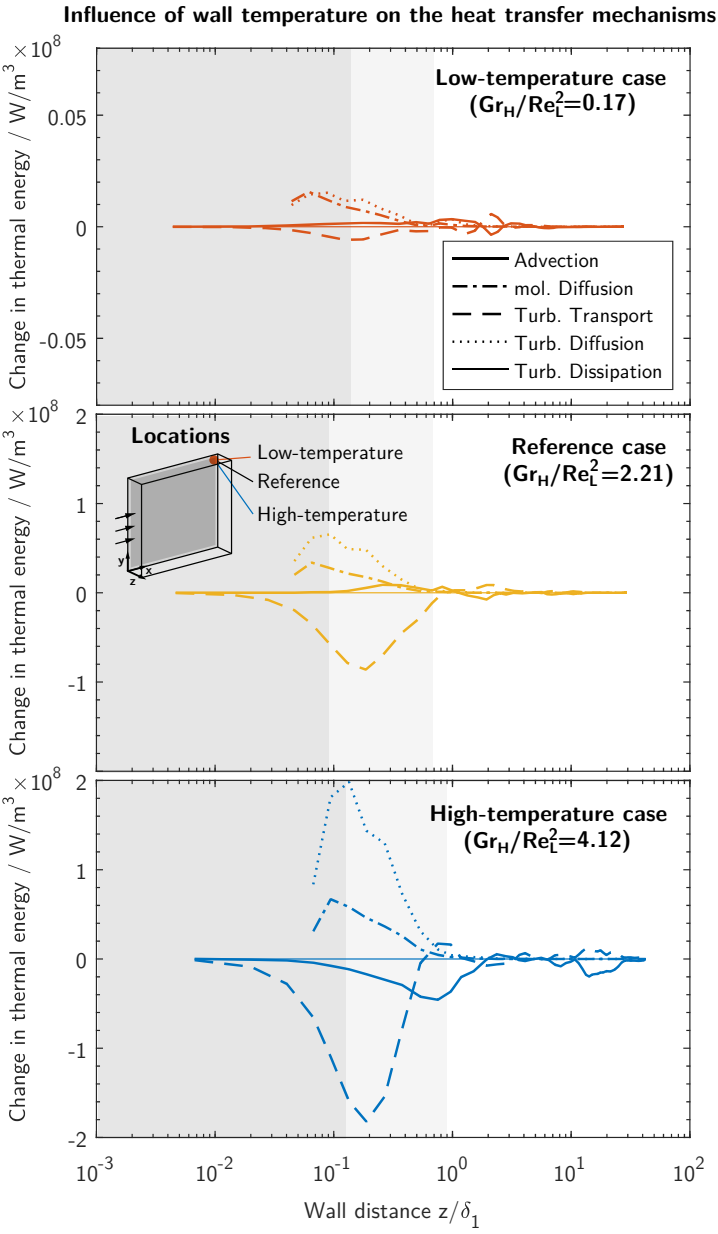


Figure C.2.: Evaluation of the influence of buoyancy on the heat transport mechanisms. Note the different scale of the low-temperature case.

Third, as discussed above, advection starts to remove heat instead of introducing it. In the high-temperature case – as in the buoyancy-dominated case above – the peak in advective transport at $z/\delta_1 \approx 10^0$ removes heat. In cases with little or moderate influence of buoyancy, the opposite is the case. Consequently, this particular peak can be attributed to the vertical updraft, while the advective transport peaks in the other cases are related to the free stream.

Appendix D.

OpenFOAM dictionary files

In this appendix, representative examples of the OpenFOAM dictionary files are shown. This includes all dictionaries concerning the numerical parameters, the turbulence, the thermophysical properties, and the boundary conditions. The choice of the respective boundary conditions has been discussed in Chapter 3.3 and will not be further commented here. As any succeeding simulation would most likely feature a different computational mesh, dictionaries concerning the mesh (blockMeshDict, topoSetDict, decomposeParDict, ...) will be skipped.

The **controlDict** dictionary includes all relevant information of the simulation:

```
/*--------------------------------*- C++ -*----------------------*\
|=========                 |                                      |
|\\      /  F ield         | OpenFOAM: The Open Source CFD Toolbox|
| \\    /   O peration     | Version:  2.3.0                      |
|  \\  /    A nd           | Web:      www.OpenFOAM.org           |
|   \\/     M anipulation  |                                      |
\*---------------------------------------------------------------*/

FoamFile
{
    version     2.3;
    format      ascii;
    class       dictionary;
    object      controlDict;
}
// * * * * * * * * * * * * * * * * * * * * * * * * * * * * * * * * //

application     convectionFoam;
startFrom       latestTime;
startTime       0;
stopAt          endTime;
endTime         10000;
deltaT          0.0004;
writeControl    timeStep;
writeInterval   250;
purgeWrite      0;
writeFormat     ascii;
writePrecision  6;
writeCompression off;
timeFormat      general;
timePrecision   6;
runTimeModifiable true;
adjustTimeStep  yes;
maxCo                   0.85;
```

```
libs
        (
        "libLEMOS-2.3.x.so"
        "libOpenFOAM.so"
        "libsampling.so"
        "libsimpleSwakFunctionObjects.so"
        "libswakFunctionObjects.so"
        );


functions
        (
        profiles
                {
                type sets;
                enabled true;
                verbose true;
                interpolationScheme cell;
                outputControlMode outputTime;
                setFormat raw;
                fields
                        (
                        U
                        k
                        T
                        p_rgh
                        rho
                        );
                sets
                        (
                        profile_1000_50
                                {
                                type midPoint;
                                axis xyz;
                                start ( 1.000010 0.050010 -0.1 );
                                end ( 1.000010 0.050010 0.5 );
                                }

                        profile_1000_54
                                {
                                type midPoint;
                                axis xyz;
                                start ( 1.000010 0.054010 -0.1 );
                                end ( 1.000010 0.054010 0.5 );
                                }

                                /* --- a huge number of sets --- */

                        );
                }
        );
```

The **fvSolution** dictionary sets the properties of the PIMPLE loop and the linear solvers:

```
FoamFile
{
    version     2.3;
    format      ascii;
    class       dictionary;
    location    "system";
    object      fvSolution;
}
// * * * * * * * * * * * * * * * * * * * * * * * * * * * * * * * * * * * * //

solvers
{
    "rho.*"
    {
        solver          PCG;
        preconditioner  DIC;
        tolerance       0;
        relTol          0;
    }

    p_rgh
    {
        solver           GAMG;
        tolerance        1e-5;
        relTol           0.01;
        smoother         GaussSeidel;
        cacheAgglomeration true;
        nCellsInCoarsestLevel 5000;
        agglomerator     faceAreaPair;
        mergeLevels      1;
    }

    p_rghFinal
    {
        $p_rgh
        smoother        DICGaussSeidel;
        tolerance       1e-08;
        relTol          0;
    }

    k
    {
        solver          GAMG;
        tolerance       1e-5;
        relTol          0.05;
        smoother        GaussSeidel;
        nPreSweeps      0;
        nPostSweeps     2;
        cacheAgglomeration true;
        nCellsInCoarsestLevel 5000;
        agglomerator    faceAreaPair;
        mergeLevels     1;
    }
```

```
    kFinal
    {
        $k
        smoother        GaussSeidel;
        tolerance       1e-08;
        relTol          0;
    }

    "U"
    {
        solver          GAMG;
        tolerance       1e-5;
        relTol          0.05;
        smoother        GaussSeidel;
        nPreSweeps      0;
        nPostSweeps     2;
        cacheAgglomeration true;
        nCellsInCoarsestLevel 5000;
        agglomerator    faceAreaPair;
        mergeLevels     1;
    }

    UFinal
    {
        $U;
        smoother        GaussSeidel;
        tolerance       1e-08;
        relTol          0;
    }

    h
    {
        solver          PBiCG;
        preconditioner  DILU;
        tolerance       1e-5;
        relTol          0.01;
    }

    hFinal
    {
        $h;
        preconditioner  DILU;
        tolerance       1e-8;
        relTol          0;
    }
}

PIMPLE
{
    momentumPredictor yes;
    nNonOrthogonalCorrectors 0;
    nCorrectors          1;
    nOuterCcorrectors    35;
    turbOnFinalIterOnly true;
```

```
    residualControl
    {
        U
        {
                tolerance  5e-3;
                relTol      0;
        }
        p_rgh
        {
                tolerance  5e-4;
                relTol      0;
        }
    }
}

relaxationFactors
{
    fields
    {
        p_rgh      0.55;
        p_rghFinal    1;
    }
    equations
    {
        "U|k|h"      0.3;
        "(U|k|h)Final"    1;
    }
}
```

In **fvOptions**, a temperature constraint is defined:

```
FoamFile
{
    version     2.3;
    format      ascii;
    class       dictionary;
    location    "system";
    object      fvOptions;
}
// * * * * * * * * * * * * * * * * * * * * * * * * * * * * * * * * * * * * //

source1
{
    type            temperatureLimitsConstraint;
    selectionMode   all;
    active          true;

        temperatureLimitsConstraintCoeffs
        {
            Tmin      290;
            Tmax      370;
        }
}
```

fvSchemes defines the numerical schemes:

```
FoamFile
{
    version     2.3;
    format      ascii;
    class       dictionary;
    object      fvSchemes;
}
// * * * * * * * * * * * * * * * * * * * * * * * * * * * * * * * * * * * * //

ddtSchemes
{
    default          backward;
}

gradSchemes
{
    default          Gauss linear;
}

divSchemes
{
    default          none;
    div(phi,U)       Gauss GranmaV 0.4;
    div(phi,h)       Gauss limitedLinear 1;
    div(phi,k)       Gauss Granma 0.4;
    div(phi,K)       Gauss linear;
    div((muEff*dev2(T(grad(U))))) Gauss linear;
}

laplacianSchemes
{
    default          Gauss linear corrected;
}

interpolationSchemes
{
    default          linear;
}

snGradSchemes
{
    default          corrected;
}

fluxRequired
{
    default          no;
    p_rgh;
}
```

All fluid thermophysical properties are given in **thermophysicalProperties**:

```
FoamFile
{
    version     2.3;
    format      ascii;
    class       dictionary;
    location    "constant";
    object      thermophysicalProperties;
}
// * * * * * * * * * * * * * * * * * * * * * * * * * * * * * * * * * * * * //

thermoType
{
    type            heRhoThermo;
    mixture         pureMixture;
    transport       polynomial;
    thermo          hPolynomial;
    equationOfState icoPolynomial;
    specie          specie;
    energy          sensibleEnthalpy;
}
mixture
{
    specie
    {
        nMoles          1;
        molWeight       1;
    }
    equationOfState
    {
        rhoCoeffs<8>    ( 1120.04  -0.421164  0  0  0  0  0  0 );
    }
    thermodynamics
    {
        Hf                                  0;
        Sf                                  0;
        CpCoeffs<8>     ( 4180  0  0  0  0  0  0  0 );
        }
    transport
    {
        muCoeffs<8>     ( 0.000532019  -0.000000200053  0  0  0  0  0  0 );
        kappaCoeffs<8>  ( 0.654  0  0  0  0  0  0  0 );
    }
}
```

The dictionary **turbulenceProperties** sets LES as turbulence treatment:

```
FoamFile
{
    version     2.3;
    format      ascii;
    class       dictionary;
    location    "constant";
    object      turbulenceProperties;
}
// * * * * * * * * * * * * * * * * * * * * * * * * * * * * * * * * * * * * //
simulationType LESModel;
```

The following **LESProperties** specifies the subgrid-scale turbulence model and the corresponding filter:

```
FoamFile
{
    version     2.3;
    format      ascii;
    class       dictionary;
    location    "constant";
    object      LESProperties;
}
// * * * * * * * * * * * * * * * * * * * * * * * * * * * * * * * * * * * * //

LESModel        oneEqEddy;
printCoeffs     on;
delta           cubeRootVol;

cubeRootVolCoeffs
{
    deltaCoeff      1;
}
```

Field and boundary condition for the sgs conductivity **alphaSgs** and for the sgs viscosity **muSgs**. For both, the boundary conditions are identical.

```
FoamFile
{
    version     2.3;
    format      ascii;
    class       volScalarField;
    location    "11.3568";
    object      alphaSgs; /* --- or muSgs --- */
}
// * * * * * * * * * * * * * * * * * * * * * * * * * * * * * * * * * * * * //

dimensions      [1 -1 -1 0 0 0 0];

internalField   nonuniform List<scalar>
    53634150
    (
    /* --- internal field ---*/
    );

boundaryField
{
    hotWall
    {
        type            zeroGradient;
    }
    top
    {
        type            zeroGradient;
    }
    downstream
    {
        type            zeroGradient;
    }
```

```
    channel
    {
        type            zeroGradient;
    }
    inlet
    {
        type            zeroGradient;
    }
    bottom
    {
        type            zeroGradient;
    }
}
```

Boundary condition for the subgrid-scale turbulent kinetic energy **k**:

```
FoamFile
{
    version     2.3;
    format      ascii;
    class       volScalarField;
    location    "11.3568";
    object      k;
}
// * * * * * * * * * * * * * * * * * * * * * * * * * * * * * * * * * * * * //

dimensions      [0 2 -2 0 0 0 0];

internalField   nonuniform List<scalar>
    53634150
    (
    /* --- internal field ---*/
    );

boundaryField
{
    hotWall
    {
        type            fixedValue;
        value           uniform 0;
    }
    top
    {
        type            inletOutlet;
        inletValue      uniform 3e-05;
        value           nonuniform List<scalar>
                45900
                (
                /* --- boundary field ------*/
                );
    }
    downstream
    {
        type            zeroGradient;
    }
```

```
    channel
    {
        type            inletOutlet;
        inletValue      uniform 3e-05;
        value           nonuniform List<scalar>
                52275
                (
                /* ---- boundary field ---*/
                );
    }
    inlet
    {
        type            fixedValue;
        value           uniform 3e-05;
    }
    bottom
    {
        type            inletOutlet;
        inletValue      uniform 3e-05;
        value           nonuniform List<scalar>
                45900
                (
                /* --- boundary field ------*/
                );
    }
}
```

Boundary conditions for the velocity field **U**:

```
FoamFile
{
    version     2.3;
    format      ascii;
    class       volVectorField;
    location    "11.3568";
    object      U;
}

// * * * * * * * * * * * * * * * * * * * * * * * * * * * * * * * * * * * * //

dimensions      [0 1 -1 0 0 0 0];

internalField   nonuniform List<vector>
53634150
(
/* --- approximatly 1.7 GB of field data --- */
);

boundaryField
{
    hotWall
    {
        type            fixedValue;
        value           uniform (0 0 0);
    }
```

```
    top
    {
        type            pressureInletOutletParSlipVelocity;
        value           nonuniform List<vector>
                        45900
                        (
                        /* --- boundary field ---*/
                        );
    }
    downstream
    {
        type            zeroGradient;
    }
    channel
    {
        type            pressureInletOutletParSlipVelocity;
        value           nonuniform List<vector>
                        52275
                        (
                        /* --- boundary field ---*/
                        );
    }
    inlet
    {
        type            decayingTurbulenceInflowGenerator;
        LField          uniform 0.04;
        refField        uniform (0.2 0 0);
        RField          uniform (3.5e-05 1.75e-05 1.75e-05 3.5e-05
                                 1.75e-05 3.5e-05);
        direction       1;
        value           nonuniform List<vector>
                        36900
                        (
                        /* --- list of values for the boundary field,
                            including the synthetic turbulence ---*/
                        );
    }
    bottom
    {
        type            pressureInletOutletParSlipVelocity;
        value           nonuniform List<vector>
                        45900
                        (
                        /* --- boundary field ---*/
                        );
    }
}
```

Boundaries for the pressure **p** and **prgh**:

```
FoamFile
{
    version     2.3;
    format      ascii;
    class       volScalarField;
    location    "11.3568";
    object      p;
}
// * * * * * * * * * * * * * * * * * * * * * * * * * * * * * * * * * * * * //

dimensions      [1 -1 -2 0 0 0 0];

internalField   nonuniform List<scalar>
53634150
(
/* --- calculated internal field ---  */
);

boundaryField
{
    hotWall
    {
        type            calculated;
        value           nonuniform List<scalar>
                3345600
                (
                /* --- calculated field --- */
                );
    }
    top
    {
        type            calculated;
        value           nonuniform List<scalar>
                45900
                (
                /* --- calculated field --- */
                );
    }
    downstream
    {
        type            calculated;
        value           nonuniform List<scalar>
                36900
                (
                /* --- calculated field --- */
                );
    }
    channel
    {
        type            calculated;
        value           nonuniform List<scalar>
                52275
                (
                /* --- calculated field --- */
                );
    }
```

```
    inlet
    {
        type            calculated;
        value           nonuniform List<scalar>
                36900
                (
                /* --- calculated field --- */
                );
    }
    bottom
    {
        type            calculated;
        value           uniform 100000;
    }
}
```

```
FoamFile
{
    version     2.3;
    format      ascii;
    class       volScalarField;
    location    "11.3568";
    object      p_rgh;
}
// * * * * * * * * * * * * * * * * * * * * * * * * * * * * * * * * * * * * //
dimensions      [1 -1 -2 0 0 0 0];

internalField   nonuniform List<scalar>
53634150
(
/* --- internal field data --- */
);

boundaryField
{
    hotWall
    {
        type            fixedFluxPressure;
        gradient        nonuniform List<scalar>
                3345600
                (
                /* --- calculated boundary field for gradient --- */
                );
        value           nonuniform List<scalar>
                3345600
                (
                /* --- calculated boundary field --- */
                );
    }
    top
    {
        type            totalYPressure;
        rho             rho;
        phi             phi;
        U               U;
```

```
        psi             none;
        gamma           1;
        p0              uniform 100000;
        value           nonuniform List<scalar>
                45900
                (
                /* --- boundary field --- */
                );
    }
    downstream
    {
        type            zeroGradient;
    }
    channel
    {
        type            totalYPressure;
        rho             rho;
        phi             phi;
        U               U;
        psi             none;
        gamma           1;
        p0              uniform 100000;
        value           nonuniform List<scalar>
                52275
                (
                /* --- boundary field --- */
                );
    }
    inlet
    {
        type            fixedValue;
        value           uniform 100000;
    }
    bottom
    {
         type            totalYPressure;
        rho             rho;
        phi             phi;
        U               U;
        psi             none;
        gamma           1;
        p0              uniform 100000;
        value           nonuniform List<scalar>
        45900
        (
        /* --- boundary field --- */
        );
    }
}
```

Temperature **T** boundary condition:

```
FoamFile
{
    version     2.3;
    format      ascii;
    class       volScalarField;
    location    "11.3568";
    object      T;
}
/ * * * * * * * * * * * * * * * * * * * * * * * * * * * * * * * * * * * * //

dimensions      [0 0 0 1 0 0 0];

internalField   nonuniform List<scalar>
53634150
(
/* --- field data --- */
);

boundaryField
{
    hotWall
    {
        type            fixedValue;
        value           nonuniform List<scalar>
                3345600
                (
                /* --- boundary field for the wall, either 298.15 K or
                     wall temperature --- */
                );
    }
    top
    {
        type            inletOutlet;
        inletValue      uniform 298.15;
        value           nonuniform List<scalar>
                45900
                (
                /* --- boundary field --- */
                );
    }
    downstream
    {
        type            zeroGradient;
    }
    channel
    {
        type            inletOutlet;
        inletValue      uniform 298.15;
        value           nonuniform List<scalar>
                52275
                (
                /* --- boundary field --- */
                );
    }
```

```
    inlet
    {
        type            fixedValue;
        value           uniform 298.15;
    }
    bottom
    {
        type            inletOutlet;
        inletValue      uniform 298.15;
        value           nonuniform List<scalar>
                45900
                (
                /* --- boundary field --- */
                );
    }
}
```

Appendix E.

Modified source code

This section includes C++ source code that has been modified. The code of the convectionFoam solver will be skipped, as it is widely identical to the buoyantPimpleFoam solver. The changes incorporated mostly cover the elimination of compressible effects.

Granma scheme is the modified version of the gamma scheme. The file granma.H is shown here, the corresponding granma.C is – in its code – identical to gamma.C.

```
Class
    Foam::GranmaLimiter

Description
    Class with limiter function which returns the limiter for the
    Granma differencing scheme based on phict obtained from the
    LimiterFunc class.

    Used in conjunction with the template class LimitedScheme.

SourceFiles
    Granma.C

\*---------------------------------------------------------------------------*/

#ifndef Granma_H
#define Granma_H

#include "vector.H"

// * * * * * * * * * * * * * * * * * * * * * * * * * * * * * * * * * * * * //

namespace Foam
{

/*---------------------------------------------------------------------------*\
                        Class GranmaLimiter Declaration
\*---------------------------------------------------------------------------*/

template<class LimiterFunc>
class GranmaLimiter
:
    public LimiterFunc
{
    scalar k_;
```

```
public:

    GranmaLimiter(Istream& is)
    :
        k_(readScalar(is))
    {
        if (k_ < 0 || k_ > 1)
        {
            FatalIOErrorIn("GranmaLimiter(Istream& is)", is)
                << "coefficient = " << k_
                << " should be >= 0 and <= 1"
                << exit(FatalIOError);
        }

        // Rescale k_ to be >= 0 and <= 0.5 (TVD conformant)
        // and avoid the /0 when k_ = 0
        k_ = max(k_/2.0, SMALL);
    }

    scalar limiter
    (
        const scalar cdWeight,
        const scalar faceFlux,
        const typename LimiterFunc::phiType& phiP,
        const typename LimiterFunc::phiType& phiN,
        const typename LimiterFunc::gradPhiType& gradcP,
        const typename LimiterFunc::gradPhiType& gradcN,
        const vector& d
    ) const
    {
        scalar phict = LimiterFunc::phict
        (
            faceFlux, phiP, phiN, gradcP, gradcN, d
        );

                if (phict > 1)
                        phict = -phict;

        return min(max(phict/k_, 0), 1);
    }
};

// * * * * * * * * * * * * * * * * * * * * * * * * * * * * * * * * * * * * //

} // End namespace Foam

// * * * * * * * * * * * * * * * * * * * * * * * * * * * * * * * * * * * * //
#endif
```

A slight modification in the totalPressure boundary condition only considers velocities normal to the boundary condition: **totalYPressure**

```
const fvPatchField<scalar>& rho =
        patch().lookupPatchField<volScalarField, scalar>(rhoName_);
        operator==(p0p -
        0.5*rho*(1.0 - pos(phip))*magSqr(Up & phip.patch().nf()));
```

initFoam is the solver used to initialize the cases. It is a modified version of buoyantSimpleFoam:

```
Application
    initFoam

Description
    Steady-state solver for buoyant, turbulent flow of
    compressible fluids,
    including radiation, for ventilation and heat-transfer
    with linearly increasing gravity

\*---------------------------------------------------------------------*/

#include "fvCFD.H"
#include "rhoThermo.H"
#include "RASModel.H"
#include "radiationModel.H"
#include "simpleControl.H"
#include "fvIOoptionList.H"
#include "fixedFluxPressureFvPatchScalarField.H"

// * * * * * * * * * * * * * * * * * * * * * * * * * * * * * * * * * * * //

int main(int argc, char *argv[])
        {const dimensionedScalar gunits("gunits", dimensionSet
             (0,1,-2,0,0,0,0), 1);

    #include "setRootCase.H"
    #include "createTime.H"
    #include "createMesh.H"
    #include "readGravitationalAcceleration.H"
    #include "readGIncrease.H"
    #include "readStartIncreaseTime.H"
    #include "createFields.H"
    #include "createFvOptions.H"
    #include "createRadiationModel.H"
    #include "initContinuityErrs.H"

    simpleControl simple(mesh);

// * * * * * * * * * * * * * * * * * * * * * * * * * * * * * * * * * * * //

    Info<< "\nIncreasing gravity at timestep " << startIncreaseTime.
         value() << nl << endl;

    Info<< "\nStarting time loop\n" << endl;


    while (simple.loop())
    {
        Info<< "Time = " << runTime.timeName() << nl << endl;



        // Pressure-velocity SIMPLE corrector
```

```
        if ((runTime.value()-startIncreaseTime.value()+1)*
             increaseFactor.value() <= 9.81 && runTime.value()>=
             startIncreaseTime.value())
        {

                // linear increase in Gravitation
                g=gunits*((runTime.value()-startIncreaseTime.value()+1)
                     *(increaseFactor.value()))*vector(0,-1,0);

                Info<< "  Gravity increase = " << increaseFactor.value()
                     << " to  Gravity = " << g.value()<< nl << endl;

                Info<< "  Re-Calculating field g.h\n" << endl;
                gh = g & mesh.C();
                ghf = g & mesh.Cf();
        }

        {
        #include "UEqn.H"
        #include "EEqn.H"
        #include "pEqn.H"
        }

        turbulence->correct();

        runTime.write();

        Info<< "ExecutionTime = " << runTime.elapsedCpuTime() << " s"
            << "  ClockTime = " << runTime.elapsedClockTime() << " s"
            << "  Gravity = " << g.value()<< nl << endl;

    }

    Info<< "End\n" << endl;

    return 0;
}
```

with the two files readGIncrease.H

```
Info<< "\nReading g increase" << endl;
uniformDimensionedScalarField increaseFactor
(
        IOobject
        (
                "increaseFactor",
                runTime.constant(),
                mesh,
                IOobject::MUST_READ,
                IOobject::NO_WRITE
        )
);
```

and readStartIncreaseTime.H

```
Info<< "\nReading g increase start time\n" << endl;
uniformDimensionedScalarField startIncreaseTime
(
        IOobject
        (
                "startIncreaseTime",
                runTime.constant(),
                mesh,
                IOobject::MUST_READ,
                IOobject::NO_WRITE
        )
);
```

which requires an input file ./constant/startIncreaseTime and ./constant/increaseFactor:

```
FoamFile
{
    version     2.3;
    format      ascii;
    class       uniformDimensionedScalarField;
    location    "constant";
    object      increaseFactor;
}
// * * * * * * * * * * * * * * * * * * * * * * * * * * * * * * * * * * * * //

dimensions      [0 1 -3 0 0 0 0];
value           0.002;
```

```
FoamFile
{
    version     2.3;
    format      ascii;
    class       uniformDimensionedScalarField;
    location    "constant";
    object      startIncreaseTime;
}
// * * * * * * * * * * * * * * * * * * * * * * * * * * * * * * * * * * * * //

dimensions      [0 0 1 0 0 0 0];
value           1300;
```

Glossary

2D mixed convection: The combination of buoyancy-driven natural convection and forced convection where the direction of the imposed flow is parallel to the direction of gravity. The buoyant updraft accelerates the boundary layer (aiding flow) or decelerates the boundary layer (opposing flow). An example is a heated vertical plate with a flow in vertical direction (p. 33).

3D mixed convection: The combination of buoyancy-driven natural convection and forced convection where the direction of gravity is perpendicular to the flow. Consequently, the boundary layer experiences an acceleration in vertical direction. An example is a heated vertical plate with an horizontal flow (p. 35).

Advective heat transport: The transport of a fluid property (in the context of this work: enthalpy) by the fluid flow itself. For heat transfer, this mechanism often is referred to as convective transport (p. 101).

Buoyancy-dominated mixed convection: A mixed convection regime where the influence of buoyancy dominates. The regime is characterized by large values of the Richardson number $\mathrm{Gr}/\mathrm{Re}^2$ (p. 116).

Diffusive heat transport: The transport of heat, driven by the temperature gradient. It is referred to as thermal conduction (molecular diffusion) (p. 101). A second diffusive heat transport mechanism in the present work is the transport described by the turbulence model on the subgrid scale (turbulent sgs diffusion) (p. 21).

Equipollent mechanism mixed convection: A mixed convection regime where both mechanisms – buoyancy and inertia – play a role. The regime is characterized by medium values of the Richardson number $\mathrm{Gr}/\mathrm{Re}^2$ (p. 116).

Hairpin vortex: A turbulent coherent structure found in turbulent wall boundary layers. Its shape reminds of a hairpin with "legs" being located close to the wall and the "top" in the outer boundary layer (p. 27).

Inertia-dominated mixed convection: A mixed convection regime where the free-stream interia dominates. The regime is characterized by small values of the Richardson number $\mathrm{Gr}/\mathrm{Re}^2$ (p. 116).

Λ-structure: A particular turbulent coherent structure found in wall-bounded flows in the zone of laminar-turbulent transition (p. 103).

LEMOS: An extension for OpenFOAM 2.3 provided by the University of Rostock. This libary was used in the present work to generate and impose synthetic turbulence on the inlet boundary condition (p. 65).

Low-velocity streak: A turbulent coherent structure in the lower wall boundary layer being characterized by its elongated shape. In the present work, streaks occur in the course of laminar-turbulent transition. The cycle of its generation and dissociation is referred to as streak instability cycle and is mostly independent from the free flow (p. 25).

PIMPLE: The combination of PISO and SIMPLE solution algorithms in OpenFOAM (p. 60).

PISO: The Pressure Implicit with Spliting of Operator solution algorithm for transient simulations in CFD (p. 60).

Resolved scales: The scales larger than the filter width in large-eddy simulations, being fully resolved by the simulation. All relevant processes are supposed to occur on these scales (p. 17).

Self-similarity: Two boundary layers are self-similar when their profiles exhibit the same value of a dimensionless (scaled) property at the same dimensionless (scaled) wall distance (p. 24) and (p. 136).

SIMPLE: The Semi-Implicit Method for Pressure-Linked Equations algorithm for steady-state simulations in CFD. It exhibits high numerical stability by taking advantage of under-relaxation (p. 60).

Subgrid scale: The scales smaller than the filter width in large-eddy simulations. All processes on these scales are modeled by a subgrid-scale model (p. 17).

Tollmien-Schlichting waves: Primary instabilities ahead of a laminar-turbulent transition for wall-bounded flows (p. 103).

Turbulent kinetic energy (TKE): The energy carried by the turbulent velocity fluctuations. TKE is a measure of the degree of turbulence in a flow. It is commonly understood as a property being subject to conservation – thus a transport equation exists in many turbulence models (p. 11).